

Lanthanide doped spectral conversion materials for solar cells

Proefschrift

ter verkrijging van de graad van doctor
aan de Technische Universiteit Delft,
op gezag van de Rector Magnificus prof.ir. K.C.A.M. Luyben,
voorzitter van het College voor Promoties,
in het openbaar te verdedigen op dinsdag 2 september 2014 om 15.00 uur
door Otmar Melvin TEN KATE
ingenieur in de scheikundige technologie
geboren te Delft.

Dit proefschrift is goedgekeurd door de promotor:

Prof dr. P. Dorenbos

Copromotor: Dr. E. van der Kolk

Samenstelling promotiecommissie:

Rector Magnificus,	voorzitter
Prof. dr. P. Dorenbos	Technische Universiteit Delft, promotor
Dr. E. van der Kolk,	Technische Universiteit Delft, copromotor
Prof. dr. E.H. Brück,	Technische Universiteit Delft
Prof. dr. L.D.A. Siebbeles,	Technische Universiteit Delft
Prof. dr. A. Meijerink,	Universiteit Utrecht
Dr. H.T.J.M. Hintzen,	Technische Universiteit Delft
Dr. K.W. Krämer,	Universität Bern
Prof. dr. C. Pappas,	Technische Universiteit Delft, reservelid

This work is part of the Joint Solar Programme of the Foundation of Fundamental Research on Matter (FOM), which is part of the Netherlands Organisation for Scientific Research (NWO), and was financially supported by HyET Solar. The research was carried out at Delft University of Technology and Eindhoven University of Technology.

Cover design: Oleksandra Ivashchenko

Printed by: Proefschriftmaken.nl | Uitgeverij BOXpress

ISBN: 978-90-8891-930-5

Table of contents

List of abbreviations	8
Chapter 1: Introduction	9
1.1 Solar cells	9
1.2 Solar spectral conversion	11
1.3 Luminescent solar concentrators	15
1.4 Luminescent materials	16
1.5 Scope and overview of the thesis	19
1.6 References	20
Chapter 2: Efficiency enhancement calculations of state-of-the-art solar cells by luminescent layers with spectral shifting, quantum cutting, and quantum tripling function	23
2.1 Introduction	24
2.2 Theory	26
2.3 Results and discussion	31
2.4 Conclusions	45
2.5 Appendix	46
2.6 References	48
Chapter 3: Yb³⁺ doped LaSi₃N₅ and YSi₃N₅ with low energy charge transfer for near-infrared light-emitting diode and solar cell application	51
3.1 Introduction	52
3.2 Experimental	53
3.3 Experimental results and discussion	54
3.4 Energy level scheme of LaSi ₃ N ₅ :Ln ²⁺ ,Ln ³⁺	62
3.5 Conclusions	65
3.6 References	66

Chapter 4: $4f$ and $5d$ energy levels of the divalent and trivalent lanthanide ions in $M_2Si_5N_8$ ($M = Ca, Sr, Ba$)	69
4.1 Introduction	70
4.2 Experimental	71
4.3 Phase formation	72
4.4 Optical properties of undoped and lanthanide doped $M_2Si_5N_8$	75
4.5 Energy schemes	86
4.6 Conclusions	94
4.7 References	95
Chapter 5: Enhanced 1G_4 emission in $NaLaF_4:Pr^{3+}, Yb^{3+}$ and charge transfer in $NaLaF_4:Ce^{3+}, Yb^{3+}$ studied by Fourier transform luminescence spectroscopy	99
5.1 Introduction	99
5.2 Experimental	101
5.3 Results and discussion	101
5.4 References	108
Chapter 6: Quantum tripling in Tm^{3+} doped La_2BaZnO_5 phosphors for efficiency enhancement of small band gap solar cells	111
6.1 Introduction	111
6.2 Experimental	114
6.3 Results and discussion	115
6.4 Conclusions	124
6.5 References	124
Chapter 7: Quantifying self-absorption losses in luminescent solar concentrators	127
7.1 Introduction	128
7.2 Self-absorption in a 2D circular LSC	129
7.3 Self-absorption in a 3D circular LSC	138

7.4 Conclusions	145
7.5 References	146
Chapter 8: Tm²⁺ doped materials for luminescent solar concentrators without self-absorption	149
8.1 Introduction	149
8.2 Experimental	151
8.3 Results and discussion	152
8.4 Conclusions	161
8.5 References	162
Chapter 9: Optical properties of Eu²⁺/Eu³⁺ mixed valence, silicon nitride based materials	165
9.1 Introduction	165
9.2 Experimental	167
9.3 Results and discussion	168
9.4 Conclusions	183
9.5 References	184
Chapter 10: Low energy 4<i>f</i>-5<i>d</i> transitions in CaLaSiN₃:Ln³⁺ with low degree of cross-linking between SiN₄ tetrahedra	187
10.1 Introduction	187
10.2 Experimental	189
10.3 Results and discussion	190
10.4 Conclusions	198
10.5 References	199
Summary	201
Samenvatting	207

Table of contents

Acknowledgements	213
Curriculum vitae	215
List of publications	217

List of abbreviations

a-Si	Amorphous silicon
CGS	Copper gallium selenide, CuGaSe_2
CIGS	Copper indium gallium selenide, $\text{CuIn}_x\text{Ga}_{1-x}\text{Se}_2$
CIS	Copper indium selenide, CuInSe_2
c-Si	Crystalline silicon
CT	Charge transfer
DFT	Density functional theory
IQE	Internal quantum efficiency
IR	Infrared
LED	Light-emitting diode
Ln	Lanthanide
LSC	Luminescent solar concentrator
pc-Si	Polycrystalline silicon
PV	Photovoltaic
QC	Quantum cutting
SQ-limit	Shockley-Queisser limit
TGA	Themogravimetric analysis
UV	Ultraviolet
XRD	X-ray diffraction

Chapter 1

Introduction

1.1 Solar cells

The amount of solar energy reaching the earth within one hour is larger than the entire human energy consumption within one year. [1] This, together with the fact that the sun will continue supplying the earth with solar energy for the next billions of years, indicates that using the energy from the sun is a sustainable way to substitute the depleting fossil fuel reserves and to provide the world in its increasing energy demand.

The direct generation of electricity out of solar radiation can be achieved with photovoltaic (PV) solar cells. The working of these cells is based on the photovoltaic effect. The energy of a photon is used to excite an electron from the valence to the conduction band over a band gap in a semiconducting material, leaving a hole (the absence of an electron) behind (Figure 1.1). By separating the holes and the electrons, collecting them at the anode and the cathode and connecting the anode and cathode externally an electrical current is generated.

Solar cells can be made out of many different types of materials, of which crystalline silicon (c-Si) is the most common one nowadays with a market share of 87% [2]. Crystalline silicon is a semiconducting material with a band gap of 1.1 eV. c-Si can be doped either positively, with for example boron, creating p-type silicon, or can be doped negatively, with for instance phosphorous, creating n-type silicon. Connecting an n-type and a p-type silicon layer results in the diffusion of electrons from the n-type to the p-type layer across the p-n junction, creating an electric field, allowing for the separation and extraction of the electron and hole. With crystalline silicon PV cells, lab scale efficiencies up to 25.0% [3] and solar panel efficiencies up to 20% [4] have been achieved. However, in order to make efficient c-Si cells, high purity Si is required, making the production of c-Si solar cells cost and energy

expensive, which therefore results in a higher price for solar electricity in comparison to electricity from traditional energy sources.

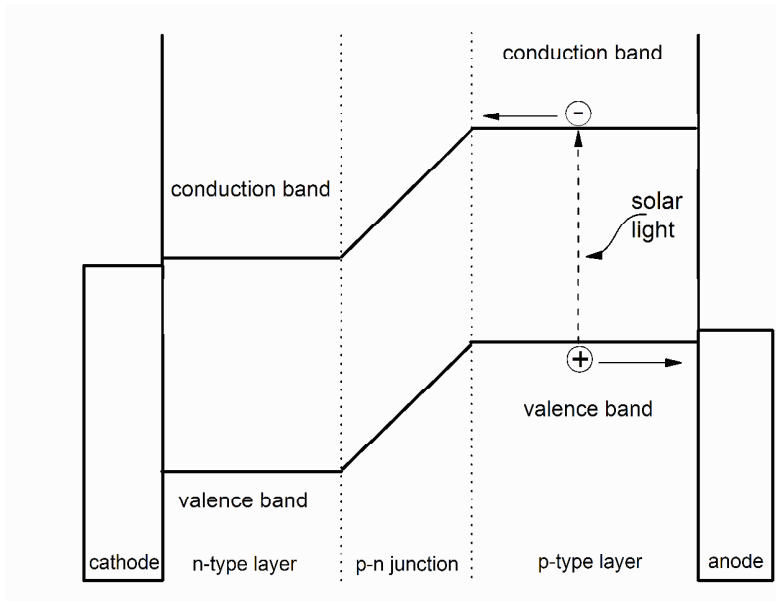


Figure 1.1: Under influence of light, an electron is excited from the valence band to the conduction band leaving a hole behind. The electrons subsequently flow towards the cathode and the holes towards the anode.

Therefore, alternatives are investigated that try to make solar cells cheaper or more efficient. Examples hereof are thin film devices made out of microcrystalline or amorphous silicon [5,6] that require much less material and consequently have lower production costs; and thin film copper indium gallium selenide (CIGS) [7], cadmium telluride (CdTe) [8], polymer [9] and dye sensitized solar cells [10] in which the silicon is replaced by a different material that is cheaper or easier to produce. Examples of concepts that try to make solar cells more efficient are multijunction solar cells [11], plasmonics [12], multiple exciton generation with quantum dots [13], spectral conversion [14,15] and luminescent solar concentrators [16]. Since this thesis will focus on improving solar cell efficiency using spectral conversion concepts the next paragraphs will focus on this approach in more detail.

1.2 Solar spectral conversion

The solar spectrum (Figure 1.2) consists of a wide range of photons with wavelengths varying between 300 to 2500 nm. In a single junction photovoltaic device only photons with energy equal to the band gap of the solar cell can be used optimally. Higher energy photons lose their excess energy due to thermalization, while photons with energy lower than the band gap of the solar cell cannot create an electron-hole pair. This means that in for example a crystalline silicon cell 32% of the energy is lost due to thermalization, while 19% of the energy is lost because the photons have energy lower than the silicon band gap. Note that the thermalization losses cannot simply be solved by using a material with a larger band gap. This reduces thermalization losses, but the larger band gap also limits the number of photons that can be absorbed. This trade-off between thermalization and reduced absorption results, together with some fundamental losses, in the well-known Shockley-Queisser [17] limit for single junction solar cells, which is at an optimum of 33% for materials with a band gap around 1.3 eV.

Besides these losses, an additional loss mechanism in solar cells is that the quantum efficiency for the conversion of each absorbed photon in collected charge carriers is often less than 100%, especially for UV and blue photons. This is a result of the higher absorption strength for UV and blue light that causes these photons to be absorbed in the outer part of the material where front surface recombinations cause radiationless losses and thus limit the solar cell efficiency. In some solar cells, like CdTe and CIGS, the response for UV/blue photons is even lower due to competitive absorption by a cadmium sulfide layer.

The losses due to a poor response for UV/blue photons might be reduced by positioning a luminescent layer on top of a solar cell, which is able to absorb light for which the solar cell response is low and reemit light at a wavelength for which the response is high. Such a layer is called a spectral shifting layer.

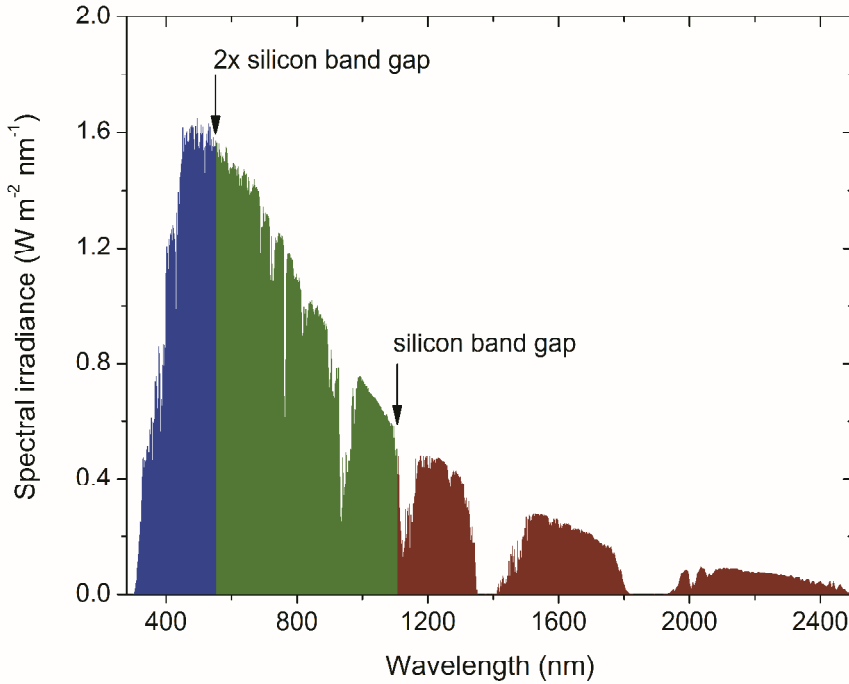


Figure 1.2: The AM 1.5 solar spectrum (ASTM G173-03). The red area is the part of the solar spectrum with photon energy below the band gap of c-Si, the green area is the part with energy between 1 and 2 times the band gap, and the blue area is the part with photon energy above 2 times the c-Si band gap.

An approach to reduce the thermalization losses without enlarging the band gap, and thus exceeding the Shockley-Queisser limit (SQ-limit), is the introduction of a down-conversion or quantum cutting layer. This is a luminescent conversion layer positioned on top of a solar cell in which the higher energy photons are not just shifted to a lower energy, but in which one higher energy photon is split into two lower energy photons. If both photons can be absorbed by the solar cell and produce electron-hole pairs, the quantum efficiency for the short wavelength light can be nearly doubled.

It has been shown [18] that quantum cutting UV/blue to infrared photons can be achieved with a Tb^{3+} - Yb^{3+} co-doped material. Tb^{3+} ions can absorb 490 nm light due to the ${}^7\text{F}_6 \rightarrow {}^5\text{D}_4$ transition. After this excitation the energy can be transferred

to two neighboring Yb^{3+} ions simultaneously via a cooperative energy transfer mechanism because the $\text{Yb}^{3+} {}^2\text{F}_{7/2} \rightarrow {}^2\text{F}_{5/2}$ absorption is half the energy of the $\text{Tb}^{3+} {}^5\text{D}_4 \rightarrow {}^7\text{F}_6$ emission (Figure 1.3). The two excited Yb^{3+} ions can subsequently each emit an infrared photon around 1000 nm by a transition to the ground state, which is ideal for application in combination with c-Si solar cells, because this energy is just above the silicon band gap. Another lanthanide couple in which the cooperative energy transfer mechanism has been suggested is $\text{Tm}^{3+}\text{-Yb}^{3+}$ [19], where the energy of the ${}^3\text{H}_6 \rightarrow {}^1\text{G}_4$ transition of Tm^{3+} is approximately twice as large as the $\text{Yb}^{3+} {}^2\text{F}_{7/2} \rightarrow {}^2\text{F}_{5/2}$ transition.

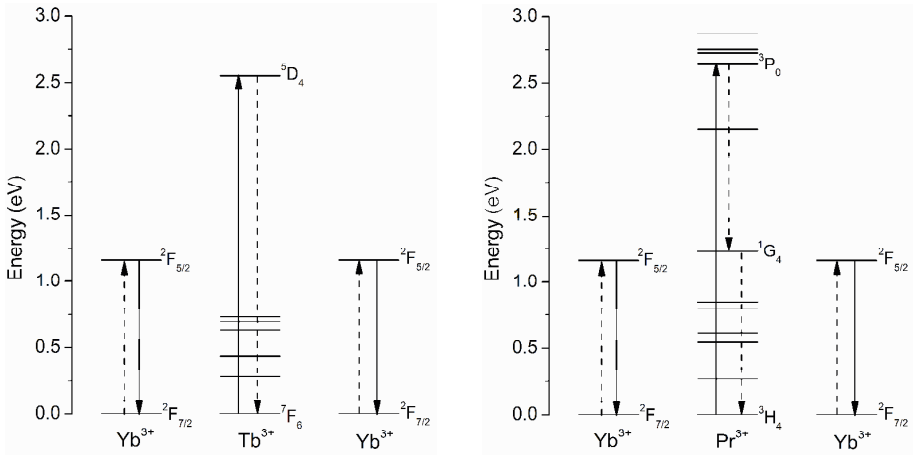


Figure 1.3: Quantum cutting mechanism in a $\text{Tb}^{3+}\text{-Yb}^{3+}$ (left) and a $\text{Pr}^{3+}\text{-Yb}^{3+}$ (right) co-doped material.

Quantum cutting has also been reported for the $\text{Pr}^{3+}\text{-Yb}^{3+}$ couple. [19,20] The mechanism leading to quantum cutting can in this case be a first order resonant two step energy transfer process instead of a second order cooperative energy transfer process. [20] After excitation and relaxation to the ${}^3\text{P}_0$ level of Pr^{3+} , energy is transferred from Pr^{3+} to Yb^{3+} in two separate steps, with the ${}^1\text{G}_4$ level of Pr^{3+} acting as an intermediate level. The first step consists of a $\text{Pr}^{3+}({}^3\text{P}_0 \rightarrow {}^1\text{G}_4), \text{Yb}^{3+}({}^2\text{F}_{7/2} \rightarrow {}^2\text{F}_{5/2})$ resonant energy transfer and this is followed in the second step by a $\text{Pr}^{3+}({}^1\text{G}_4 \rightarrow {}^3\text{H}_4), \text{Yb}^{3+}({}^2\text{F}_{7/2} \rightarrow {}^2\text{F}_{5/2})$ resonant energy transfer, resulting in two excited Yb^{3+}

ions that each emit an infrared photon (Figure 1.3). Other quantum cutting couples in which a similar mechanism has been proposed are $\text{Nd}^{3+}\text{-Yb}^{3+}$ [21], $\text{Ho}^{3+}\text{-Yb}^{3+}$ [22] and $\text{Er}^{3+}\text{-Yb}^{3+}$ [23]. In these materials however, the quantum cutting mechanism has to compete with multi-phonon relaxation.

Despite the many quantum cutting couples that have been discovered and the large variety of hosts in which quantum cutting has been observed [24] with energy transfer efficiencies up to nearly 200%, several problems have been manifested that severely limit the applicability of quantum cutting layers on solar cells. One of these is the high Yb^{3+} concentration that is required for an efficient energy transfer from the co-dopant to Yb^{3+} , but that at the same time also quenches the Yb^{3+} $f\text{-}f$ emission. Another problem concerns the weak absorption strength and narrow wavelength range of the $f\text{-}f$ transitions, due to which only a very small part of the solar spectrum will actually be absorbed. Therefore, the use of Ce^{3+} has been suggested, to enhance the absorption strength of the phosphors and to extend the range of absorption. [25] However, Ce^{3+} can also transfer the energy directly to Yb^{3+} without quantum cutting involved. With the $\text{Pr}^{3+}\text{-Yb}^{3+}$ quantum cutting couple the additional problem arises that there might be back-transfer from Yb^{3+} to Pr^{3+} which competes with the Yb^{3+} emission. [26,27]

Another point that should be noted is that light emitted in a spectral conversion layer is usually emitted isotropically, which means that half of the light will not be emitted in the direction of the solar cell, but in the opposite direction. However, due to the higher refractive index of the conversion layer with respect to that of air which results in total internal reflection, a large part of this wrongly emitted light will not escape from the device and can eventually still end up in the active layer of the cell. Nevertheless, still about 15% of the emitted light will be lost, meaning that the gain in efficiency by spectral conversion should at least compensate for this loss.

1.3 Luminescent solar concentrators

A luminescent solar concentrator (LSC) or power window is a device that consists of a luminescent glass or plastic plate at which to the edges PV cells are attached (Figure 1.4). If solar light is absorbed by a luminescent material that is integrated in the window, the light is reemitted isotropically, with a certain Stokes shift, by the luminescent material. This emitted light will largely be trapped within the plate due to the higher refractive index as compared to that of air. Subsequently, the light will be waveguided towards the edges of the window, where the PV cells are attached. As a result, the solar light captured by the whole plate is concentrated on a relatively small area at the edges. An LSC therefore requires much less PV cells than a conventional solar cell, which makes the LSC in principle a cheap way of producing electricity from solar light. In addition, by using a luminescent plate for light concentration instead of a system with lenses, the device will have a better performance on cloudy days when there is no direct solar radiation. Besides, no solar tracking mechanics are required to keep the lenses pointed at the sun. An additional interesting application of an LSC is that it can be integrated as a window in for example office buildings and serve as a power supply. [28]

Nevertheless, a successful commercial implementation of an LSC has unfortunately been a castle in the air since the moment of conception of the idea about forty years ago. [29-31] It has proven difficult to find a luminescent material that combines all properties needed to efficiently concentrate the solar light. [16,32] The material should be able to absorb a broad portion of the solar spectrum and subsequently reemit the light with high quantum efficiency. It is furthermore very important that there is negligible spectral overlap between the absorption and emission spectrum of the luminescent material, since otherwise the light emitted in one part of the LSC will be reabsorbed in another part of the LSC before reaching the LSC-PV edge. And since each reemission is associated with losses due to a non-ideal luminescence quantum efficiency and due to emission within the escape cone, this self-absorption will result in LSC efficiencies that are reduced up to a factor of four. [33]

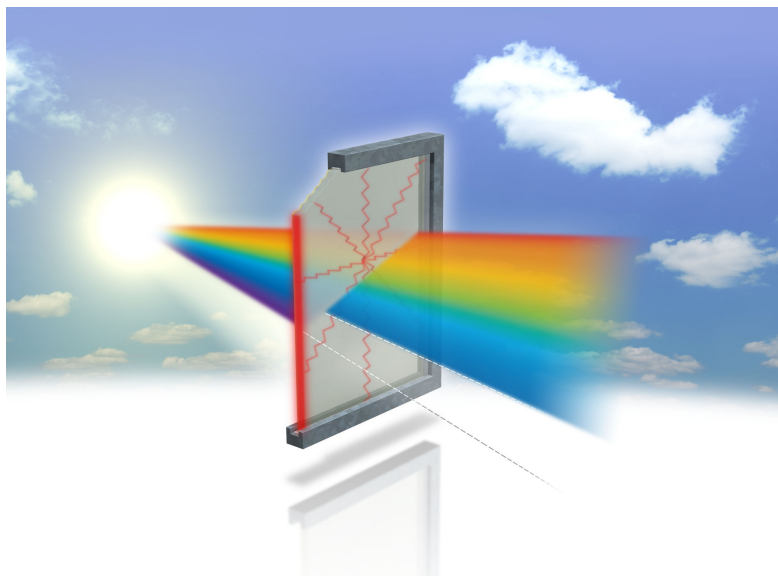


Figure 1.4: Solar light is absorbed in an LSC and the reemitted light is waveguided to the edges of the window where solar cells are attached.

1.4 Luminescent materials

The luminescent materials considered in this thesis have the common property that the luminescence originates from lanthanide ions which are doped in an inorganic semiconductor or insulator. These lanthanides, which range from La with atomic number 57 to Lu with atomic number 71, are sometimes also grouped as the rare earths, together with Sc and Y. Despite the relatively high price, the usage of lanthanides has increased rapidly over the last decades and they are nowadays applied in for example lasers, magnets, cathode ray tubes, catalysts, LEDs and scintillators.

The most common valency for the lanthanide ions is the trivalent state. In that case the lanthanide ions are in the ground state in the $[\text{Xe}]4f^n$ electronic configuration with n ranging from 0, an empty $4f$ shell, in the case of La^{3+} , to 14, a completely filled $4f$ shell, in the case of Lu^{3+} . For those ions with a partly filled $4f$ shell the $4f$ state is split into several $^{2S+1}L_J$ states separated in energy. Energetic

transitions from the $4f$ ground state to the $4f$ excited states are parity forbidden, but can often still be observed as narrow, weak absorption lines (forced electric dipole transitions). After excitation to a higher $4f$ state, emission to the lower states can occur as narrow $4f$ - $4f$ emission lines. A characteristic property of the $4f$ states is that the energy separation between them, as listed in the Dieke diagram [34], is almost independent of the host material, because the $4f$ electrons are shielded from the environment by the outer $5p$ electrons. Apart from the narrow $4f$ - $4f$ transitions, more strongly absorbing $4f$ - $5d$ transitions in which one electron is promoted to the $5d$ band can sometimes be observed as much broader absorption bands, which might be followed by $5d$ - $4f$ emission. As opposed to the f - f transitions, the energy of the $4f$ - $5d$ absorption strongly depends on the host crystal because the $5d$ orbitals are directly involved in the chemical bonding with the coordinating anions. In some hosts the lanthanide ions can be doped as divalent ions. This is most common for Eu, but also Sm, Yb and Tm can be observed in the divalent state. Just as in the trivalent state, the divalent ions are characterized by $4f$ - $4f$ and $4f$ - $5d$ transitions, though at lower energies. Other absorption features that are sometimes observed in trivalent lanthanide doped hosts are charge transfer (CT) transitions, which are due to the transfer of an electron from a coordinating anion to the trivalent lanthanide, which shortly produces a divalent lanthanide. The energy level positions of the $4f$ and $5d$ states of the divalent and trivalent lanthanide ions relative to the valence and conduction band of the host lattice in which the lanthanide ion is doped, and relative to the vacuum, have been described by Dorenbos. [35-37]

When showing and discussing optical spectra, the energy can be displayed in either electron volts (eV), nanometers (nm) or reciprocal centimeters (cm^{-1}). Since sometimes one unit is more convenient than the other, all of these three units are used within this thesis. In order to help the reader with quickly converting one unit into the other, a conversion table is shown in Table 1.1.

One class of rather novel host materials in which the lanthanides can be doped, and which are considered in this thesis in several chapters, are the nitridosilicates. When doped with lanthanides, these materials have shown to exhibit excellent luminescence properties. Examples are Eu^{2+} doped $\text{Sr}_2\text{Si}_5\text{N}_8$ [38]

and Eu^{2+} doped CaAlSiN_3 [39] which are applied as orange to red emitting spectral conversion phosphors for white light LEDs. [40] The reason for considering these types of materials for application as a spectral conversion layer on top of a solar cell is that an amorphous silicon nitride layer is already used on top of solar cells, serving as a passivation and anti-reflection coating. Another advantage of the silicon nitride based materials is that the properties of these materials such as the chemical stability, the band gap and the $4f$ - $5d$ transitions can be tuned by varying the composition, such as the partial substitution of silicon by aluminum, the replacement of nitrogen by oxygen, as well as by varying the silicon to nitrogen ratio. [41,42] Furthermore, the absorption bands of the lanthanides, such as $4f$ - $5d$ and charge transfer transitions, are generally of lower energy in nitrides than in oxides and fluorides, which makes nitride based materials potential candidates to absorb solar light.

Table 1.1 Conversion table for the conversion of electron volt (eV) into nanometer (nm) and reciprocal centimeter (cm^{-1}) and vice versa.

eV	nm	cm^{-1}	eV	nm	cm^{-1}
0.1	12398	807	1.25	992	10082
0.2	6199	1613	1.5	827	12098
0.3	4132	2420	1.75	708	14115
0.4	3100	3226	2	620	16131
0.5	2480	4033	2.5	496	20164
0.6	2066	4839	3	413	24197
0.7	1771	5646	3.5	354	28229
0.8	1550	6452	4	310	32262
0.9	1378	7259	4.5	276	36295
1	1240	8066	5	248	40328

1.5 Scope and overview of the thesis

The aim of the work presented in this thesis is to find new lanthanide doped luminescent materials that can be used as spectral conversion materials to enhance the efficiency of solar cells and luminescent solar concentrators. In this work the syntheses and optical studies of these materials are presented, as well as calculations discussing their applicability to enhance solar cell efficiency.

This thesis consists of 3 parts. The first part of the thesis, including chapters 2 till 6, is focused on spectral conversion materials which may be of potential interest for photovoltaic cells. In chapter 2 it is calculated whether and to what extent spectral conversion layers would enhance the efficiency of different types of existing state-of-the-art solar cells. The calculations consider three different classes of spectral conversion materials: spectral shifting, quantum cutting and quantum tripling materials. In the subsequent chapters specific luminescent materials from each of these classes are investigated and their applicability to be used for spectral shifting, quantum cutting or quantum tripling will be discussed. Chapter 3 describes spectral conversion via charge transfer band absorption and subsequent $4f-4f$ emission of Yb^{3+} in LSi_3N_5 ($\text{L} = \text{La}, \text{Y}$) and chapter 4 discusses spectral conversion via $4f-5d$ band absorption and the optical properties of different lanthanides in $\text{M}_2\text{Si}_5\text{N}_8$ ($\text{M} = \text{Ca}, \text{Sr}, \text{Ba}$). Quantum cutting, or rather its absence, in rare-earth doped NaLaF_4 is the main topic of chapter 5, and finally in chapter 6 the quantum tripling properties of Tm^{3+} doped $\text{La}_2\text{BaZnO}_5$ are investigated as a function of the Tm^{3+} concentration.

The second part of the thesis, which includes chapters 7 and 8, deals with a different concept of harvesting solar light with luminescent materials: the luminescent solar concentrator or LSC. As has been mentioned in section 1.3, one of the main factors limiting LSC efficiency, and with it the commercial applicability, are the losses related to self-absorption. In chapter 7 a generally applicable analytical model is presented with which the self-absorption losses in circular LSCs can be calculated and which gives insight in how the emitted light is distributed over an LSC after generations of reabsorptions and reemissions.

Chapter 8 continues with a class of luminescent materials that have been found to show a broad absorption range without self-absorption. The synthesis and optical properties of these Tm^{2+} doped halides are discussed, together with the applicability of these materials as luminescent materials for LSCs.

In the final part of the thesis a novel class of silicon nitride based materials is studied in which the lanthanides show special optical properties, such as very low-energy $4f-5d$ transitions and low energy charge transfer bands. The stability of these $MLSiN_3$ structures in which M is a divalent ion (such as Eu^{2+} or Ca^{2+}) and L is a trivalent ion (such as Eu^{3+} or La^{3+}) is predicted in chapter 9 based on density functional theory (DFT) calculations, resulting in the synthesis of $CaLaSiN_3$, $CaEuSiN_3$, $EuLaSiN_3$ and Eu_2SiN_3 . Additionally, the presence of europium in these materials in both the divalent and the trivalent state is discussed in the same chapter. Finally, in chapter 10 the optical properties of the lanthanides doped in $CaLaSiN_3$ are studied.

1.6 References

- [1] O. Morton; Nature 443 (2006) 19.
- [2] Website of the U.S. Department of Energy; http://www1.eere.energy.gov/solar/sunshot/pv_crystalline_silicon.html; Retrieved on 28 January 2014.
- [3] M.A. Green, K. Emery, Y. Hishikawa, W. Warta, E.D. Dunlop; Prog. Photovoltaics: Res. Appl. 22 (2014) 1.
- [4] Website of SunPower E20/333 and E20/327 Solar Panels http://img.en25.com/Web/SunPowerCorporation/11_252_sp_e20_333_327_ds_en_a4_w.pdf; Retrieved on 28 January 2014.
- [5] A.V. Shah, H. Schade, M. Vanecek, J. Meier, E. Vallat-Sauvain, N. Wyrsh, U. Kroll, C. Droz, J. Bailat; Prog. Photovoltaics: Res. Appl. 12 (2004) 113.
- [6] D.E. Carlson; Appl. Phys. Lett. 28 (1976) 671.
- [7] P. Jackson, D. Hariskos, E. Lotter, S. Paetel, R. Wuerz, R. Menner, W. Wischmann, M. Powalla; Prog. Photovoltaics: Res. Appl. 19 (2011) 894.

- [8] J. Britt, C. Ferekides; *Appl. Phys. Lett.* 62 (1993) 2851.
- [9] H.Y. Chen, J. Hou, S. Zhang, Y. Liang, G. Yang, Y. Yang, L. Yu, Y. Wu, G. Li; *Nat. Photonics* 3 (2009) 649.
- [10] M. Grätzel; *J. Photoch. Photobio. C* 4 (2003) 145.
- [11] R.R. King, D.C. Law, K.M. Edmondson, C.M. Fetzer, G.S. Kinsey, H. Yoon, R.A. Sherif, N.H. Karam; *Appl. Phys. Lett.* 90 (2007) 183516.
- [12] H.A. Atwater, A. Polman; *Nat. Mater.* 9 (2010) 205.
- [13] A.J. Nozik; *Chem. Phys. Lett.* 457 (2008) 3.
- [14] B.S. Richards; *Sol. Energ. Mat. Sol. C.* 90 (2006) 1189.
- [15] A. Shalav, B.S. Richards, M.A. Green; *Sol. Energ. Mat. Sol. C.* 91 (2007) 829.
- [16] M.G. Debije, P.C. Verbunt; *Adv. Energ. Mater.* 2 (2012) 12.
- [17] W. Shockley, H.J. Queisser; *J. Appl. Phys.* 32 (1961) 510.
- [18] P. Vergeer, T.J.H. Vlugt, M.H.F. Kox, M.I. Den Hertog, J.P.J.M. van der Eerden, A. Meijerink; *Phys. Rev. B* 71 (2005) 014119.
- [19] Q. Zhang, G. Yang, Z. Jiang; *Appl. Phys. Lett.* 91 (2007) 051903.
- [20] B. Ende, L. Aarts, A. Meijerink; *Adv. Mater.* 21 (2009) 3073.
- [21] J. Meijer, L. Aarts, B. van der Ende, T. Vlugt, A. Meijerink; *Phys. Rev. B* 81 (2010) 035107.
- [22] K. Deng, T. Gong, L. Hu, X. Wei, Y. Chen, M. Yin; *Opt. Express* 19 (2011) 1749.
- [23] L. Aarts, B. van der Ende, A. Meijerink; *J. Appl. Phys.* 106 (2009) 023522.
- [24] Q.Y. Zhang, X.Y. Huang; *Prog. Mater. Sci.* 55 (2010) 353.
- [25] Q. Zhang, J. Wang, G. Zhang, Q. Su; *J. Mater. Chem.* 19 (2009) 7088.
- [26] E. van der Kolk, O.M. ten Kate, J.W. Wiegman, D. Biner, K.W. Krämer; *Opt. Mater.* 33 (2011) 1024.
- [27] A. Guille, A. Pereira, C. Martinet, B. Moine; *Opt. Lett.* 37 (2012) 2280.
- [28] B. Norton, P.C. Eames, T.K. Mallick, M.J. Huang, S.J. McCormack, J.D. Mondol, Y.G. Yohanis; *Sol. Energy* 85 (2011) 1629.
- [29] W.H. Weber, J. Lambe; *Appl. Opt.* 15 (1976) 2299.
- [30] A. Goetzberger, W. Greube; *Appl. Phys. A-Mater.* 14 (1977) 123.
- [31] J.S. Batchelder, A.H. Zewail, T. Cole; *Appl. Opt.* 18 (1979) 3090.

- [32] B.C. Rowan, L.R. Wilson, B.S. Richards; *Appl. Opt.* 20 (1981) 2934.
- [33] A.A. Earp, G.B. Smith, P.D. Swift, J. Franklin; *Sol. Energy* 76 (2004) 655.
- [34] G.H. Dieke; H.M. Crosswhite; *Appl. Opt.* 2 (1963) 675.
- [35] P. Dorenbos; *J. Phys.-Condens. Mat.* 15 (2003) 8417.
- [36] P. Dorenbos; *J. Alloy. Compd.* 488 (2009) 568.
- [37] P. Dorenbos; *Phys. Rev. B* 85 (2012) 165107.
- [38] Y.Q. Li, J.W.H. Krevel, G. Botty, A.C.A. Delsing, F.J. DiSalvo, G. de With, H.T. Hintzen; *J. Alloy. Compd.* 417 (2006) 273.
- [39] K. Uheda, N. Hirosaki, H. Yamamoto; *Phys. Stat. Sol. A* 203 (2006) 2712.
- [40] S.E. Brinkley, N. Pfaff, K.A. Denault, Z. Zhang, H.T. Hintzen, R. Seshadri, S. Nakamura, S.P. DenBaars; *Appl. Phys. Lett.* 99 (2011) 241106.
- [41] J.W.H. van Krevel, H.T. Hintzen, R. Metselaar, A. Meijerink; *J. Alloy. Compd.* 268 (1998) 272.
- [42] R.J. Xie, N. Hirosaki; *Sci. Technol. Adv. Mater.* 8 (2007) 588.

Chapter 2

Efficiency enhancement calculations of state-of-the-art solar cells by luminescent layers with spectral shifting, quantum cutting and quantum tripling function

The content of this chapter has been published as: O.M. ten Kate, M. de Jong, H.T. Hintzen, E. van der Kolk; “Efficiency enhancement calculations of state-of-the-art solar cells by luminescent layers with spectral shifting, quantum cutting and quantum tripling function”; Journal of Applied Physics 114 (2013) 084502.

Solar cells of which the efficiency is not limited by the Shockley-Queisser limit can be obtained by integrating a luminescent spectral conversion layer into the cell structure. The maximum efficiency has been calculated of state-of-the-art c-Si, pc-Si, a-Si, CdTe, GaAs, CIS, CIGS, CGS, GaSb, and Ge solar cells with and without an integrated spectral shifting, quantum cutting, or quantum tripling layer using their measured internal quantum efficiency (IQE) curves. The detailed balance limit calculations not only take into account light in-coupling efficiency of the direct AM1.5 spectral irradiance but also wavelength dependence of the refractive index and the IQEs of the cells and the angular dependent light in-coupling of the indirect spectral irradiance. An ideal quantum cutting layer enhances all cell efficiencies ranging from a modest 2.9% for c-Si to much larger values of 4.0%, 7.7%, and 11.2% for CIGS, Ge, and GaSb, respectively. A quantum tripling layer also enhances cell efficiencies, but to a lesser extent. These efficiency enhancements are largest for small band gap cells like GaSb (7.5%) and Ge (3.8%). Combining a quantum tripling and a quantum cutting layer would enhance efficiency of these cells by a factor of two. Efficiency enhancement by a simple

spectral shifting layer is limited to less than 1% in case the IQE is high for blue and UV light. However, for CdTe and GaSb solar cells, efficiency enhancements are as high as 4.6% and 3.5%, respectively. A shifting layer based on available red LED phosphors like $\text{Sr}_2\text{Si}_5\text{N}_8:\text{Eu}^{2+}$ will raise CdTe efficiency by 3.0%.

2.1 Introduction

The main limitation for the efficiency of photovoltaic cells is the mismatch between the solar spectrum and the solar cell response. In a single junction device only photons with energy equal to the band gap of the solar cell can be used optimally. Photons with higher energy lose their excess energy due to thermalization, while photons with energy lower than the band gap of the solar cell cannot be absorbed at all. An additional loss mechanism for solar cells is that the quantum efficiency for the conversion of each absorbed photon into electricity, called the internal quantum efficiency (IQE), is often lower than 1 due to low exciton diffusion lengths, and rear and front surface recombinations. Especially the front surface recombinations limit the IQE of solar cells for the high energy photons.

Several approaches have been suggested in order to solve the spectral mismatch problem, either by adapting the solar cell to the solar spectrum or by adapting the solar spectrum to the solar cell. Examples of the former one are tandem solar cells and multiple exciton generation. The latter approach, adapting the solar spectrum to the solar cell, can conveniently be applied to existing solar cells. A spectral shifting layer on top of a cell can increase the solar cell efficiency by converting high energy photons for which the IQE is low into lower energy photons for which the IQE is high. Furthermore, efficiency can be increased even further if the conversion layer does not just shift the photons to a lower energy, but in addition cuts each high energy photon into two lower energy photons that still can be absorbed by the solar cell. [1] Such a layer is called a quantum cutting or down-conversion layer.

Since for small band gap cells the efficiency is limited due to large thermalization of the absorbed photons, while for large band gap cells the efficiency is limited due to a reduction in the number of photons that can be absorbed, there will be an optimum in the efficiency as a function of the band gap. This optimum has been calculated by Shockley and Queisser [2] while taking into account the principle of detailed balance. In the model described by Shockley and Queisser the solar cell is described as a blackbody radiator that absorbs all light above the band gap of the cell and no light below the band gap. In the calculations the cell has a refractive index of 1 and operates at a temperature of 300 K under illumination of a blackbody with a temperature of 6000 K (the sun). In the absence of non-radiative recombination, the efficiency reaches a maximum, the so-called Shockley-Queisser limit, for a cell with a band gap of 1.3 eV.

Based on the model of Shockley and Queisser, Trupke et al. [3] calculated the maximum efficiency of solar cells containing a quantum cutting layer. In these kinds of solar cells the efficiency can exceed the Shockley-Queisser limit, since the thermalization of high energy photons is reduced by cutting a high energy photon into two lower energy photons. Badescu et al. [4,5] extended the model by carefully taking into account the influence of the refractive indices of the different layers on the light in-coupling into the solar cell. Thomas et al. [6] recently extended these models to calculate the efficiency of a cell with a spectral shifting layer on top.

In this chapter the efficiencies of solar cells containing spectral shifting and quantum cutting layers are calculated based on the models of Trupke and Badescu. However, the model is extended by including the IQE curves of different types of existing state-of-the-art solar cells into the calculations, in order to get an understanding whether, and to what extent, spectral conversion layers would improve the efficiencies of existing solar cells. Additionally, the solar radiation is simulated with the AM 1.5 spectrum instead of pure blackbody radiation of the sun, since the AM 1.5 spectrum better describes the solar radiation and because it is used as a standard for measuring solar cell efficiencies. A third difference with previously published papers is that the refractive index of the solar cell is not

considered to be constant, but instead the wavelength dependency of the refractive index is taken into account. Additionally, real spectral shifting, quantum cutting, and quantum tripling materials are considered containing lanthanide ions (Eu^{2+} , Yb^{3+} , Tm^{3+}) as the luminescent centers.

2.2 Theory

In Figure 2.1 a schematic overview of the photovoltaic device that is considered is shown. It consists of the cell itself, which is called medium 4 with on top of it a spectral conversion layer, which is called medium 3. At the rear side of the cell a back-reflector is present, which is assumed to reflect 100% of the light at all wavelengths. The air surrounding the device is called medium 1. Additionally, the cell has an encapsulation layer (medium 2) on top of the conversion layer. This encapsulation layer represents a glass or plastic material that protects the device from the environment. It is considered to be completely transparent for light of all wavelengths with a refractive index of 1.5.

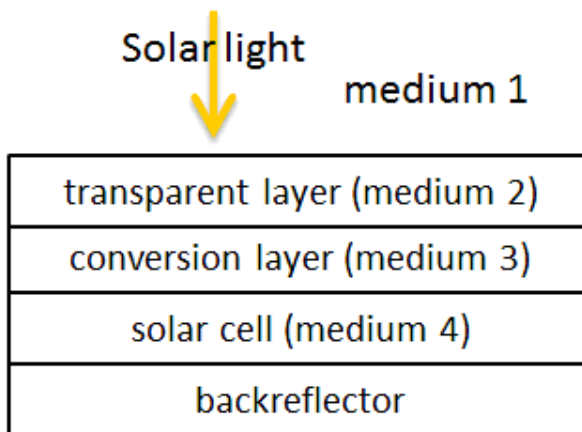


Figure 2.1 a) Schematic overview of the solar cell (medium 4) with a conversion layer (medium 3), an encapsulation layer (medium 2), and a back-reflector, surrounded by air (medium 1).

The maximum efficiency η of the photovoltaic device is given by the maximum electrical power P_e that is generated by the cell divided by the power of the solar radiation incident on the device P_s , where P_e is equal to the product of the current I and the voltage V at the point where the product is at its maximum:

$$\eta = \frac{P_e}{P_s} = \frac{(IV)_{\max}}{P_s} . \quad (2.1)$$

The solar cell efficiency depends on the spectral irradiance of the light incident on the device. The efficiency is therefore usually determined using two standardized AM 1.5 spectra (ASTM G173-03), which both correspond to a solar zenith angle of 48.2° . The two spectra define a total hemispherical spectral irradiance that includes both the direct and the indirect radiation, and a direct normal spectral irradiance that only includes the direct and circumsolar radiation. In our calculations, the direct normal spectral irradiance Φ_d is described by a Gaussian fit of the standardized direct normal spectrum. A Gaussian fit of the difference between the total hemispherical irradiance and the direct normal irradiance is used to describe the indirect spectral irradiance Φ_i . Both fits are shown in Figure 2.2. The integral of the spectral irradiance over all wavelengths λ gives the solar radiation power P_s incident on the device (the area of the solar cell is taken as unity):

$$P_s = \int_0^\infty \Phi_d d\lambda + \int_0^\infty \Phi_i d\lambda . \quad (2.2)$$

In order to get an expression for the current through the cell, expressions are needed for the number of photons that are absorbed in the cell and the number of photons that are emitted by the cell. The number of photons that are absorbed in the cell (medium 4) is equal to the sum of three contributions: photons from the direct solar radiation N_{1d4} , the indirect solar radiation N_{1i4} , and photons emitted by the spectral conversion layer (medium 3) N_{34} .

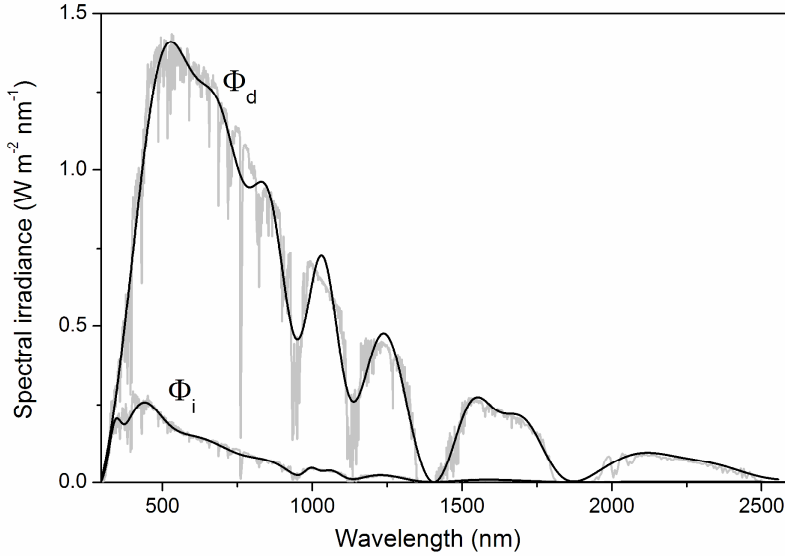


Figure 2.2 Gaussian fit (black) and original curve (grey) of the direct normal spectral irradiance Φ_d and the indirect spectral irradiance Φ_i .

Only photons with energy higher than the band gap of the solar cell are taken into account, since other photons cannot be absorbed and will not contribute to the current. N_{1d4} , the number of photons from the direct solar radiation that are transmitted through the conversion layer and that can be absorbed in the cell, is equal to:

$$N_{1d4} = \frac{1}{hc} \int_0^{\lambda_g} f_{1d4} IQE (1 - \alpha_3) \Phi_d d\lambda. \quad (2.3)$$

Here is h the Planck constant, c the speed of light, λ_g the wavelength that corresponds to the band gap energy E_g and α_3 the spectral fraction of the light absorbed by the spectral conversion layer. f_{1d4} is a factor that describes the fraction of the direct solar radiation that is transmitted via the intermediate layers into medium 4, taking into account the wavelength dependency of the radiation, as well as the refractive indices of the different layers, but neglecting interference effects, as is described in the appendix (section 2.5). Since a part of the electrons and holes

will recombine non-radiatively and therefore not contribute to the current, the factor IQE , which is the internal quantum efficiency of the solar cell, is also included in equation (2.3). Similarly the indirect solar radiation N_{i4} that is absorbed in the cell is equal to:

$$N_{i4} = \frac{1}{hc} \int_0^{\lambda_3} f_{i4} IQE (1 - \alpha_3) \Phi_i d\lambda, \quad (2.4)$$

where f_{i4} is the factor for the transmittance of the indirect solar radiation into medium 4 (see appendix, section 2.5).

Photons that are absorbed in the conversion layer (medium 3) enter this layer either from medium 1 via medium 2 as direct and indirect solar radiation, or from medium 4 due to radiative recombination in the cell. In practice the contribution of the latter term can be neglected, since the radiation of the cell is primarily at wavelengths at or just above the band gap of the cell and therefore cannot be absorbed by the conversion layer. The number of photons that are emitted by the conversion layer is determined by the fraction of the incoming photons that are absorbed α_3 and the quantum efficiency of the spectral conversion η_{em} . The number of photons leaving the conversion layer is therefore equal to:

$$N_{3out} = \frac{1}{hc} \int_0^{\infty} \alpha_3 \eta_{em} (f_{i43} \Phi_d + f_{i13} \Phi_i) d\lambda, \quad (2.5)$$

where f_{i43} and f_{i13} are transmittance factors (see appendix, section 2.5). All photons emitted by medium 3 have to go either to medium 1 (outside the device) or to medium 4. The number of photons going to medium 3 and contributing to the current is:

$$N_{34} = f_{34} N_{3out} IQE_{av}, \quad (2.6)$$

where f_{34} is the fraction of the photons emitted by the conversion layer that reach medium 4 (see appendix, section 2.5) and IQE_{av} is the average internal quantum efficiency of the solar cell at the energy of the emission of the spectral converter:

$$IQE_{av} = \frac{\int_0^{\infty} IQE \cdot I_{em} d\lambda}{\int_0^{\infty} I_{em} d\lambda}. \quad (2.7)$$

Here is I_{em} the emission intensity of the spectral converter. The number of photons emitted by the cell due to radiative recombination depends on the temperature T_c of the cell and the voltage V over the cell and is described by a generalization of Kirchhoff's law of radiation. [2,3] The photon flux N_{41} for the emission of light from medium 4 via medium 3 and 2 to medium 1 is therefore described by:

$$N_{41} = \frac{2\pi n_4^2}{h^3 c^2} \int_{E_i}^{\infty} \frac{f_{41} (h\nu)^2 (1-\alpha_3)}{\exp\left(\frac{h\nu - qV}{kT_c}\right) - 1} d(h\nu). \quad (2.8)$$

Here is f_{41} a factor that accounts for the transmission of light from medium 4 to medium 1 (see appendix, section 2.5). Note that the factor $(1-\alpha_3)$ could be omitted since the radiation is primarily at wavelengths that cannot be absorbed by the spectral converter.

The amount of current that can be extracted out of the solar cell is equal to the elementary charge unit q times the amount of minority charge carriers that are collected at the electrodes. The latter is equal to the number of photons that are absorbed and do not give rise to non-radiative recombinations, minus the number of photons that are emitted by the solar cell. The current through the cell is therefore equal to the sum of the contributions given by equations (2.3), (2.4) and (2.6) minus the contribution given by equation (2.8):

$$I = q(N_{1d4} + N_{1i4} + N_{34} - N_{41}). \quad (2.9)$$

This current is therefore a function of the voltage V . The maximum efficiency is now given by equation (2.1) at the point where IV is at its maximum.

2.3 Results and discussion

2.3.1 Solar cell without spectral conversion layer

If the conversion layer (medium 3) and the encapsulation layer (medium 2) are omitted from the calculations, if the refractive index of the cell (medium 4) is 1, and if the internal quantum efficiency of the cell is 100%, the Shockley-Queisser limit (SQ-limit) is obtained, with the difference that Shockley and Queisser simulated the solar spectrum with a blackbody spectrum at 6000 K [2], while in these calculations the AM 1.5 spectrum is used. The SQ-limit as a function of the band gap is shown for sake of completeness in Figure 2.3 and the SQ-limits for some common solar cells are also shown in Table 2.1. The efficiency is at a maximum of 33.5% at 1.15 eV, which is equal to the band gap of the CIGS cell that is considered in this chapter. Also for the band gaps of crystalline silicon (1.12 eV), GaAs (1.4 eV) and CdTe (1.44 eV) the efficiency is close to the optimum value. For small band gap solar cells like GaSb and Ge solar cells, the SQ-limit is considerably lower, due to the large thermalization of the high energy photons in these cells. For solar cells with larger band gaps the efficiency limit decreases due to a smaller number of photons that can be absorbed.

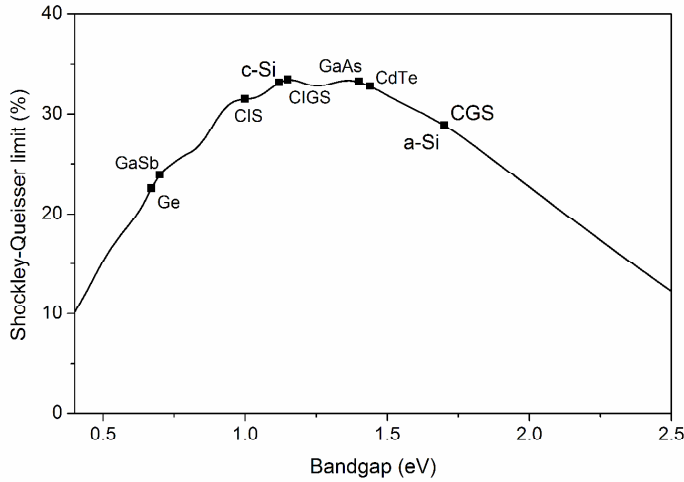


Figure 2.3 SQ-limit of a solar cell with refractive index of 1 under the AM 1.5 solar spectrum as a function of the band gap of the cell. The SQ-limits for some frequently used solar cell materials are indicated.

Table 2.1 η_{SQ} indicates the SQ-limit for various solar cells with band gap E_g with refractive index of 1 under AM 1.5 solar radiation. η_{ref} is the efficiency limit when the refractive index in Figure 2.4 is taken into account and η_{iqe} is the efficiency when both the refractive index and the IQE (Figure 2.5) of the cell are taken into account.

	E_g (eV)	η_{SQ} (%)	η_{ref} (%)	η_{iqe} (%)
c-Si	1.12	33.2	21.7	19.2
pc-Si	1.12	33.2	21.7	17.1
a-Si	1.7	28.9	17.9	14.6
CdTe	1.44	32.8	24.4	16.3
GaAs	1.4	33.2	21.4	19.2
CIS	1.0	31.5	23.8	19.7
CIGS	1.15	33.4	24.9	21.1
CGS	1.7	28.9	20.0	15.7
GaSb	0.7	23.9	14.6	10.1
Ge	0.67	22.5	13.2	10.5

In practice the refractive index of the solar cell will be larger than one, resulting in a less than 100% efficient in-coupling of the light, and as a result lower efficiencies. The wavelength dependency of the refractive index for some common solar cell materials is shown in Figure 2.4. By including these wavelength dependent refractive indices in the calculations, the maximum efficiencies of the solar cells drop significantly, especially for those cells with a relatively high refractive index like c-Si and Ge, as is shown in Table 2.1.

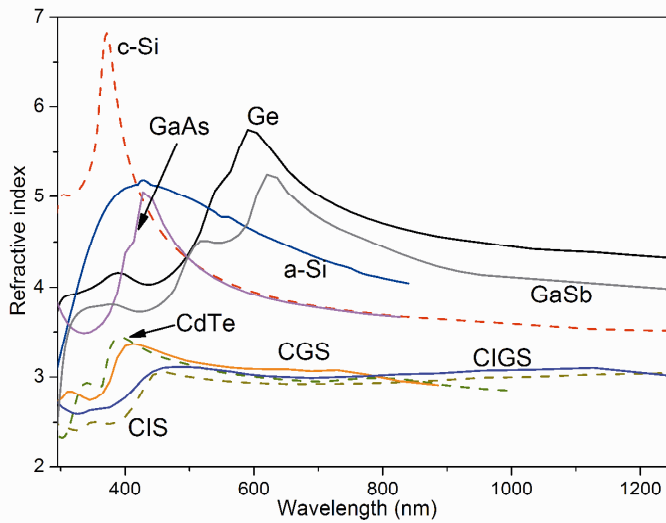


Figure 2.4 Refractive index of c-Si [7], a-Si (SOPRA Database), GaAs [8], CdTe (SOPRA Database) and Ge (SOPRA Database), CGS [9], CIGS [10], and CIS [9].

Another loss mechanism for existing solar cells is the fact that the internal quantum efficiency (IQE) is less than 1 and varies with the wavelength of the light. The short wavelength photons are mainly absorbed in the front part of the solar cell and are therefore strongly affected by surface recombinations, lowering the IQE at the short wavelength side. The long wavelength photons on the other hand are also absorbed in the rear part of the solar cell, where rear surface recombinations drop the IQE. In reality the IQE of one type of solar cell will be different from cell to cell, depending on cell properties like thickness of the layers and specific

processing conditions. Nevertheless, the general shape is the same for one type of cell. Therefore the IQE curves of some types of solar cells shown in Figure 2.5, as obtained from literature, are used as the typical IQE curves for these cells in our calculations. The calculated solar cell efficiencies with these IQE curves are shown in Table 2.1. The relative drop in efficiency due to a non-ideal IQE varies from 10% in GaAs to 33% in CdTe.

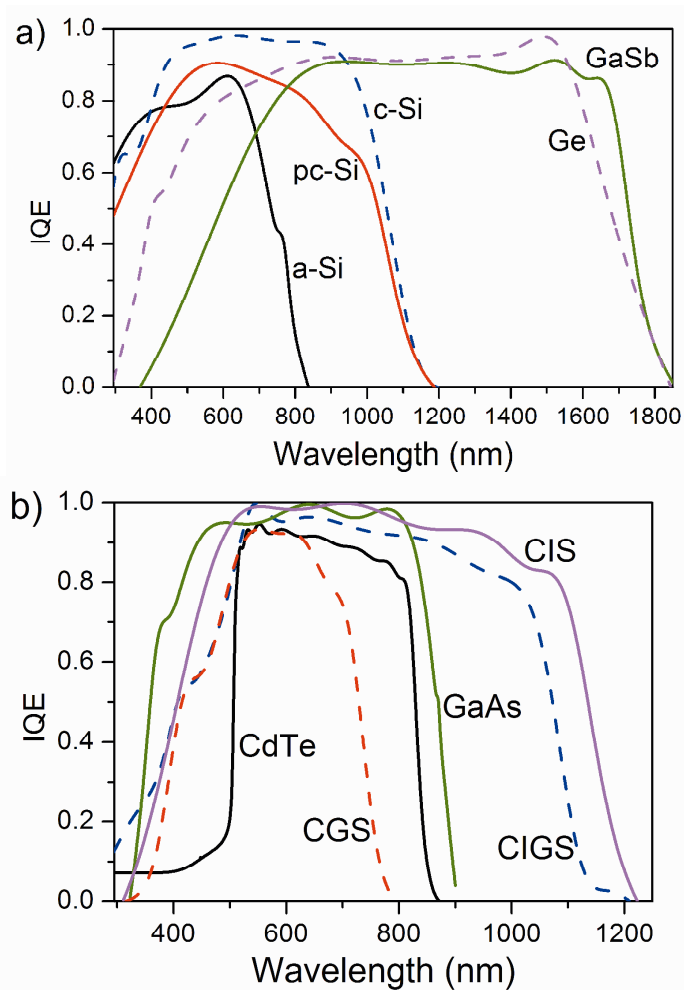


Figure 2.5 a) IQE curves of c-Si [11], pc-Si [12], a-Si [13], GaSb [14] and Ge [15] solar cells and b) IQE curves of CdTe [16], GaAs [17], CIS [18], CIGS [19] and CGS [20] solar cells.

2.3.2 Spectral shifting layer

Since the IQE, which is shown in Figure 2.5, decreases at the short wavelength side, a spectral shifting layer positioned on top of the cell which absorbs the short wavelength photons for which the IQE is low and emits photons at a wavelength for which the IQE is at its maximum, could increase the solar cell efficiency. A cell with a single conversion layer and an encapsulation layer (configuration in Figure 2.1) will be considered and compared with a cell with a non-converting layer with the same refractive index. This could represent a comparison between a cell with a SiN_x or SiO_x index matching layer that has no or a hypothetical spectral shifting function.

Table 2.2 Calculated efficiencies η_{conv} of various solar cells with encapsulation layer ($n = 1.5$) and an ideal spectral shifting layer with an optimal refractive index n_3 , an optimal absorption edge λ_a and an optimal emission wavelength λ_{em} . η_{transp} is the efficiency of a similar cell, but with a transparent layer instead of a conversion layer.

	λ_{em} (nm)	λ_a (nm)	n_3	η_{conv} (%)	η_{transp} (%)
c-Si	633	461	2.3	25.7	25.3
pc-Si	648	533	2.3	23.5	22.4
a-Si	611	565	2.2	21.0	20.3
CdTe	552	515	2.0	24.3	19.6
GaAs	640	554	2.4	26.5	25.6
CIS	555	482	2.1	24.6	23.7
CIGS	548	519	2.2	27.3	25.6
CGS	552	513	2.3	22.5	19.9
GaSb	1219	842	2.4	17.6	13.9
Ge	1490	1440	2.4	17.0	14.8

In order to calculate the efficiency of a cell with a spectral shifting layer, four different properties of the spectral shifting layer should be considered: the quantum efficiency of the conversion layer η_{em} , the absorptivity of the layer α_3 , the emission spectrum of the layer I_{em} and the refractive index n_3 . In the ideal case the quantum efficiency of the spectral shifting layer is equal to 1 and its emission spectrum is a peak function with the maximum at the wavelength for which the IQE of the cell is at a maximum. The absorptivity α_3 of the spectral shifting layer is, ideally, a step function, being equal to 1 for absorption below a certain absorption edge λ_a and 0 above this wavelength. This corresponds to complete absorption of light below λ_a and no light absorption above λ_a . The properties of an ideal spectral shifting layer can then be found by finding the optimal combination of λ_a and n_3 . These values, along with the corresponding solar cell efficiency, are shown in Table 2.2.

The spectral shifting layer will not only enhance the efficiency due to spectral shifting, but also due to a decrease of the reflectance of the device if the refractive index is in between that of the solar cell and the air. In order to get an understanding of the efficiency increase due to spectral shifting itself, the efficiencies should be compared with the case in which the device would have a “shifting” layer with the same refractive index, but for which the absorptivity α_3 is 0 for light of all wavelengths, i.e. a transparent layer. These efficiencies η_{transp} are also shown in Table 2.2.

Table 2.2 shows that an ideal spectral shifting layer would be beneficial for the efficiency of all listed solar cells. However, for all cells the efficiency gain is somewhat limited due to the fact that a certain fraction of the light emitted by the conversion layer will be emitted out of the device instead of in the direction of the solar cell. Although the light will emit randomly in every direction, this loss factor will not be as high as 50% since the light in-coupling in the direction of the cell (which has a higher refractive index) is better than in the direction out of the cell (where the refractive index is lower). However, still circa 15% of the light is lost, which is equal to $1-f_{34}$ as explained in the appendix (section 2.5). The combination of this loss factor with the fact that the IQE for the silicon solar cells is still relatively high at the short wavelength side explains why the gain in efficiency is

only small for the silicon based solar cells. The usefulness of using a conversion layer for silicon solar cells is therefore limited. On the other hand, the CdTe cell would largely profit from a spectral shifting layer. The poor IQE below 10% at wavelengths below 450 nm compensates for the fact that about 20% of the converted light is emitted in the wrong direction. A spectral shifting layer would therefore be very beneficial for CdTe solar cells. Note that for the CdTe solar cell the emission wavelength and absorption edge of the spectral converter do not necessarily have to be exactly at the optimum values given in Table 2.2. As can be seen in Figure 2.6, for a large range of values the efficiency will be well above 20% and therefore significantly increase the efficiency of the cell.

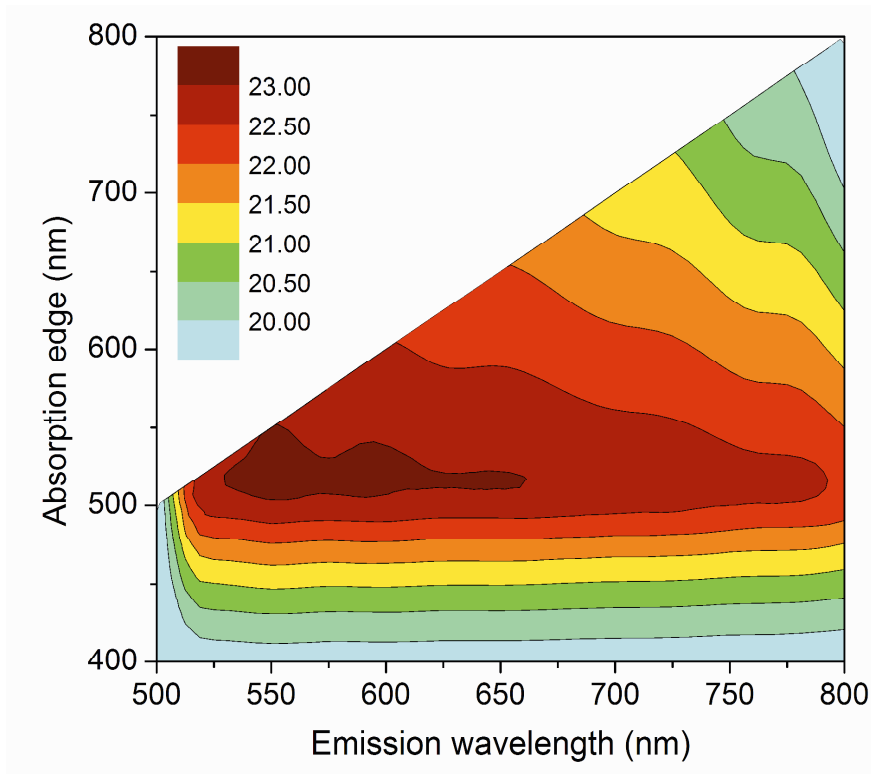


Figure 2.6 Calculated efficiencies of a CdTe solar with a spectral shifting layer as a function of the absorption edge λ_a and the emission wavelength λ_{em} .

Since for some solar cells the efficiency gain is relatively small, even for an idealized spectral shifting material, it is useful to know whether an already existing conversion material would still improve cell efficiency. As an example a layer made out of an orange-emitting Eu^{2+} doped $\text{Sr}_2\text{Si}_5\text{N}_8$ phosphor is considered, which has a refractive index of 2.55 [21]. This phosphor is known to have a strong absorption in the UV/blue part of the spectrum (see Figure 2.7) and an efficient emission around 630 nm, depending on the dopant concentration. [22]

The $\text{Sr}_2\text{Si}_5\text{N}_8:\text{Eu}^{2+}$ phosphor is commercially used as conversion phosphor for white LEDs and its efficiency is expected to be around 90%. From Figure 2.7 it can be seen that the shape of the excitation and the absorption curves are very similar. Therefore, it is assumed that the quantum efficiency is constant over this region. The absorption strength will depend on the thickness of the film. For the calculations, an absorption strength is considered that approaches 100% at 420 nm and drops at longer wavelengths according to the absorption spectrum shown in Figure 2.7. The emission spectrum of the $\text{Sr}_2\text{Si}_5\text{N}_8:\text{Eu}^{2+}$ phosphor, as it is used for the calculations, is shown in Figure 2.7.

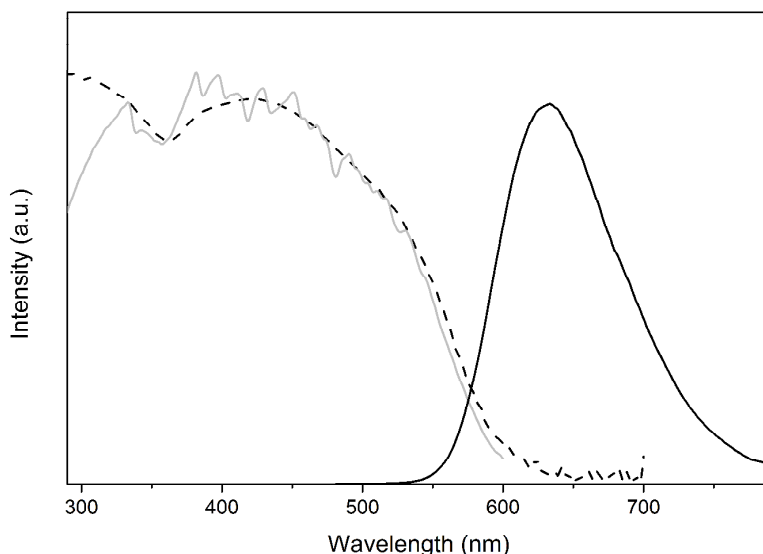


Figure 2.7 Absorption (dashed line), excitation (solid line) and emission (solid line) spectra of $\text{Sr}_2\text{Si}_5\text{N}_8:10\%\text{Eu}$ phosphor.

The results of the calculations are shown in Table 2.3. For some cells (c-Si, a-Si, CIS and CIG) the $\text{Sr}_2\text{Si}_5\text{N}_8:\text{Eu}^{2+}$ conversion layer will decrease solar cell efficiency as compared to a transparent layer. This can easily be explained, since the efficiency gain was already very small for an ideal conversion layer. In addition, the $\text{Sr}_2\text{Si}_5\text{N}_8:\text{Eu}^{2+}$ conversion phosphor has a tail in the absorption which extends up to 600 nm. At this wavelength the IQE of these solar cells is already approaching 100%. Therefore, light that would normally be absorbed in the cell will now be absorbed in the conversion layer. As a result 20% of the absorbed light is already lost because it is emitted in the wrong direction and 10% is lost since the quantum efficiency of the conversion is 90%. Furthermore, for the CGS cell another loss is introduced by the conversion layer: a part of its emission (above 700 nm) is at a wavelength for which the IQE of the CGS cell is already decreasing. On the other hand, the calculations show that a CdTe or GaSb cell would benefit from the $\text{Sr}_2\text{Si}_5\text{N}_8:\text{Eu}^{2+}$ conversion layer with absolute gains of 3.2 and 1.0% respectively if there is no encapsulation layer.

Table 2.3 Calculated efficiencies of various solar cells with a $\text{Sr}_2\text{Si}_5\text{N}_8:\text{Eu}^{2+}$ conversion layer.

	$\eta_{\text{transp}} (\%)$	$\eta_{\text{conv}} (\%)$
c-Si	25.3	25.1
pc-Si	22.4	23.0
a-Si	20.6	19.9
CdTe	19.3	22.5
GaAs	25.6	25.5
CIS	23.3	23.6
CIGS	25.2	25.9
CGS	19.8	20.2
GaSb	13.9	14.9
Ge	14.9	15.2

It should be noted that the $\text{Sr}_2\text{Si}_5\text{N}_8:\text{Eu}^{2+}$ phosphor used in the calculations is a phosphor that has not been optimized as a spectral conversion phosphor for solar cells. Phosphors for which the emission wavelength, absorption range and refractive index are optimized for a specific solar cell, would better approach the efficiencies shown in Table 2.2. The $\text{Sr}_2\text{Si}_5\text{N}_8:\text{Eu}^{2+}$ could for example be optimized by the partly substitution of Sr by Ba or Ca or by changing the Eu^{2+} concentration. [22,23]

2.3.3. Quantum cutting layer

One of the main limiting factors for the solar cell efficiency is the thermalization of high energy photons. For photons with energy of more than twice the band gap of the solar cell, more than half of the energy is lost. In silicon solar cells about 21% of the absorbed photons have an energy of more than twice the band gap and in germanium solar cells this is even 54% of the absorbed photons. One way to solve this problem would be the positioning of a quantum cutting layer on top of the solar cell. In such a layer high energy photons, with an energy of more than twice the band gap, are absorbed, followed by the emission of two photons for each photon absorbed with an energy just above the band gap of the solar cell, which therefore both can be absorbed in the cell.

For solar cells with an IQE of 100% an ideal quantum cutter would absorb all photons with an energy of $2 E_g$ and above, and emit at a wavelength of exactly $1 E_g$ with a quantum efficiency of 200%. In practice, solar cells have an IQE which decreases at longer wavelengths (see Figure 2.5). Therefore, cutting the emission to exactly $1 E_g$ will not be optimal. The emission should therefore be at somewhat higher energy. However, the higher the energy of the emission is, the less photons can be cut, so there will be an optimum energy for the emission of the quantum cutting layer.

In Table 2.4 the results of the calculations are shown for solar cells with a quantum cutting layer of which both the refractive index and the emission wavelength are optimized. Note that for all cells the efficiency is higher than with a

normal spectral shifting layer, but that the largest gains are obtained for the small band gap solar cells. For these cells many photons have an energy of more than $2 E_g$. The solar cells with a larger band gap, a-Si and CGS, have not been included in Table 2.4. Their band gaps are too large to be useful in combination with a quantum cutting layer.

Table 2.4 Calculated efficiencies of various solar cells with a quantum cutting layer with encapsulation layer.

	η_{transp} (%)	n_3	λ_{em} (nm)	η_{conv} (%)
c-Si	25.3	2.4	964	28.3
pc-Si	22.5	2.4	936	25.2
CdTe	19.6	2.1	814	21.8
GaAs	25.6	2.4	826	27.4
CIS	23.7	2.2	1072	27.6
CIGS	25.6	2.2	1012	32.8
GaSb	13.9	2.4	1650	25.5
Ge	15.9	2.5	1514	24.0

For silicon solar cells a Tb^{3+} - Yb^{3+} doped quantum cutting layer has been proposed. In such a quantum cutting material 485 nm light is absorbed by Tb^{3+} ions and subsequently transferred in one step, via a cooperative energy transfer process, to two neighboring Yb^{3+} ions. [1] Due to the transfer process the two Yb^{3+} ions are excited in the ${}^2\text{F}_{5/2}$ excited state, and as a consequence will each be able to decay to the ground state of Yb^{3+} with the emission of a 1000 nm photon. Note that this emission is close to the calculated optimal emission wavelength of 950 nm for crystalline silicon solar cells (see Table 2.4). Also the optimum emission wavelengths of the CIGS and CIS cells are close to this Yb^{3+} emission.

In practice the quantum cutting process has some problems that still have to be solved before a quantum cutting layer could be implemented, such as a poor UV and blue light absorption of the Tb^{3+} ions and the high Yb^{3+} concentration that is needed for an efficient energy transfer process, but that at the same time quenches

the Yb^{3+} f - f emission. It is nevertheless interesting to know to what extent a Tb^{3+} - Yb^{3+} quantum cutter could improve the efficiency once these problems are solved. In the calculations it is therefore assumed that there is no concentration quenching and that the conversion layer contains a sensitizer which efficiently absorbs all light below 485 nm and transfers this energy to the Tb^{3+} ion, which cuts the photons into 1000 nm photons with a quantum efficiency of 200%. The results of the calculations are shown in Table 2.5. The efficiencies are circa 0.5% lower than for the ideal case due to the fact that the Yb^{3+} f - f emission is not exactly at the optimal wavelength and the fact that only light below 485 nm is absorbed, while the light between 485 and 500 could also theoretically be cut to 1000 nm photons. However, the efficiencies are still 2 to 3% higher if a Tb^{3+} - Yb^{3+} quantum cutting layer is applied.

Table 2.5 Calculated efficiencies of various solar cells with a Tb^{3+} - Yb^{3+} quantum cutting layer.

	η_{transp} (%)	η_{conv} (%)
c-Si	25.3	27.7
pc-Si	22.5	24.5
CIGS	25.6	29.1

2.3.4 Quantum tripling layer

The advantage of small band gap solar cells is that the absorber materials are able to absorb a large portion of the solar spectrum. However, as a consequence the energy that is obtained per absorbed photon is limited as a result of the large thermalization of the photons. With a quantum cutting layer, which converts the photons above $2 E_g$ into two photons of $1 E_g$ the thermalization is reduced. However, for cells with very small band gaps like germanium or GaSb cells, a part of the solar spectrum will have an energy above $3 E_g$. For these cells a quantum tripling layer, which absorbs the photons above $3 E_g$ and converts each photon into three photons of $1 E_g$, could be beneficial. The efficiency calculations for solar

cells with a quantum tripling layer are shown in Table 2.6. Although the efficiencies are a significant improvement compared to a cell with a transparent layer, the efficiencies are lower than for a cell with a quantum cutting (doubling) layer. The reason for this is that less photons can actually be cut if a quantum tripling layer is used, in comparison with a quantum doubling layer, and that the solar spectrum is most intense for those wavelengths that cannot be converted anymore with a quantum tripling layer.

Table 2.6 Calculated efficiencies of various solar cells with a quantum tripling layer.

	η_{transp} (%)	n_3	λ_{em} (nm)	η_{conv} (%)
GaSb	13.9	2	1662	21.6
Ge	15.9	2.1	1551	19.9

Although the quantum tripling layer appears to be less effective than the quantum doubling layer, one could still make use of the benefit of the quantum tripling process if it is used in combination with a quantum doubling process. The two properties could be combined in one layer, or alternatively in two different layers, where light above $3 E_g$ is absorbed by the quantum tripler and light between $2 E_g$ and $3 E_g$ is absorbed by the quantum doubler. If the two properties are combined in one layer the efficiencies could increase to the values shown in Table 2.7. As can be seen, such a combined doubling-tripling layer would largely improve solar cell efficiency.

Table 2.7 Calculated efficiencies of various solar cells with a conversion layer with both a quantum doubling and quantum tripling function.

	n_3	η_{transp} (%)	λ_{em} (nm)	η_{conv} (%)
GaSb	2	13.9	1648	26.4
Ge	2.1	15.9	1528	27.4

An example of a luminescent material that could be used for quantum tripling is a Tm^{3+} doped material, since cross-relaxation can occur between Tm^{3+} ions after excitation in the $^1\text{G}_4$ level (465 nm) of the Tm^{3+} ion. [24] Due to the cross-relaxations, three Tm^{3+} ions can get excited in the $^3\text{F}_4$ level, as is shown in Figure 2.8. As a result three 1750 nm photons can be emitted for each photon absorbed. Note that 1750 nm is above the band gap of GaSb and Ge, so in principle these photons can be absorbed by a GaSb or Ge solar cell. However, a higher IQE would be required at that wavelength than the IQE shown in Figure 2.5, in order to make efficient use of a Tm^{3+} based quantum tripling layer.

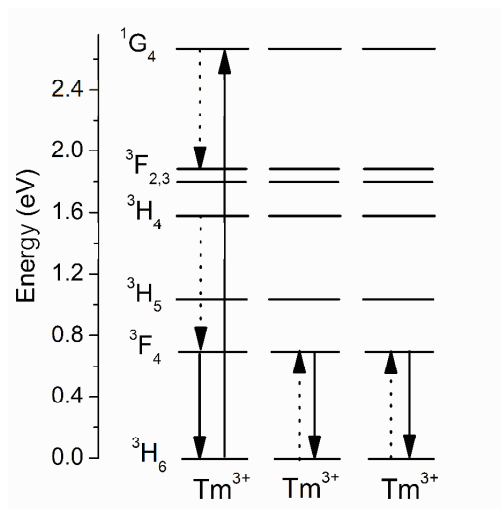


Figure 2.8 Tm^{3+} $4f$ energy levels, showing possible cross-relaxations between three Tm^{3+} ions, resulting in quantum tripling.

Note that for all calculations in this chapter IQE curves are used of solar cells that were published in literature. Therefore the IQE curves represent cells that were optimized for functioning under AM 1.5 solar illumination. As an example, crystalline silicon solar cells had an IQE which was relatively poor for UV and blue light irradiation, but years of optimization nowadays result in crystalline silicon solar cells of which the IQE is still relatively good in the UV and blue. As a result the efficiency gain by using spectral conversion layers on top of silicon solar

cells has decreased. However, for cells with a spectral conversion layer, the optimization of the IQE at short wavelengths becomes unnecessary. Therefore, the extra costs that are needed in order to obtain cells with a high IQE for short wavelength light could be avoided if a conversion layer is used.

Another point that one should consider is that a conversion layer will also change the efficiency of a cell in another way that is not taken into account in the calculations. Due to the conversion layer, the thermalization of high energy photons will now partly take place in the conversion layer instead of in the solar cell itself, which might result in a lower cell temperature. And if the temperature of the cell is lower the efficiency of the cell will increase, since it will decrease the amount of black body radiation from the cell, as can be seen in equation (2.8).

2.4 Conclusions

It has been shown that it is important to include the wavelength dependency of the refractive index and the IQE of solar cells to calculate realistic values for the efficiency enhancement of solar cells by the integration of a luminescent spectral conversion layer. With quantum cutting layers, the efficiency is enhanced for all cells considered and ranges from 3% for c-Si to 7.2% for CIGS to 8.1% for Ge. Quantum tripling layers also enhance efficiencies of all cells, especially small band gap cells. However, efficiency enhancements are lower compared to quantum cutting layers due to the smaller number of photons that can be absorbed by a quantum tripling layer. Combination of the quantum tripling and the quantum cutting layer doubles the efficiency of small band gap solar cells like GaSb or Ge. Efficiency calculations of solar cells with and without a simple spectral shifting layer show that for cells like c-Si, with a relatively high IQE at the high energy side, the efficiency enhancement is limited and can even lower the efficiency. For other cells that have a low IQE at the short wavelength side, like for example CdTe, the efficiency enhancement is much larger and even the application of available non-optimized spectral shifting materials like $\text{Sr}_2\text{Si}_5\text{N}_8:\text{Eu}^{2+}$ can increase efficiency by

3.2%. It would be interesting to take a spectral conversion layer as an integral part of the design and optimization of a solar cell instead of considering such a layer only after the solar cell has already been optimized.

2.5 Appendix

The transmittance of an unpolarized light ray from medium a with refractive index n_a to medium b with refractive index n_b as a function of the angle of incidence θ_a can be derived from the Fresnel equations [4]:

$$\tau_{ab}(\theta_a) = \frac{2 \cos \theta_a \sqrt{n_{ab}^2 - \sin^2 \theta_a}}{\left(\cos \theta_a + \sqrt{n_{ab}^2 - \sin^2 \theta_a}\right)^2} + \frac{2 n_{ab}^2 \cos \theta_a \sqrt{n_{ab}^2 - \sin^2 \theta_a}}{\left(n_{ab}^2 \cos \theta_a + \sqrt{n_{ab}^2 - \sin^2 \theta_a}\right)^2}. \quad (2.10)$$

Here is n_{ab} equal to n_b/n_a . Note that this equation is valid for all θ_a if $n_{ab} \geq 1$, but if $n_{ab} < 1$ the equation is only valid if $\theta_a < \arcsin(n_{ab})$. At larger angles $\tau_{ab} = 0$ due to total internal reflection. The transmittance of a light ray from medium a, via medium b, to medium c is given by (neglecting any interference effects) [4]:

$$\tau_{ac}(\theta_a) = \frac{\tau_{ab}(\theta_a) \tau_{bc}(\theta_b)}{\tau_{ab}(\theta_a) + \tau_{bc}(\theta_b) - \tau_{ab}(\theta_a) \tau_{bc}(\theta_b)}, \quad (2.11)$$

where θ_b is equal to $\arcsin(n_{ab} \sin \theta_a)$. Note that τ_{ac} will be 0 if either τ_{ac} or τ_{bc} becomes 0 due to total internal reflection. If both are 0, equation (2.11) is not valid and τ_{ac} should be zero as well. Similarly, the transmittance of a light ray from medium a via medium b and c to medium d as a function of θ_a is given by:

$$\tau_{ad}(\theta_a) = \frac{\tau_{ac}(\theta_a) \tau_{cd}(\theta_c)}{\tau_{ac}(\theta_a) + \tau_{cd}(\theta_c) - \tau_{ac}(\theta_a) \tau_{cd}(\theta_c)}, \quad (2.12)$$

where θ_c is equal to $\arcsin((n_a/n_c) \sin \theta_a)$. The geometrical factor B_{ab} for the transmittance of radiation, in case of an axi-symmetrical source of radiation, from medium a to medium b is given by [4]:

$$B_{ab} = 2\pi \int_0^{\delta} \tau_{ab}(\theta_a) \cos \theta_a \sin \theta_a d\theta_a, \quad (2.13)$$

where δ is equal to $\pi/2$ in the case of a hemispherical radiation source. When direct solar radiation is considered δ is given by the sine of the radius of the sun ($0.6955 \cdot 10^6$ km) divided over the distance from the sun to the earth ($149.6 \cdot 10^6$ km): 0.00465 rad. The fraction of the spectral radiation that is transmitted from medium a to medium b with respect to the fraction of radiation that can be transmitted when the refractive indices of the layers would be the same, is equal to:

$$f_{ab} = \frac{2\pi \int_0^{\delta} \tau_{ab}(\theta_a) \cos \theta_a \sin \theta_a d\theta_a}{2\pi \int_0^{\delta} \cos \theta_a \sin \theta_a d\theta_a} = \frac{2}{\sin^2 \delta} \int_0^{\delta} \tau_{ab}(\theta_a) \cos \theta_a \sin \theta_a d\theta_a. \quad (2.14)$$

Similarly, the fraction for the transmittance of radiation form medium a via medium b to medium c is equal to:

$$f_{ac} = \frac{2}{\sin^2 \delta} \int_0^{\delta} \tau_{ac}(\theta_a) \cos \theta_a \sin \theta_a d\theta_a. \quad (2.15)$$

The fraction of the radiation that is transmitted from medium *a* via media *b* and *c* to medium *d* (f_{ad}) is calculated in a similar way. Radiation emitted by the spectral conversion layer (medium 3) has to be emitted either in the direction of the solar cell (medium 4) or in the direction out of the cell. The transmittance of an unpolarized light ray from medium 3 to medium 4 is then given by:

$$T_{34}(\theta_3) = \frac{\tau_{34}(\theta_3)}{\tau_{34}(\theta_3) + \tau_{31}(\theta_3)}. \quad (2.16)$$

Therefore the fraction of the radiation emitted by the conversion layer that is transmitted to medium 4 is:

$$f_{34} = 2 \int_0^{\pi/2} T_{34}(\theta_3) \cos \theta_3 \sin \theta_3 d\theta_3. \quad (2.17)$$

2.6 References

- [1] P. Vergeer, T.J.H. Vlugt, M.H.F. Kox, M.I. Den Hertog, J.P.J.M. van der Eerden, A. Meijerink; Phys. Rev. B 71 (2005) 014119.
- [2] W. Shockley, H.J. Queisser; J. Appl. Phys. 32 (1961) 510.
- [3] T. Trupke, M.A. Green, P. Würfel; J. Appl. Phys. 92 (2002) 1668.
- [4] V. Badescu, A. De Vos, A.M. Badescu, A. Szymanska. J. Phys. D: Appl. Phys. 40 (2007) 341.
- [5] V. Badescu, A. De Vos; J. Appl. Phys. 102 (2007) 073102.
- [6] C.P. Thomas, A.B. Wedding, S.O. Martin; Sol. Energy Mater. Sol. C. 98 (2012) 455.
- [7] E.D. Palik, Handbook of Optical Constants of Solids, Academic Press, Boston, 1985.
- [8] D.E. Aspnes DE, A.A. Studna; Phys. Rev. B 27 (1983) 985.
- [9] M.I. Alonso, K. Wakita, J. Pascual, M. Garriga, N. Yamamoto; Phys. Rev. B 63 (2001) 075203.
- [10] M.I. Alonso, M. Garriga, C.A. Durante Rincón, E. Hernandez, M. León; Appl. Phys. A 74 (2002) 659.
- [11] B. Thaidigsmann, A. Wolf, D. Biro D. Proceedings of the 24th European Solar Energy Conference and Exhibition, Hamburg, Germany, 21-25 September 2009.

- [12] H. Morikawa, Y. Nishimoto, H. Naomoto, Y. Kawama, A. Takami, S. Arimoto, T. Ishihara, K. Namba; *Sol. Energy Mater. Sol. C.* 53 (1998) 23.
- [13] J.S.C. Prentice; *Sol. Energy Mater. Sol. C.* 69 (2001) 303.
- [14] G. Stollwerck, O.V. Sulima, A.W. Bett.; *IEEE T. Electron Dev.* 47 (2000) 448.
- [15] N.E. Posthuma, G. Flamand, J. Poortmans; 3rd World Conference on Photovoltaic Energy Conversion, May 11-18, 2003, Osaka, Japan.
- [16] M. Hädrich, H. Metzner, U. Reislöhner, C. Kraft; *Sol. Energy Mater. Sol. C.* 95 (2011) 887.
- [17] K. Xiong, S. Lu, T. Zhou, D. Jiang, R. Wang, K. Qiu, J. Dong, H. Yang; *Sol. Energy* 84 (2010) 1888.
- [18] J.A.M. Abushama, S. Johnston, T. Moriarty, G. Teeter, K. Ramanathan, R. Noufi; *Prog. Photovoltaics: Res. Appl.* 2004; 12 : 39-45.
- [19] W.K. Metzger, M. Gloeckler; *J. Appl. Phys.* 98 (2005) 063701.
- [20] S. Nishiwaki, A. Ennaoui, S. Schuler, S. Siebentritt, M.C. Lux-Steiner; *Thin Solid Films* 431 (2003) 296.
- [21] H. Lutz, S. Joosten, J. Hoffmann, P. Lehmeier, A. Seilmeier, H.A. Höpfe, W. Schnick; *J. Phys. Chem. Solids* 65 (2004) 1285.
- [22] Y.Q. Li, J.E.J. van Steen, J.W.H. Krevel, G. Botty, A.C.A. Delsing, F.J. DiSalvo, G. de With, H.T. Hintzen; *J. Alloy. Compd.* 417 (2006) 273.
- [23] Y.Q. Li, G. de With, H.T. Hintzen; *J. Solid State Chem.* 181 (2008) 515.
- [24] A. Jaffrès, B. Viana, E. van der Kolk; *Chem. Phys. Lett.* 527 (2012) 42.

Chapter 3

Yb³⁺ doped LaSi₃N₅ and YSi₃N₅ with low energy charge transfer for near-infrared light-emitting diode and solar cell application

*The content of this chapter has been published as: O.M. ten Kate, H.T. Hintzen, P. Dorenbos, E. van der Kolk; “Yb³⁺ doped LaSi₃N₅ and YSi₃N₅ with low energy charge transfer for near-infrared light-emitting diode and solar cell application”; *Journal of Materials Chemistry* 21 (2011) 18289.*

Yb³⁺ doped LaSi₃N₅ phosphors have been prepared by solid-state synthesis in a high temperature furnace directly coupled to a glove box. The charge transfer (CT) band of Yb³⁺ in LaSi₃N₅ was observed at an unusually low energy of 3.1 eV. CT excitation results in *f-f* emission of Yb³⁺ at 1.2 eV, which could make Yb³⁺ doped LaSi₃N₅ suitable for application as a spectral conversion material for infrared light-emitting diodes or solar cells. Substitution of La³⁺ by the smaller Y³⁺ ion shifts the CT to higher energy (3.9 eV). A clear relation between the CT energy and the Yb³⁺ *f-f* emission intensity was found. With the help of a detailed energy level diagram that contains the position of the 4*f* and 5*d* levels of all divalent and trivalent ions with respect to the valence and conduction band, all hitherto observed luminescence properties of divalent and trivalent lanthanide dopants in LaSi₃N₅ are reviewed and explained.

3.1 Introduction

In the last decade, silicon nitride based materials have received considerable interest in luminescence research. Lanthanide (Ln) ions, like Eu^{2+} and Ce^{3+} , have successfully been doped in for example $\text{M}_2\text{Si}_5\text{N}_8$ ($\text{M} = \text{Ca}, \text{Sr}, \text{Ba}$), [1,2] LaSi_3N_5 , [3-6] MSiN_2 ($\text{M} = \text{Sr}, \text{Ba}$) [7] and $\text{BaSi}_7\text{N}_{10}$ [8] and have shown efficient red, green or blue emission.

Silicon nitride host materials have the advantage that their spectroscopic properties can be tuned by the partial substitution of silicon by aluminum and the replacement of nitrogen by oxygen, as well as by varying the silicon to nitrogen ratio. [9,10] Besides, amorphous silicon nitride (a-SiN_x) is applied in solar cells nowadays as anti-reflection coating and surface passivation layer. [11,12] Integrating the anti-reflection with the spectral conversion function by developing luminescent thin films is therefore an attractive route to enhance the efficiency of solar cells.

In the last few years the interest in the luminescence properties of Yb^{3+} doped materials has grown substantially. Trivalent ytterbium can emit at about 1.2 eV due to its $^2\text{F}_{5/2} \rightarrow ^2\text{F}_{7/2}$ transition, of which the energy is just above the band gap of crystalline silicon (circa 1.1 eV). [13] In addition ytterbium is considered in $\text{Yb}^{3+}\text{-Ln}^{3+}$ doubly doped quantum cutting phosphors that can emit two infrared (IR) photons for each absorbed ultraviolet (UV) or visible photon. [13,14]

Because of the research interest in the solid-state lighting field, doping of the silicon nitrides was focused mainly on the rare-earths Ce^{3+} , Tb^{3+} , and Eu^{2+} , which emit visible light and have therefore been applied as spectral converters in white light-emitting diodes (LEDs). If the IR Yb^{3+} emission can be efficiently excited by the blue or UV light of LEDs, then Yb^{3+} may form the basis of new phosphors for IR light-emitting LEDs.

In this chapter ytterbium doping in LaSi_3N_5 and YSi_3N_5 is reported. Uheda et al. doped LaSi_3N_5 with europium and observed Eu^{2+} $d\text{-}f$ emission at 549 nm, while no Eu^{3+} absorption or emission was detected. [3] It was therefore concluded that all europium is present in the divalent state. The charge difference due to the

substitution of La³⁺ by Eu²⁺ was assumed to be compensated by the replacement of N³⁻ by O²⁻. Besides Eu²⁺, also Ce³⁺ has been studied as a dopant in LaSi₃N₅, in which it shows *d-f* emission. [4,5] Eu²⁺ and Ce³⁺ emission have also been reported in YSi₃N₅. [15,16] It should be noted that Liddell et al. [17] pointed out that the YSi₃N₅ structure may not exist and that the structure originally identified as YSi₃N₅ [18] should in fact be described with the chemical composition Y₆Si₁₁N₂₀O.

In the next section the synthesis and characterization methods of ytterbium doped LaSi₃N₅ and YSi₃N₅ are described. The absorption and luminescence of these materials are presented and discussed in section 3.3. In section 3.4 the presented experimental results and those published earlier are reviewed in the light of a detailed energy level scheme. Finally conclusions will be drawn on the applicability of Yb³⁺ in photovoltaics and LEDs, and more general on the luminescence properties of Ln³⁺ and Ln²⁺ ions in LaSi₃N₅ and YSi₃N₅.

3.2 Experimental

3.2.1 Synthesis

For the synthesis of La_{1-x}Yb_xSi₃N₅ (x = 0, 0.003, 0.01, 0.02, 0.03), the binary compound LaN was pre-synthesized by the nitridation of lanthanum powder (CSRE, 99%) at 800 °C in a horizontal tube furnace connected to a glove box and purged with a nitrogen atmosphere. The resultant LaN was then thoroughly mixed with α-Si₃N₄ (Akzo Nobel, P95H) and ytterbium powder (Alfa Aesar, 99.9%) in the appropriate molar ratio in a nitrogen filled glove box and ground with a pestle and an agate mortar. The mixed powders were then transferred to a boron nitride crucible and fired twice at 1700 °C, with intermediate grinding in between, in a horizontal tube furnace purged with a nitrogen atmosphere.

Y_{1-x}Yb_xSi₃N₅ (x = 0, 0.01, 0.05) was made by starting directly from silicon powder (Aldrich, 99%), ytterbium and yttrium powder (CSRE, 99.5%). These powders were mixed in the appropriate molar ratio and fired in a horizontal tube

furnace purged with a nitrogen atmosphere at 800 and 1300 °C for the nitridation of Y and Si respectively, and finally at 1700 °C to form the final product.

3.2.2 Characterization

Crystalline phases were checked by X-ray powder diffraction (XRD) analysis with a Bruker D4 Endeavor with Cu K α radiation. Diffraction data were collected by step scanning from 12° to 65° in 2θ with a step size of 0.05° and a counting time of 1 s per step. Diffuse reflectance in the UV and visible were measured with a Perkin Elmer LS50B spectrophotometer with Xe lamp and an R952 photomultiplier. White BaSO $_4$ and black felt were used as a reference. Diffuse reflectance spectra in the red and infrared were recorded with a Bruker Vertex 80v FT interferometer using a tungsten lamp as a light source and a cooled InGaAs detector. BaSO $_4$ was taken as a reference. Emission spectra were recorded with the same interferometer for excitation by the second or third harmonic of a tunable femtosecond laser, using a cooled InGaAs detector. Excitation spectra of the Yb $^{3+}$ f - f emission were measured with a silicon detector with a longpass filter (> 900 nm) in front of the detector. The samples were excited with a xenon light source with a double grating monochromator.

3.3 Experimental results and discussion

3.3.1 Phase formation

The obtained LaSi $_3$ N $_5$ powder has a light grey color, while the samples doped with ytterbium have a yellow color. The X-ray diffraction pattern of 1% Yb doped LaSi $_3$ N $_5$ is shown in Figure 3.1a. The LaSi $_3$ N $_5$ structure was described by Inoue et al. as orthorhombic $P2_12_12_1$. [19] However, the corresponding structure from the database (JCPDS 00-042-1144) does not contain all diffraction peaks belonging to

the P2₁2₁2₁ structure. The profile of La_{0.9}Ce_{0.1}Si₃N₅ reported by Cai et al. [4] (ICSD 165875) is therefore shown for comparison in Figure 3.1b. The Yb doped sample appeared to have an identical XRD pattern except for one small peak at 31.0°, which is indicated with an arrow in Figure 3.1a. This line belongs to a very small impurity phase that has been detected by others as well in LaSi₃N₅. [4,20,21] The phase could be identified as La₂Si₆N₈O₃ (Figure 3.1c), that crystallizes in the monoclinic C2/c structure. [22] Note that the impurity phase is not related to ytterbium, since the peak at 31.0° is also observed in the undoped samples, and also note that the intensity of this peak decreased when LaSi₃N₅ was made from Si powder instead of α-Si₃N₄ as a starting material.

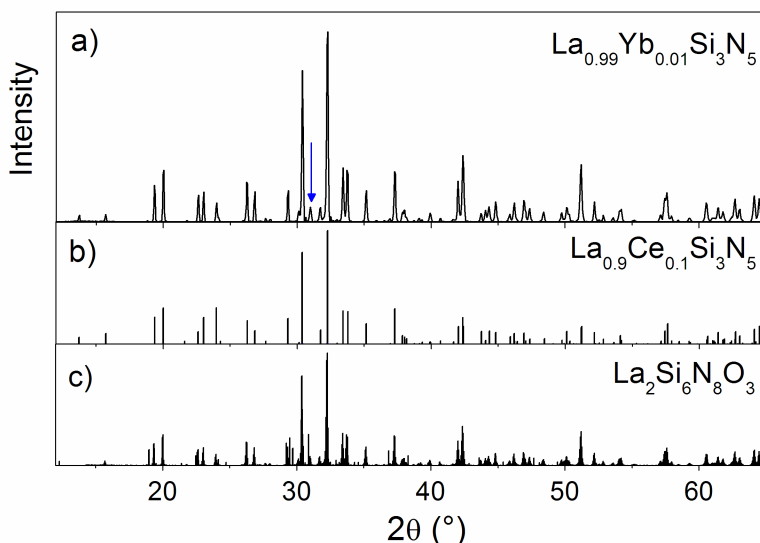


Figure 3.1 a) X-ray diffraction pattern of La_{0.99}Yb_{0.01}Si₃N₅. The pattern is compared with the b) La_{0.9}Ce_{0.1}Si₃N₅ (ICSD 165875) and c) La₂Si₆N₈O₃ (ref. 22) patterns from literature. The arrow indicates a diffraction line belonging to the P2₁2₁2₁ structure.

The X-ray diffraction pattern of an Y_{0.99}Yb_{0.01}Si₃N₅ sample is shown in Figure 3.2a. The main phase in the sample is the hexagonal YSi₃N₅ phase (JCPDS 00-051-0812). Besides YSi₃N₅, also Si₃N₄ (JCPDS 01-071-0632) is observed, and possibly

a very small amount of YN (JCPDS 01-071-9847). Note that an excess of Si_3N_4 would also be expected based on the assumption that $\text{Y}_6\text{Si}_{11}\text{N}_{20}\text{O}$ was formed instead of YSi_3N_5 , as was suggested by Liddell et al. [17] The sample was made from silicon powder as a starting material. When $\alpha\text{-Si}_3\text{N}_4$ was used as a starting material, $\text{Y}_2\text{Si}_3\text{O}_3\text{N}_4$ was formed as well, probably due to significant oxygen impurities in the $\alpha\text{-Si}_3\text{N}_4$ (over 1 wt.-%). The Yb doped and undoped YSi_3N_5 powders both have a light grey color, which can be due to reduced transition metal impurities or the Si_3N_4 phase.

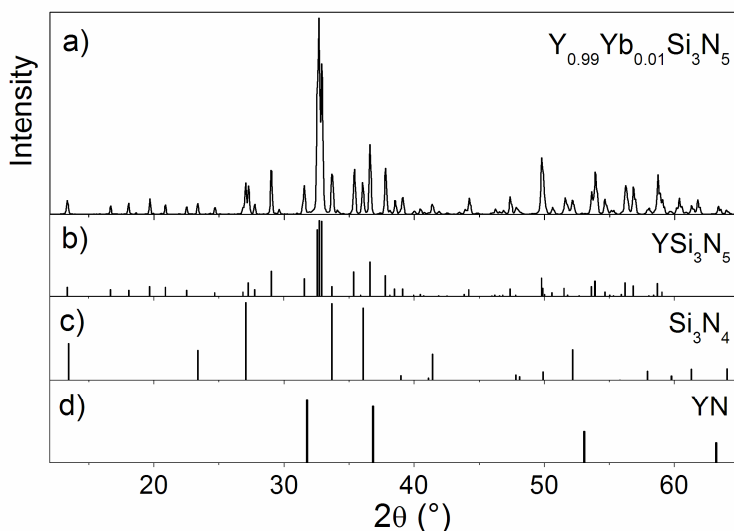


Figure 3.2 a) X-ray diffraction pattern of $\text{Y}_{0.99}\text{Yb}_{0.01}\text{Si}_3\text{N}_5$. The pattern is compared with the b) YSi_3N_5 (JCPDS 00-051-0812), c) Si_3N_4 (JCPDS 01-071-0632) and d) YN (JCPDS 01-071-9847) patterns from literature.

3.3.2 Optical properties of Yb^{3+} doped LaSi_3N_5

The measured diffuse reflectance patterns were used to calculate the absorption according to the Kubelka-Munk procedure. [23] In Figure 3.3a the absorption spectra of LaSi_3N_5 doped with different ytterbium concentrations are compared. Host lattice absorption is observed in the undoped sample above 4.5 eV. The

undoped sample also has some absorption just below the band edge between 4.0 and 4.5 eV.

The Yb doped samples have a broad absorption band centered around 3.1 eV as is shown in Figure 3.3a. This absorption band increases in intensity with higher ytterbium concentrations and is therefore attributed to the charge transfer (CT) of an electron from nitrogen to Yb³⁺. The energy of the CT band (3.1 eV) is discussed further in section 3.4.

The ytterbium doped samples have other type of absorption in addition to the host lattice and CT absorption, as can be seen in Figure 3.4a. Sharp peaks are observed at about 1.2 eV that are typical for the $^2F_{7/2} \rightarrow ^2F_{5/2}$ absorption of Yb³⁺, indicating that ytterbium is indeed present in the trivalent state. The intensity of this absorption peak increases linearly with the ytterbium concentration as can be seen in the inset of Figure 3.4a.

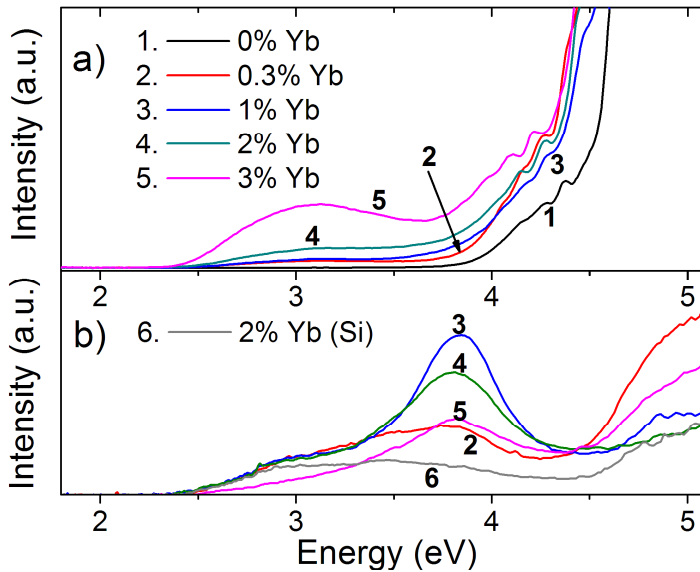


Figure 3.3 a) Kubelka-Munk absorption spectra of Yb doped LaSi₃N₅ and b) excitation spectra of the Yb³⁺ *f-f* emission in LaSi₃N₅ doped with different Yb concentrations. Line 6 is the excitation spectrum of a 2% Yb doped LaSi₃N₅ sample made from Si powder.

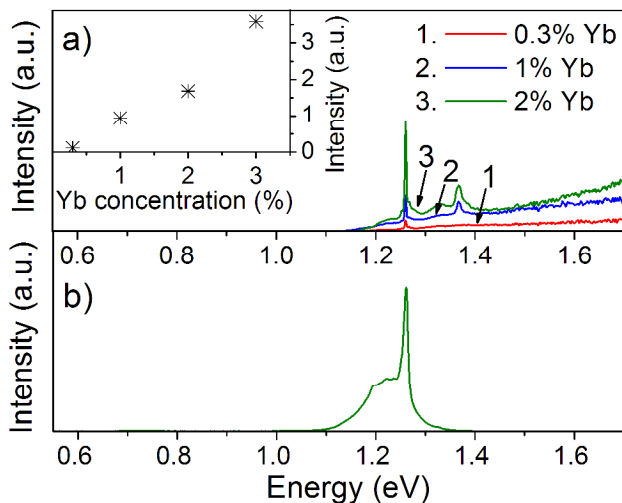


Figure 3.4 a) Kubelka-Munk absorption spectrum of Yb doped LaSi_3N_5 and b) emission spectrum of $\text{La}_{0.98}\text{Yb}_{0.02}\text{Si}_3\text{N}_5$ excited at 3.4 eV. The inset of 3.4a shows the intensity of the ${}^2\text{F}_{7/2} \rightarrow {}^2\text{F}_{5/2}$ absorption peak as a function of the ytterbium concentration.

Yb^{3+} doped LaSi_3N_5 can be excited with energies above 2.5 eV resulting in ${}^2\text{F}_{5/2} \rightarrow {}^2\text{F}_{7/2}$ emission of Yb^{3+} around 1.2 eV, as is shown in Figure 3.4b. No other type of emission was observed, not even at 10 K. The excitation spectrum of the Yb^{3+} $f-f$ emission is presented in Figure 3.3b. Spectral features can be observed above 4.5 eV, around 3.8 eV and around 3.1 eV. The band at 3.1 eV corresponds with the CT band that was also observed in the absorption spectra shown in Figure 3.3a. Note that the intensity of this excitation band is weak. The band starting at 4.5 eV corresponds to host lattice absorption. The excitation band centered around 3.8 eV on the other hand cannot be correlated to any absorption feature in the absorption spectra. This indicates that it is related to a weak absorption process with relatively high luminescence efficiency. One possible origin of this band could be a charge transfer from oxygen impurities to Yb^{3+} in LaSi_3N_5 or in the $\text{La}_2\text{Si}_6\text{N}_8\text{O}_3$ impurity phase that was found in the XRD pattern (Figure 3.1). Note that this excitation band cannot be due to charge transfer from nitrogen to Yb^{3+} , since such a nitrogen related CT band should be at lower energy, as will be explained in section 3.4. The

relation of the 3.8 eV excitation band with oxygen impurities is confirmed when the excitation spectra of a sample made from Si powder as a starting material (which has a relatively low oxygen content) is compared with a sample made from α -Si₃N₄ (which has a relatively high oxygen content). The 3.8 eV excitation band of a 2% Yb doped sample made from Si powder (line 6 in Figure 3.3b) is much less intense than the excitation band of a sample made from α -Si₃N₄ (line 4). So, based on the optical spectra in Figure 3.3b and the XRD spectra of Figure 3.1 it is believed that by using α -Si₃N₄ a mixture of LaSi₃N₅ and La₂Si₆N₈O₃ is formed, resulting in the excitation band at 3.8 eV. When Si is used a purer LaSi₃N₅ phase is formed with almost no excitation band at 3.8 eV. Also note that the stoichiometry of La₂Si₆N₈O₃ is very similar to that of LaSi₃N₅ (which can also be written as La₂Si₆N₁₀), indicating that in La₂Si₆N₈O₃, two nitrogen atoms are substituted by three oxygen atoms.

It was found that the intensity of the Yb³⁺ *f-f* emission in Yb doped LaSi₃N₅ phosphors after direct excitation into the ²F_{5/2} state is comparable to the *f-f* emission of commercial Yb³⁺ based phosphors after direct *f-f* excitation. It is concluded that the low emission intensity after CT excitation is not due to Yb³⁺ *f-f* quenching but rather due to direct quenching from the charge transfer state to the ground state. This quenching mechanism is shown in the configuration coordinate diagram plotted in Figure 3.5a. After CT band excitation, the electron will decay non-radiatively to the ground state of Yb³⁺ via the crossing point of the CT parabola with the ²F_{7/2} parabola. As can be seen in Figure 3.6, the intensity of the CT excitation band stays constant when the temperature is decreased to 80 K. This can be explained when the cross section of the CT parabola with the ground state parabola is near the bottom of the CT parabola so that only little or no thermal stimulation is needed to relax down the ²F_{7/2} parabola. Above 550 K the intensity of the CT band starts to decrease, which is attributed to multi-phonon *f-f* quenching.

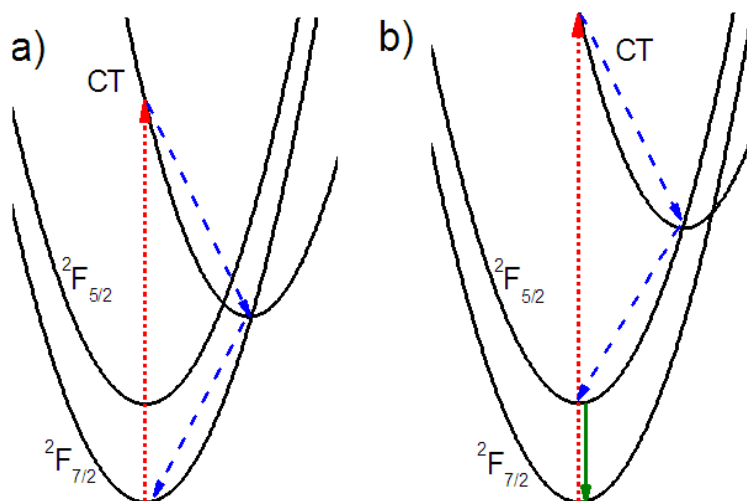


Figure 3.5 a) Configuration coordinate diagram for the Yb^{3+} CT state and the Yb^{3+} $4f$ ground and excited states in Yb^{3+} doped LaSi_3N_5 . The CT excitation is shown with a dotted arrow and the dashed arrow indicates the non-radiative decay. b) The same configuration coordinate diagram with a CT state at higher energy, giving Yb^{3+} f - f emission (solid arrow).

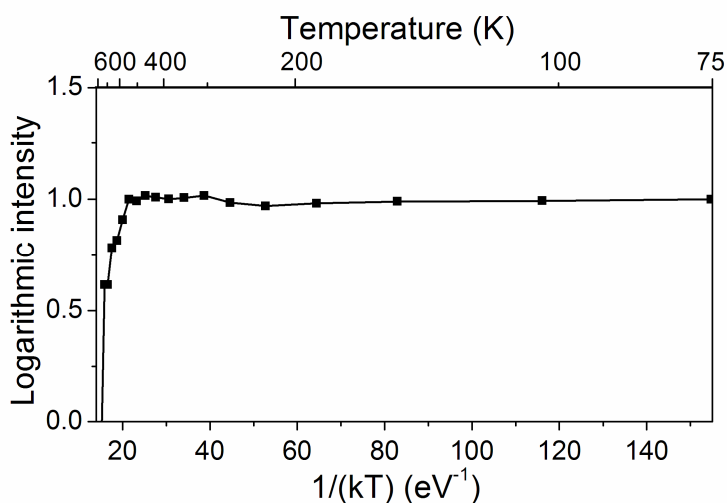


Figure 3.6 Temperature dependence of the CT excitation band of the Yb^{3+} f - f emission of 1% Yb doped LaSi_3N_5 .

3.3.3 Optical properties of Yb³⁺ doped YSi₃N₅

In Figure 3.7a the absorption spectra of undoped and 5% Yb doped YSi₃N₅ are shown. The spectrum of the Yb doped sample has a strong absorption band around 3.9 eV, while no absorption band is observed around 3.1 eV, indicating that the charge transfer band has shifted from 3.1 to 3.9 eV. This is supported by the excitation spectrum of the Yb³⁺ *f-f* emission of this sample, shown in Figure 3.7b. In this spectrum two excitation bands are observed; host lattice excitation above 4.4 eV and a broad charge transfer band around 3.9 eV. It has been shown in literature that the CT band of Eu³⁺ shifts to higher energy when the distance between the Eu³⁺ ion and the coordinating ligands, as well as the coordination number of the Eu³⁺ ion are reduced. [24] The 3.9 eV band in YSi₃N₅ is therefore assigned to the Yb³⁺ CT band that has shifted to higher energy compared to LaSi₃N₅ because the relatively large lanthanum ion was substituted for the smaller yttrium ion.

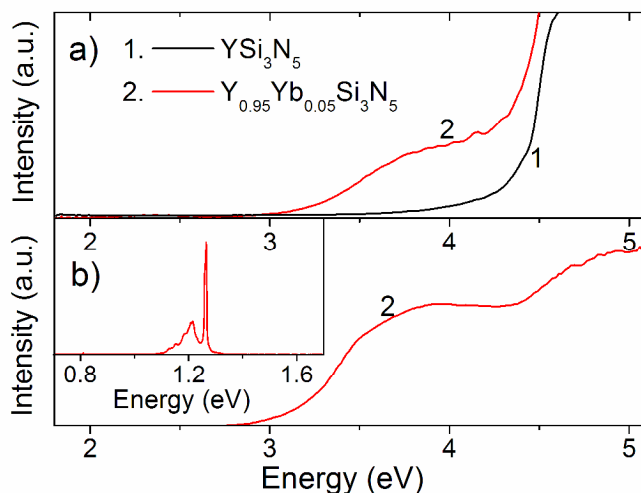


Figure 3.7 a) Kubelka-Munk absorption spectra of undoped YSi₃N₅ and 5% Yb doped YSi₃N₅. b) Excitation spectrum of the Yb³⁺ *f-f* emission of 5% Yb doped YSi₃N₅. The inset of Figure 3.7b shows the emission spectrum of 5% Yb doped YSi₃N₅ excited at 3.4 eV.

Note that under CT excitation the Yb^{3+} f - f emission is about ten times more efficient in YSi_3N_5 than in LaSi_3N_5 . This is due to the fact that the CT band is at higher energy in YSi_3N_5 resulting in a higher probability of relaxation to the Yb^{3+} ${}^2\text{F}_{5/2}$ excited state parabola. As can be seen in Figure 3.5b, when the CT is shifted to higher energy in the configuration coordinate diagram the ${}^2\text{F}_{5/2}$ level instead of the ${}^2\text{F}_{7/2}$ ground state is populated after CT excitation.

3.4 Energy level scheme of $\text{LaSi}_3\text{N}_5:\text{Ln}^{2+},\text{Ln}^{3+}$

Luminescence and optical spectroscopy data of Ln^{2+} and Ln^{3+} ions in LaSi_3N_5 can be used to construct a detailed energy level scheme that shows the energy of the $4f$ and $5d$ states of all divalent and trivalent lanthanides with respect to the valence and conduction band. With such a scheme originally developed by Dorenbos [25,26] the luminescence properties of all Ln^{3+} and Ln^{2+} in a certain host can be related to each other.

Four different experimentally determined parameters were used to construct the LaSi_3N_5 energy scheme that is shown in Figure 3.8: (i) the LaSi_3N_5 band gap (arrow 1), (ii) the Ce^{3+} f - d absorption (arrow 2), (iii) the Eu^{2+} f - d absorption (arrow 3) and (iv) the charge transfer band of Yb^{3+} (arrow 4). The band gap of 5.2 eV was deduced from the excitation spectra of the Eu^{2+} and Ce^{3+} d - f emission in LaSi_3N_5 described in literature [5,6], and is in agreement with the excitation spectra shown in Figure 3.3b. Note that derived band gap energy is a best estimate and includes the exciton binding energy, resulting in a band gap that is about 8% higher [27] than the optical band gap of 4.8 eV. The $4f$ - $5d$ absorption of Ce^{3+} was taken from literature [5] to determine the energy difference between the lowest $4f$ and lowest $5d$ states of the trivalent ions (3.5 eV, arrow 2). Information on the $4f$ - $5d$ absorption of Eu^{2+} obtained by Zhou et al. [6] was used to determine the energy difference between the lowest $4f$ and lowest $5d$ states of the divalent ions (2.7 eV, arrow 3). The energy of the Yb^{3+} CT band (3.1 eV) equals the energy difference between the $4f$ ground state of Yb^{2+} and the top of the valence band (arrow 4) and

was deduced from Figure 3.3a. Since no information is available about the CT energy of any tetravalent lanthanide ion, the energy difference between the 4*f* ground state of Ln³⁺ and the top of the valence band was based on luminescence temperature quenching data of the Ce³⁺ *d-f* emission in LaSi₃N₅ obtained by Suehiro et al. [5] Their quenching data imply that the Ce³⁺ 5*d* emitting state (indicated with number 5 in Figure 3.8) is circa 0.7 eV below the bottom of the conduction band. Taking the 0.4 eV Stokes shift of the Ce³⁺ emission into account, the unrelaxed lowest 5*d* state is placed about 0.3 eV below the bottom of the conduction band. This energy value was used to position the Ln³⁺ states relative to the conduction and valence band.

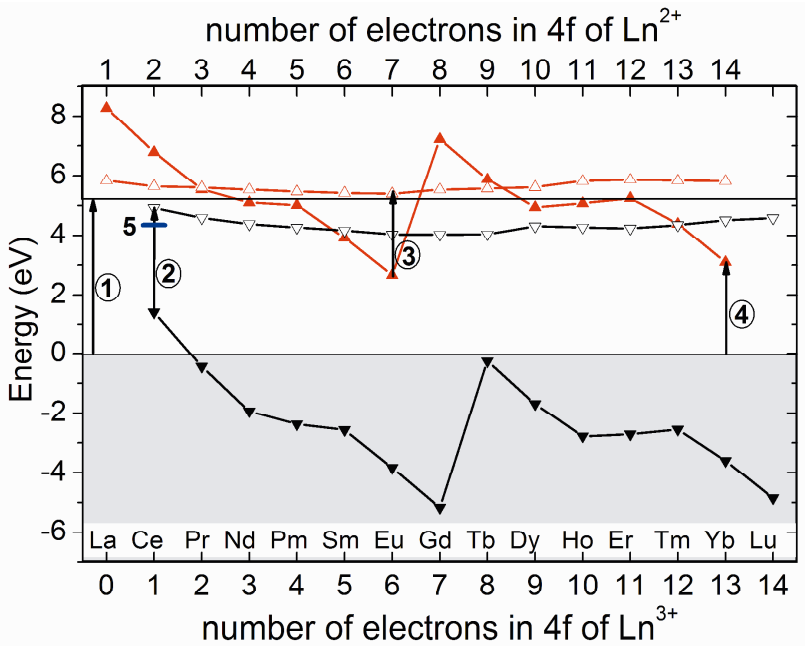


Figure 3.8 Energy level scheme showing the 4*f* ground states of the trivalent (▼) and divalent ions (▲) and lowest energy 5*d* states of the trivalent (▽) and divalent ions (△) with respect to the valence (grey area at the bottom) and conduction band (white area at the top) of LaSi₃N₅. The arrows indicate the experimentally determined optical transition used to construct this scheme.

The resulting energy level scheme is a strong aid in the interpretation of the excitation, emission and absorption spectra. If for example the band observed in the excitation spectrum at 3.8 eV (Figure 3.2b) is interpreted as the CT band of Yb^{3+} instead of the 3.1 eV band, no Eu^{2+} d - f emission would be possible which is in contradiction to what is observed. A CT band at 3.8 eV would namely position the $4f$ and $5d$ levels of the divalent ions 0.7 eV higher in energy. This would place the lowest energy Eu^{2+} $5d$ level deep inside the conduction band causing the loss of the electron to the conduction band instead of $5d$ - $4f$ emission. This quenching process is referred to as auto-ionization and has been studied in detail for fluoride and oxide materials like $\text{CaF}_2:\text{Yb}^{2+}$ and $\text{LaAlO}_3:\text{Ce}^{3+}$. [28,29] However, in LaSi_3N_5 the Eu^{2+} d - f emission is reported [6], indicating that auto-ionization does not occur, that the relaxed $5d$ state is below the conduction band and that the Yb^{3+} CT band is at 3.1 eV rather than 3.8 eV.

The energy scheme also allows commenting on the preferred divalent and trivalent states of Ln ions in LaSi_3N_5 . When the energy difference between the ground state of the divalent ion and the bottom of the conduction band is large the divalent ion will be more stable and it will be more likely that the divalent ion is formed during synthesis. Note that in the scheme in Figure 3.8 the $4f$ ground state of Eu^{2+} is slightly closer to the valence band than to the conduction band, and that all europium is found in the divalent state. [3] The $4f$ ground state of Yb^{2+} on the other hand, is 0.43 eV higher in energy than Eu^{2+} and therefore closer to the conduction band than to the valence band. Yb is indeed found in the trivalent state, although the presence of a small amount of Yb^{2+} cannot be excluded. X-ray photoelectron spectroscopy (XPS) could not be used to verify the presence of Yb^{2+} since the ytterbium concentration (3 at.%) appeared to be too low to detect ytterbium at all. Detection of Yb^{2+} by observing d - f emission is not possible as according to Figure 3.8 this type of emission is quenched by auto-ionization, since the emitting Yb^{2+} $5d$ states are located too far into the conduction band. Detection of a small amount of Yb^{2+} by looking at the absorption spectrum is not possible either, since the Yb^{2+} f - d absorption is, according to Figure 3.8, expected in the same energy range as the Yb^{3+} CT absorption band.

Figure 3.8 can be used to predict luminescence properties of other Ln ions in this host as well. Tm and Sm will, like Yb, enter the structure as trivalent ions and have a CT energy of about 4 eV. Exciting in the CT band will likely give the typical 4*f*-4*f* emission of these ions in the visible and infrared. All other Ln ions will either be in the divalent state (Eu²⁺) or have a CT energy close to or higher than the band gap of LaSi₃N₅. Sm³⁺, Tm³⁺ and Yb³⁺ are the only ions that are stable electron traps at room temperature as their divalent ground states are sufficiently below the conduction band. As the Ce³⁺ ground state is above the valence band maximum it is the only Ln ion that can act as a stable hole trap. Doubly doped LaSi₃N₅:Ce³⁺,Ln³⁺ (Ln = Sm, Tm and Yb) therefore has both stable hole and electron traps and may therefore display Ce³⁺ *d-f* afterglow behavior. [30] *f-d* transitions of Ln³⁺ ions as observed for Ce³⁺ are only expected for Tb³⁺ at about 4 eV. All other Ln³⁺ ions have *f-d* transitions at energies larger than the optical band gap of LaSi₃N₅.

3.5 Conclusions

A low energy 3.1 eV charge transfer (CT) band of Yb³⁺ is observed in LaSi₃N₅ that causes strong absorption of blue and UV light and exclusively generates infrared Yb³⁺ *f-f* emission around 1.2 eV. This UV/blue to near-infrared spectral conversion is interesting for application as spectral converter on solar cells or near-infrared LEDs. The quantum efficiency of UV/blue to infrared spectral conversion after CT excitation seems limited due to non-radiative relaxation from the low energy CT state to the ²F_{7/2} ground state of Yb³⁺. The CT band shifts to higher energy (3.9 eV) when La is replaced by the smaller Y ion. A higher energy CT band results in more efficient spectral conversion due to more efficient relaxation from the CT state to the excited ²F_{5/2} state of Yb³⁺.

It would be interesting to look at silicon nitride based materials doped with two lanthanide ions, like Tb³⁺-Yb³⁺, Pr³⁺-Yb³⁺ or Tm³⁺-Yb³⁺, since the material could then be used for quantum cutting for solar cell applications. The low energy Yb³⁺ CT absorption band in LaSi₃N₅ will absorb solar light and therefore compete

with the absorption by the Tb^{3+} , Pr^{3+} or Tm^{3+} ion, reducing the quantum cutting efficiency. The higher energy CT band in YSi_3N_5 on the other hand, will not absorb solar light, and this host is therefore interesting to investigate quantum cutting. Studying $LaSi_3N_5$ doped with Ce^{3+} - Sm^{3+} , Ce^{3+} - Tm^{3+} or Ce^{3+} - Yb^{3+} couples is interesting for afterglow applications.

3.6 References

- [1] Y.Q. Li, J.W.H. Kovel, G. Botty, A.C.A. Delsing, F.J. DiSalvo, G. de With, H.T. Hintzen; *J. Alloy. Compd.* 417 (2006) 273.
- [2] Y.Q. Li, G. de With, H.T. Hintzen, *J. Lumin.* 116 (2006) 107.
- [3] K. Uheda, H. Takizawa, T. Endo, H. Yamane, M. Shimada, C.M. Wang, M. Mitomo, *J. Lumin.* 87-89 (2000) 967.
- [4] L.Y. Cai, X.D. Wei, H. Li, Q.L. Liu, *J. Lumin.* 129 (2009) 165.
- [5] T. Suehiro, N. Hirosaki, R.J. Xie, T. Sato, *Appl. Phys. Lett.* 95 (2009) 051903.
- [6] Y. Zhou, Y. Yoshizawa, K. Hirao, Z. Lenčič, P. Šajgalík, *J. Eur. Ceram. Soc.* 31 (2011) 151
- [7] C.J. Duan, X.J. Wang, W.M. Otten, A.C.A. Delsing, J.T. Zhao, H.T. Hintzen, *Chem. Mater.* 20 (2008) 1597.
- [8] Y.Q. Li, A.C.A. Delsing, R. Metselaar, G. de With, H.T. Hintzen, *J. Alloy. Compd.* 487 (2009) 28.
- [9] J.W.H. van Kovel, H.T. Hintzen, R. Metselaar, A. Meijerink, *J. Alloy. Compd.* 268 (1998) 272.
- [10] R.J. Xie, N. Hirosaki, *Sci. Technol. Adv. Mater.* 8 (2007) 588.
- [11] P.E. Doshi, G.E. Jellison, A. Rohatgi, *Appl. Opt.* 36 (1997) 7826.
- [12] J. Schmidt, M. Kerr, A. Cuevas, *Semicond. Sci. Tech.* 16 (2001) 164.
- [13] P. Vergeer, T.J.H. Vlugt, M.H.F. Kox, M.I. den Hertog, J.P.J.M. van der Eerden, A. Meijerink, *Phys. Rev. B* 71 (2005) 014119.
- [14] Q.Y. Zhang, X.Y. Huang, *Prog. Mater. Sci.* 55 (2010) 353.

- [15] H.C. Yang, C.Y. Liu, R. Pang, G. Lakshminarayana, S.F. Zhou, Y. Teng, J.R. Qiu, *Chin. Phys. Lett.* 25 (2008) 3444.
- [16] H. Yang, Y. Liu, S. Ye, J. Qiu, *Chem. Phys. Lett.* 451 (2008) 218.
- [17] K. Liddell, D.P. Thompson, *J. Mater. Chem.* 11 (2001) 507.
- [18] T.C. Ekström, K.J.D. MacKenzie, M.J. Ryan, I.W.M. Brown, G.V. White, *J. Mater. Chem.* 7 (1997) 505.
- [19] Z. Inoue, M. Mitomo, N. Ii, *J. Mater. Sci.* 15 (1980) 2915.
- [20] A. Yaguchi, T. Suehiro, T. Sato, N. Hirosaki, *Appl. Phys. Express* 4 (2011) 022101.
- [21] J.W. Park, S.T. Singh, K.S. Sohn, *J. Electrochem. Soc.* 185 (2011) J184.
- [22] M. Mitomo, F. Izumi, S. Horiuchi, Y. Matsui, *J. Mater. Sci.* 17 (1982) 2359.
- [23] P. Kubelka, F. Munk, *Z. Technische Physik* 12 (1931) 593.
- [24] H.E. Hoefdraad, *J. Solid State Chem.* 15 (1975) 175.
- [25] P. Dorenbos, *J. Phys.-Condens. Mat.* 15 (2003) 8417.
- [26] P. Dorenbos, *J. Alloy. Compd.* 488 (2009) 568.
- [27] P. Dorenbos, *J. Lumin.* 111 (2005) 89.
- [28] B. Moine, B. Courtois, C. Pedrini; *J. Phys. France* 50 (1989) 2105.
- [29] E. van der Kolk, J.T.M. de Haas, A.J.J. Bos, C.W.E. van Eijk, P.Dorenbos; *J. Appl. Phys.* 101 (2007) 083703.
- [30] A.H. Krumpel, A.J.J. Bos, A. Bessière, E. van der Kolk, P. Dorenbos, *Phys. Rev. B* 80 (2009) 085103.

Chapter 4

4*f* and 5*d* energy levels of the divalent and trivalent lanthanide ions in $M_2Si_5N_8$ (M = Ca, Sr, Ba)

*The content of this chapter has been published as: O.M. ten Kate, Z. Zhang, P. Dorenbos, H.T. Hintzen, E. van der Kolk; “4*f* and 5*d* energy levels of the divalent and trivalent lanthanide ions in $M_2Si_5N_8$ (M = Ca, Sr, Ba)”;* *Journal of Solid State Chemistry* 197 (2013) 209.

Optical data of Sm, Tb and Yb doped $Ca_2Si_5N_8$ and $Sr_2Si_5N_8$ phosphors that have been prepared by solid-state synthesis, are presented. Together with luminescence data from literature on Ce^{3+} and Eu^{2+} doping in the $M_2Si_5N_8$ (M = Ca, Sr, Ba) hosts, energy level schemes were constructed showing the energy of the 4*f* and 5*d* levels of all divalent and trivalent lanthanide ions relative to the valence and conduction band. The schemes were of great help in interpreting the optical data of the lanthanide doped phosphors and allow commenting on the valence stability of the ions, as well as the stability against thermal quenching of the Eu^{2+} *d-f* emission. Tb^{3+} substitutes on both a high energy and a low energy site in $Ca_2Si_5N_8$, due to which excitation at 4.77 eV led to emission from both the 5D_3 and 5D_4 levels, while excitation at 4.34 eV gave rise to mainly 5D_4 emission. Doping with Sm resulted in typical Sm^{3+} *f-f* line absorption, as well as an absorption band around 4.1 eV in $Ca_2Si_5N_8$ and 3.6 eV in $Sr_2Si_5N_8$ that could be identified as the Sm^{3+} charge transfer band. Yb on the other hand was incorporated in both the divalent and the trivalent state in $Ca_2Si_5N_8$.

4.1 Introduction

In recent years, rare-earth doped silicon nitride based materials have received considerable interest in luminescence research due to their good luminescence properties, high chemical inertness and thermal stability. Examples are Eu^{2+} or Ce^{3+} doped $\text{M}_2\text{Si}_5\text{N}_8$ ($\text{M} = \text{Ca}, \text{Sr}, \text{Ba}$) [1,2], MSiN_2 ($\text{M} = \text{Sr}, \text{Ba}$) [3], and CaAlSiN_3 [4,5]. Among these materials Eu^{2+} doped $\text{M}_2\text{Si}_5\text{N}_8$ phosphors have attracted special attention due to the very efficient red emission after UV or blue light excitation, making these phosphors suitable as conversion phosphors for white light emitting diodes (LEDs). A combination of a blue emitting InGaN based LED chip with green and red emitting phosphors gives rise to a white LED with a high color rendering index. Eu^{2+} doped $\text{Sr}_2\text{Si}_5\text{N}_8$ has already been applied as a blue to red conversion phosphor for this purpose. [6,7]

When co-doped with other lanthanide ions, the Eu^{2+} doped $\text{M}_2\text{Si}_5\text{N}_8$ phosphors (especially $\text{M} = \text{Ca}$ or Ba) are also interesting for long persistent luminescence applications. [8-13] The high quantum efficiency and chemical stability of these phosphors in combination with their long afterglow component make these phosphors attractive for persistent luminescence in the orange to red region.

Besides Eu^{2+} , also Ce^{3+} has been studied as a lanthanide dopant in $\text{M}_2\text{Si}_5\text{N}_8$ for the interest of LED phosphor research. [2] The combination of a strong absorption in the UV/blue range and a broad emission band around 550 nm pointed out that these phosphors are promising conversion phosphors for white LEDs as well.

In this chapter, the results obtained for three other lanthanide dopants (Tb, Sm and Yb) in the $\text{M}_2\text{Si}_5\text{N}_8$ hosts will be presented and discussed. Optical data of lanthanide ions in $\text{M}_2\text{Si}_5\text{N}_8$ hosts, both from this chapter and from literature, are then combined to construct energy level schemes showing the energy of the $4f$ and $5d$ states of all divalent and trivalent lanthanides in the $\text{Ca}_2\text{Si}_5\text{N}_8$ and $\text{Sr}_2\text{Si}_5\text{N}_8$ hosts with respect to their valence and conduction band. By using the schemes the optical

properties of all lanthanide ions within these hosts will be discussed and it will be commented on their valence stability.

4.2 Experimental

4.2.1 Synthesis

Lanthanide doped M₂Si₅N₈ (M = Ca, Sr, Ba) phosphors have been prepared by solid-state synthesis. For the synthesis of Sm doped Sr₂Si₅N₈, strontium nitride was first prepared from pure Sr metal (Aldrich, 99.9%, pieces) by firing at 800 °C in a horizontal tube furnace purged with a nitrogen atmosphere. The strontium nitride was then ground together with α -Si₃N₄ (Permascand, P95H, oxygen content 1.5 wt.%) and Sm metal (Aldrich, 99%, mesh) in the appropriate molar ratio. The mixture was then transferred in a Mo crucible to a horizontal tube furnace and fired twice, with intermediate grinding in between, at 1400 °C in a N₂/H₂ atmosphere.

Yb or Tb doped samples were synthesized in a similar way with Yb (Alfa Aesar, 99.9%, powder) or Tb metal (CSRE) as raw material. For Ca₂Si₅N₈ and Ba₂Si₅N₈ samples, Ca₃N₂ powder (Alfa Aesar, 98%) and Ba metal (Alfa Aesar, 99.2%) were used as starting materials respectively. Li₃N (Aldrich, 99.9%, mesh) and Na (Merck, >99%, pieces) were used as starting materials for co-doping with Li⁺ and Na⁺ respectively.

4.2.2 Characterization

Crystalline phases were checked by X-ray powder diffraction (XRD) analysis with a Bruker D4 Endeavor with Cu K α radiation. Diffraction data were collected by step scanning from 12° to 65° in 2 θ with a step size of 0.05° and a counting time of 1 s per step. Diffuse reflectance spectra in the UV and visible range, as well as the excitation spectrum of Tb³⁺ doped Sr₂Si₅N₈, were measured with a Perkin Elmer LS50B spectrophotometer with a Xe lamp and an R952 photomultiplier. White

BaSO₄ and black felt were used as a reference for the diffuse reflectance measurement. Diffuse reflectance spectra in the red and infrared range were recorded with a Bruker Vertex 80v FT interferometer using tungsten as a light source and cooled InGaAs and Si detectors. BaSO₄ was taken as a reference. Excitation and emission spectra were recorded with a xenon light source with a double grating monochromator and a Hamamatsu EM CCD camera (C9100-13).

4.3 Phase formation

Ca₂Si₅N₈ crystallizes in a monoclinic crystal structure with space group *Cc* (9). The structure consists of corner sharing SiN₄ tetrahedra, where half of the nitrogen ions are twofold coordinated by Si and the other half are threefold coordinated by Si. [14] In this structure two different Ca sites with different sizes exist. At one Ca site the shortest Ca-N distance is 2.32 Å and the average distance to the six nearest nitrogen anions is 2.59 Å. At the other Ca site the shortest Ca-N distance is 2.40 Å and the average distance to the six nearest nitrogen anions is 2.64 Å. [14]

In Figure 4.1 the X-ray diffraction patterns of Ca_{1.98}Yb_{0.01}Li_{0.01}Si₅N₈, Ca_{1.94}Tb_{0.03}Na_{0.03}Si₅N₈ and Ca_{1.9}Sm_{0.05}Li_{0.05}Si₅N₈ are shown and compared with the Ca₂Si₅N₈ reference (JCPDS 01-082-2489). The lines observed in the X-ray diffraction patterns of the doped samples are in good agreement with the reference pattern. In the Ca_{1.98}Yb_{0.01}Li_{0.01}Si₅N₈ sample a very small fraction of CaSi₂O₂N₂ (JCPDS 01-073-5499) has been observed. Note that this sample was the one with the highest Yb doping concentration for which still an almost pure phase could be obtained. For higher Yb concentrations, unidentified phases were observed in the diffraction pattern.

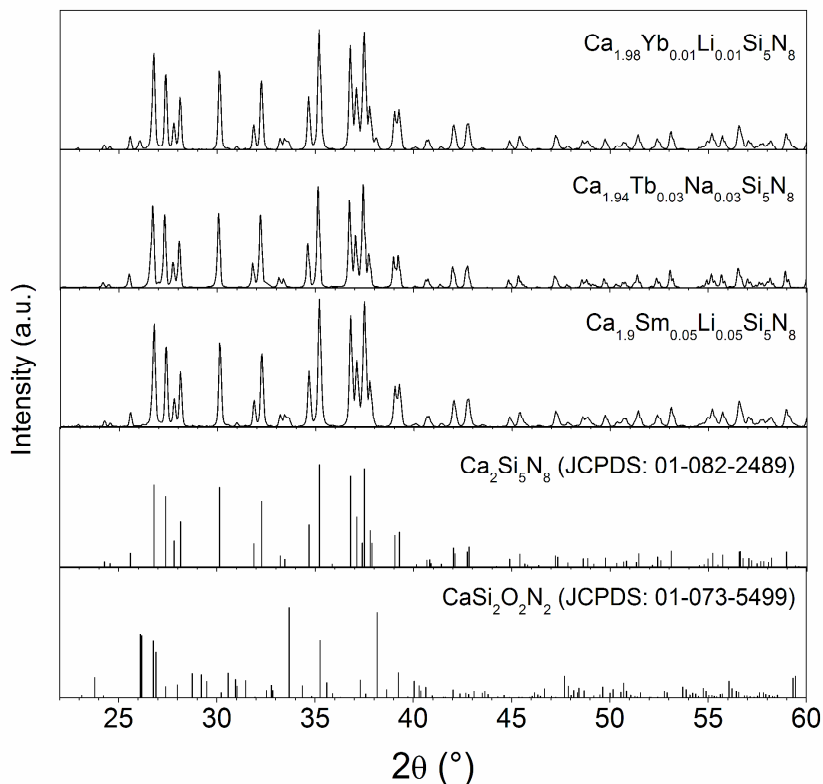


Figure 4.1 X-ray diffraction patterns of a) $Ca_{1.98}Yb_{0.01}Li_{0.01}Si_5N_8$, b) $Ca_{1.94}Tb_{0.03}Na_{0.03}Si_5N_8$, c) $Ca_{1.9}Sm_{0.05}Li_{0.05}Si_5N_8$, d) $Ca_2Si_5N_8$ reference (JCPDS 01-082-2489) and e) $CaSi_2O_2N_2$ reference (JCPDS 01-073-5499).

$Sr_2Si_5N_8$ and $Ba_2Si_5N_8$ crystallize both in an orthorhombic crystal structure with space group $Pmn2_1$ (31). Also in this structure the metal is located on two sites with different sizes. At one Sr site in $Sr_2Si_5N_8$ the shortest Sr-N distance is 2.57 Å and the average distance to the nearest six nitrogen anions is 2.75 Å. At the other Sr site the shortest Sr-N distance is 2.54 Å and the average distance to the six closest nitrogen atoms is 2.79 Å. At one Ba site in $Ba_2Si_5N_8$ the shortest Ba-N distance is 2.71 Å and the average Ba-N distance to the nearest six nitrogen anions is 2.83 Å. At the other Ba site the shortest Ba-N distance is 2.68 Å and the average distance to the six nearest nitrogen anions is 2.87 Å. [15]

In Figure 4.2 the X-ray diffraction patterns of $\text{Sr}_{1.8}\text{Sm}_{0.2}\text{Si}_5\text{N}_8$ and $\text{Sr}_{1.94}\text{Tb}_{0.03}\text{Na}_{0.03}\text{Si}_5\text{N}_8$ are shown and compared with the $\text{Sr}_2\text{Si}_5\text{N}_8$ reference (JCPDS 01-085-0101). The lines observed in the X-ray diffraction patterns of the doped samples are in good agreement with the reference pattern. Only for the sample with a high Sm concentration a small difference is observed with respect to the reference pattern, mainly indicated by the small peaks at 25.4° and 37.7° . These peaks do not belong to any of the silicon (oxy-)nitride, strontium nitride or strontium silicon (oxy-)nitride phases that were found in the database and might be related to the fact that a relatively large amount of trivalent Sm has to be substituted on a divalent Sm position, requiring some charge compensation. Note also that for the sample with a smaller amount of Sm the peaks are not observed.

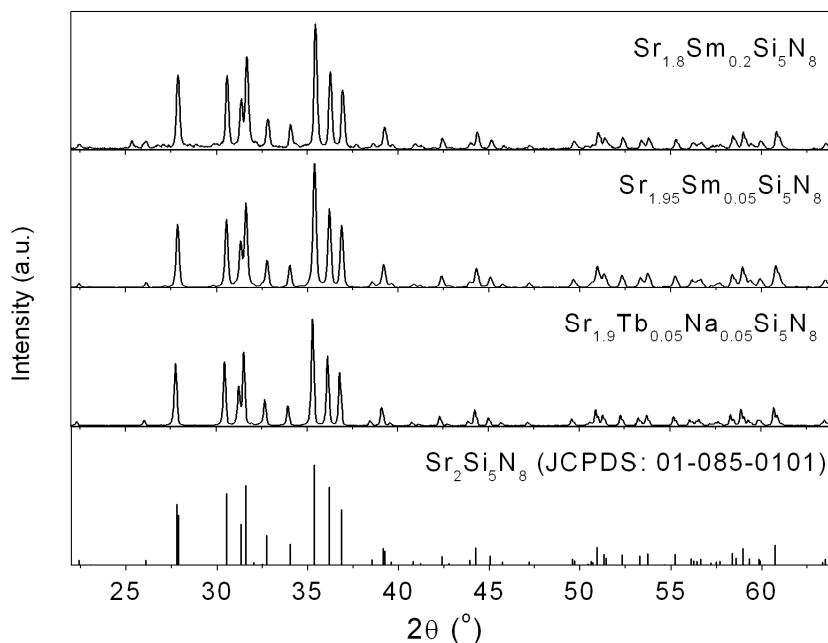


Figure 4.2 X-ray diffraction patterns of a) $\text{Sr}_{1.8}\text{Sm}_{0.2}\text{Si}_5\text{N}_8$, b) $\text{Sr}_{1.95}\text{Sm}_{0.05}\text{Si}_5\text{N}_8$, c) $\text{Sr}_{1.94}\text{Tb}_{0.03}\text{Na}_{0.03}\text{Si}_5\text{N}_8$ and d) $\text{Sr}_2\text{Si}_5\text{N}_8$ reference (JCPDS 01-085-0101).

4.4 Optical data of undoped and lanthanide doped $M_2Si_5N_8$

4.4.1 Band gap of $M_2Si_5N_8$

An estimation of the band gap of $Ca_2Si_5N_8$ can be given based on optical data presented in literature. The diffuse reflectance pattern of $Ca_2Si_5N_8$ obtained by Li et al. [1] suggests an optical band gap of about 5.0 eV, which is confirmed by the band like structure at the same energy in the excitation spectra of the Eu^{2+} *d-f* emission in Eu^{2+} doped $Ca_2Si_5N_8$. A maximum at 5.0 eV is also observed in the excitation spectra of Ce^{3+} doped $Ca_2Si_5N_8$. [2] Piao et al. [16] on the other hand, observed strong absorption of the undoped sample around 4.75 eV.

When the diffuse reflectance spectra of $Ca_2Si_5N_8$ and $Sr_2Si_5N_8$ obtained by Li et al. [1] are compared, the band gap of $Sr_2Si_5N_8$ seems to be about 0.1 eV lower in energy. The same shift is observed when the excitation spectra of the Ce^{3+} doped compounds are compared. [2] The diffuse reflectance pattern of $Sr_2Si_5N_8$ obtained by Piao et al. [17], as well as the excitation spectra of Eu^{2+} doped $Sr_2Si_5N_8$ obtained by Xie et al. [18] and Piao et al. [19] suggest that the optical band gap of $Sr_2Si_5N_8$ is located at about 4.9 eV.

According to the diffuse reflectance spectra obtained by Li et al. [1] the band gap of $Ba_2Si_5N_8$ is located at about the same energy as in $Sr_2Si_5N_8$. In the excitation spectra of the Eu^{2+} doped compounds, band like features are observed between 4.6 and 5.0 eV [1], while the host lattice excitation in the Ce^{3+} doped samples is located around 4.8 eV [2]. Piao et al. [20] observed the absorption band of the pure compound around 4.95 eV.

To summarize, the optical band gap is estimated at about 5.0 eV for $Ca_2Si_5N_8$ and at 4.9 eV for both $Sr_2Si_5N_8$ and $Ba_2Si_5N_8$, with a standard deviation of 0.1 eV.

4.4.2 Eu doped $M_2Si_5N_8$

Several reports can be found concerning europium doping in $Ca_2Si_5N_8$. [1,9,21,22] In all reports europium has been solely observed in the divalent state with a $4f-5d$ excitation band in the UV/blue region. Excitation results in an orange $Eu^{2+} 5d-4f$ emission. The energy of the lowest $4f^65d$ level can be derived from the excitation spectra as the first step of the staircase at the low energy side of the excitation band. If the staircase is not well resolved, the lowest $5d$ state can be estimated at the point at which the excitation energy has dropped to 15-20% intensity at the low energy side of the first maximum. [23] From the excitation spectrum obtained by Li et al. [1] the location of the lowest $4f^65d$ state can be estimated at about 2.3 eV in $Ca_{1.98}Eu_{0.02}Si_5N_8$. The position of the $Eu^{2+} d-f$ emission band slightly depends on concentration, ranging between 2.05 eV for $Ca_{1.98}Eu_{0.02}Si_5N_8$ to 2.0 eV for $Ca_{1.86}Eu_{0.14}Si_5N_8$. Piao et al. [21] reported that the maximum in the $Eu^{2+} 5d-4f$ emission ranges from 2.1 eV to 2.0 eV for increasing Eu^{2+} concentrations. The $5d-4f$ emission bands are not symmetrical, but can be fit by a combination of two Gaussians, as has been shown by Li et al. [1] for $Ca_{1.9}Eu_{0.1}Si_5N_8$, with maxima located around 2.05 eV and 1.88 eV. Others obtained similar results by fitting the $Eu^{2+} 5d-4f$ emission band of $Ca_{1.96}Eu_{0.04}Si_5N_8$. [9] In both papers the origin of the two bands has been attributed to $Eu^{2+} d-f$ emission from Eu^{2+} ions located on the two different Ca sites in the lattice.

Also in $Sr_2Si_5N_8$, europium is observed in the divalent state. [1,9,17,22,24-26] The excitation spectrum of the $Eu^{2+} d-f$ emission obtained by Piao et al. [17] suggests that the lowest $4f^65d$ band is located at 2.2 eV in $Sr_{1.96}Eu_{0.04}Si_5N_8$. This value is consistent with the data observed by others for $Sr_{1.98}Eu_{0.02}Si_5N_8$ [24] and for $Sr_{1.9}Eu_{0.1}Si_5N_8$ [22]. The data obtained by Li et al. [1] show a variation of the $5d$ excitation band with Eu^{2+} concentration, ranging from 2.3 eV in $Sr_{1.98}Eu_{0.02}Si_5N_8$ to 2.1 eV in $Eu_2Si_5N_8$. The energy of the emission band strongly depends on concentration. According to Li et al. the maximum of the emission band varies between 2.03 eV in $Sr_{1.98}Eu_{0.02}Si_5N_8$ to 1.80 eV in $Eu_2Si_5N_8$. A similar behavior is seen by Piao et al. [17] and Xie et al. [24] with emissions ranging from 2.0 eV for

low europium concentrations to 1.8 eV in $Eu_2Si_5N_8$. Just as in $Ca_2Si_5N_8$, the Eu^{2+} emission band in $Sr_2Si_5N_8$ seems to consist of two partially overlapping bands, located at about 2.02 eV and 1.89 eV in $Sr_{1.9}Eu_{0.1}Si_5N_8$. [1]

In $Ba_2Si_5N_8$ europium is observed in the divalent state as well. [1,9,20,27] The data of Li et al. [1] locate the lowest $5d$ state at about 2.3 eV in $Ba_{1.98}Eu_{0.02}Si_5N_8$. Low temperature (4 K) emission spectra were obtained by Piao et al. [20] At low Eu concentrations ($Ba_{1.96}Eu_{0.04}Si_5N_8$) the Eu^{2+} $d-f$ emission band is observed at 2.14 eV. At higher concentrations ($Ba_{1.85}Eu_{0.15}Si_5N_8$) two bands can be observed in the emission spectrum, located at 2.10 and 1.97 eV. For even higher concentrations ($Ba_{1.8}Eu_{0.2}Si_5N_8$) the $5d-4f$ emission band at lower energy is dominant.

4.4.3 Ce doped $M_2Si_5N_8$

As far as we know, Ce^{3+} doping in $M_2Si_5N_8$ phosphors has only been reported by Li et al. [2] In $Ca_{1.96}Ce_{0.02}Li_{0.02}Si_5N_8$ the maximum of the lowest Ce^{3+} $f-d$ excitation band was observed at 3.15 eV without any significant shift for increasing Ce concentrations. In the emission spectra a Ce^{3+} $d-f$ emission band was observed at 2.65 eV. No substructure is observed that can be attributed to emission to the two 2F_J states. Therefore the emission to the $^2F_{5/2}$ state is estimated at 2.7 eV. Separate emission bands due to emission from Ce^{3+} ions located at different sites are not observed in the emission spectra.

The Ce^{3+} $f-d$ excitation band in $Sr_{1.96}Ce_{0.02}Li_{0.02}Si_5N_8$ consists of two partly overlapping bands centered at about 2.85 and 3.25 eV. [2] Excitation at 2.85 eV resulted in an emission band with a maximum around 2.55 eV, while after excitation at 3.25 eV an emission band centered around 2.15 eV was observed.

In $Ba_2Si_5N_8$ a similar effect was observed. Excitation at 3.0 eV resulted in an emission band at 2.75 eV with a shoulder at 2.5 eV and an additional band at 2.2 eV. [2] The first two bands were ascribed to the transitions from the lowest $5d$ state to the $^2F_{5/2}$ and $^2F_{7/2}$ state of Ce^{3+} . The latter one was ascribed to Ce^{3+} $d-f$ emission as well, but with the Ce^{3+} ion located on the other Ba site. The excitation spectrum

of the 2.75 eV emission showed an excitation band with a maximum at 3.0 eV and a shoulder at 3.2 eV, while the excitation spectrum of the 2.2 eV emission showed an excitation band with a maximum at 3.05 eV.

4.4.4 Sm doped $\text{Ca}_2\text{Si}_5\text{N}_8$ and $\text{Sr}_2\text{Si}_5\text{N}_8$

The diffuse reflectance spectrum of Sm doped $\text{Ca}_2\text{Si}_5\text{N}_8$ is shown in Figure 4.3a. In the infrared region Sm^{3+} f - f absorption lines can be seen from the ${}^6\text{H}_{5/2}$ ground state to the ${}^6\text{F}_{11/2}$ (1.31 eV), ${}^6\text{F}_{9/2}$ (1.16 eV), ${}^6\text{F}_{7/2}$ (1.02 eV) and ${}^6\text{F}_{5/2}$ (0.91 eV) state, as indicated in the figure. The absorption lines between 0.85 and 0.75 eV can be assigned to transitions from the ground state to the ${}^6\text{H}_{15/2}$, ${}^6\text{F}_{3/2}$, and ${}^6\text{F}_{1/2}$ states. The absorption peak around 3.0 eV is also related to Sm^{3+} f - f absorption lines (${}^6\text{H}_{5/2} \rightarrow {}^6\text{P}_{3/2}$, among others). Besides the absorption lines, a 1 eV broad absorption band is observed around 4.1 eV. The absorption band can be assigned to the charge transfer (CT) of an electron from N^{3-} to Sm^{3+} , as will be discussed in section 4.5. Any signs for the presence of Sm^{2+} , such as Sm^{2+} f - f absorption lines, are not observed in the diffuse reflectance pattern.

The emission spectrum of $\text{Ca}_{1.9}\text{Sm}_{0.05}\text{Li}_{0.05}\text{Si}_5\text{N}_8$, after excitation at 4.0 eV, is shown in Figure 4.4a. Several emission lines are observed between 1.7 and 2.3 eV. The lines are typical f - f emission lines from the ${}^4\text{G}_{5/2}$ level of Sm^{3+} to the ${}^6\text{H}_{5/2}$ (2.20 eV), ${}^6\text{H}_{7/2}$ (2.06 eV), ${}^6\text{H}_{9/2}$ (1.90 eV) and ${}^6\text{H}_{11/2}$ (1.74 eV) levels.

The excitation spectrum of the ${}^4\text{G}_{5/2} \rightarrow {}^6\text{H}_{7/2}$ emission is shown in Figure 4.4b. In this spectrum several excitation peaks are observed between 2.5 and 3.5 eV. These lines correspond to Sm^{3+} f - f absorption lines from the ${}^6\text{H}_{5/2}$ ground state to higher $4f$ levels, of which some are indicated in the figure. The most intense excitation line is located at 2.98 eV and corresponds to the ${}^6\text{H}_{5/2} \rightarrow {}^6\text{P}_{3/2}$ transition that is observed in the diffuse reflectance spectrum (Figure 4.3a). At higher energy, around 4.1 eV, a broad excitation band can be seen, which is at the same position as the absorption band that was observed in the diffuse reflectance spectrum (Figure 4.3a) and that was attributed to the Sm^{3+} CT band.

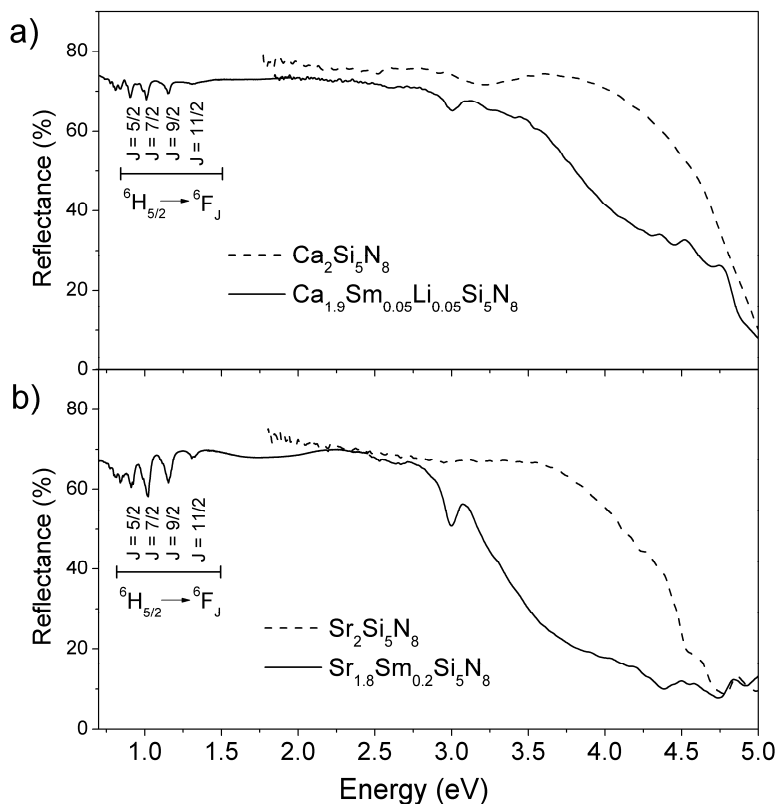


Figure 4.3 a) Diffuse reflectance spectra of $Ca_2Si_5N_8$ (dashed line) and $Ca_{1.9}Sm_{0.05}Li_{0.05}Si_5N_8$ (solid line) and b) diffuse reflectance spectra of $Sr_2Si_5N_8$ (dashed line) and $Sr_{1.8}Sm_{0.2}Si_5N_8$ (solid line).

In Figure 4.3b the diffuse reflectance spectrum of $Sr_{1.8}Sm_{0.2}Si_5N_8$ is presented and compared with the diffuse reflectance spectrum of an undoped $Sr_2Si_5N_8$ sample. In the spectrum of the Sm doped sample several $Sm^{3+} f-f$ absorption lines are observed, similar as for the $Ca_{1.9}Sm_{0.05}Li_{0.05}Si_5N_8$ sample shown in Figure 4.3a, despite the absence of Li^+ or Na^+ as charge compensating ion. A difference between the Ca and the Sr sample can be seen in the position of the CT band, which has shifted from about 4.1 eV in $Ca_2Si_5N_8$ to about 3.6 eV in $Sr_2Si_5N_8$.

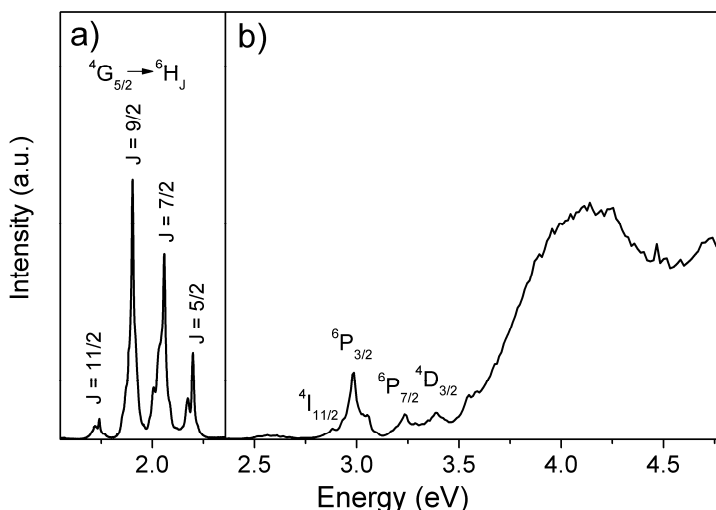


Figure 4.4 a) Emission (excitation at 4.0 eV) and b) excitation spectrum (2.06 eV emission) of $\text{Ca}_{1.9}\text{Sm}_{0.05}\text{Li}_{0.05}\text{Si}_5\text{N}_8$.

When the Sm doped $\text{Sr}_2\text{Si}_5\text{N}_8$ sample is excited at 3.0 eV, several emission lines are observed between 1.7 and 2.3 eV, as is shown in Figure 4.5a. These Sm^{3+} f - f lines are at the same position as was observed in $\text{Ca}_{1.9}\text{Sm}_{0.05}\text{Li}_{0.05}\text{Si}_5\text{N}_8$, though the relative intensity between the lines is different. Besides the f - f emission lines, no other emission bands are observed, neither did excitation at any other energy between 2.5 and 5.0 eV result in any other emission bands.

The excitation spectrum of the $\text{Sm}^{3+} \ ^4\text{G}_{5/2} \rightarrow \ ^6\text{H}_{7/2}$ line emission is shown in Figure 4.5b. Besides the Sm^{3+} f - f absorption lines there is a 1 eV broad excitation band centered around 3.6 eV, which corresponds to the absorption band observed in the diffuse reflectance spectrum (Figure 4.3b), and which is assigned to the Sm^{3+} CT band. Note that the intensity of the CT band with respect to the intensity of the f - f lines is much weaker in $\text{Sr}_2\text{Si}_5\text{N}_8$ than in $\text{Ca}_2\text{Si}_5\text{N}_8$. This can be explained by the fact that the CT is lower in energy in $\text{Sr}_2\text{Si}_5\text{N}_8$, due to which direct quenching to the ground state will be more probable.

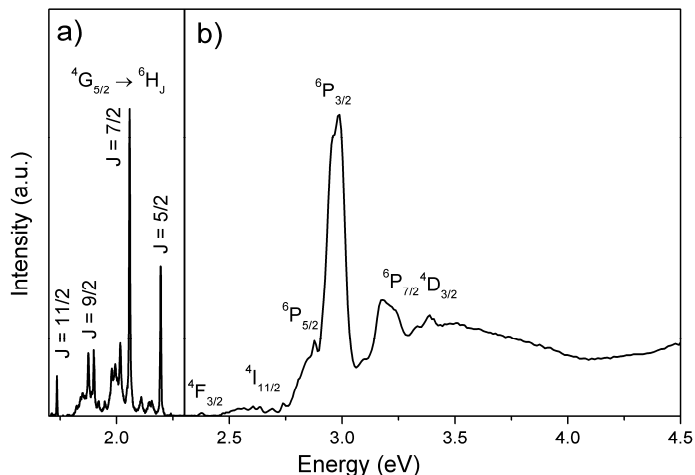


Figure 4.5 a) Emission (excited at 3.0 eV) and b) excitation spectrum (2.06 eV emission) of $Sr_{1.8}Sm_{0.2}Si_5N_8$.

4.4.5 Tb doped $Ca_2Si_5N_8$ and $Sr_2Si_5N_8$

The diffuse reflectance spectrum of Tb^{3+} doped $Ca_2Si_5N_8$ is shown in Figure 4.6a. As compared to the undoped sample, a broad absorption band is observed around 4.4 eV. This absorption can most likely be attributed to Tb^{3+} *f-d* absorption. A similar band is observed in the Tb^{3+} doped $Sr_2Si_5N_8$ sample, which is shown in Figure 4.6b.

In Figure 4.7a the emission spectrum is shown of a Tb^{3+} doped $Ca_2Si_5N_8$ sample excited at 4.77 eV. Emission lines are observed at 3.24, 2.98, 2.83, 2.70 and 2.61 eV, which correspond to Tb^{3+} *f-f* transitions from the 5D_3 state to the 7F_6 , 7F_5 , 7F_4 , 7F_3 and 7F_2 states respectively. Furthermore, emission lines are observed at 2.52, 2.26, 2.11, 1.99 and, very weak, at 1.90 eV, corresponding to emissions from the 5D_4 state to the 7F_6 , 7F_5 , 7F_4 , 7F_3 and 7F_2 states respectively. Excitation at 4.34 eV results in the same emission peaks as excitation at 4.77 eV but with different relative luminescence intensities. After excitation at 4.77 eV emissions from the 5D_3 state are relatively strong compared to emissions from the 5D_4 state, but after

excitation at 4.34 eV the intensity ratio has changed: emissions from 5D_3 level are much weaker compared to the emissions from the 5D_4 level.

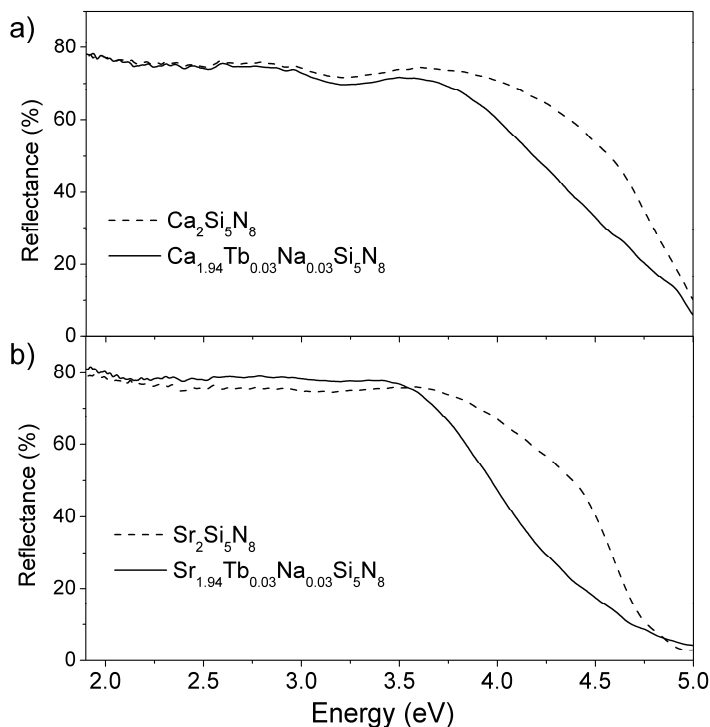


Figure 4.6 Diffuse reflectance of Tb^{3+} doped (solid line) and undoped (dashed line) a) $\text{Ca}_2\text{Si}_5\text{N}_8$ and b) $\text{Sr}_2\text{Si}_5\text{N}_8$.

The difference is also observed when the excitation spectrum of the ${}^5D_3 \rightarrow {}^7F_4$ emission is compared with the excitation spectrum of the ${}^5D_4 \rightarrow {}^7F_5$ emission, that are both shown in Figure 4.7b. In both excitation spectra a broad excitation band is observed, but the positions of the bands are different. The maximum of the excitation band of the emission from the 5D_3 level is situated at 4.75 eV, while the excitation band of the emission from the 5D_4 level has an additional band around 4.25 eV. Since Tb^{3+} could be substituted on two different Ca sites, both bands are tentatively assigned to the spin-allowed $\text{Tb}^{3+} f-d$ absorption bands where Tb^{3+} is located on two different Ca sites, as will be further discussed in section 4.5.

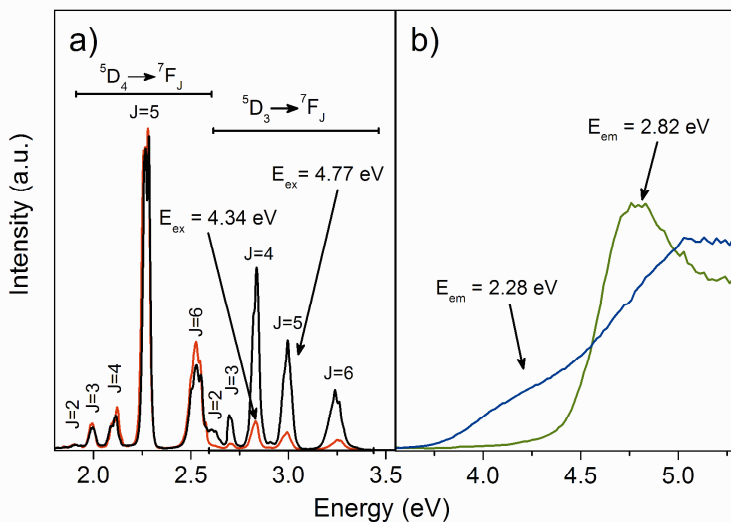


Figure 4.7 a) Emission spectra (excitation at 4.34 and 4.77 eV) and b) excitation spectra (2.82 and 2.28 eV emission) of $Ca_{1.88}Tb_{0.06}Na_{0.06}Si_5N_8$.

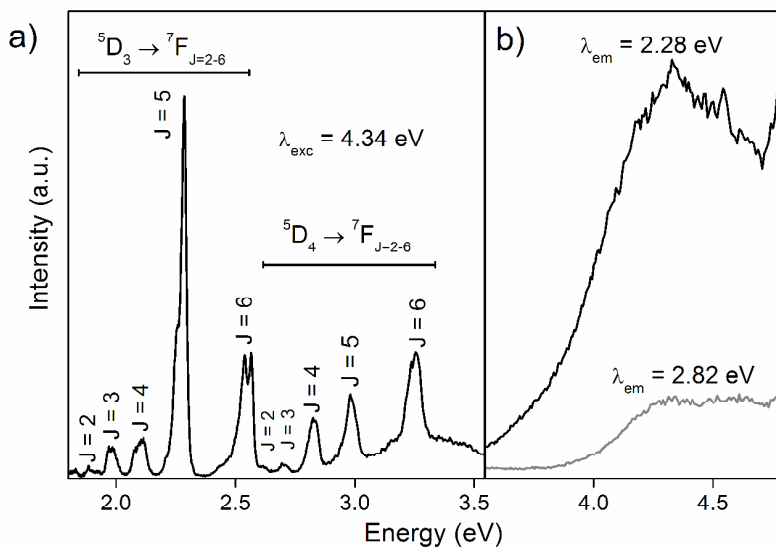


Figure 4.8 a) Emission and b) excitation spectra of $Sr_{1.88}Tb_{0.06}Na_{0.06}Si_5N_8$.

4.4.6 Yb doped $M_2Si_5N_8$

The emission spectrum of Tb^{3+} doped $Sr_2Si_5N_8$ is shown in Figure 4.8a. Similar as for Tb^{3+} doping in $Ca_2Si_5N_8$, several $f-f$ emissions lines are observed, which originate from the 5D_3 and 5D_4 level. The excitation spectra of the $^5D_3 \rightarrow ^7F_4$ emission and the $^5D_4 \rightarrow ^7F_5$ emission are shown in Figure 4.8b. In contrast to the $Ca_2Si_5N_8$ sample, the two excitation bands are located at almost the same position with a maximum around 4.35 eV.

In Figure 4.9 the diffuse reflectance spectrum of Yb doped $Ca_2Si_5N_8$ is shown. A weak absorption line between 1.2 and 1.3 eV is observed, which is the typical $f-f$ absorption of Yb^{3+} . This indicates that at least a part of the Yb ions is present in the trivalent state. Furthermore, a very broad absorption can be seen between 2 and 4.5 eV, which is probably a combination of multiple absorption bands of different origin. The absorption could be due to a combination of $4f-5d$ absorption of Yb^{2+} and CT absorption of Yb^{3+} , as will be further commented on in section 4.5.2.

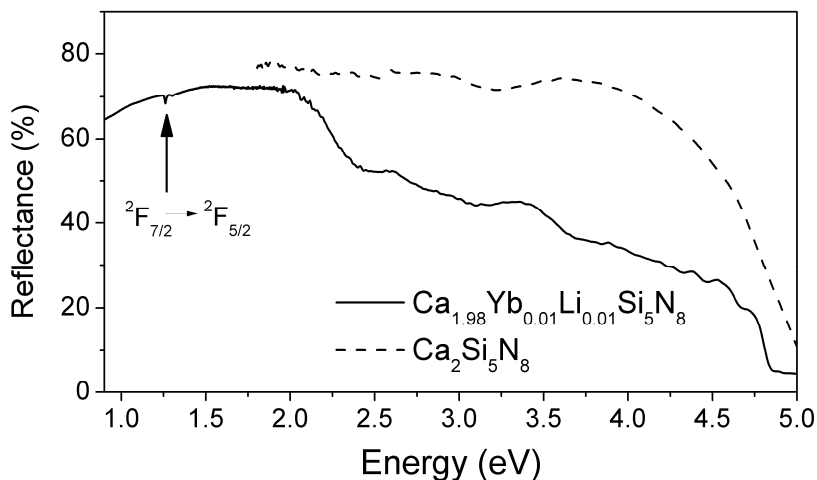


Figure 4.9 Diffuse reflectance spectra of $Ca_{1.98}Yb_{0.01}Li_{0.01}Si_5N_8$ (solid line) and $Ca_2Si_5N_8$ (dashed line).

Excitation of the Yb doped $Ca_2Si_5N_8$ at 3.5 eV resulted in an Yb^{3+} $f-f$ emission line around 1.25 eV, as is shown in Figure 4.10. Besides this emission at 1.25 eV, a weak emission band is observed between 1.5 and 2.5 eV with a maximum at 2.05 eV, which is assigned to Yb^{2+} $d-f$ emission. The band is not symmetrical and seems to consist of two bands, one around 2.1 eV and the other one around 1.7 eV. After excitation at 3.0 eV the same emissions are observed, but the broad emission bands around 2.1 eV are now more intense than the $f-f$ line emission.

In the excitation spectrum of the Yb^{3+} $f-f$ line emission, shown in Figure 4.10 as well, bands are observed around 2.4 eV, 2.9 eV, 3.4 eV, 4.0 eV and 5.0 eV. The absorption at 5.0 eV can be attributed to host lattice absorption, but the nature of the other excitation bands is unclear. In the excitation spectrum of the 2.03 eV emission, broad bands are observed as well, but the relative intensities between the bands are different. The emission and excitation spectra will be discussed further on in section 4.5.2.

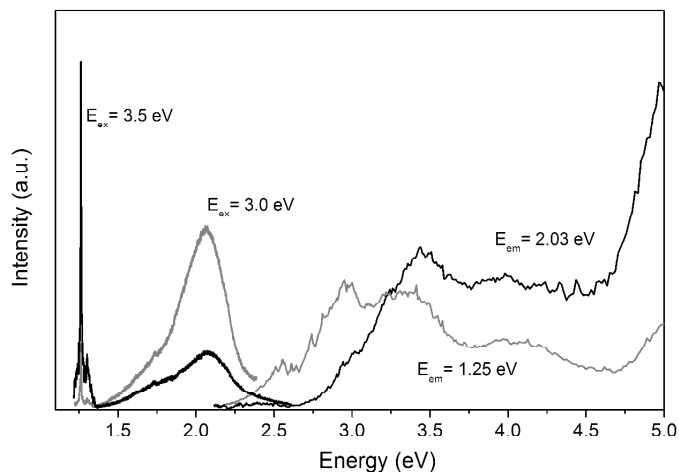


Figure 4.10 Emission spectra and excitation spectra of $Ca_{1.98}Yb_{0.01}Li_{0.01}Si_5N_8$.

Yb doping in $Sr_2Si_5N_8$ or $Ba_2Si_5N_8$ was unsuccessful. Synthesis of these compounds resulted in the formation of $SrYbSi_4N_7$ and $BaYbSi_4N_7$ as secondary phases. This implies that the Yb ion, in either the divalent or the trivalent state, is unstable on the Sr^{2+} or Ba^{2+} sites in $M_2Si_5N_8$. These sites are probably too large for

the smaller Yb³⁺ ion. On the Ca²⁺ site, being smaller than Sr²⁺ or Ba²⁺, the Yb³⁺ ion will fit much better. Moreover, as far as we know a CaYbSi₄N₇ has never been reported and may not exist or is very difficult to obtain, implying that this phase will not be formed when Yb doped Ca₂Si₅N₈ is prepared.

Table 4.1 Overview of the experimental values obtained for the band gap; the 4*f*-5*d* excitation bands of Ce³⁺, Eu²⁺ and Tb³⁺; and the CT band of Sm³⁺ in M₂Si₅N₈ (M = Ca, Sr, Ba).

	Ca ₂ Si ₅ N ₈	Sr ₂ Si ₅ N ₈	Ba ₂ Si ₅ N ₈
optical band gap	5.0 eV	4.9 eV	4.9 eV
Ce ³⁺ 4 <i>f</i> -5 <i>d</i>	3.1 eV	2.85 eV	2.95 eV
Sm ³⁺ CT	4.1 eV	3.25 eV	3.1 eV
Eu ²⁺ 4 <i>f</i> -5 <i>d</i>	4.1 eV	3.6 eV	-
Tb ³⁺ 4 <i>f</i> -5 <i>d</i>	2.3 eV	2.2 eV	2.3 eV
(spin-allowed)	4.25 eV	4.35 eV	-
	4.75 eV		

4.5 Energy schemes

4.5.1 Construction

The optical data on the lanthanide doped M₂Si₅N₈ phosphors described in section 4.4 are summarized in Table 4.1. The data can be used to construct detailed energy level schemes, shown in Figure 4.11, locating the energy levels of the 4*f* and 5*d* states of all divalent and trivalent lanthanides with respect to the valence and conduction band of these materials. With such schemes originally developed by Dorenbos [28,29] the spectroscopic properties of one specific lanthanide, like Ce³⁺ or Eu²⁺, in a certain host can be used to predict the properties of all the other lanthanide ions in the same host.

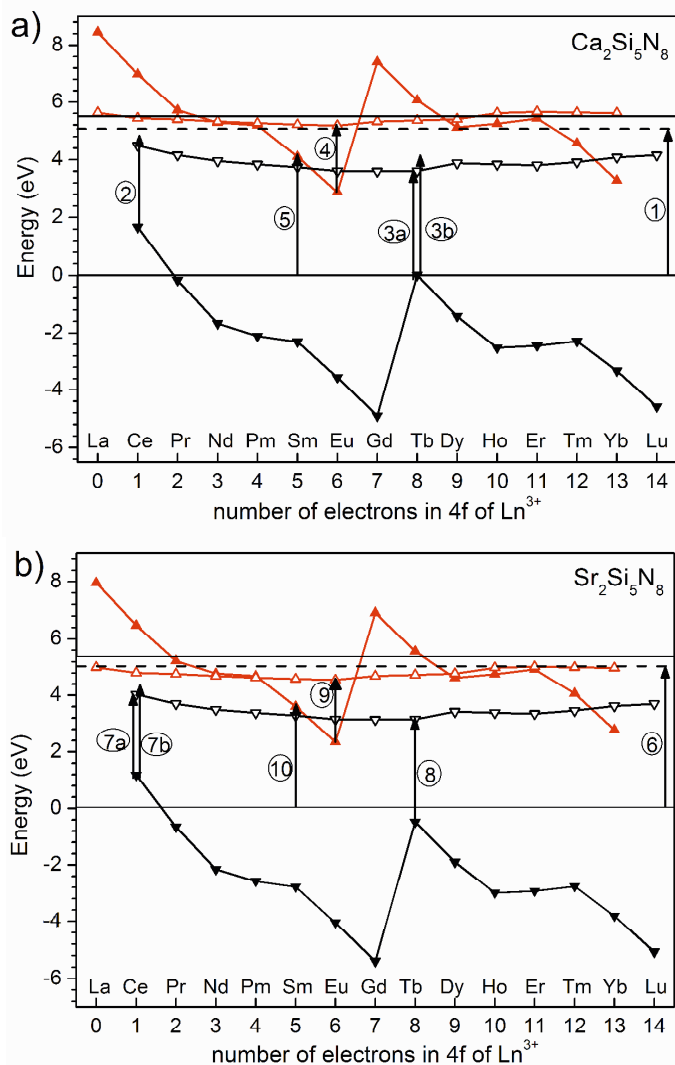


Figure 4.11 Energy level schemes showing the 4f ground states of the trivalent (\blacktriangledown) and divalent (\blacktriangle) lanthanide ions and lowest energy 5d states of the trivalent (∇) and divalent (\triangle) ions with respect to the valence and conduction bands of a) $Ca_2Si_5N_8$ and b) $Sr_2Si_5N_8$. The 4f and 5d states of the divalent ions are connected by grey lines and the states of the trivalent ions are connected by black lines. The horizontal dashed line indicates E^{ex} , the energy needed to create an exciton. The schemes are based on lanthanides occupying the low energy sites in the lattice.

In section 4.1 the optical band gaps of $\text{Ca}_2\text{Si}_5\text{N}_8$ and $\text{Sr}_2\text{Si}_5\text{N}_8$, obtained from the room temperature excitation spectra of the doped compounds, were estimated at 5.0 and 4.9 eV respectively. This band gap marks the exciton creation energy E^{ex} and would be located about 0.1 eV higher in energy if the spectra would be measured at a temperature of 10 K. [30] This means that the optical band gaps at low temperature will be about 5.1 and 5.0 eV respectively, as is indicated in Figures 4.11a (arrow 1) for $\text{Ca}_2\text{Si}_5\text{N}_8$ and 4.11b (arrow 6) for $\text{Sr}_2\text{Si}_5\text{N}_8$. To obtain the mobility band gap as defined in the schemes in Figure 4.11 the exciton binding energy has to be included, resulting in a band gap which is about 8% higher in energy than the optical band gap at low temperature [30]: 5.5 eV for $\text{Ca}_2\text{Si}_5\text{N}_8$ and 5.4 eV for $\text{Sr}_2\text{Si}_5\text{N}_8$.

The energy difference between the lowest $4f$ and $5d$ states of the trivalent lanthanide ions can be derived from both the excitation spectra of the Ce^{3+} d - f emission band, as well as the excitation spectra of the Tb^{3+} f - f emission lines, since in both excitation spectra an f - d absorption band is seen. In Tb^{3+} doped $\text{Ca}_2\text{Si}_5\text{N}_8$, two Tb^{3+} $4f$ - $5d$ absorption bands were observed, which are positioned at 4.25 and 4.75 eV (see section 4.4.5 or Table 4.1). The two bands were assigned to Tb^{3+} located on a low energy site and a high energy site. The transitions observed are the spin-allowed f - d transitions. The spin-forbidden transitions, which will be about 0.75 eV lower in energy, are too weak to be observed. From the Tb^{3+} f - d transitions, the energy of the lowest $5d$ band of Ce^{3+} can be predicted, since the $4f$ - $5d$ of Ce^{3+} is about 0.8 eV lower in energy than the spin-forbidden $4f$ - $5d$ of Tb^{3+} . This predicts the f - d transition of Ce^{3+} at 2.7 eV for Ce^{3+} on the low energy site and at 3.2 eV for Ce^{3+} on the high energy site. The actually observed value for the $4f$ - $5d$ of Ce^{3+} is 3.1 eV, which is close to the predicted value for Ce^{3+} on the high energy site.

The energy of the $4f$ - $5d$ transition of Tb^{3+} in $\text{Ca}_2\text{Si}_5\text{N}_8$ can also be used to predict the $4f$ - $5d$ of Eu^{2+} in the same host by using the relation between the red shift of the divalent $D(2+)$ and the trivalent $D(3+)$ ions [31]:

$$D(2+) = 0.64 D(3+) - 0.233 \text{ eV.} \quad (4.1)$$

Here is the red shift defined as the difference between the energy of the $4f-5d$ transition of a lanthanide in a compound with respect to the same transition for the free lanthanide ion. The relation predicts the Eu^{2+} $5d$ at 2.2 eV for Eu^{2+} on a low energy site and at 2.6 eV for Eu^{2+} on a high energy site. So, the observed value of 2.3 eV is close to the predicted value for Eu^{2+} on the low energy site. An overview of the predicted and observed values for the $5d$ energies of Eu^{2+} and Ce^{3+} in $Ca_2Si_5N_8$ is given in Table 4.2.

Table 4.2 Prediction of the Eu^{2+} and Ce^{3+} $f-d$ absorption in $Ca_2Si_5N_8$ based on the $f-d$ absorption of Tb^{3+} .

	Eu^{2+} $f-d$	Ce^{3+} $f-d$
predicted high energy site	2.6 eV	3.2 eV
predicted low energy site	2.2 eV	2.7 eV
observed	2.3 eV	3.1 eV

In Ce^{3+} doped $Sr_2Si_5N_8$ two Ce^{3+} $f-d$ excitation bands were observed, located at 2.85 and 3.25 eV. [2] If these bands are attributed to Ce^{3+} on a low and a high energy site respectively, the energy of the $4f-5d$ transition of Tb^{3+} can be predicted. This predicts the spin-allowed $f-d$ transition of Tb^{3+} at 4.4 eV for Tb^{3+} at the low energy site and at 4.8 eV for Tb^{3+} at the high energy site. The observed value for the $4f-5d$ of Tb^{3+} is 4.35 eV (see Figure 4.8), which is in good agreement with the value predicted for the low energy site.

The $f-d$ of Ce^{3+} in $Sr_2Si_5N_8$ can also be used to predict the $f-d$ of Eu^{2+} , which gives 2.35 eV for Eu^{2+} on a low energy site and 2.6 eV for Eu^{2+} on a high energy site. The experimental value for the $4f-5d$ of Eu^{2+} is 2.2 eV (see section 4.4.2), which is closest to the prediction for Eu^{2+} located on the low energy site. The predicted and observed values for the $5d$ of Eu^{2+} and Tb^{3+} in $Sr_2Si_5N_8$ are summarized in Table 4.3.

Information on the charge transfer band of a trivalent lanthanide ion can be used to locate the ground state of the divalent lanthanide ions with respect to the valence band. The CT energy of the trivalent lanthanide should correspond to the

energy needed to bring an electron from the top of the valence band to the 4*f* ground state of the divalent ion. [28] In Sm doped Ca₂Si₅N₈ the CT band was observed around 4.1 eV (section 4.4.4), determining the length of arrow 5 in Figure 4.11a, and in Sr₂Si₅N₈ the CT was observed at 3.6 eV (section 4.4.4), determining the size of arrow 10 in Figure 4.11b.

Table 4.3 Prediction of the Eu²⁺ and Tb³⁺ *f-d* absorption in Sr₂Si₅N₈ based on the *f-d* absorption of Ce³⁺.

	Eu ²⁺ <i>f-d</i>	Tb ³⁺ <i>f-d</i> (spin-allowed)
predicted high energy site	2.6 eV	4.8 eV
predicted low energy site	2.35 eV	4.4 eV
observed	2.2 eV	4.35 eV

The energy level schemes from Figure 4.11 can now be constructed. Note that it has been chosen to draw the schemes for lanthanide ions located on the low energy sites. In the scheme for the high energy sites, the difference between the 4*f* and 5*d* states would be somewhat higher in energy, in accordance with the results described above. In the schemes, the top of the valence band is defined at 0 eV. The optical band gap determines arrow 1 in Figure 4.11a and arrow 6 in Figure 4.11b, and with that the position of the dashed horizontal line in the figure. At 8% higher energy the bottom of the conduction band is located. The CT of Sm³⁺ determines the position of the divalent 4*f* ground state with respect to the top of the valence band (arrow 5 and arrow 10), while the distance between the 4*f* and 5*d* of the divalent ions is given by the *f-d* of Eu²⁺ (arrow 4 and arrow 9). The distance between the 4*f* and 5*d* of the trivalent ions in Sr₂Si₅N₈ is determined by the low energy site 4*f-5d* of Ce³⁺ (arrow 7a) and the spin-forbidden 4*f-5d* of Tb³⁺ (arrow 8). For the scheme of Ca₂Si₅N₈ the spin-forbidden 4*f-5d* of Tb³⁺ on the low energy site (arrow 3a) is used. The 4*f-5d* of Ce³⁺ (arrow 2) could not be used, since the Ce³⁺ is located on the high energy site. To position the energy levels of the trivalent ions with respect to the valence and conduction band one needs either luminescence thermal quenching data on the 5*d-4f* emission of the trivalent ions, or data on the

charge transfer band of any tetravalent lanthanide ion. The first one relates the 5d levels to the bottom of the conduction band, while the latter relates the lowest 4f level to the top of the valence band. However, neither luminescence quenching data of trivalent *d-f* emissions, nor information on tetravalent ions in these host lattices is available. Therefore the position is estimated based on what is expected for the energy difference between the 4f ground state of Eu^{2+} and the 4f ground state of Eu^{3+} . This Coulomb repulsion energy, which expresses the Coulomb repulsion experienced by an electron when it is added to the 4f shell [32], is about 6.4 eV in nitridosilicates. See for example the energy level scheme of $LaSi_3N_5$. [33]

It should be noted that, for constructing the energy level diagrams, it is assumed that the position of the energy levels of the lanthanide ions only depends on the nitrogen atoms in the first coordination sphere. Therefore, the effect of charge compensation needed when a trivalent lanthanide ion is substituted on a divalent position, for example by Li^+ or Na^+ ions or by defects, has been neglected. In practice however, the co-dopants or defects needed for charge compensation might have a small influence on the energy level positions within the host.

The energy level scheme for $Ba_2Si_5N_8$ has not been constructed, since optical data on the charge transfer band of any trivalent lanthanide ion in this host is missing. However, since the optical properties of Ce^{3+} and Eu^{2+} in $Ba_2Si_5N_8$ are quite similar to the properties in $Sr_2Si_5N_8$ (within 0.2 eV) and the crystal structure is the same, the energy level scheme will probably be very similar as well.

4.5.2. Discussion

The absorption spectrum of Yb^{3+} doped $Ca_2Si_5N_8$ shown in Figure 4.9 is difficult to interpret, but with the help of the energy level scheme of $Ca_2Si_5N_8$ (Figure 4.11a) some things can be said on the absorption bands observed. The scheme predicts the Yb^{3+} CT band at 3.3 eV, so some of the absorption around 3.3 eV (Figure 4.9) can probably be related to the Yb^{3+} CT band. Also note that in the excitation spectrum of the Yb^{3+} *f-f* emission (Figure 4.10), the maximum of the excitation band is observed at 3.4 eV.

Furthermore, the scheme indicates that the absorption observed at lower energy (around 2.5 eV) could be related to the spin-allowed $f-d$ transition of Yb^{2+} , since the scheme predicts the spin-forbidden Yb^{2+} $f-d$ absorption band around 2.35 eV. If Yb^{2+} is substituted on the high energy site, the spin-forbidden $f-d$ transition would be located around 2.75 eV. This would mean that the absorption observed around 2.9 eV can be related to the spin-allowed $f-d$ transition of Yb^{2+} on the high energy site. Note that the assignment of the 2.5 and 2.9 eV absorption to $f-d$ transitions of Yb^{2+} is in agreement with the excitation spectra in Figure 4.10. Exactly these two bands are more intense in the excitation spectrum of the Yb^{2+} $d-f$ emission than in the excitation spectrum of the Yb^{3+} $f-f$ emission. This would imply that ytterbium is present in both the divalent and the trivalent state.

Several reports can be found in literature concerning the thermal quenching behavior of the Eu^{2+} $d-f$ emission in Eu doped $\text{M}_2\text{Si}_5\text{N}_8$ ($\text{M} = \text{Ca}, \text{Sr}, \text{Ba}$) phosphors. [1,20,22] From these reports it can be concluded that the Eu^{2+} $d-f$ emission is most stable against thermal quenching in $\text{Sr}_2\text{Si}_5\text{N}_8$ and least stable in $\text{Ca}_2\text{Si}_5\text{N}_8$. With the help of the energy level schemes from Figure 4.11 the difference can be explained. The schemes show that the lowest Eu^{2+} $5d$ state in $\text{Sr}_2\text{Si}_5\text{N}_8$ is located well below the bottom of the conduction band, while the difference between the bottom of the conduction band and the lowest $5d$ state in $\text{Ca}_2\text{Si}_5\text{N}_8$ is much smaller. Since $d-f$ luminescence will be quenched by thermal ionization of the $5d$ electron to the conduction band [34], the difference between Eu^{2+} in $\text{Ca}_2\text{Si}_5\text{N}_8$ and $\text{Sr}_2\text{Si}_5\text{N}_8$ can well be explained.

An interesting observation for Tb^{3+} doped $\text{Ca}_2\text{Si}_5\text{N}_8$ is that $f-d$ excitation of Tb^{3+} ions on the high energy site results in $f-f$ emission lines from the $^5\text{D}_3$ and $^5\text{D}_4$ levels, while $f-d$ excitation of the Tb^{3+} ion on the low energy site results mainly in emission from the $^5\text{D}_4$ level (Figure 4.7). With the help of the energy scheme this observation can be understood. The lowest $5d$ level of Tb^{3+} is located at 4.0 eV for Tb^{3+} on the high energy site. The Stokes shift after Ce^{3+} $f-d$ excitation, where the Ce^{3+} ion is located on the high energy site, is 0.45 eV. [2] The 0.45 eV Stokes shift can be used to estimate the position of the relaxed $5d$ state of Tb^{3+} on the high energy site, giving an energy of 3.55 eV above the $4f$ ground state. The $^5\text{D}_3$ level is

located at 3.21 eV above the 4*f* ground state. The ⁵D₃ emission is therefore not quenched on the high energy site. However, the 5*d* of Tb³⁺ on the low energy site is 0.5 eV lower in energy, meaning that the relaxed 5*d* state could be located below the ⁵D₃ level. Emission from the ⁵D₃ would then be quenched, resulting in emission from mainly the ⁵D₄ level.

As has been discussed in section 4.5.1, the Tb³⁺ ion is located on the low energy site in Sr₂Si₅N₈. However, different as in Ca₂Si₅N₈, in Sr₂Si₅N₈ both ⁵D₃ and ⁵D₄ emission of Tb³⁺ are observed (Figure 4.8a). This could be explained with the energy level scheme in Figure 4.11b. The lowest, spin-forbidden 5*d* state is located at 3.6 eV (arrow 8, Figure 4.11b). The Stokes shift for the Ce³⁺ 5*d* band on the low energy site is 0.35 eV. If this is subtracted the relaxed Tb³⁺ 5*d* state is found at 3.25 eV, which is slightly higher in energy than the ⁵D₃ level (3.21 eV). This might explain why the emission from the ⁵D₃ level is not completely quenched in Sr₂Si₅N₈.

The schemes allow commenting on trivalent ion versus divalent ion formation and stability. When the energy distance from the ground state of the divalent ion to the bottom of the conduction band is smaller than the distance to the top of the valence band, it will be more likely that the ion will be present in the trivalent state. [35] This is in agreement with the observation that Ce, Tb, and Sm are observed in the trivalent state. If it is the other way around and the 4*f* ground state of the divalent ion is closer to the valence band, the lanthanide ion will prefer the divalent state, as is the case for Eu. For Yb in Ca₂Si₅N₈ the energy level is slightly closer to the conduction band and this atom is indeed observed in the trivalent state. However, the difference is small in the case of Yb, and therefore the presence of Yb²⁺ cannot be excluded, especially if it is taken into account that the divalent ions do not require charge compensation and the fact that the Yb²⁺ ion has a size similar to that of the Ca²⁺ ion, while the Yb³⁺ ion is much smaller.

The schemes can also be used to predict the optical properties of the lanthanide ions in the M₂Si₅N₈ hosts that have not been investigated so far. It is expected that all these lanthanides will be present in the trivalent state. Apart from Ce³⁺ and Tb³⁺, the Pr³⁺ ion will be the only ion for which *f-d* transitions are

expected in the absorption spectrum, which might result in Pr^{3+} $d-f$ emission. A charge transfer band, as was observed for Yb^{3+} and Sm^{3+} , would be expected for Tm^{3+} around 4.6 eV in $\text{Ca}_2\text{Si}_5\text{N}_8$ and around 4.1 eV in $\text{Sr}_2\text{Si}_5\text{N}_8$. For the other ions the charge transfer band will probably not be observed, since the energy is too close to the host lattice absorption.

From the energy schemes in Figure 4.11 it can be concluded that Tm^{3+} can act as a shallow electron trap, since the Tm^{2+} ground state is well below the bottom of the conduction band. This might therefore explain why co-doping with Tm^{3+} enhances the afterglow of the Eu^{2+} $d-f$ emission in $\text{Ca}_2\text{Si}_5\text{N}_8$. [8,10-13] Note that Ce^{3+} could form a stable hole trap in $\text{Ca}_2\text{Si}_5\text{N}_8$ and $\text{Sr}_2\text{Si}_5\text{N}_8$.

Yb^{3+} doped phosphors co-doped with another lanthanide ion, such as Tb^{3+} , are intensively studied for quantum cutting applications, where one UV or blue photon is converted into two infrared photons. [36] However, the efficiency of a Tb^{3+} - Yb^{3+} doped $\text{Ca}_2\text{Si}_5\text{N}_8$ phosphor will be limited by competing Yb^{3+} CT band absorption and Yb^{2+} $f-d$ absorption, both of which will not result in any quantum cutting.

4.6 Conclusions

Energy level schemes showing the positions of the $4f$ and $5d$ energy levels of all divalent and trivalent lanthanide ions with respect to the valence and conduction band of the $\text{M}_2\text{Si}_5\text{N}_8$ ($\text{M} = \text{Ca}, \text{Sr}$) phosphors have been constructed. The schemes were based on a critical evaluation of literature data of Ce^{3+} and Eu^{2+} doping in these hosts, as well as new data presented in this work on Sm , Tb and Yb doping in these materials. The schemes were of great help in interpreting the optical spectra and could be used to comment on the valence stability of the ions and thermal quenching of the Eu^{2+} $d-f$ emission.

Due to the presence of two different M sites in the $\text{M}_2\text{Si}_5\text{N}_8$ hosts, the lanthanide ions doped in these phosphors can be substituted on either the low or the high energy site or on both sites. Doping on the different sites resulted in different

positions of the 5d levels of the lanthanide ions with respect to the 4f ground state. This influences the luminescence behavior of the lanthanide ions significantly, as has been observed for the *f-f* emission of Tb³⁺ doped Ca₂Si₅N₈ after *f-d* excitation. Substitution on the high energy Ca site resulted in emission from both the ⁵D₃ and ⁵D₄ levels, while substitution on the low energy site gave rise to mainly ⁵D₄ emission.

4.7 References

- [1] Y.Q. Li, J.E.J. van Steen, J.W.H. van Krevel, G. Botty, A.C.A. Delsing, F.J. DiSalvo, G. de With, H.T. Hintzen; *J. Alloy. Compd.* 417 (2006) 273.
- [2] Y.Q. Li, G. de With, H.T. Hintzen; *J. Lumin.* 116 (2006) 107.
- [3] C.J. Duan, X.J. Wang, W.M. Otten, A.C.A. Delsing, J.T. Zhao, H.T. Hintzen; *Chem. Mater.* 20 (2008) 1597.
- [4] K. Uheda, N. Hirosaki, H. Yamamoto; *Phys. Status Solidi A* 203 (2006) 2712.
- [5] Y.Q. Li, N. Hirosaki, R.J. Xie, T. Takeda, M. Mitomo; *Chem. Mater.* 20 (2008) 6704.
- [6] R. Mueller-Mach, G. Mueller, M.R. Krames, H.A. Höpfe, F. Stadler, W. Schnick, T. Juestel, P. Schmidt; *Phys. Status Solidi A* 202 (2005) 1727.
- [7] S.E. Brinkley, N. Pfaff, K.A. Denault, Z. Zhang, H.T. Hintzen, R. Seshadri, S. Nakamura, S.P. DenBaars; *Appl. Phys. Lett.* 99 (2011) 241106.
- [8] K. Van den Eeckhout, P.F. Smet, D. Poelman; *J. Lumin.* 129 (2009) 1140.
- [9] H.L. Li, R.J. Xie, N. Hirosaki, T. Takeda, G.H. Zhou; *Int. J. Appl. Ceram. Tec.* 6 (2009) 459.
- [10] Y. Miyamoto, H. Kato, Y. Honna, H. Yamamoto, K. Ohmi; *J. Electrochem. Soc.* 156 (2009) J235.
- [11] B. Lei, K. Machida, T. Horikawa, H. Hanzawa, N. Kijima, Y. Shimomura, H. Yamamoto; *J. Electrochem. Soc.* 157 (2010) J196.
- [12] K. Van den Eeckhout, P.F. Smet, D. Poelman; *Mater.* 4 (2011) 980.

- [13] P.F. Smet, K. Van den Eeckhout, A.J.J. Bos, E. van der Kolk, P. Dorenbos; *J. Lumin.* 132 (2012) 682.
- [14] T. Schlieper, W. Schnick; *Z. Anorg. Allg. Chem.* 621 (1995) 1037.
- [15] T. Schlieper, W. Milius, W. Schnick; *Z. Anorg. Allg. Chem.* 621 (1995) 1380.
- [16] X. Piao, K. Machida, T. Horikawa, H. Hanzawa; *J. Electrochem. Soc.* 155 (2008) J17.
- [17] X. Piao, T. Horikawa, H. Hanzawa, K. Machida; *Appl. Phys. Lett.* 88 (2006) 161908.
- [18] R.J. Xie, N. Hirosaki, N. Kimura, K. Sakuma, M. Mitomo; *Appl. Phys. Lett.* 90 (2007) 191101.
- [19] X. Piao, K. Machida, T. Horikawa, B. Yun; *J. Lumin.* 130 (2010) 8.
- [20] X. Piao, K. Machida, T. Horikawa, H. Hanzawa; *Appl. Phys. Lett.* 91 (2007) 041908.
- [21] X. Piao, T. Horikawa, H. Hanzawa, K. Machida; *Chem. Lett.* 35 (2006) 334.
- [22] Y.Q. Li, G. de With, H.T. Hintzen; *J. Solid State Chem.* 181 (2008) 515.
- [23] P. Dorenbos; *J. Phys.-Condens. Mat.* 15 (2003) 575.
- [24] R.J. Xie, N. Hirosaki, T. Suehiro, F.F. Xu, M. Mitomo; *Chem. Mater.* 18 (2006) 5578.
- [25] M. Zeuner, F. Hintze, W. Schnick; *Chem. Mater.* 21 (2009) 336.
- [26] M. Zeuner, P.J. Schmidt, W. Schnick; *Chem. Mater.* 21 (2009) 2467.
- [27] H.A. Höpfe, H. Lutz, P. Morys, W. Schnick; A. Seilmeier; *J. Phys. Chem. Solids* 61 (2000) 2001.
- [28] P. Dorenbos; *J. Phys.-Condens. Mat.* 15 (2003) 8417.
- [29] P. Dorenbos; *J. Alloy. Compd.* 488 (2009) 568.
- [30] P. Dorenbos; *J. Lumin.* 111 (2005) 89.
- [31] P. Dorenbos; *J. Phys.-Condens. Mat.* 15 (2003) 4797.
- [32] P. Dorenbos; *Phys. Rev. B* 85 (2012) 165107.
- [33] O.M. ten Kate, H.T. Hintzen; P. Dorenbos; E. van der Kolk; *J. Mater. Chem.* 21 (2011) 18289.
- [34] E. van der Kolk, P. Dorenbos, J.T.M. de Haas, C.W.E. van Eijk; *Phys. Rev. B.* 71 (2005) 045121.

[35] P. Dorenbos; Chem. Mater. 17 (2005) 6452.

[36] P. Vergeer, T.J.H. Vlugt, M.H.F. Kox, M.I. den Hertog, J.P.J.M. van der Eerden, A. Meijerink; Phys. Rev. B 71 (2005) 014119.

Chapter 5

Enhanced 1G_4 emission in $\text{NaLaF}_4:\text{Pr}^{3+},\text{Yb}^{3+}$ and charge transfer in $\text{NaLaF}_4:\text{Ce}^{3+},\text{Yb}^{3+}$ studied by Fourier transform luminescence spectroscopy

*The content of this chapter has been published as: E. van der Kolk, O.M. ten Kate, J.W. Wiegman, D. Biner, K.W. Krämer; “Enhanced 1G_4 emission in $\text{NaLaF}_4:\text{Pr}^{3+},\text{Yb}^{3+}$ and charge transfer in $\text{NaLaF}_4:\text{Ce}^{3+},\text{Yb}^{3+}$ studied by Fourier transform luminescence spectroscopy”; *Optical Materials* 33 (2011) 1024-1027.*

A high resolution luminescence study of $\text{NaLaF}_4:1\%\text{Pr}^{3+},5\%\text{Yb}^{3+}$ and $\text{NaLaF}_4:1\%\text{Ce}^{3+},5\%\text{Yb}^{3+}$ in the UV to NIR spectral range using an InGaAs detector and a Fourier transform interferometer is reported. Although the Pr^{3+} ($^3P_0 \rightarrow ^1G_4$), Yb^{3+} ($^2F_{7/2} \rightarrow ^2F_{5/2}$) energy transfer step takes place, significant Pr^{3+} 1G_4 emission around 993, 1330 and 1850 nm is observed. No experimental proof for the second energy transfer step in the down-conversion process between Pr^{3+} and Yb^{3+} can be given. In the case of $\text{NaLaF}_4:\text{Ce}^{3+},\text{Yb}^{3+}$ it is concluded that the observed Yb^{3+} emission upon Ce^{3+} $5d$ excitation is the result of a charge transfer process instead of down-conversion.

5.1 Introduction

Solar cells have a limited efficiency because the energy of absorbed photons in excess of the band gap of the solar cell is lost by thermalization. This well

recognized color mismatch problem is an important loss mechanism in silicon solar cells. An attractive way to solve this problem is to use so called quantum cutting (QC) spectral conversion materials. Such luminescent materials are able to convert an ultraviolet or blue photon into two infrared (IR) photons that are used more efficiently by the solar cell. It has been calculated that by using quantum cutting materials an efficiency gain of 1.25 is in principle possible. [1,2] There has been an enormous progress in the development of QC materials by using combinations of lanthanide (Ln) ions like Yb^{3+} and Pr^{3+} or Yb^{3+} and Ce^{3+} [3,4] (in this case QC is referred to as down-conversion). Figure 5.1a shows the down-conversion concept for the Pr^{3+} - Yb^{3+} ion pair. Once a Pr^{3+} ion is excited into the ${}^3\text{P}_0$ $4f^2$ level the ion couple can relax to the ground state in a two step energy transfer process. In the first resonant energy transfer step the Pr^{3+} ion loses half of its energy by transferring it to a neighboring Yb^{3+} ion (see solid arrow in Figure 5.1a). In a second energy transfer step the Pr^{3+} ion loses the remaining energy by transferring it to a second neighboring Yb^{3+} ion (dashed arrows).

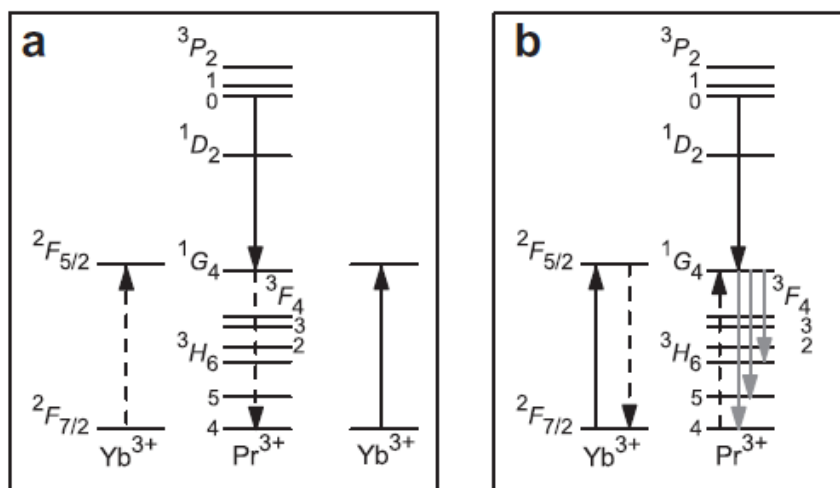


Figure 5.1: (a) Down-conversion between Pr^{3+} and Yb^{3+} . Step 1: $\text{Pr}^{3+} {}^3\text{P}_0 \rightarrow {}^1\text{G}_4$ excites the first Yb^{3+} ion (solid arrows). Step 2: $\text{Pr}^{3+} {}^1\text{G}_4 \rightarrow {}^3\text{H}_4$ excites a second Yb^{3+} ion (dashed arrows). (b) Step one is followed by ${}^1\text{G}_4$ emission (gray arrows). Dashed arrows indicate back-transfer from Yb^{3+} to Pr^{3+} .

In this chapter the down-conversion in NaLaF₄ doped Yb³⁺-Pr³⁺ and Yb³⁺-Ce³⁺ is reported. By using an InGaAs detector that is sensitive beyond 1000 nm it is shown that the second step in the down-conversion between Yb³⁺ and Pr³⁺ is inefficient or does not take place. In the case of NaLaF₄:Yb³⁺,Ce³⁺ it is shown that down-conversion does not occur but instead energy is transferred by charge transfer from Ce³⁺ to Yb³⁺.

5.2 Experimental

Diffuse reflection spectra were recorded with a Bruker Vertex 80v FT interferometer using different light sources (deuterium, tungsten and glowbar), detectors (GaP, Si, InGaAs) and a Pike Easydiff reflection accessory. Emission spectra were recorded using the same FT interferometer under excitation by the second or third harmonic of a tunable femtosecond laser. A cooled InGaAs detector sensitive to 4000 cm⁻¹ was used for detection. Phosphor preparation was described elsewhere. [5]

5.3 Results and discussion

5.3.1 Down-conversion in NaLaF₄:1%Pr³⁺,5%Yb³⁺

Figure 5.2 shows the absorption spectra (derived from diffuse reflection spectra using Kubelka–Munk) of NaLaF₄:2%Pr³⁺ and NaLaF₄:2%Yb³⁺. The observed $4f^2$ and $4f^{13}$ absorption lines are indicated in Figure 5.2a and b for Pr³⁺ and Yb³⁺ respectively.

The emission spectrum of NaLaF₄:2%Pr³⁺ is shown in Figure 5.3 by the black curve. As expected in a low phonon energy host lattice like NaLaF₄, mainly 3P_0 emission lines are observed upon 3P_2 excitation. Note that weak $^1G_4 \rightarrow ^3H_{6,5,4}$ emission in the NIR is observed that is the result of the $^3P_0 \rightarrow ^1G_4$ radiative feeding.

When the emission spectrum is compared with $\text{NaLaF}_4:1\%\text{Pr}^{3+},5\%\text{Yb}^{3+}$ three strong emission lines are observed around 993 nm, 1330 nm and 1850 nm. The lines around 1330 nm and 1850 nm are caused by the ${}^1\text{G}_4 \rightarrow {}^3\text{H}_6$ and ${}^1\text{G}_4 \rightarrow {}^3\text{H}_5$ transition on Pr^{3+} respectively. This enhanced ${}^1\text{G}_4$ emission is a direct consequence of the first step of the down-conversion process indicated in Figure 5.1a. Close inspection of the peak around 993 nm reveals that it partly consists of $\text{Pr}^{3+} {}^1\text{G}_4 \rightarrow {}^3\text{H}_6$ emission and partly of $\text{Yb}^{3+} {}^2\text{F}_{5/2} \rightarrow {}^2\text{F}_{7/2}$ emission. This becomes clear by comparing the Yb^{3+} emission in a $\text{NaLaF}_4:1\%\text{Ce}^{3+},5\%\text{Yb}^{3+}$ sample with the ${}^1\text{G}_4 \rightarrow {}^3\text{H}_4$ emission in a $\text{NaLaF}_4:2\%\text{Pr}^{3+}$ sample (see inset of Figure 5.3). The assignment of the Yb^{3+} and Pr^{3+} emission lines is in agreement with the absorption spectra presented in Figure 5.2.

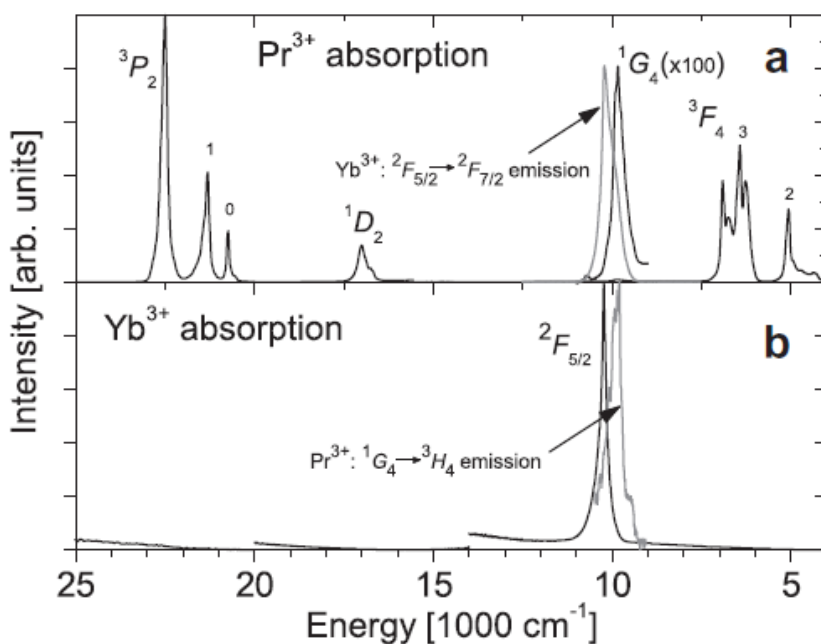


Figure 5.2: Absorption spectrum of (a) $\text{NaLaF}_4:2\%\text{Pr}^{3+}$ and (b) $\text{NaLaF}_4:2\%\text{Yb}^{3+}$ as well as the $\text{Yb}^{3+} {}^2\text{F}_{5/2}$ and $\text{Pr}^{3+} {}^1\text{G}_4$ emission, both to the ground state.

In previous studies of the $\text{Pr}^{3+}\text{-Yb}^{3+}$ down-conversion ion couple the energy transfer efficiency (ETE) of the first transfer step (see Figure 5.1) has been established by measuring the reduction of the decay time of the $\text{Pr}^{3+} \ ^3P_0$ emission with increasing Yb^{3+} emission. [6,7] After the first energy transfer step from Pr^{3+} to Yb^{3+} both ions are still in an excited state. Pr^{3+} is excited in the 1G_4 state while Yb^{3+} is excited in the $^2F_{5/2}$ state. So far it has been assumed [6–8] that Pr^{3+} transfers its remaining energy to a second Yb^{3+} in the second resonant energy transfer step. The energy transfer efficiency of this process has so far not been established. By measuring the emission spectra of Pr^{3+} and Yb^{3+} with a cooled InGaAs detector that is sensitive beyond a typical silicon detector until at least 4000 cm^{-1} (2500 nm) it becomes clear from the presence of 1G_4 emission that the efficiency of the second energy transfer step in NaLaF_4 is low or that the transfer does not take place.

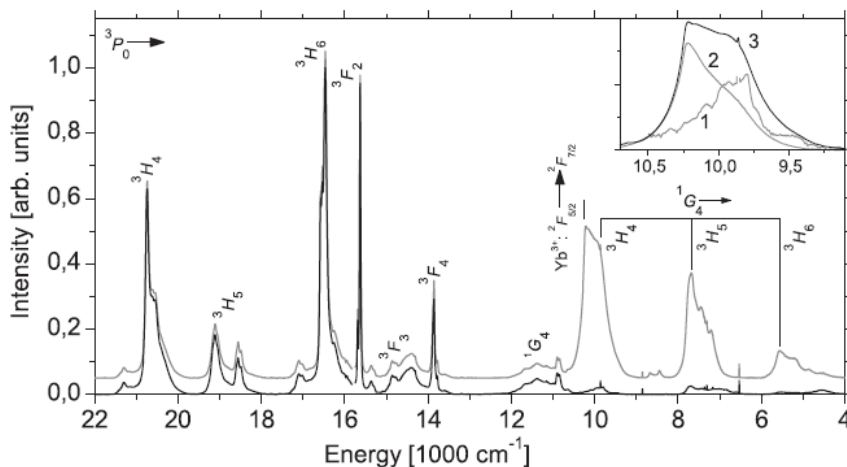


Figure 5.3: 3P_2 excited emission spectra of $\text{NaLaF}_4:2\%\text{Pr}^{3+}$ (black) and $\text{NaLaF}_4:1\%\text{Pr}^{3+}, 5\%\text{Yb}^{3+}$ (gray). The inset shows that the emission around 1000 nm of $\text{NaLaF}_4:1\%\text{Pr}^{3+}, 5\%\text{Yb}^{3+}$ (3) consists of both $\text{Yb}^{3+} \ ^2F_{5/2} \rightarrow \ ^2F_{7/2}$ emission (2) and $\text{Pr}^{3+} \ ^1G_4 \rightarrow \ ^3H_4$ emission (1).

If the diffuse reflection spectra of $\text{NaLaF}_4:2\%\text{Pr}^{3+}$ and $\text{NaLaF}_4:2\%\text{Yb}^{3+}$ are compared (see Figure 5.2) it can be observed that the 1G_4 state of Pr^{3+} is lower in energy than the $^2F_{5/2}$ state of Yb^{3+} which suggests that a Yb^{3+} to Pr^{3+} energy transfer

is energetically more favorable than the desired reverse energy transfer from Pr^{3+} to Yb^{3+} . Furthermore the relevant spectral overlap between the Yb^{3+} emission and the $\text{Pr}^{3+} {}^3\text{H}_4 \rightarrow {}^1\text{G}_4$ absorption (see Figure 5.2a) that is required for transfer from Yb^{3+} to Pr^{3+} , is at least equal to the overlap between the $\text{Pr}^{3+} {}^1\text{G}_4 \rightarrow {}^3\text{H}_4$ emission and $\text{Yb}^{3+} {}^2\text{F}_{7/2} \rightarrow {}^2\text{F}_{5/2}$ absorption (see Figure 5.2b).

Energy transfer from Yb^{3+} to Pr^{3+} can be shown by the excitation spectrum monitoring the ${}^1\text{G}_4$ emission of Pr^{3+} around 1850 nm or 1330 nm that in case of transfer should show the $\text{Yb}^{3+} {}^2\text{F}_{5/2}$ excited state. The efficiency of the transfer from Yb^{3+} to Pr^{3+} may be established by measuring the reduction of the Yb^{3+} decay time under direct Yb^{3+} excitation as a function of the Pr^{3+} doping concentration. Such studies have so far not been published. Note that in the case of high phonon energy host lattices there is no obvious way to establish the transfer efficiency by monitoring the presence of ${}^1\text{G}_4$ emission as the ${}^1\text{G}_4$ emission is fully quenched by multi-phonon relaxation due to the relatively small energy gap between the ${}^1\text{G}_4$ state and the next lower energy ${}^3\text{F}_4$ state of about 3000 cm^{-1} . In these cases only the above measured Yb^{3+} decay time measurements can reveal the transfer efficiency.

Down-conversion in the Pr^{3+} - Yb^{3+} system has also been explained [9–11] by a one-step cooperative energy transfer process identical to that observed in the Tb^{3+} , Yb^{3+} system. [12] In this type of transfer, the Pr^{3+} ion loses its energy in one step to two neighboring Yb^{3+} ions and therefore no Pr^{3+} ions will get excited in the ${}^1\text{G}_4$ state. If this would be the case, then the ${}^1\text{G}_4$ emission that has been observed in NaLaF_4 can only be the result of back-transfer from the ${}^2\text{F}_{5/2}$ state of Yb^{3+} to the ${}^1\text{G}_4$ state of Pr^{3+} . It is concluded that detailed NIR luminescence studies like those presented here are needed to establish whether down-conversion in the Pr^{3+} - Yb^{3+} ion pair is indeed an attractive approach to enhance the efficiency of silicon solar cells. Besides the well recognized problems of weak sunlight absorption by the ${}^3\text{P}_j$ lines of Pr^{3+} and the Yb^{3+} concentration quenching at Yb^{3+} concentrations for which the Pr^{3+} to Yb^{3+} transfer is significantly high [6] it is noted that there are three additional loss processes involving the ${}^1\text{G}_4$ state: (i) emission from the ${}^1\text{G}_4$ state that is partly at 1330 nm and 1850 nm, (ii) non-radiative ${}^1\text{G}_4 \rightarrow {}^3\text{F}_4$ relaxation and possibly, (iii) $\text{Yb}^{3+} ({}^2\text{F}_{5/2}) \rightarrow \text{Pr}^{3+} ({}^1\text{G}_4)$ energy backtransfer.

5.3.2 Charge transfer in $\text{NaLaF}_4:1\%\text{Ce}^{3+}, 5\%\text{Yb}^{3+}$

There have been several recent studies of the energy transfer between Ce^{3+} and Yb^{3+} in $\text{Y}_3\text{Al}_5\text{O}_{12}$ (YAG) [13,14], YBO_3 [15] and borate glasses. [16] In these studies it was shown that Ce^{3+} 5d excitation resulted in Yb^{3+} emission and that the Ce^{3+} decay time as well as the emission intensity gradually decreased when the Yb^{3+} concentration was increased. On the basis of these experimental observations it was concluded that there is a cooperative energy transfer process between Ce^{3+} and Yb^{3+} resulting in the excitation of two Yb^{3+} infrared photons for each excited Ce^{3+} ion. This is particularly interesting because the Ce^{3+} 4f-5d transition strongly absorbs the UV and blue part of the solar spectrum which is a highly desirable property for a spectral conversion material. Ueda and Tanabe [17] however conclude on the basis of the rise time of the Yb^{3+} emission in YAG, after Ce^{3+} 4f-5d excitation that there must be an intermediate state in the energy transfer to Yb^{3+} . This intermediate state involves the formation of Ce^{4+} and Yb^{2+} . Experimental results of $\text{NaLaF}_4:1\%\text{Ce}^{3+}, 5\%\text{Yb}^{3+}$ are presented in this work, showing that the energy transfer in NaLaF_4 involves charge transfer from Yb^{3+} to Ce^{3+} .

Figure 5.4 shows the emission spectrum of $\text{NaLaF}_4:1\%\text{Ce}^{3+}, 5\%\text{Yb}^{3+}$ excited in the Ce^{3+} 5d states together with the excitation spectrum of $\text{NaLaF}_4:2\%\text{Ce}^{3+}$ monitoring Ce^{3+} 5d-4f emission. In addition to the Ce^{3+} 5d-4f emission, also Yb^{3+} emission is observed around 1000 nm. An important conclusion that can be drawn from our results for $\text{NaLaF}_4:1\%\text{Ce}^{3+}, 5\%\text{Yb}^{3+}$ is that the energy of Ce^{3+} emission in NaLaF_4 is too high to excite two Yb^{3+} ions by a cooperative transfer process as can be seen from spectrum c in Figure 5.4. Still Ce^{3+} to Yb^{3+} energy transfer is observed in $\text{NaLaF}_4:1\%\text{Ce}^{3+}, 5\%\text{Yb}^{3+}$.

Figure 5.5 shows a detailed energy level diagram of NaLaF_4 in which the ground state energies of all Ln^{2+} and Ln^{3+} ions are plotted as a function of the type of lanthanide with respect to the conduction and valence band. This type of energy scheme has been developed by Dorenbos [18] and has successfully been used to explain in detail mechanisms of charge transfer [19], charge trapping and afterglow luminescence [20] and luminescence temperature quenching [21] For this work on

NaLaF₄ it is important to use this scheme to establish that the 5*d* states of Ce³⁺ have a higher energy than the (empty) Yb²⁺ ground state.

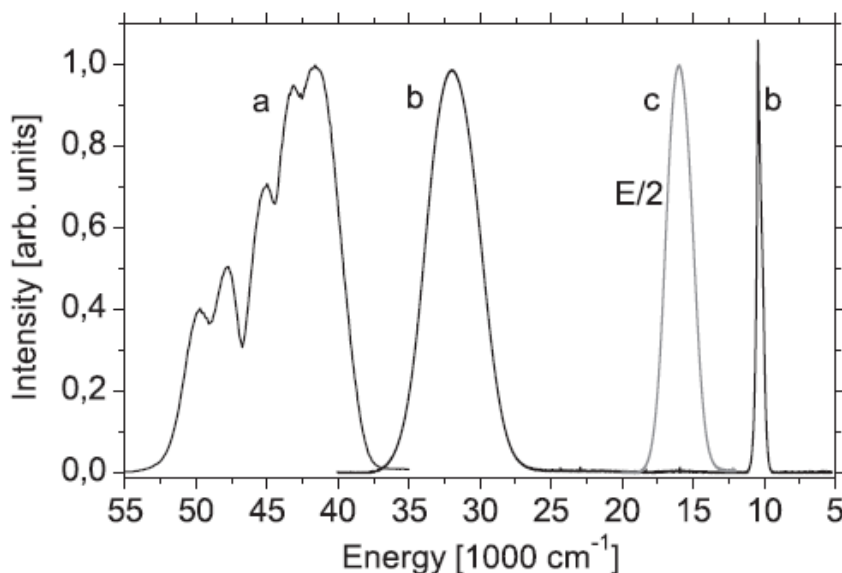


Figure 5.4: (a) Excitation spectrum of NaLaF₄:2%Ce³⁺ monitoring Ce³⁺ 5*d*-4*f* emission, (b) emission spectrum of NaLaF₄:1%Ce³⁺,5%Yb³⁺ excited in the Ce³⁺ 5*d* states. (c) Same as (b) but the energy scale divided by 2 (*E*/2).

It is therefore energetically favorable for an excited Ce³⁺ ion to donate an electron to a neighboring Yb³⁺ ion. The resulting excited state, involving a Ce⁴⁺ ion and a Yb²⁺ ion (both in their ground state) will, after a large amount of lattice relaxation, lower its energy further by transferring the electron back to Ce⁴⁺. In this way Ce³⁺ is again formed in its ground state while Yb³⁺ will be excited in its ²F_{5/2} state. Note that this type of Yb³⁺ emission through charge transfer is very similar to the better known charge transfer excited Yb³⁺ (or Eu³⁺) emission in which the charge is transferred by optical excitation from the valence band. In both types of charge transfer excitation, Yb²⁺ (or Eu²⁺) is formed after which efficient Eu³⁺ or Yb³⁺ emission follows. It is concluded that the energy transfer from Ce³⁺ to Yb³⁺ in NaLaF₄ must be the result of a charge transfer process because the Ce³⁺ 5*d*-4*f*

emission energy is too high to excite two Yb^{3+} ions. Because of the very interesting absorption and emission properties of $\text{Ce}^{3+}\text{-Yb}^{3+}$ doped YAG it is important to establish which type of energy transfer dominates in YAG. In $\text{YAG}:\text{Ce}^{3+}, \text{Yb}^{3+}$ the Ce^{3+} to Yb^{3+} energy transfer via a cooperative process is energetically possible because the Ce^{3+} $5d\text{-}4f$ emission is at a much lower energy. However the detailed energy level scheme for YAG, plotted in Figure 5.6, shows that also in YAG charge transfer from $5d$ excited Ce^{3+} ions to Yb^{3+} is a real possibility and cannot be excluded. All experimental results published so far for $\text{YAG}:\text{Ce}^{3+}, \text{Yb}^{3+}$ can also be explained by the charge transfer model.

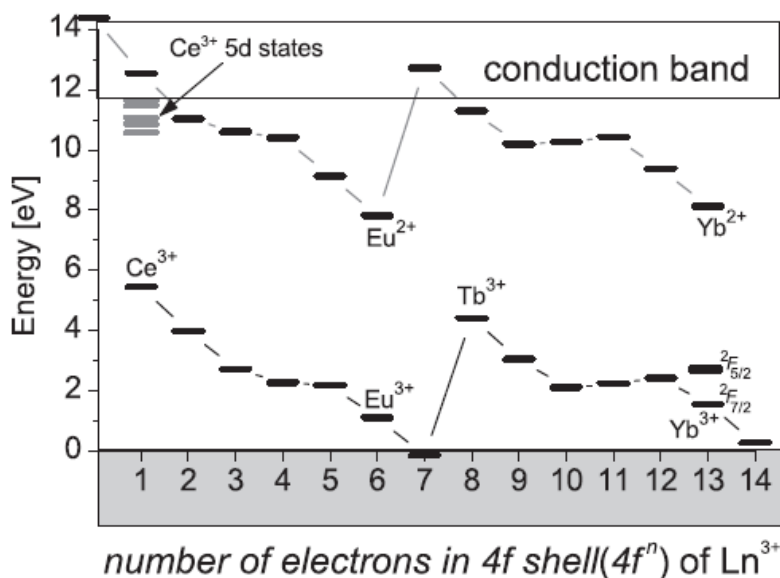


Figure 5.5: Energy level scheme of NaLaF_4 showing the ground state energy of all the Ln^{2+} and Ln^{3+} ions with respect to the valence band and conduction band.

In order to further establish the nature of the energy transfer mechanism between Ce^{3+} and Yb^{3+} one could try to directly optically detect Ce^{4+} and Yb^{2+} impurities in a diffuse reflection or transmission experiment during intense Ce^{3+} $5d\text{-}4f$ excitation. It should be finally noted that the second order energy transfer process from the 5D_4

level of Tb^{3+} to two Yb^{3+} ions is efficient [12,22], partly because the competing process, the normal $\text{Tb}^{3+} \ ^5\text{D}_4$ emission, is strongly forbidden as evidenced by the very long decay time of about 10 ms. The Ce^{3+} decay time on the contrary is about 20 ns which is almost six orders of magnitude shorter. An efficient Ce^{3+} to Yb^{3+} energy transfer by a cooperative transfer process can compete much less with the $\text{Ce}^{3+} \ 5d-4f$ emission. In that respect Ce^{3+} - Yb^{3+} energy transfer by charge transfer is a more likely process.

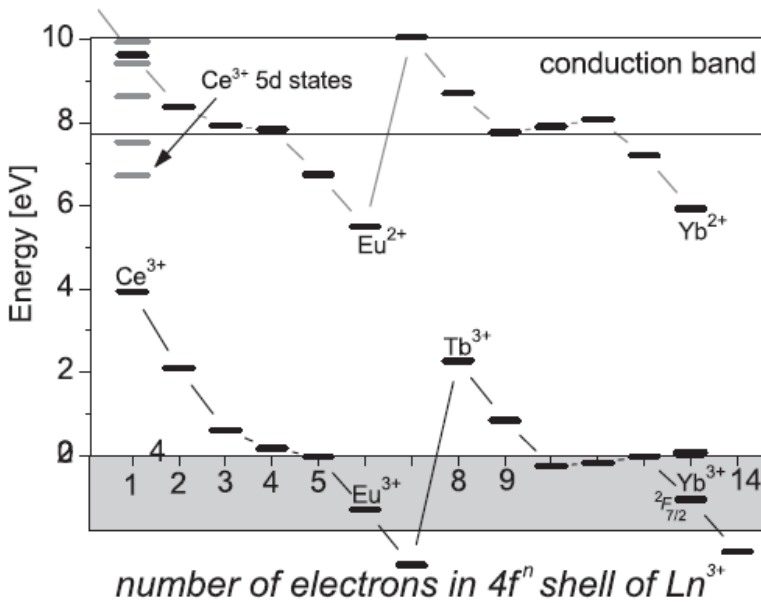


Figure 5.6: Energy level scheme of $\text{Y}_3\text{Al}_5\text{O}_{12}$ (YAG) showing the ground state energy of all the Ln^{2+} and Ln^{3+} ions with respect to the valence band and conduction band.

5.4 References

- [1] T. Trupke, M.A. Green, P. Würfel; J. Appl. Phys. 92 (2002) 1668.
- [2] H. Shpaisman, O. Niitsoo, I. Lubomirsky, D. Cahen; Sol. Energy Mater. Sol. C. 92 (2008) 1541.

- [3] B.M. van der Ende, L. Aarts, A. Meijerink; *Phys. Chem. Chem. Phys.* 11 (2009) 11081.
- [4] Q.Y. Zhang, X.Y. Huang; *Prog. Mater. Sci.* 55 (5) (2010) 353.
- [5] E. van der Kolk, P. Dorenbos, K. Krämer, D. Biner, H.U. Güdel; *Phys. Rev. B* 77 (2008) 125110.
- [6] B.M. van der Ende, L. Aarts, A. Meijerink; *Adv. Mater.* 21 (2009) 3073.
- [7] Y. Katayama, S. Tanabe; *Mater.* 3 (2010) 2405.
- [8] J.T. van Wijngaarden, S. Scheidelaar, T.J.H. Vlugt, M.F. Reid, A. Meijerink, *Phys. Rev. B* 81 (2010) 155112.
- [9] D. Chen, Y. Wang, Y. Yu, P. Huang, F. Weng; *Opt. Lett.* 33 (2008) 1884.
- [10] X. Chen, X. Huang, Q. Zhang; *J. Appl. Phys.* 106 (2009) 063518.
- [11] G. Lakshminarayana, H. Yang, S. Ye, Y. Liu, J. Qiu; *J. Mater. Res.* 23 (2008) 3090.
- [12] P. Vergeer, T.J.H. Vlugt, M.H.F. Kox, M.I. den Hertog, J.P.J.M. van der Eerden, A. Meijerink; *Phys. Rev. B* 71 (2005) 014119.
- [13] X. Liu, Y. Teng, Y. Zhuang, J. Xie, Y. Qiao, G. Dong, D. Chen, J. Qiu; *Opt. Lett.* 34 (2009) 3565.
- [14] H. Lin, S. Zhou, H. Teng, Y. Li, W. Li, X. Hou, T. Jia; *J. Appl. Phys.* 107 (2010) 043107.
- [15] J. Chen, H. Guo, Z. Li, H. Zhang, Y. Zhuang; *Opt. Mater.* (2010), doi:10.1016/j.optmat.2010.01.040.
- [16] D. Chen, Y. Wang, Y. Yu, P. Huang, F. Weng; *J. Appl. Phys.* 104 (2008) 116105.
- [17] J. Ueada, S. Tanabe; *J. Appl. Phys.* 106 (2009) 043101.
- [18] P. Dorenbos; *J. Phys.-Condens. Mat.* 15 (2003) 8417.
- [19] N.R.J. Poolton, A.J.J. Bos, G.O. Jones, P. Dorenbos; *J. Phys.-Condens. Mat.* 22 (2010) 185403.
- [20] P. Dorenbos, A.J.J. Bos; *Radiat. Meas.* 43 (2–6) (2008) 139.
- [21] E. van der Kolk, P. Dorenbos, J.T.M. de Haas, C.W.E. van Eijk; *Phys. Rev. B* 71 (2005) 045121.
- [22] Q.Y. Zhang, C.H. Yang, Z.H. Jiang, X. Ji; *Appl. Phys. Lett.* 90 (2007) 061914

Chapter 6

Quantum tripling in Tm^{3+} doped $\text{La}_2\text{BaZnO}_5$ phosphors for efficiency enhancement of small band gap solar cells

The content of this chapter has been submitted to Journal of Luminescence as: O.M. ten Kate, E. van der Kolk; “Quantum tripling in Tm^{3+} doped $\text{La}_2\text{BaZnO}_5$ phosphors for efficiency enhancement of small band gap solar cells”.

The emission of three infrared photons at 1700 nm by Tm^{3+} for each absorbed photon at 465 nm is reported as a function of the Tm^{3+} concentration in $\text{La}_{2-2x}\text{Tm}_{2x}\text{BaZnO}_5$ phosphors. It was observed that the intensity of the $\text{Tm}^{3+} \ ^3\text{F}_4 \rightarrow \ ^3\text{H}_6$ emission with respect to emissions from the $\ ^1\text{G}_4$ state after $\ ^1\text{G}_4$ excitation at 465 nm increases when the Tm^{3+} concentration is raised from $x = 0.001$ to $x = 0.032$. This increase is the accumulated effect of four different possibilities for cross-relaxation that can take place between neighboring Tm^{3+} ions, which explains the efficiency of the quantum tripling process. An optimum in the cross-relaxation efficiency was found for the $\text{La}_{1.936}\text{Tm}_{0.064}\text{BaZnO}_5$ phosphor. At higher Tm^{3+} concentrations the $\ ^3\text{F}_4 \rightarrow \ ^3\text{H}_6$ emission decreases as a result of concentration quenching. Quantum tripling can be used in high power IR phosphor converted LEDs or to increase the efficiency of small band gap solar cells like germanium.

6.1 Introduction

The solar cell efficiency is mainly limited by the mismatch between the solar spectrum and the solar cell response. In a single junction photovoltaic device photons with energy lower than the band gap of the solar cell absorber material are

lost because they cannot be absorbed, while the excess energy of the photons with energy higher than the band gap is lost by thermalization. By choosing a small band gap semiconductor material like GaSb or Ge, losses due to limited absorption are reduced. However, thermalization losses are greatly enhanced as compared to larger band gap cells like Si, CIGS or CdTe. As a result, the Shockley-Queisser limits [1] of GaSb (band gap of 0.7 eV) and Ge (band gap of 0.67 eV) are 22 and 21% respectively, which is much smaller than the Shockley-Queisser limit of 30% for crystalline silicon (band gap of 1.12 eV).

One approach to reduce the thermalization losses in solar cells is the integration of a luminescent quantum cutting layer on top of the cell, which converts a photon with more than twice the band gap energy into two photons with an energy just above the band gap of the cell. This quantum cutting mechanism has been demonstrated in for example Tb³⁺ and Yb³⁺ co-doped YPO₄. [2] In this material absorption of a 490 nm photon by Tb³⁺ is followed by a cooperative energy transfer to two neighboring Yb³⁺ ions, resulting in the emission of two 1000 nm photons by the Yb³⁺ ions. These photons can subsequently be absorbed by a Si solar cell.

For solar cells with smaller band gaps it could be beneficial to not just split the high energy photons into two lower energy photons, but to split them into three photons. In a Ge solar cell about 24% of the absorbed photons have an energy of at least three times the band gap. Calculations show that an ideal quantum tripling layer on top of a Ge cell would result in a relative efficiency increase of almost 25%. [3] When integrating a combination of a quantum tripling layer and a quantum cutting layer, the relative increase in efficiency could even be 80%. [3]

Jaffrès et al. showed that the quantum tripling mechanism takes place in Tm³⁺ doped La₂BaZnO₅ phosphors. [4] The Tm³⁺ ion has several *4f-4f* transitions of the same energy. For example, the ³H₆ → ³F₂ absorption and the ¹G₄ → ³F₄ emission are both located around 670 nm. Because of this, different cross-relaxations can take place between the Tm³⁺ ions, which can result in the emission of three 1700 nm photons after the absorption of one 465 nm photon. Tm³⁺ cross-

relaxation has also been studied in other materials, like TeO_2 - $CdCl_2$ glasses [5], $Ge_{30}As_{10}S_{60}$ glasses [6] and silica [7].

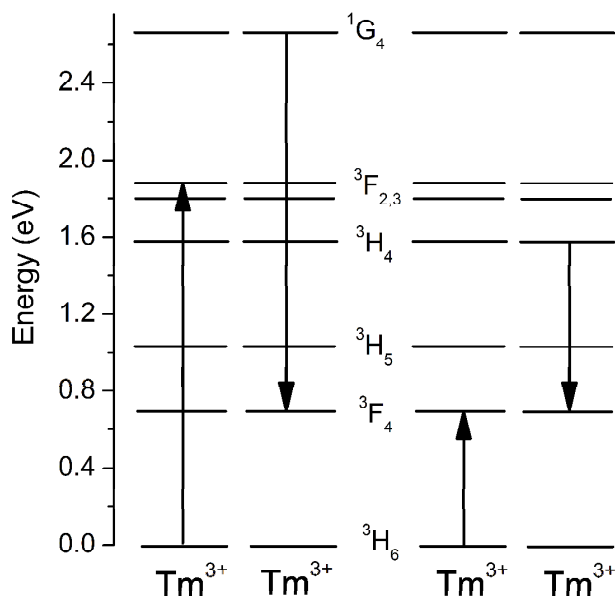


Figure 6.1: Two examples of Tm^{3+} $4f$ - $4f$ transitions with similar energy. The ${}^3H_6 \rightarrow {}^3F_2$ absorption and ${}^1G_4 \rightarrow {}^3F_4$ emission around 670 nm and the ${}^3H_6 \rightarrow {}^3H_5$ absorption and ${}^3H_4 \rightarrow {}^3F_4$ emission around 1180 nm.

For the research described in this chapter, La_2BaZnO_5 phosphors with different Tm^{3+} concentrations have been prepared and the spectroscopic properties of phosphors are discussed as a function of the Tm^{3+} concentration. From these results the efficiency of the quantum tripling mechanism of this phosphor will be discussed, and with it the applicability for the efficiency enhancement of small band gap solar cells.

6.2 Experimental

6.2.1 Synthesis

Tm³⁺ doped La₂BaZnO₅ samples have been prepared by solid-state reaction synthesis. BaCO₃ (Merck, 99%), La₂O₃ (Aldrich, 99.99%), ZnO (Aldrich, 99.999%) and Tm₂O₃ (Aldrich, 99.9%) were used as starting materials. These powders were combined in the appropriate molar ratio and thoroughly mixed with mortar and pestle. The samples were fired twice at 1200 °C in a high temperature tube furnace in air atmosphere with intermediate crunching in between. After firing, the samples were crunched and the resulting powders were used for the measurements without any additional treatment.

6.2.2 Measurements

Crystalline phases were checked by X-ray powder diffraction (XRD) analysis with a Bruker D4 Endeavor with Cu K_α radiation. XRD data were collected by scanning with a step size of 0.05° in 2θ and a counting time of 1 s per step. Diffuse reflectance spectra, which were converted in Kubelka-Munk [8] absorption spectra, were measured with a Bruker Vertex 80v FT interferometer using a tungsten lamp as a light source and InGaAs, Si and GaP detectors. Emission spectra were also recorded with the Bruker Vertex 80v using a laser as excitation source and InGaAs as detector. Excitation spectra were measured with a Hamamatsu H10330A-75 NIR PMT using two double grating monochromators and a xenon lamp as a light source.

6.3 Results and discussion

The crystal structure of La_2BaZnO_5 has first been reported by Michel et al. [9] The material has a tetragonal crystal structure with space group $I4/mcm$. The X-ray diffraction pattern of a $La_{2-2x}Tm_{2x}BaZnO_5$ sample with $x = 0.032$ is shown in Figure 6.2 and compared with the reference pattern (ICSD 87078). The patterns of the samples with other Tm^{3+} concentrations (up to $x = 0.128$) looked very similar. Note that in the La_2BaZnO_5 crystal the shortest distance between two La ions is about 3.40 \AA (ICSD 87078), which is relatively short as compared to the shortest La-La distance in other crystals like La_2O_3 (3.80 \AA , ICSD 151763), $LaCl_3$ (4.37 \AA , ICSD 23146) and LaF_3 (4.08 \AA , ICSD 27089). This short distance is favorable for the cross-relaxation between two Tm^{3+} ions doped on the La sites.

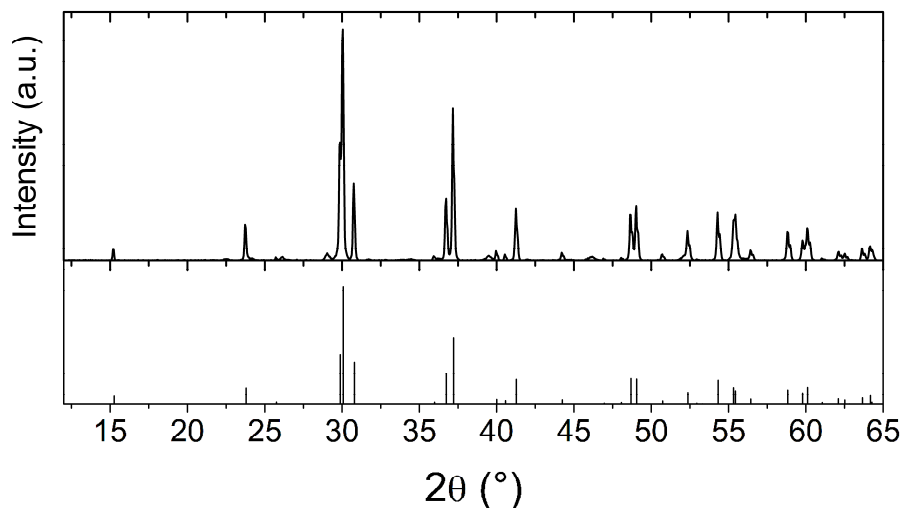


Figure 6.2: XRD pattern of $La_{1.936}Tm_{0.064}BaZnO_5$ (above) and the La_2BaZnO_5 reference pattern (ICSD 87078) (below).

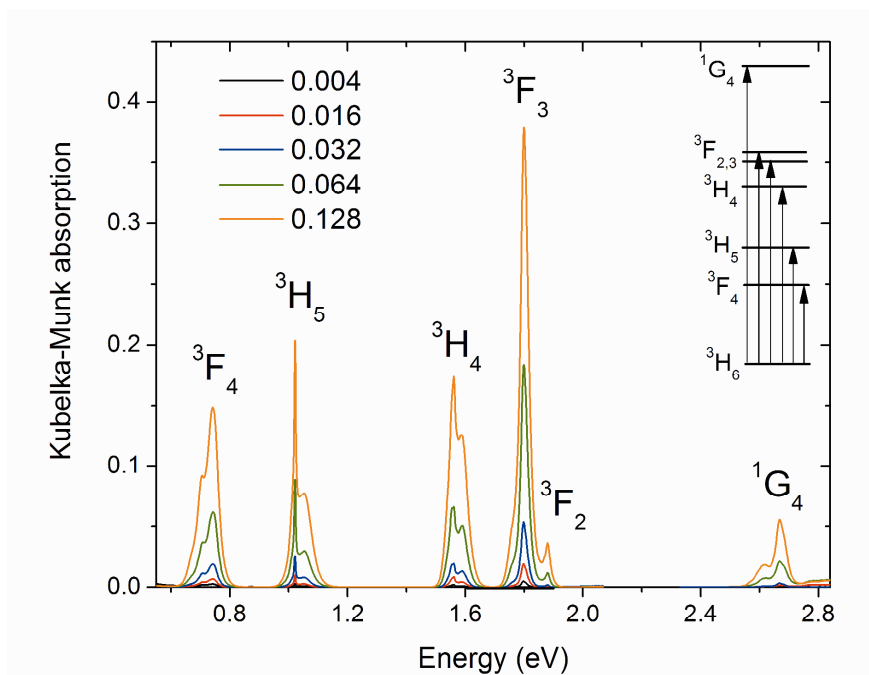


Figure 6.3: Kubelka-Munk [8] absorption spectra of $\text{La}_{2-2x}\text{Tm}_{2x}\text{BaZnO}_5$ samples for different Tm concentrations.

In Figure 6.3 the Kubelka-Munk absorption spectra are shown of the Tm^{3+} doped $\text{La}_2\text{BaZnO}_5$ phosphors for different Tm^{3+} concentrations. Several absorption peaks are observed around 0.74 eV, 1.02 eV, 1.56 eV, 1.80 eV, 1.88 eV and 2.67 eV corresponding to absorption from the $\text{Tm}^{3+} {}^3\text{H}_6$ ground state to the ${}^3\text{F}_4$, ${}^3\text{H}_5$, ${}^3\text{H}_4$, ${}^3\text{F}_3$, ${}^3\text{F}_2$ and ${}^1\text{G}_4$ excited states respectively, as indicated in Figure 6.3. As expected, the intensity of the absorption peaks increases linearly with increasing Tm^{3+} concentration from $x = 0.00025$ to $x = 0.128$, as is shown in Figure 6.4 for the ${}^3\text{H}_6 \rightarrow {}^3\text{H}_5$ absorption. Apart from the $4f-4f$ absorption peaks no other absorptions were observed.

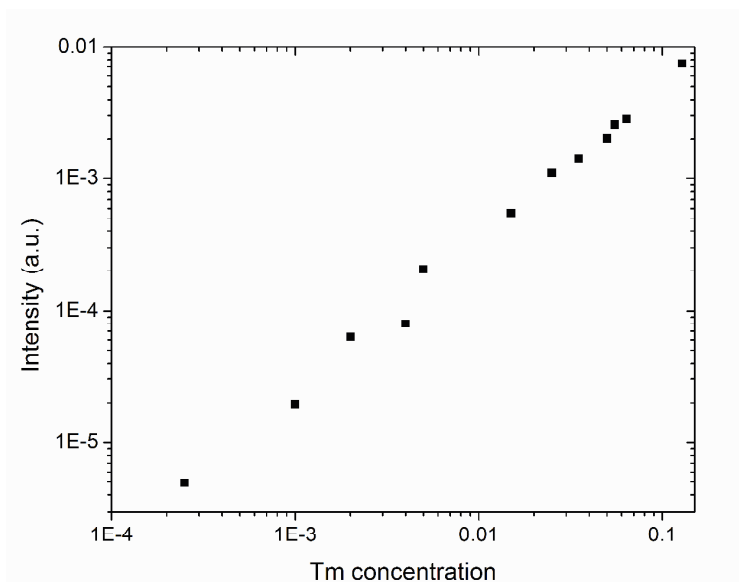


Figure 6.4: Integrated intensity of the ${}^3H_6 \rightarrow {}^3H_5$ absorption peak of Tm^{3+} in $La_{2-2x}Tm_{2x}BaZnO_5$ as a function of the Tm concentration x .

Excitation of the $La_{1.998}Tm_{0.002}BaZnO_5$ sample in the 1G_4 state of Tm^{3+} at 2.67 eV results in the emission pattern shown in Figure 6.5. Emission lines are observed around 0.7 eV, 0.8 eV, 1.0 eV, 1.55 eV and 1.9 eV, which can all be associated with Tm^{3+} $4f-4f$ transitions, as has been indicated by Jaffrès et al. [4] The line at 1.9 eV corresponds to emission from the 1G_4 state to the 3F_4 state and the emission line at 1.0 eV corresponds to ${}^1G_4 \rightarrow {}^3H_4$ emission. The emission around 1.55 eV can be attributed to a combination of two different emissions, ${}^1G_4 \rightarrow {}^3H_5$ and ${}^3H_4 \rightarrow {}^3H_6$ emission, which is supported by the observation that the shape of the emission peak changes with changing Tm^{3+} concentration, as will be discussed later. The emission lines observed between 0.6 and 1.1 eV can be, in order of increasing energy, associated with ${}^3F_4 \rightarrow {}^3H_6$ emission, ${}^1G_4 \rightarrow {}^3F_2$ emission, ${}^1G_4 \rightarrow {}^3F_3$ emission and ${}^3H_4 \rightarrow {}^3F_4$ emission.

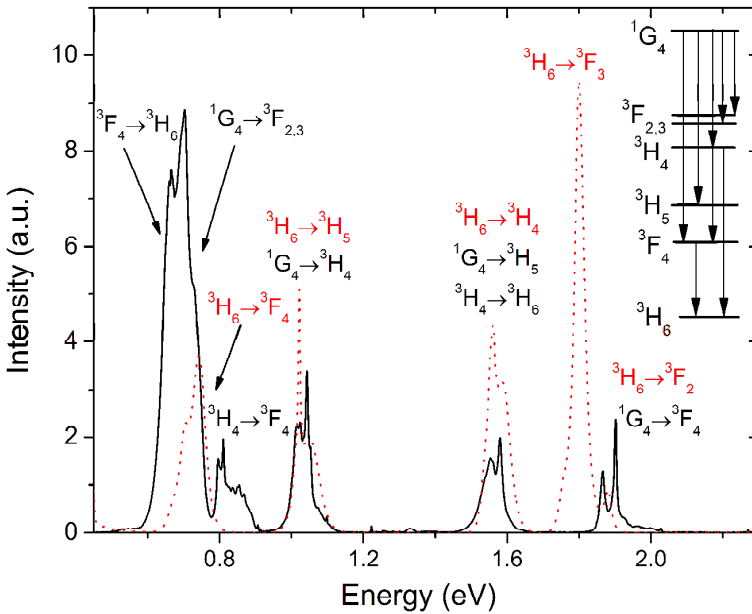


Figure 6.5: Emission spectrum (black solid line) of $\text{La}_{1.998}\text{Tm}_{0.002}\text{BaZnO}_5$ after excitation with 2.67 eV light, and Kubelka-Munk [8] absorption spectrum (red dotted line) of the same sample.

Note that there are only emissions from the $^1\text{G}_4$, $^3\text{H}_4$ and $^3\text{F}_4$ states and not from other states such as the $^3\text{H}_5$, although this state is populated by the $^1\text{G}_4 \rightarrow ^3\text{H}_5$ transition. The $^3\text{H}_5 \rightarrow ^3\text{H}_6$ emission line would have about the same energy as the $^1\text{G}_4 \rightarrow ^3\text{H}_4$ emission. However, in the excitation spectrum of this 1.04 eV emission (Figure 6.6) only the $^1\text{G}_4$ state is observed and not any other states like the $^3\text{F}_2$ or the $^3\text{F}_3$, indicating that the peak around 1.04 eV is only due to $^1\text{G}_4 \rightarrow ^3\text{H}_4$ emission. The absence of emission from the $^3\text{H}_5$ can be explained by multi-phonon relaxation to the $^3\text{F}_4$ state, since the energy difference is 4 times the phonon energy of 650 cm^{-1} , based on the phonon energy of $\text{Nd}_2\text{BaZnO}_5$. [10]

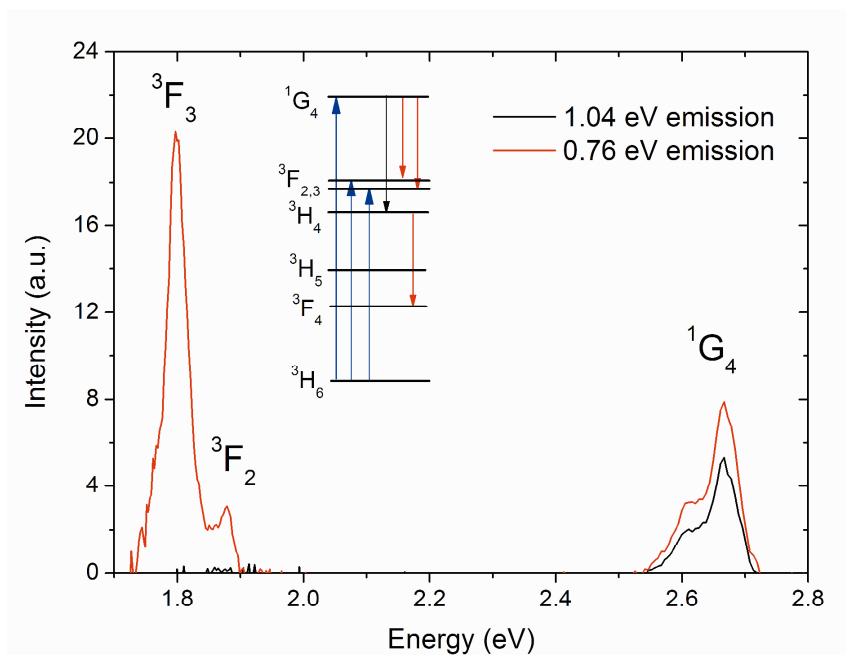


Figure 6.6: Excitation spectra of the 1.04 eV emission (black line) and the 0.76 eV emission (blue line) of $La_{1.936}Tm_{0.064}BaZnO_5$.

In Figure 6.7 the emission spectra after 1G_4 excitation of the $La_{2-2x}Tm_{2x}BaZnO_5$ samples are shown for different Tm^{3+} concentrations. The emission spectra are normalized to the $^3H_4 \rightarrow ^3F_4$ emission at 0.85 eV in order to study the relative changes. From the figure it can be seen that the $^3F_4 \rightarrow ^3H_6$ emission around 0.7 eV increases with respect to the 0.85 eV emission when the Tm^{3+} concentration is raised from $x = 0.001$ to $x = 0.032$, while at the same time the emissions originating from the 1G_4 state at 1.0 eV and 1.9 eV decrease with increasing Tm^{3+} concentration. At higher Tm^{3+} concentrations the intensity of the $^3F_4 \rightarrow ^3H_6$ emission decreases again with respect to the $^3H_4 \rightarrow ^3F_4$ emission with increasing Tm^{3+} concentration.

Additionally it can be seen that the shape of the emission peak around 1.55 eV changes with varying Tm^{3+} concentration. Note that the emission peak is a combination of $^1G_4 \rightarrow ^3H_5$ and $^3H_4 \rightarrow ^3H_6$ emission, of which the emission from the 1G_4 (the high energy side of the peak) is expected to decrease with increasing Tm

concentration just as the other emissions from the 1G_4 level, while emission from the 3H_4 level (the low energy side of the peak) is expected to be constant with respect to the $^3H_4 \rightarrow ^3F_4$ emission.

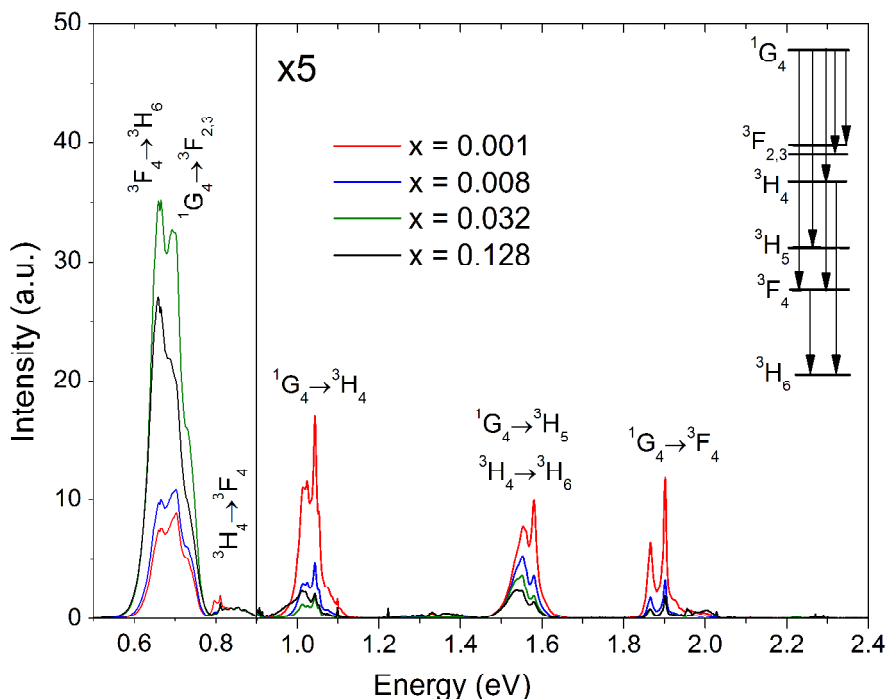


Figure 6.7: Emission spectra of various $\text{La}_{2-2x}\text{Tm}_{2x}\text{BaZnO}_5$ samples after 1G_4 excitation (2.67 eV). The spectra are normalized on the $^3H_4 \rightarrow ^3F_4$ emission at 0.85 eV. The part of the spectra above 0.9 eV is multiplied by a factor 5.

The intensity ratio of the $^3F_4 \rightarrow ^3H_6$ emission over the $^1G_4 \rightarrow ^3F_4$ emission after 1G_4 excitation is plotted in Figure 6.8. Up to $x = 0.032$ the ratio increases with increasing Tm^{3+} concentration. At higher concentrations there is no increase anymore. A similar pattern is observed when the $^3F_4 \rightarrow ^3H_6$ emission at 0.64 eV over the $^3H_4 \rightarrow ^3F_4$ emission at 1.90 eV is plotted, as is also shown in Figure 6.7. However the increase of 3F_4 emission relative to the 3H_4 emission is less strong as the increase relative to 1G_4 emission, which will be explained below.

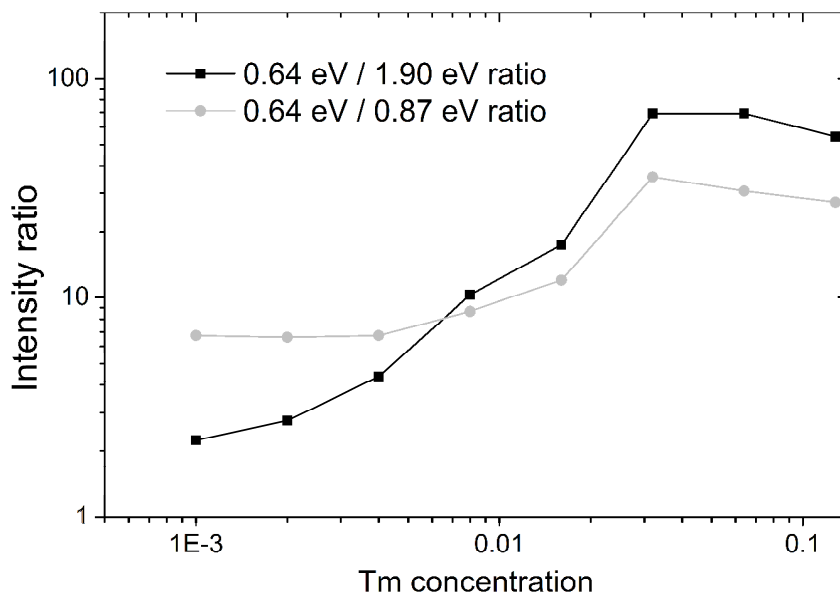


Figure 6.8: Intensity ratio of the 0.64 eV emission (${}^3F_4 \rightarrow {}^3H_6$) over the 1.90 eV emission (${}^1G_4 \rightarrow {}^3F_4$) in black and 0.87 eV emission (${}^3H_4 \rightarrow {}^3F_4$) in grey after 2.67 eV excitation (1G_4) as a function of the Tm concentration x in $La_{2-2x}Tm_{2x}BaZnO_5$.

The change in relative emission intensity with increasing Tm^{3+} concentration can be explained by cross-relaxation between the Tm^{3+} ions. From Figure 6.5 it can be seen that there is a strong overlap between the emission spectrum after 1G_4 excitation and the absorption spectrum. The ${}^1G_4 \rightarrow {}^3F_4$ emission overlaps with the ${}^3H_6 \rightarrow {}^3F_2$ absorption around 1.85 eV, the ${}^1G_4 \rightarrow {}^3H_5$ emission overlaps with the ${}^3H_6 \rightarrow {}^3H_4$ emission around 1.55 eV, the ${}^1G_4 \rightarrow {}^3H_4$ emission overlaps with the ${}^3H_6 \rightarrow {}^3H_5$ absorption around 1.05 eV and the ${}^1G_4 \rightarrow {}^3F_2$ emission overlaps with the ${}^3H_6 \rightarrow {}^3F_4$ absorption around 0.75 eV. Furthermore there is a small overlap between the ${}^3H_4 \rightarrow {}^3F_4$ emission and the ${}^3H_6 \rightarrow {}^3H_5$ absorption around 0.8 eV. Due to these different overlaps four non-trivial (i.e. the ones in which there is no complete energy transfer to another Tm^{3+} ion) cross-relaxations can take place between neighboring Tm^{3+} ions after excitation in the 1G_4 level. For example, as shown by mechanism 1 in Figure 6.9, the ${}^1G_4 \rightarrow {}^3F_2$ relaxation can result in the ${}^3H_6 \rightarrow {}^3F_4$ excitation of a neighboring Tm^{3+} ion, resulting in one Tm^{3+} ion excited in

the 3F_4 state and the other Tm^{3+} ion excited in the 3H_4 state, since an excited 3F_2 state will directly relax to the 3H_4 . From this 3H_4 state a second cross-relaxation can take place in which the ion relaxes to the 3F_4 , while another neighboring Tm^{3+} ion is also excited in the 3F_4 state. As a result, three Tm^{3+} ions can end up in the 3F_4 excited state after excitation of only one Tm^{3+} ion in the 1G_4 .

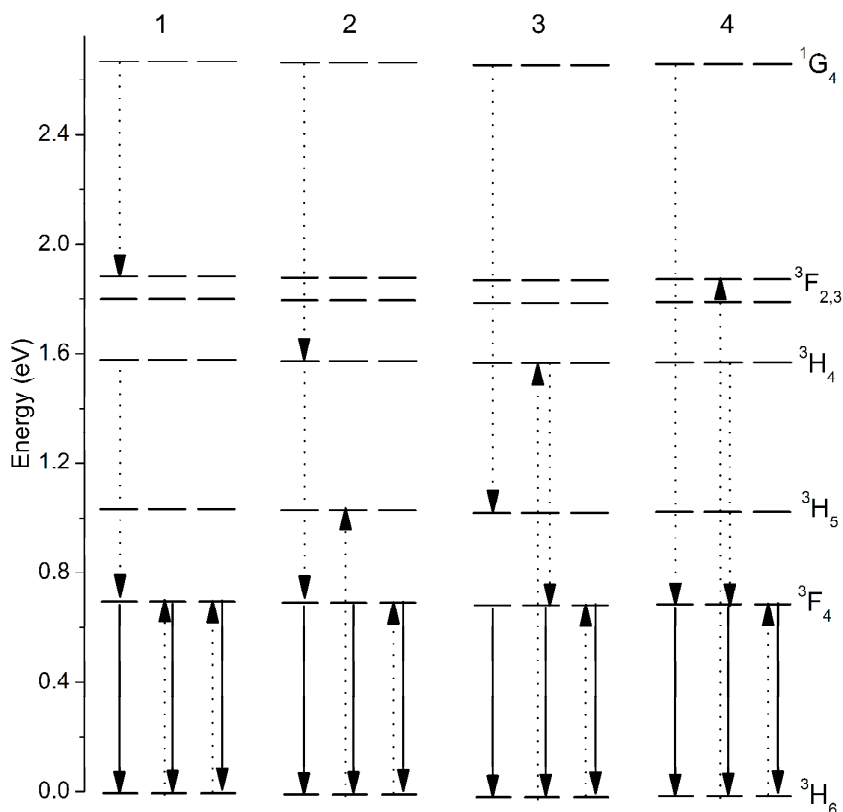


Figure 6.9: Four different cross-relaxation mechanisms between three Tm^{3+} ions resulting in quantum tripling.

As noted before the relaxation path described above is not the only way in which cross-relaxation between Tm^{3+} ions can occur. In the first step, instead of (${}^1G_4 \rightarrow {}^3F_2$) \times (${}^3H_6 \rightarrow {}^3F_4$) cross-relaxation (mechanism 1, Figure 6.9), (${}^1G_4 \rightarrow {}^3H_4$) \times (${}^3H_6 \rightarrow {}^3H_5$) cross-relaxation (mechanism 2) might also take place. However, excitation

in the ³H₅ state will result in relaxation to the ³F₄ state, so the final result after the first cross-relaxation step is the same: one ion excited in the ³H₄ state and the other ion in the ³F₄ state. Also the (¹G₄ → ³H₅) × (³H₆ → ³H₄) and the (¹G₄ → ³F₄) × (³H₆ → ³F₂) cross-relaxations, shown in Figure 6.9 by mechanisms 3 and 4 respectively, will give the same result.

With increasing Tm³⁺ concentration the average distance between Tm³⁺ ions will decrease and with it will the probability of cross-relaxation increase. However, as can be seen from Figure 6.8, the ³F₄ → ³H₆ emission is at a maximum in La_{1.936}Tm_{0.064}BaZnO₅. At higher Tm³⁺ concentrations, the ³F₄ → ³H₆ emission starts to decrease, which is attributed to concentration quenching. Although a high Tm³⁺ concentration favors cross-relaxation, it can also result in complete energy transfer between neighboring Tm³⁺ ions, referred to as energy migration over the Tm sublattice. Efficient migration increases the probability that a lattice defect center will be reached that quenches the luminescence. At the same time a higher Tm³⁺ concentration might also increase the number of defects that may act as quenching centers, since the Tm³⁺ ion is much smaller than the La³⁺ ion for which it substitutes.

It was noted before based on Figure 6.8 that the increase of ³F₄ emission relative to the ³H₄ emission is less strong as the increase relative to ¹G₄ emission. This can be explained using the cross-relaxation mechanisms shown in Figure 6.9. The emissions from the ³H₄ state decrease with increasing Tm³⁺ concentration as a result of the (³H₄ → ³F₄) × (³H₆ → ³F₄) cross-relaxation. However, due to several cross-relaxations involving the ¹G₄ state, the population of the ³H₄ state increases with increasing Tm³⁺ concentration. As a result, the decrease in emission from the ³H₄ is smaller than the decrease in ¹G₄ emission.

6.4 Conclusions

The Tm^{3+} concentration dependence of doped $\text{La}_2\text{BaZnO}_5$ shows an enhancement of $\text{Tm}^{3+} \ ^3\text{F}_4 \rightarrow \ ^3\text{H}_6$ emission with increasing Tm^{3+} concentration. This is due to four different cross-relaxation mechanisms that can take place between Tm^{3+} ions, resulting in the emission of three 1700 nm photons after the absorption of one 465 nm photon. This quantum tripling process makes Tm^{3+} doped phosphors interesting for increasing the efficiency of small band gap solar cells like germanium. However, the higher Tm^{3+} concentration also enhances concentration quenching, and thus limits the luminescence efficiency. In order to maximize the quantum tripling efficiency, one requires a material in which cross-relaxation between Tm^{3+} ions is efficient, but in which defect concentration is as low as possible in order to reduce concentration quenching. Another point that has to be addressed is the low absorption strength of the $\text{Tm}^{3+} \ ^1\text{G}_4$ level, which may be solved by using a sensitizing ion that strongly absorbs UV/blue light and transfers the energy to the $\text{Tm}^{3+} \ ^1\text{G}_4$ level.

6.5 References

- [1] W. Shockley, H.J. Queisser; *J. Appl. Phys.* 32 (1961) 510.
- [2] P. Vergeer, T.J.H. Vlugt, M.H.F. Kox, M.I. Den Hertog, J.P.J.M. van der Eerden, A. Meijerink; *Phys. Rev. B* 71 (2005) 014119.
- [3] O.M. ten Kate, M. de Jong, H.T. Hintzen, E. van der Kolk; *J. Appl. Phys.* 114 (2013) 084502.
- [4] A. Jaffrès, B. Viana, E. van der Kolk; *Chem. Phys. Lett.* 527 (2012) 42.
- [5] A. Sennaroglu, A. Kurt, G. Özen, *J. Phys.: Condens. Matter* 16 (2004) 2471.
- [6] Y.B. Shin, W.Y. Cho, J. Heo, *J. Non-Crystalline Solids* 208 (1996) 29.
- [7] S.D. Jackson, *Optics Communications* 230 (2004) 197.
- [8] P. Kubelka, F. Munk, *Z. Technische Physik* 12 (1931) 593.
- [9] C. Michel, L. Er-Rakho, B. Raveau, *J. Solid State Chem.* 42 (1982) 176.

[10] M.V. Abrashev, G.A. Zlateva, M.N. Iliev, M. Gyulmezov, Phys. Rev. B 49 (1994) 11783.

Chapter 7

Quantifying self-absorption losses in luminescent solar concentrators

The content of this chapter has been accepted for publication in Applied Optics as: O.M. ten Kate, K.M. Hooning, E. van der Kolk; “Quantifying self-absorption losses in luminescent solar concentrators”.

Analytical equations quantifying self-absorption losses in luminescent solar concentrators (LSCs) are presented that can easily be solved numerically by commercial math software packages. With the quantum efficiency, the absorption and emission spectra of a luminescent material and the LSC dimensions and refractive index as the only input parameters, the model gives an accurate account of the decrease of LSC efficiency due to self-absorption as a function of LSC radius, thickness and luminescence quantum efficiency. Results give insight in how many times light is reabsorbed and reemitted, the red shift of the emission spectrum, and on how multiple reabsorptions and reemissions are distributed over the LSC. When as an example case the equations are solved for a circular LSC containing a Lumogen F Red 305 dye with 80% luminescence quantum efficiency, it follows that for an LSC with 50 cm radius the self-absorption reduces the number of photons reaching the LSC edge by a factor of four compared to the case when there would be no self-absorption. Equations can just as well be solved for any material for which the optical properties are known like type I and type II quantum dots.

7.1 Introduction

A luminescent solar concentrator (LSC) reduces solar electricity costs by using a relatively inexpensive plate containing a luminescent material that absorbs solar light that enters the plate via its front surface. The luminescent material subsequently reemits the light at longer wavelengths. The reemitted light is largely trapped within the LSC plate due to its higher refractive index as compared to the surrounding air and is waveguided to the edges of the LSC where photovoltaic (PV) cells are attached. Since the area of these edges can be more than 100 times smaller than the area of the front surface that collects the solar light, less area of PV cells are needed. [1-3]

The quantum efficiency of an LSC depends on many different factors such as the light in-coupling efficiency, the light harvesting efficiency [4], the luminescence quantum efficiency [5], the light trapping efficiency [6] and the waveguide efficiency [7,8]. But one of the main factors limiting the overall LSC efficiency are losses associated with self-absorption. [9] For many luminescent materials considered for LSC applications, such as many organic dyes and luminescent quantum dots, a certain part of the emission spectrum overlaps with the absorption spectrum. This spectral overlap results in substantial reabsorption of the emitted light before the photons can reach the edges of the LSC where the PV cells are attached. And although reabsorption can again result in reemission, non-unity luminescence quantum efficiency and non-unity light trapping efficiency limit the fraction of light finally reaching the LSC-PV interface significantly. [4,7,10]

Batchelder et al. [11,12] described a way to quantify the self-absorption effects analytically. It was realized that self-absorption leads to different generations of luminescence since each reabsorption leads to reemission. A way was described to determine the reemission distribution over the LSC given the distribution of photons absorbed within the LSC. The set of equations was solved for the simplified case of a semi-infinite rod. Others, such as Olson [13], Sansregret [9], Sholin [14], Sahin [15], Wilson [5] and Kerrouche [16] calculated self-

absorption losses using a Monte Carlo simulation or ray-tracing approach. Chatten [17] and Fang [18] used a thermodynamic approach to describe self-absorption losses in luminescent solar concentrators. Sahin et al. [19] presented an analytical approach using a generalization of radiative transport theory. Their equations were solved numerically for a semi-infinite rectangular LSC and compared with Monte Carlo simulations.

In this work an analytical set of equations will be given which describe the self-absorption efficiency in a non-scattering circular LSC. As an example the equations will be solved numerically for a circular LSC plate containing a Lumogen F Red 305 dye which is equally distributed over the LSC. The sun light enters the LSC via its front surface and the solar cells are attached as a strip to the edge of the circular plate. The advantage of our analytical approach is that more insights can be obtained in the process, such as the self-absorption intensity as a function of the location in the LSC and the edge transmission per generation of emission. The derivation of the equations is split into two parts. At first, in section 7.2, equations that describe self-absorption in a flat circular LSC without any thickness (a 2D circular LSC) are derived. Secondly, in section 7.3, the procedure is repeated for a 3D circular LSC, taking the thickness of the LSC into account.

7.2 Self-absorption in a 2D circular LSC

7.2.1 Theory

The transmission of a light beam through a medium with absorption coefficient α is given by the Beer-Lambert law:

$$I(x) = I_0 e^{-\alpha x}. \quad (7.1)$$

Here is I_0 the original intensity and $I(x)$ the remaining intensity at a distance x travelled. $I(x)$ can also be interpreted as the remaining light intensity going through

a line segment dx located a distance x away from a point light source in case the light was emitted in one direction. In case of isotropic, circularly radiated point emission, the expression with x replaced by s corresponds to the light intensity going through a circle with radius s where the source point is located in the centre of the circle. The derivative of the equation with respect to s then gives the change in intensity as a function of s . The difference in intensity going through a circle with radius s and a circle with radius $s+ds$ then equals $-αI_0e^{-αs}ds$. The corresponding absorption per unit area $γ$ at a distance s from the emission center is therefore

$$\gamma = \frac{\alpha I_0 e^{-\alpha s}}{2\pi s}. \quad (7.2)$$

Consider a 2D circular LSC with radius R as shown in Figure 7.1, with initial emission distribution $\sigma_1(r',\varphi',\lambda)$ expressed in power per unit area per wavelength, which is a function of the location (r',φ') in the LSC and the wavelength λ of the emitted light. This emission will, as shown by equation 7.2, lead to an absorption dA in the infinitesimally small element $s d\xi ds$ in the LSC of

$$dA = \frac{\alpha(\lambda)\sigma_1(r',\varphi',\lambda)e^{-\alpha(\lambda)s}}{2\pi} d\xi ds. \quad (7.3)$$

Integrating this expression over all absorption positions (s,ξ) on the LSC and subsequently integrating over all emission points (r',φ') yields the total absorption $A_1(\lambda)$ in the LSC of all light emitted within the LSC:

$$A_1(\lambda) = \frac{\alpha(\lambda)}{2\pi} \int_0^R \int_0^{2\pi} \int_{\xi_{\min}}^{\xi_{\max}} r' \sigma_1(r',\varphi',\lambda) e^{-\alpha(\lambda)s} d\xi ds d\varphi' dr'. \quad (7.4)$$

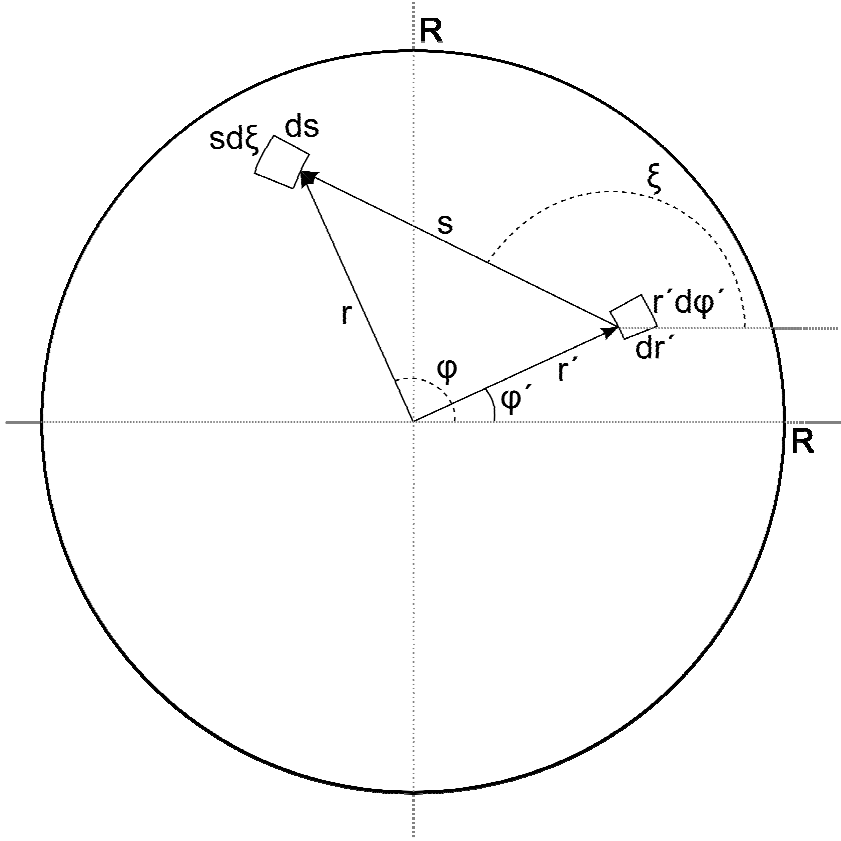


Figure 7.1: Schematic representation of light emitted in a 2D circular LSC from a surface element located at position (r', φ') with respect to the center of the circle, that is subsequently reabsorbed in a surface element located at position (s, ξ) with respect to the emission point and located at position (r, φ) with respect to the center of the circle.

By applying standard geometric relations the variables s and ξ can be expressed as a function of r' , φ' , r and φ . The integrals over s and ξ can therefore be replaced by integrals over r and φ , resulting in

$$A_1(\lambda) = \frac{\alpha(\lambda)}{2\pi} \int_0^R \int_0^{2\pi} \int_0^R \int_0^{2\pi} -r' \sigma_1(r', \varphi', \lambda) e^{-\alpha(\lambda)s} d\varphi dr d\varphi' dr' . \quad (7.5)$$

With:

$$s = \sqrt{r^2 + (r')^2 - 2rr' \cos(\varphi - \varphi')} . \quad (7.6)$$

Consequently, the reabsorption per unit area $\gamma_1(r, \varphi, \lambda)$ at a point (r, φ) in the LSC equals

$$\gamma_1(r, \varphi, \lambda) = \frac{\alpha(\lambda)}{2\pi} \int_0^R \int_0^{2\pi} \frac{r'}{s} \sigma_1(r', \varphi', \lambda) e^{-\alpha(\lambda)s} d\varphi' dr' . \quad (7.7)$$

The reabsorption per unit area can thus be calculated if the initial emission distribution σ_1 is known. Next, the reemission per unit area σ_2 can be determined given this reabsorption per unit area.

$$\sigma_2(r, \varphi, \lambda) = \frac{\Phi_{em}(\lambda)}{\lambda} \int_0^\infty \lambda \eta_{LQE} \gamma_1(r, \varphi, \lambda) d\lambda . \quad (7.8)$$

Here is η_{lqe} the luminescence quantum efficiency and Φ_{em} the normalized photon emission spectrum, which is equal to

$$\Phi_{em} = \frac{\sigma_1(\lambda)}{\int_0^\infty \sigma_1(\lambda) d\lambda} . \quad (7.9)$$

The so obtained reemission distribution can then be used to determine the next reabsorption γ_2 and so on.

Note that as a result of the fact that a 2D luminescent plate is considered, any escape cone losses, which are an important loss factor after each emission in any real 3D device, are not included. Therefore, in order to obtain any meaningful results from this 2D approach, the emission distribution σ should be multiplied by a light trapping efficiency η_{trap} in equation (7.7) in order to consider only those photons that are not emitted within the two escape cones. This trapping efficiency depends on the refractive index n of the LSC and is equal to:

$$\eta_{trap} = \sqrt{1 - \frac{1}{n^2}}. \quad (7.10)$$

All photons that are emitted outside the escape cones and that are not reabsorbed will reach the edges of the LSC. This edge transmission per generation i is thus given by

$$T_i(\lambda) = \eta_{trap} \int_0^R \int_0^{2\pi} \sigma_i r' d\phi' dr' - \eta_{trap} A_i(\lambda). \quad (7.11)$$

The total edge transmission per generation is now given by the integral of T_i over all wavelengths and the overall edge transmission is the total sum of all T_i over all generations i .

Note that the equations mentioned above do not take into account any scattering losses within the LSC. However, the same model might be applied to describe elastic light scattering within the LSC by considering scattering as absorption followed by reemission at the same wavelength. In that case the absorption coefficient α in equation (7.1) should be replaced by a scattering coefficient.

7.2.2 Results

The equations mentioned above can now be used to calculate the self-absorption losses in a 2D circular LSC. As an example a PMMA LSC doped with a Lumogen F Red 305 dye with a concentration of 115 ppm is considered with the absorbance and emission intensity as determined by Desmet et al. [20] and shown in Figure 7.2. The results per generation for an LSC with a radius of 50 cm and a refractive index of 1.5 are shown in Table 7.1. Although the luminescence quantum efficiency of the Red 305 dye is closer to 100% [5], an efficiency of 80% has been used in the calculations in order to show the effect of non-unity luminescence quantum efficiency on self-absorption losses. Hence that many dyes do not have 100% luminescence quantum efficiency.

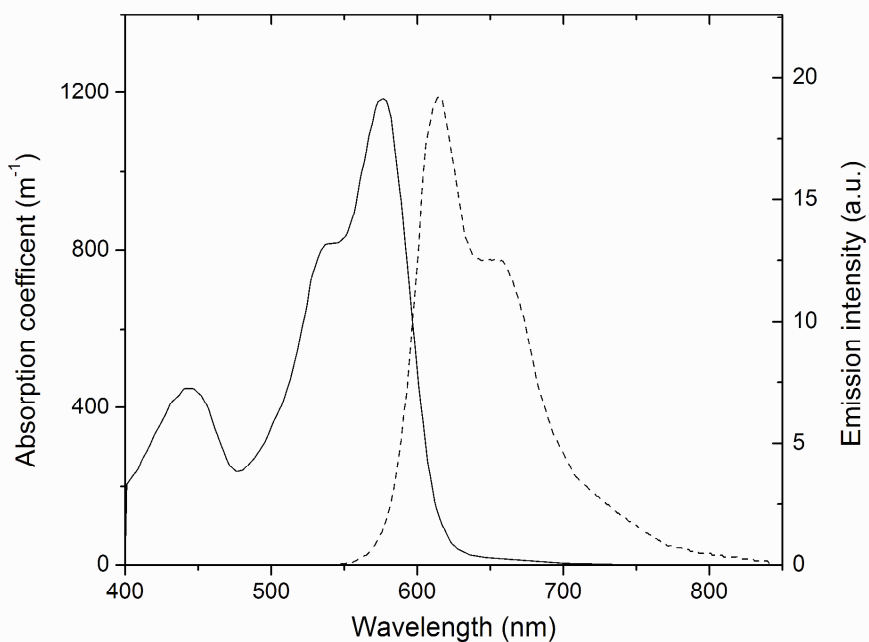


Figure 7.2: Absorption coefficient (straight line) and emission spectrum (dashed line) of a PMMA plate doped with 115 ppm Lumogen F Red 305 dye. [20]

As can be seen from Table 7.1, after 8 generations of emission and absorption only 0.6% of the initial amount of absorbed photons is still present in the LSC and can be emitted a 9th time. The results after 8 generations will therefore be close to the results obtained after an infinite number of generations. After these 8 generations 15.2% of the initial number of absorbed photons has reached the edges of the LSC. In case there would be no self-absorption this would be 59.6% of the initially absorbed photons. The difference is due to two loss factors. Due to self-absorption the total losses via the escape cones account for 42.4% of the initially absorbed photons, as compared to 20.4% when there would be no self-absorption. The other loss-factor is the non-unity luminescence quantum efficiency, which results in a difference between the number of photons absorbed in generation i and the number of photons emitted in generation $i+1$. These losses account for 41.8% of the initially absorbed photons, instead of 20% when there would be no self-absorption.

Table 7.1: Fraction of the number of photons per generation i that are emitted f_{em} , lost via the escape cones f_{esc} , absorbed f_{abs} and transmitted to the LSC-PV interface f_{trans} with respect to the initial number of absorbed photons in a circular 2D LSC with $R = 50$ cm with a Red 305 dye with $n = 1.5$ and $\eta_{LOE} = 0.8$.

i	f_{em} (%)	f_{esc} (%)	f_{abs} (%)	f_{trans} (%)
1	80.0	20.4	52.3	7.3
2	41.8	10.6	27.3	3.9
3	21.8	5.6	14.3	1.9
4	11.4	2.9	7.5	1.0
5	6.0	1.5	4.0	0.5
6	3.2	0.8	2.1	0.3
7	1.7	0.4	1.1	0.2
8	0.9	0.2	0.6	0.1
Total		42.4		15.2

In Figure 7.3 the total transmitted fraction with respect to the initial number of absorbed photons is shown for different luminescence quantum efficiencies as a function of the radius of the 2D LSC. The transmitted fraction decreases by half when the radius increases from 0.1 to 0.5 m. At even larger radii the transmitted fraction further decrease, but less significantly. The reason for this is that the self-absorption does only have effect on the emission wavelengths that can be reabsorbed and does not influence the photons emitted at longer wavelengths. For these photons the radius is unimportant, since the long wavelength photons will reach the LSC edge anyway.

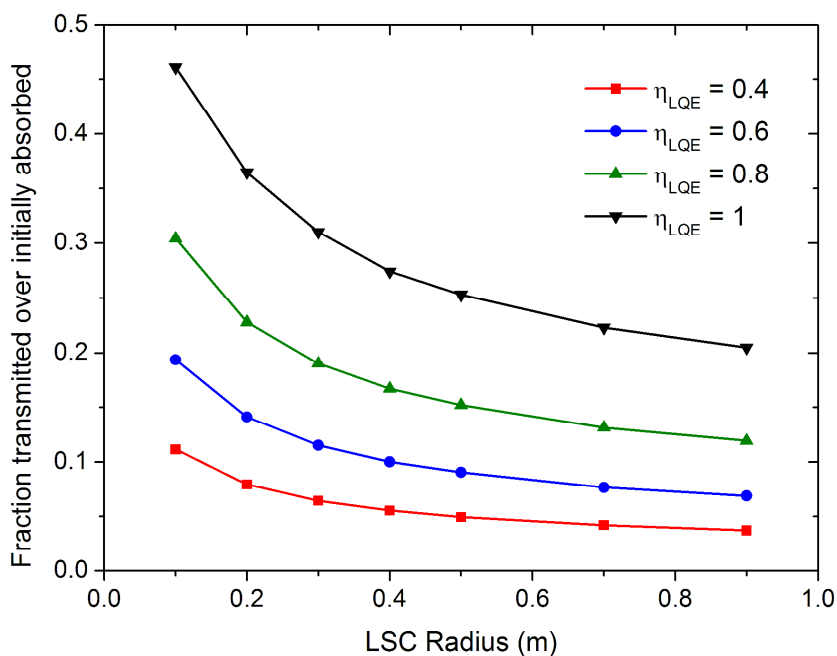


Figure 7.3: Fraction of the number of photons transmitted to the LSC edge with respect to the initial number of absorbed photons as a function of the LSC radius for a 2D circular LSC with a Red 305 dye for different luminescence quantum efficiencies (η_{LQE}).

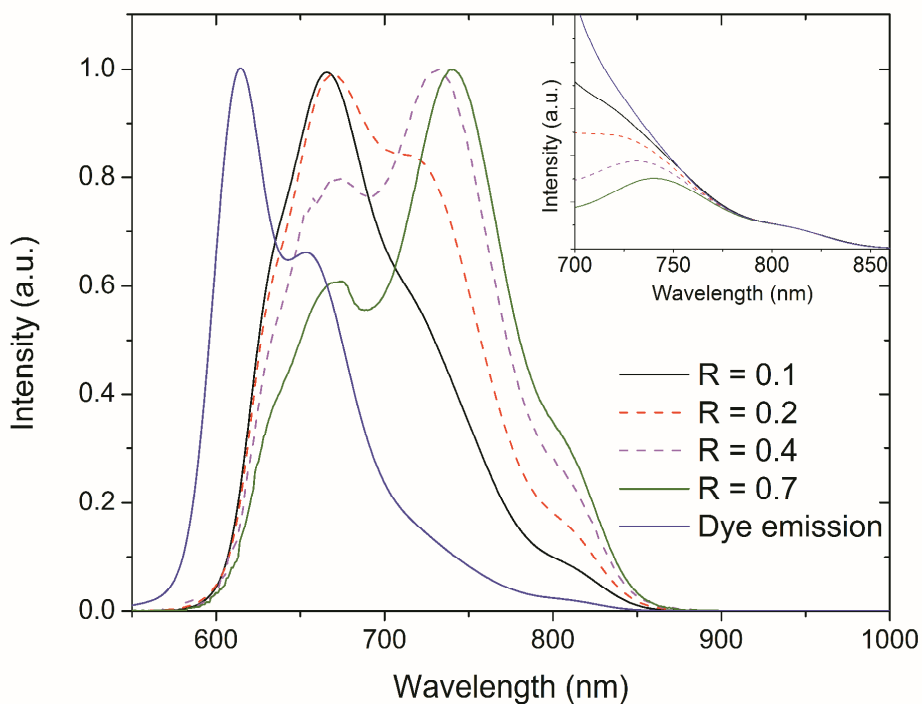


Figure 7.4: Dye emission spectrum and edge transmission spectra for 2D circular LSCs with different radii containing a Red 305 dye with 100% luminescence quantum efficiency. In the main graph, the spectra are normalized on the highest peak, while in the inset the same spectra are normalized on the long wavelength side at 815 nm.

In Figure 7.4 the normalized emission spectra of transmitted radiation for LSCs with different radii are shown together with the original emission spectrum of the dye. The larger the radius of the LSC, the more red-shifted the emission is. The cause of this red-shift is that short wavelength light emitted by the dye is mostly reabsorbed in the LSC, while the longer wavelength light is not reabsorbed. This results in relatively more longer wavelength light that reaches the edges of the LSC as compared to short wavelength light. Larger LSCs have an on average longer photon travel distance, resulting in more reabsorption and thus a larger red-shift. The average emission wavelength increases from about 640 nm for the dye

emission spectrum to 680 nm, 700 nm and 715 nm for the edge transmission of an LSC with a radius of 0.1 m, 0.2 m and 0.4 m respectively. Note that the shape of the edge transmission spectra at the long wavelength side is the same as the shape of the emission spectrum of the dye, as is shown in the inset of Figure 7.4, since these wavelengths are not absorbed.

7.3 Self-absorption in a 3D circular LSC

7.3.1 Theory

Although the 2D model gives nice insights in processes associated with self-absorption losses, it is a simplification as light emission is assumed to be circular instead of spherical. As a result the distance a photon needs to travel through the LSC is underestimated. If a photon is emitted under an angle θ with respect to the line normal to the LSC plain, it actually needs to travel a distance $\hat{s} = s / \sin(\theta)$ to cover a distance s in the LSC plain, as shown in Figure 7.5.

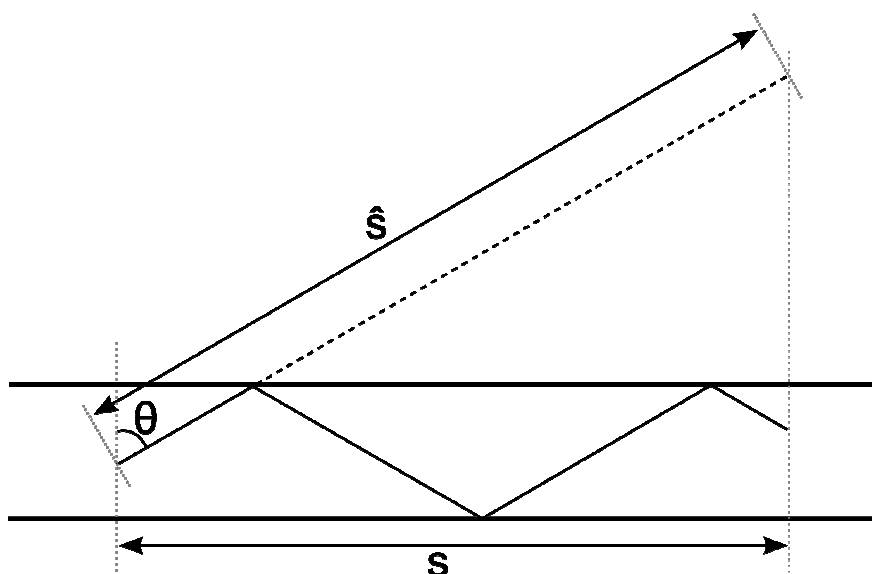


Figure 7.5: Directional light transport in a 3D LSC.

To account for the extra travel distance in three dimensions, a 3D version of the 2D model from section 7.2.1 is derived. In this 3D approach the LSC can still be treated as a 2D plate (in fact a 2D projection) but now with the path length of the light based on three dimensions. This can be done because the distance that a photon needs to travel before it reaches the LSC edge is independent of the depth within the LSC where the photon is emitted, and also the size of the escape cone, the absorption probability, and the luminescence quantum efficiency are independent of the depth within the LSC.

Comparable to equation (7.2) for the 2D case, the absorption per unit volume δ at a distance \hat{s} from the emission center is given by

$$\delta = \frac{\alpha I_0 e^{-\alpha \hat{s}}}{4\pi \hat{s}^2}. \quad (7.12)$$

The absorption per unit area γ in the LSC plain now corresponds to the integral over all absorptions in the volume elements located in the column that is bounded by the critical angles θ_c and $\pi - \theta_c$ and has a cross-section $r dr d\phi$. Comparable to equation (7.5) the total reabsorption for generation i in a 3D circular LSC of all emitted light in the LSC is given by

$$A_i(\lambda) = \frac{\alpha(\lambda)}{4\pi} \int_0^R \int_0^{2\pi} \int_0^R \int_{\theta_c}^{\pi-\theta_c} \int_0^s \frac{r}{s} r' \sigma_i(r', \phi', \lambda) e^{-\alpha(\lambda)s/\sin\theta} d\theta d\phi dr d\phi' dr'. \quad (7.13)$$

This results in an absorption per unit area for generation i of

$$\gamma_i(\lambda) = \frac{\alpha(\lambda)}{4\pi} \int_0^R \int_0^{2\pi} \int_{\theta_c}^{\pi-\theta_c} \frac{r'}{s} \sigma_i(r', \phi', \lambda) e^{-\alpha(\lambda)s/\sin\theta} d\theta d\phi' dr'. \quad (7.14)$$

Note that in the 3D approach the trapping efficiency η_{trap} is already accounted for in the reabsorption calculations as the integrals over θ range from θ_c to $\pi - \theta_c$. Similar to equation (7.11) the edge transmission for a 3D LSC is given by

$$T_i(\lambda) = \eta_{trap} \int_0^R \int_0^{2\pi} \sigma_i(r', \varphi', \lambda) r' d\varphi' dr' - A_i(\lambda). \quad (7.15)$$

It should be noted that the equations above do not include any thickness of the LSC. The reason for this is that the travel distance of a photon to the LSC edge is independent of the LSC thickness. As a result, the amount of photons reaching the edge does not change with LSC thickness. However, this last statement is not completely true because the escape cone losses slightly depend on the LSC thickness, as will be discussed in section 7.3.3.

Table 7.2. Fraction of the number of photons per generation i that are emitted f_{em} , lost via the escape cones f_{esc} , absorbed f_{abs} and transmitted to the LSC-PV interface f_{trans} with respect to the initial number of absorbed photons in a circular 3D LSC with $R = 50$ cm with Red 305 dye with $n = 1.5$ and $\eta_{LOE} = 0.8$.

i	f_{em} (%)	f_{esc} (%)	f_{abs} (%)	f_{trans} (%)
1	80.0	20.4	52.7	6.9
2	42.2	10.7	27.7	3.8
3	22.2	5.7	14.6	1.9
4	11.7	3.0	7.7	1.0
5	6.2	1.6	4.1	0.5
6	3.3	0.8	2.2	0.3
7	1.8	0.5	1.2	0.1
8	1.0	0.3	0.6	0.1
Total		43.0		14.6

7.3.2 Results

The results for the 3D circular LSC with a radius of 50 cm, containing the same Red 305 dye as used for the 2D case with 80% luminescence quantum efficiency, are shown in Table 7.2. The fraction of photons absorbed in each generation is a bit larger as compared to the results for the 2D model shown in Table 7.1. This is due to the on average longer travel distance to the LSC-PV edge in three dimensions, which is not taken into account in the 2D model. As a consequence, the total transmission over all generations is somewhat smaller in the 3D model as compared to the 2D model: 14.6% instead of 15.2%. Note however that this difference is only small and that the 2D case thus gives a relatively good approximation.

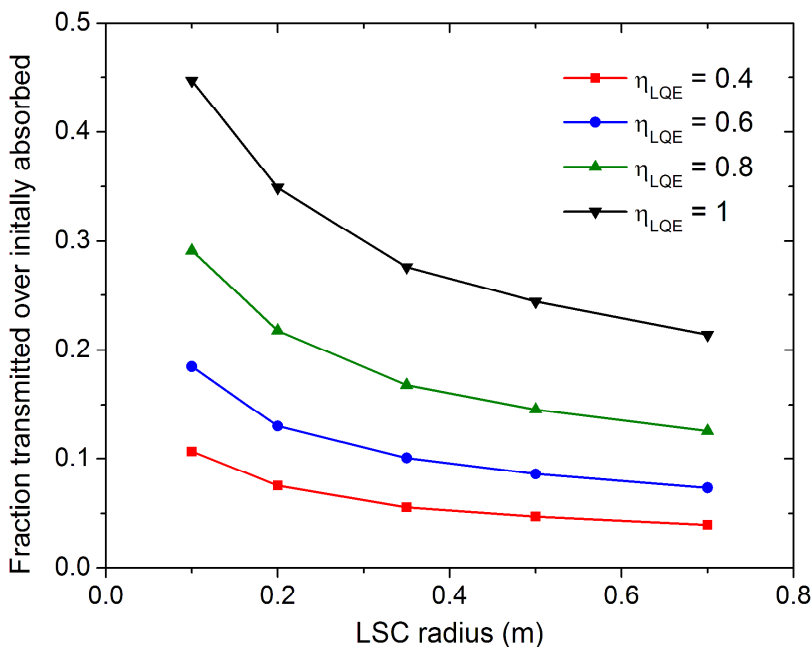


Figure 7.6: Fraction of the number of photons transmitted to the LSC edge with respect to the initial number of absorbed photons as a function of the LSC radius for a 3D circular LSC with a Red 305 dye for different luminescence efficiencies.

Note that without self-absorption the transmitted fraction would be 59.6% if the luminescence quantum efficiency is 80%, similar as for the 2D LSC (section 7.2.2) because in the absence of self-absorption the amount of photons reaching the edge is independent of the travel distance. Hence that we do not consider scattering or parasitic absorption. This means that for an LSC with a radius of 0.5 m the efficiency would be reduced by a factor of 4.

In Figure 7.6 the fractions of photons transmitted to the LSC edge are shown as a function of the radius of the 3D LSC for different luminescence quantum efficiencies. The trend is similar as for the 2D case shown in Figure 7.3, but the transmitted fractions are slightly smaller as explained before.

The initial photon absorption distribution within the LSC and the absorption distribution after three subsequent generations of reemission and reabsorption are shown in Figure 7.7 for an LSC with a radius of 0.5 m and 80% luminescence quantum efficiency. As can be seen, the number of photons that are absorbed per surface area remains almost constant over the first 40 cm from the center of the LSC. Only near the edge of the LSC the absorption density is lower. This effect can be explained as follows: the initial emission distribution is constant over the LSC. In that case all positions more than 10 cm away from the LSC edge receive the same amount of light, as if the LSC is infinitely large. This is because photons that will be reabsorbed are very likely to be absorbed within 10 cm from the point of emission, since for most of these photons the absorption coefficient is much larger than 1 m^{-1} . Only near the edges the absorption density is lower, because these points do not receive light from points beyond the LSC edge.

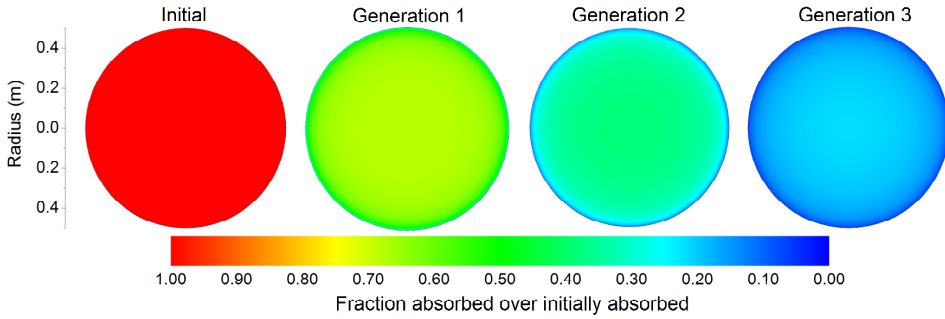


Figure 7.7: Distribution of the number of absorbed photons (initial and after the first three generations) with respect to the initial number of absorbed photons as a function of the distance and angle to the LSC center for a 3D circular LSC with a radius of 0.5 m and 80% luminescence quantum efficiency.

7.3.3 Cone angle absorption

In the derivation for the self-absorption in a 3D LSC in section 7.3.1 it has been assumed that all photons emitted within the two escape cones will be lost and that only the photons emitted outside these cones will be trapped. However, this is not entirely true in case of self-absorption due to cone angle absorption: a photon emitted within the escape cone has a certain chance of being reabsorbed before it can escape from the LSC plate. And since this reabsorption also results in reemission randomly in all directions, a certain fraction of these reemitted photons is trapped and attributes to the second generation of emission. As a result the edge transmission fractions shown in Figure 7.6 are slightly underestimated. One can however correct for this underestimation by including correction factors for the absorption into the equations.

The chance for a photon of being reabsorbed before reaching the LSC surface is a function of the depth z of the emission point within the LSC and the angle of emission θ with respect to a line perpendicular to the LSC surface. For emission within an LSC with thickness h originating from a point (z', r', ϕ') with

emission intensity per unit volume τ_i the total cone angle absorption $\gamma_{ca,i}$ due to emission at point (r',φ') in the LSC plain is equal to

$$\gamma_{ca,i}(r',\varphi',\lambda) = \frac{1}{h} \int_0^h \int_0^\theta \tau_i(r',\varphi',\lambda) (1 - e^{-\alpha(\lambda)z/\cos\theta}) \sin\theta d\theta dz. \quad (7.16)$$

Note that equation (7.16) is not exactly true for the case in which a photon is emitted within the escape cone close to the edge of the PV-LSC interface. Some of these photons will be able to reach this PV-LSC interface and are thus not absorbed within the LSC. However, due to the very small thickness of the LSC with respect to the radius of the LSC (about a factor 100 to 1000) these effects account for much less than 1% of the cone angle absorption and can safely be neglected.

Since the radius of the LSC is much larger than the thickness, the point of emission (r',φ') is very close to the point of absorption (r,φ) within the escape cone. As a result the total cone angle absorption due to emission originating from the point (r',φ') is approximately equal to the total absorption in the point $(r=r',\varphi=\varphi')$ due to cone angle emission from neighboring points in the LSC plain. The cone angle correction factor for the absorption $\gamma_{ca,i}(r,\varphi,\lambda)$ is therefore given by equation (7.16). This correction factor can now be added to the original absorption γ_i (equation (7.14)) and be used to calculate a new emission and a new edge transmission.

The results for a 3D circular LSC with a radius of 0.5 m and a η_{LQE} of 80% are shown in Table 7.3. Without taking into account the cone angle absorption the transmitted fraction would be 14.6% of the initially absorbed photons. This number increases to 14.7% for an LSC with a thickness of 0.1 mm and to 16.4% for an LSC thickness of 5 mm. So, for relatively thick LSCs this contribution should be included in the calculations. Note that, although Table 7.3 seems to suggest that the self-absorption losses can be reduced by using thicker LSCs, this is only partly true. In a thicker LSC the cone angle losses in each generation of emission are reduced. However, if the η_{LQE} is not 100%, each reemission step is still associated with losses due to a non-unity η_{LQE} . Furthermore, the transmitted fractions shown in

Table 7.3 are still far-off from the 59.6% that would be achieved when there is no self-absorption.

Table 7.3: Fraction of the number of photons that are transmitted to the LSC-PV interface f_{trans} with respect to the initial number of absorbed photons in a circular 3D LSC with $R = 50$ cm with a Red 305 dye with $n = 1.5$ and $\eta_{LQE} = 0.8$, when cone angle absorption is taken into account.

h (mm)	f_{trans} (%)
0.1	14.7
0.5	14.9
1	15.2
3	15.9
5	16.4

7.4 Conclusions

An analytical model has been presented with which the effects of self-absorption in a luminescent solar concentrator can be described. The equations only require the absorption and emission spectra and the quantum efficiency of the concerning dye and the LSC dimensions and refractive index as input parameters and can be solved easily using standard commercial math software, as opposed to more elaborate ways of modeling self-absorption, such as Monte Carlo simulations. In this work the model has been used to describe self-absorption by a Red 305 dye as an example, but the model is applicable to any other luminescent material of which the absorption and emission spectrum are known, such as type I and type II quantum dots. By doing this, insight is obtained not only on the efficiency losses due to self-absorption, but also on the absorption and emission distribution of the light within the LSC as a function of LSC size and thickness and luminescence quantum efficiency. The calculations may furthermore be extended with equations

describing other losses within a luminescent solar concentrator, such as light scattering.

7.5 References

- [1] M.G. Debije, P.C. Verbunt; *Adv. Energ. Mater.* 2 (2012) 12.
- [2] B.C. Rowan, L.R. Wilson, B.S. Richards; *IEEE J. Sel. Top. Quantum Electron.* 14 (2008) 1312.
- [3] W.G.J.H.M. van Sark, K.W.J. Barnham, L.H. Slooff, A.J. Chatten, A. Büchtemann, A. Meyer, S.J. McCormack, R. Koole, D.J. Farrell, R.H. Bose, E.E. Bende, A.R. Burgers, T. Budel, J. Quilitz, M. Kennedy, T. Meyer, C. De Mello Donegá, A. Meijerink, D. Vanmaekelbergh; *Optics Express* 16 (2008) 21773.
- [4] T. Diemel, C. Bauer, I. Dolamic, D. Brühwiler; *Sol. Energy* 84 (2010) 1366.
- [5] L.R. Wilson, B.S. Richards; *Appl. Opt.* 48 (2009) 212.
- [6] A. Goetzberger, W. Greubel; *Appl. Phys.* 14 (1977) 123.
- [7] A.A. Earp, G.B. Smith, P.D. Swift, J. Franklin; *Sol. Energy* 76 (2004) 655.
- [8] J.W.E. Wiegman, E. van der Kolk; *Sol. Energy Mater. Sol. C.* 103 (2012) 41.
- [9] J. Sansregret, J.M. Drake, W.R.L. Thomas, M.L. Lesiecki; *Appl. Opt.* 22 (1983) 573.
- [10] T. Wang, B. Yu, B. Chen, Z. Hu, Y. Luo, G. Zou, Q. Zhang; *J. Opt.* 15 (2013) 055709.
- [11] J.S. Batchelder, A.H. Zewail, T. Cole; *Appl. Opt.* 18 (1979) 3090.
- [12] J.S. Batchelder, A.H. Zewail, T. Cole; *Appl. Opt.* 20 (1981) 3733.
- [13] R.W. Olson, R.F. Loring, M.D. Fayer; *Appl. Opt.* 20 (1981) 2934.
- [14] V. Sholin, J.D. Olson, S.A. Carter; *J. Appl. Phys.* 101 (2007) 123114.
- [15] D. Sahin, B. Ilan; *J. Appl. Phys.* 110 (2011) 033108.
- [16] A. Kerrouche, D.A. Hardy, D. Ross, B.S. Richards; *Sol. Energy Mater. Sol. C.* 122 (2014) 99.
- [17] A.J. Chatten, K.W.J. Barnham, B.F. Buxton, N.J. Ekins-Daukes, M.A. Malik; *Sol. Energy Mater. Sol. C.* 75 (2003) 363.

- [18] L. Fang, T.S. Parel, L. Danos, T. Markvart; J. Appl. Phys. 111 (2012) 076104.
- [19] D. Sahin, B. Ilan; J. Opt. Soc. Am. A 30 (2013) 813.
- [20] L. Desmet, A.J.M. Ras, D.K.G. de Boer, M.G. Debije; Opt. Lett. 37 (2012) 3087.

Chapter 8

Tm²⁺ doped materials for luminescent solar concentrators without self-absorption

The content of this chapter has been submitted, in a modified form, to Advanced Energy Materials as: O.M. ten Kate, K.W. Krämer, E. van der Kolk; “Self-absorption free, ultra broad-band absorbing, colorless, Tm²⁺ doped halides for highly efficient luminescent solar concentrators”.

Tm²⁺ doped luminescent halides (NaCl, NaBr, NaI, KBr and CaI₂) of which the optical properties are suited to obtain luminescent solar concentrators (LSCs) without self-absorption are reported. The materials strongly absorb solar light from the UV up to as far 900 nm due to $4f^{13} \rightarrow 4f^{12}5d^1$ transitions of Tm²⁺. The absorption is followed by relaxation to the Tm²⁺ ²F_{5/2} excited state of the 4f¹³ configuration, which leads to an intense narrow emission line centered at 1140 nm. The Stokes shift of the emission is sufficiently large to prevent self-absorption of the emitted light. The Tm²⁺ doped halides might therefore be of interest to obtain efficient colorless tinted power windows.

8.1 Introduction

In a luminescent solar concentrator (LSC) luminescent materials integrated in a window capture and reemit solar light and waveguide this light to the edges of the window where solar cells are attached. Since the area of the edge of a window is much smaller than its front surface, light concentrating means that much less of expensive photovoltaic (PV) material is needed to harvest the same amount of solar light as compared to a standard solar panel. An interesting application is that an

LSC can be integrated as a semi-transparent window in for example office buildings. [1] LSCs should therefore in the first place be considered as building-integrated concentrated photovoltaic (BI-CPV) technology.

Although the LSC concept dates back from the late 1970s [2-4], any successful commercial implementation has not yet been realized, since it has proven to be difficult to find adequate luminescent materials that fulfill all necessary properties to efficiently concentrate solar light: absorption of a broad range of the solar spectrum, reemission of the absorbed light with high luminescence quantum efficiency, and efficient light transport to the solar cells with no reabsorption or scattering.

The luminescent materials that have been considered as LSC materials, such as the organic dyes Rhodamine 6G [5] and Red 305 [6], have strong absorption bands and high luminescence quantum efficiency. However, these dyes do not absorb the entire visible spectrum, resulting in colored windows. But even more important, there is a spectral overlap between the absorption and emission spectra of the dyes. As a result light emitted in one part of the LSC will be reabsorbed by the dye itself in another part of the LSC before the light reaches the solar cells. Since reabsorption will also lead to reemission, this self-absorption is not a loss factor on its own. However, since each reemission step is associated with non-unity luminescence quantum efficiency and trapping losses due to emission within the escape cone, the amount of light finally reaching the solar cells is significantly reduced as a result of self-absorption. As an example, the efficiency of a 1 m² LSC containing a Red 305 dye is reduced by a factor of four due to self-absorption (see chapter 7). [7]

In many thulium doped compounds, of which many oxides, the thulium ion is present in the trivalent state. Tm³⁺ is optically recognized by the presence of several narrow Tm³⁺ 4*f*-4*f* absorption lines in the infrared, visible and UV part of the spectrum. In some compounds however, such as SrB₄O₇ [8,9], SrB₆O₁₁ [10], CaF₂ [11], SrCl₂ [11] and CsCaI₃ [12,13], the thulium ion is stable in the divalent state. This Tm²⁺ ion gives rise to only one typical 4*f*-4*f* absorption line around 1140 nm due to the ²F_{7/2} → ²F_{5/2} transition. At higher energies strong Tm²⁺ absorption

bands are present due to $4f^{13} \rightarrow 4f^{12}5d^1$ transitions, of which the energy depends on the crystalline environment.

In this work the synthesis and optical properties of Tm²⁺ doped halides (NaCl, NaBr, NaI, KBr and CaI₂) are reported of which the lowest Tm²⁺ $4f^{12}5d^1$ state is located just above the ²F_{5/2} state of the $4f^{13}$ configuration. Therefore, excitation in the $5d$ bands of Tm²⁺ results in relaxation to the ²F_{5/2} state, which is followed by ²F_{5/2} → ²F_{7/2} emission around 1140 nm instead of Tm²⁺ $5d-4f$ emission. As a result these Tm²⁺ based compounds are able to strongly absorb visible light via $4f-5d$ transitions and efficiently reemit light via a narrow $4f-4f$ transition around 1140 nm that can only be reabsorbed very weakly. Based on these results, the applicability of these materials for luminescent solar concentrators is discussed.

8.2 Experimental

8.2.1 Synthesis

The Tm doped halides were synthesized via two different methods. For the first method NaBr (Sigma-Aldrich, 99.995%), NaI (Sigma-Aldrich, 99.999%) or KBr (Pike Technologies) were mixed in the preferred molar ratio with TmI₂ (Sigma-Aldrich, 99.9%) in a nitrogen filled glove-box. The mixtures were then put in a quartz ampoule and connected to a vacuum pump without intermediary contact with the air. While under vacuum, the ampoules were rapidly heated to a temperature above the melting point of the sample. When the samples were fully melted, heating was stopped. When cooled down, the ampoules were opened inside a glove-box. The samples were crunched to powder before further characterization.

For method 2, used for the CaI₂:Tm and NaCl:Tm synthesis, NaCl (Merck) or CaI₂ were mixed inside a glove-box together with TmCl₃ (in case of NaCl) or TmI₃ (in case of CaI₂) and an excess of Tm metal. The mixtures were put in tantalum ampoules, which were then sealed by arc-welding and enclosed inside a glass ampoule under inert atmosphere. The ampoules were then heated in a furnace

to a temperature of 830 °C for 24 hours and gradually (8 °C/hour) cooled down. As with the samples prepared via the previous method, the samples were crunched to powder before further characterization.

8.2.2 Characterization

Diffuse reflectance spectra were recorded with a Bruker Vertex 80v FT interferometer, using a tungsten lamp as a light source and cooled InGaAs, Si and GaP detectors. KBr was taken as a reference. Excitation and emission measurements were recorded with a Hamamatsu H10330A-75 NIR PMT with two double grating monochromators using a xenon lamp as a light source.

8.3 Results and discussion

8.3.1 Absorption

In Figure 8.1 the Kubelka-Munk [14] absorption spectra of the Tm doped CaI₂ samples for different Tm concentrations are shown. Above 900 nm the samples do not absorb any light, except for a weak absorption line with a maximum at 1140 nm. This absorption feature, of which the intensity increases with increasing Tm concentration, is the typical $4f-4f$ transition of Tm²⁺ from the ²F_{7/2} ground state to the ²F_{5/2} excited state.

Above 900 nm, several strong absorption bands can be observed, of which the intensity also increases with increasing Tm concentration. These bands can be assigned as the Tm²⁺ $4f-5d$ absorption bands. The $4f^{12}5d^1$ electronic configuration of Tm²⁺ is split as a result of several interactions. The crystal field splitting of the $5d$ electron splits the $5d$ orbitals depending on the site symmetry. CaI₂ crystallizes in the $P-3m1$ (164) space group. If the Tm²⁺ ion is substituted on the Ca²⁺ site in the lattice, the ion is in an octahedral environment with 6-fold coordination with site symmetry D_{3d} [15], which is a distortion from full octahedral symmetry. An

additional splitting within the $4f^{12}5d^1$ configuration arises due to Coulomb repulsion and spin-orbit coupling within the $4f^{12}$ electronic configuration into the $2S+1L_J$ terms, which are similar to the Tm^{3+} multiplets of the Dieke [16] diagram. The energy separation between the lowest energy term (3H_6) and the next term (3F_4) should be about 6000 cm^{-1} . A third splitting due to Coulomb repulsion of the $4f$ and $5d$ electrons results in low-spin and high-spin states, of which the latter ones are at lower energy in Tm^{2+} and usually very weak due to the spin-forbidden nature of the transition.

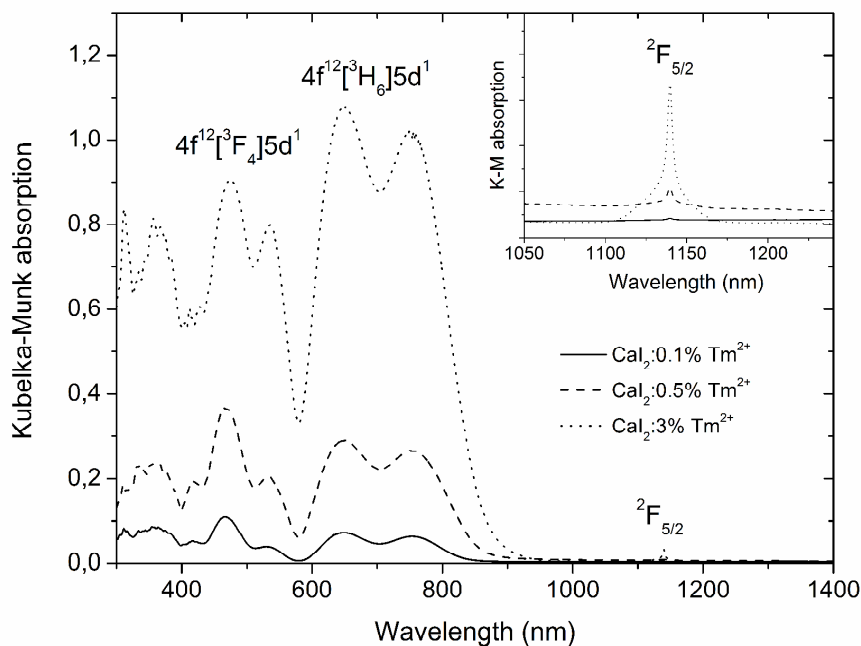


Figure 8.1: Kubelka-Munk absorption spectra of Tm^{2+} doped CaI_2 samples. The inset shows a magnification of the absorption around 1150 nm.

The four lowest energy maxima of the $5d$ absorption bands in the 0.1% Tm doped CaI_2 sample are located at 753, 647, 531 and 466 nm. The energy separation between the first and the third maximum is 5552 cm^{-1} , and the energy separation between the second and the fourth maximum is 6003 cm^{-1} . These energies nicely agree with the expected energy separation between the 3H_6 and 3F_4 terms. The

bands at 647 and 753 nm are therefore assigned to absorption to the spin-allowed $4f^{12}[^3H_6]5d^1$ electronic configuration and the bands at 466 and 531 nm are assigned to the spin-allowed $4f^{12}[^3F_4]5d^1$ electronic configuration.

The lowest energy $5d$ state of Eu^{2+} in CaI_2 , the $4f^6[{}^7F_0]5d^1$, is located at about 440 nm. [17,18] Using the relations between the $4f$ - $5d$ transitions of the divalent lanthanide ions described by Dorenbos [19] predicts the absorption to the Tm^{2+} spin-forbidden state around 800 nm and the spin-allowed $4f^6[{}^3H_6]5d^1$ around 700 nm. The latter wavelength is the location of the first couple of absorption bands in the absorption spectrum.

Apart from the divalent state, thulium can also be present in the trivalent state. The presence of Tm^{3+} would be characterized by, among others, Tm^{3+} $4f$ - $4f$ transitions around 800 nm and 1220 nm due to the ${}^3H_6 \rightarrow {}^3H_4$ and ${}^3H_6 \rightarrow {}^3H_5$ absorptions respectively. These lines cannot be observed in the absorption spectrum in Figure 8.1. This indicates that Tm is only present in the divalent state and not in the trivalent state.

In Figure 8.2 the absorption spectra of Tm doped NaCl are shown for different Tm concentrations. In the infrared the typical $4f$ - $4f$ absorption line of Tm^{2+} around 1137 nm is observed, indicating that all samples contain Tm^{2+} . In the sample with the highest Tm concentration, additional absorption lines can be seen centered at 1220 and 798 nm which can be assigned to the ${}^3H_6 \rightarrow {}^3H_5$ and ${}^3H_6 \rightarrow {}^3H_4$ absorptions of Tm^{3+} respectively, indicating that at this concentration some of the Tm is present in the trivalent state. These absorptions are not observed in the samples with lower Tm concentration.

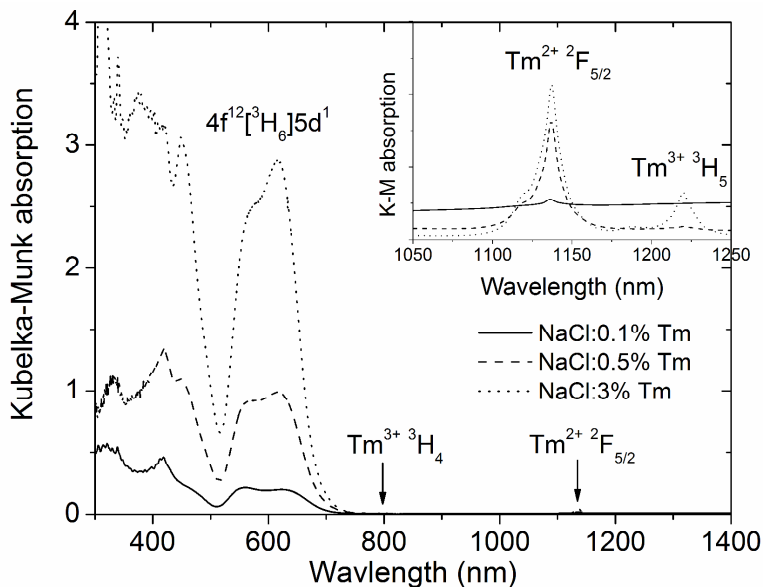


Figure 8.2: Kubelka-Munk absorption spectra of Tm doped NaCl samples. The inset shows a magnification of the absorption around 1150 nm.

Just as for Tm doped CaI₂, strong Tm²⁺ 4*f*-5*d* absorption bands are observed in the NaCl samples, although the maximum of the lowest energy band is located at higher energy as compared to the one in CaI₂. Note that the lowest energy 4*f*-5*d* transition of Eu²⁺ in NaCl (410 nm) [18,20] is also at higher energy than the one in CaI₂ (440 nm). The Yb²⁺ spin forbidden 4*f*-5*d* transition in NaCl has been observed at 423 nm [19,21], which would predict the lowest energy spin-forbidden Tm²⁺ 4*f*-5*d* transition around 745 nm, which agrees with the observation of stronger spin-allowed absorption bands at higher energy. Since NaCl forms a simple cubic lattice, the Na⁺ ions are in octahedral symmetry with 6-fold coordination. By substituting the Tm²⁺ ions on the Na⁺ sites, a splitting of the 5*d* bands in a threefold degenerate t_{2g} at lower energy and a twofold degenerate e_g at higher energy would be expected with an energy difference of 12849 cm⁻¹ (based on NaCl:Eu²⁺ [22]). However, as can be seen from Figure 8.2 the lowest energy band located around 600 nm is clearly split into two bands of which the relative intensity varies with changing Tm concentration. This splitting of the band may be caused by a change in symmetry

around the Tm^{2+} ions, which might be the result of charge compensation needed when a divalent thulium ion is substituted on a monovalent sodium site.

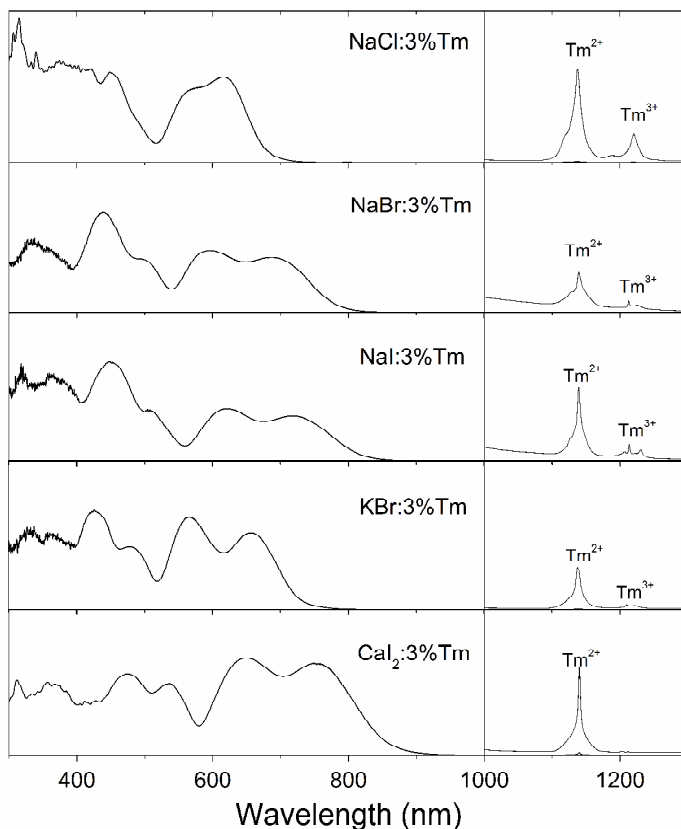


Figure 8.3: Kubelka-Munk absorption spectra of Tm doped NaCl, NaBr, NaI, KBr and CaI_2 . The spectrum above 1000 nm has been magnified in order to show the f - f transitions.

The absorption spectra of several Tm doped halides are compared in Figure 8.3. All samples absorb visible light due to Tm^{2+} $4f$ - $5d$ transitions. The absorption extends up to 700 nm in NaCl and shifts to longer wavelengths in NaBr and NaI. Such a red shift from chlorides to bromides to iodides due to an increasing spectroscopic polarizability has also been observed for the Ce^{3+} $4f$ - $5d$ transitions in halide compounds. [23] Furthermore it is observed that the Tm^{2+} $4f$ - $5d$ transitions

are at higher energy in KBr as compared to NaBr. This is in agreement with the higher Eu²⁺ 4f-5d absorption in KBr (395 nm) as compared to NaBr (410 nm). [19] Though the samples contain Tm²⁺ as indicated by the absorption peak at 1140 nm, all samples, with the exception of CaI₂, also contain some Tm³⁺ indicated by the ³H₆ → ³H₅ absorption centered around 1220 nm. Note that the NaBr, NaI and KBr samples were made according to method 1 (see section 8.2), which always resulted in the formation of some Tm³⁺. This might be caused by oxidation of Tm²⁺ by oxygen or water contaminations within the quartz ampoule or by reaction with the quartz ampoule itself.

8.3.2 Luminescence

Excitation of the Tm²⁺ doped CaI₂ samples with 400 nm light results in line emission at 1140 nm, as is shown in Figure 8.4. This emission is typical ²F_{5/2} → ²F_{7/2} emission of Tm²⁺. The shape of the emission line is the same for all Tm concentrations. Besides this *f-f* line emission, no other emissions are observed. Excitation of the samples with any other wavelength in the 300 to 800 nm range resulted in the same emission spectrum. In the excitation spectrum of this emission, the Tm²⁺ 5*d* bands are observed, similar to the bands observed in the absorption spectrum. Note that the lowest energy excitation band shifts to longer wavelengths in the sample with the highest Tm concentration, just as can be seen in the absorption spectrum, which might indicate that the coordination around the Tm²⁺ ions changes at higher Tm concentration (Figure 8.1).

The mechanism resulting in Tm²⁺ 4*f*-4*f* emission after excitation in the 5*d* bands is illustrated with the configurational coordinate diagram shown in Figure 8.5. Excitation within the 5*d* bands is followed by relaxation to the ²F_{5/2} excited state, which subsequently results in emission to the ²F_{7/2} ground state.

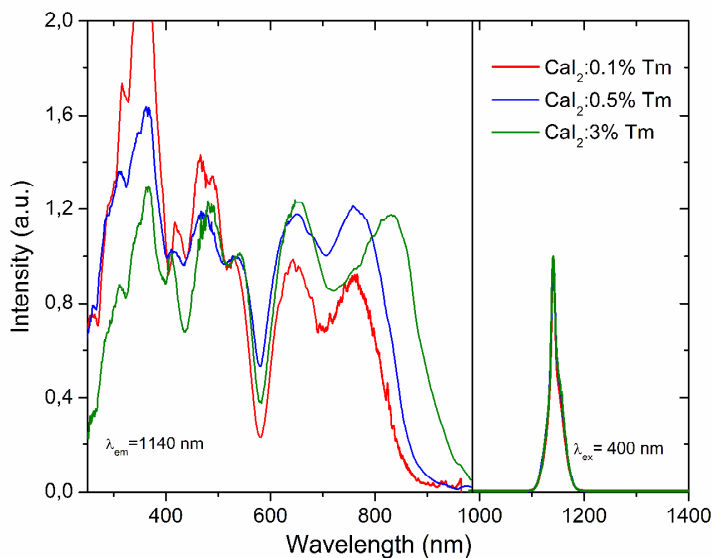


Figure 8.4: (left) excitation spectrum of the 1140 nm emission (normalized at 340 nm), and (right) emission spectrum after 400 nm excitation of (normalized at 1140 nm) Tm doped CaI_2 samples.

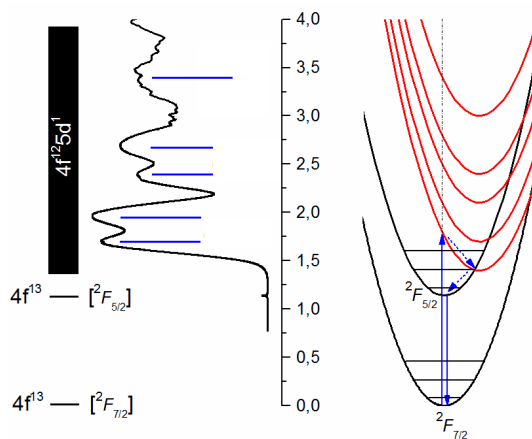


Figure 8.5: (left) Energy level scheme showing the two states of the $\text{Tm}^{2+} 4f^{13}$ electron configuration and the excited $4f^{12}5d^1$ state. (middle) Absorption spectrum of Tm^{2+} in CaI_2 showing the weak parity and spin forbidden transitions to the ${}^2F_{5/2} 4f^{13}$ state and the much stronger allowed transitions to the $4f^{12}5d^1$ configuration. (right) Configurational coordinate diagram of the ground and excited states of Tm^{2+} in CaI_2 showing the favorable relative position of the $5d$ (black) and $4f$ (red) parabolas.

Excitation of the Tm doped NaCl samples results, just as for CaI₂:Tm, in the emission of 1140 nm light due to the Tm²⁺ *f-f* transition (Figure 8.6). The excitation spectra of this emission show the Tm²⁺ *4f-5d* excitation bands that were also observed in the absorption spectra. Some changes in these excitation spectra can be seen when Tm doping concentration is increased, most notably a larger energy separation between the bands around 550 and 700 nm. This change might be due to a change in symmetry around the Tm²⁺ ions when the Tm concentration is increased. Note that the *4f-5d* energy of Eu²⁺ in NaCl also varies considerably, depending on the coordination of the Eu²⁺ ion. [24] The shape of the emission band at 1140 nm does not change considerably with the variation in Tm concentration.

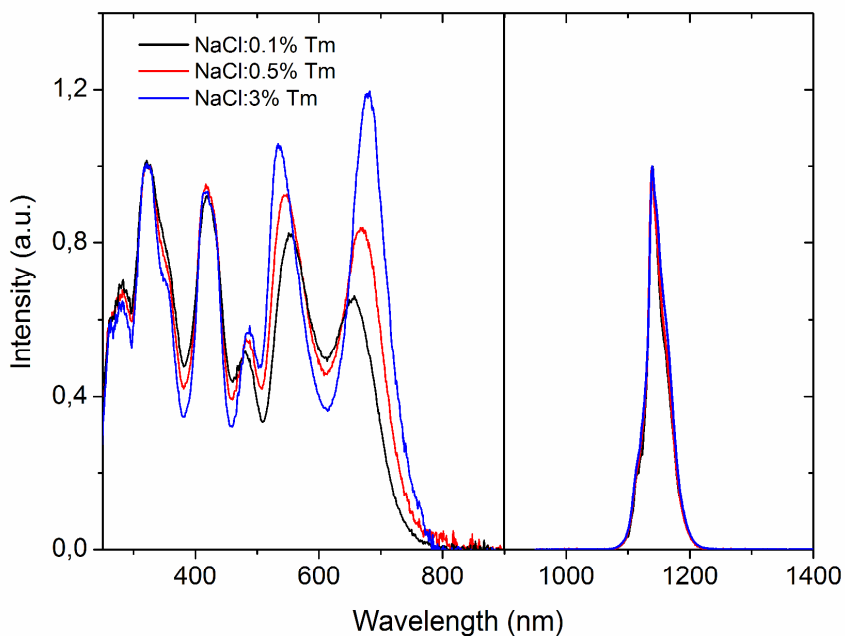


Figure 8.6: (left) normalized excitation spectra of the 1140 nm emission, and (right) normalized emission spectra after 400 nm excitation of Tm doped NaCl samples.

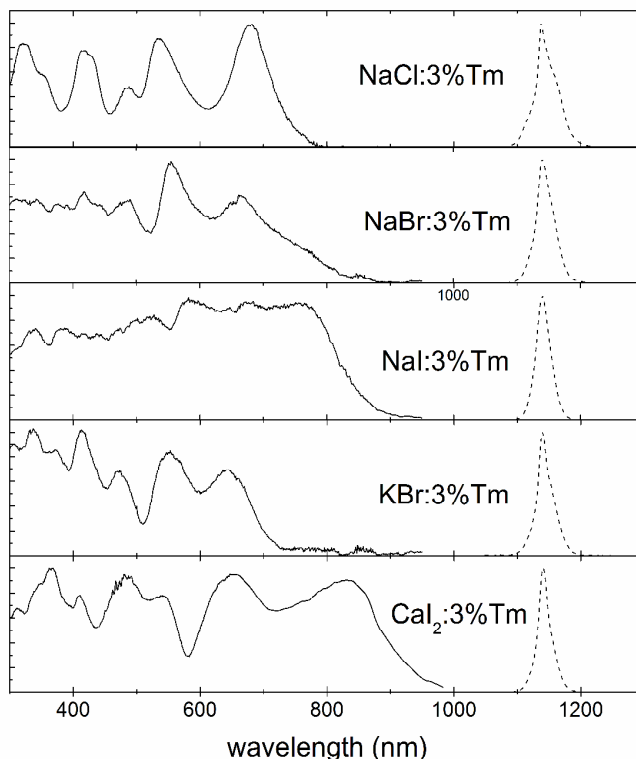


Figure 8.7: excitation spectrum (straight line) of the 1140 nm emission, and emission spectrum after 400 nm excitation (dotted line) of Tm doped NaCl, NaBr, NaI, KBr and CaI₂.

The excitation and emission spectra of the 3% Tm doped NaBr, NaI and KBr samples are shown in Figure 8.7. Just as for the NaCl and CaI₂ samples, excitation with UV or visible light results in a single emission peak around 1140 nm. In the excitation spectra of this emission, the $4f-5d$ bands are observed, which were also seen in the absorption spectra. Note that Tm²⁺ $f-f$ emission around 1140 nm is the only emission that is observed after excitation with UV or visible light. This behavior is different than what has been observed by for example Wenger et al. [25] in Tm²⁺ doped SrCl₂, in which also some $5d-4f$ emission is observed at room temperature. In our samples, the relaxation from the $4f^{12}5d^1$ states to the $^2F_{5/2}$ state of the $4f^{13}$ configuration is apparently efficient enough to prevent $5d-4f$ emission.

8.4. Conclusions

In Figure 8.8 the absorption and emission spectra of a CaI₂:Tm sample are compared with the spectra of a Red 305 dye [26], as well as the AM1.5 solar spectrum (ASTM G173-03). The Red 305 dye can only absorb 30% of the solar energy, while Tm²⁺ doped CaI₂ absorbs up to 63% of the energy. Another notable difference is the overlap between the absorption and emission spectra. There is a strong overlap between these spectra in the 550-650 nm range in case of the Red 305 dye. As a result strong self-absorption will occur in an LSC based on this dye, limiting the efficiencies to values typically around 2%. [27] With CaI₂:Tm on the other hand, the Stokes shift between absorption up to 900 nm and emission around 1140 nm guarantees that self-absorption cannot occur. There is only a small overlap between the emission spectrum and the ²F_{7/2} → ²F_{5/2} absorption line. However, this absorption is very weak and will not result in considerable self-absorption. The strong absorption of the Tm²⁺ doped halides combined with an efficient emission without self-absorption makes these materials very promising for LSC applications. Note that, as a result of the wide absorption range, an LSC based on the Tm²⁺ doped halides will be colorless, as opposed to an LSC based on the Red 305 dye, which has an orange/red color. Such a colorless LSC is an advantage when used as a window in buildings.

It should be noted that, in order to obtain an efficient luminescent solar concentrator in combination with the Tm²⁺ doped halides, a solar cell is needed that efficiently converts the 1140 nm light into electricity. For this purpose, a solar cell with a band gap in the 1200 to 1250 nm range with a near unity quantum efficiency for the 1140 nm light would be ideal. This might for example be a copper indium (gallium) selenide (CIGS) cell [28], though any other type of cell that is efficient for 1140 nm light might be applicable as well. Hence that the solar cell is only required to be efficient for 1140 nm light and does not necessarily have to be efficient for UV or visible light.

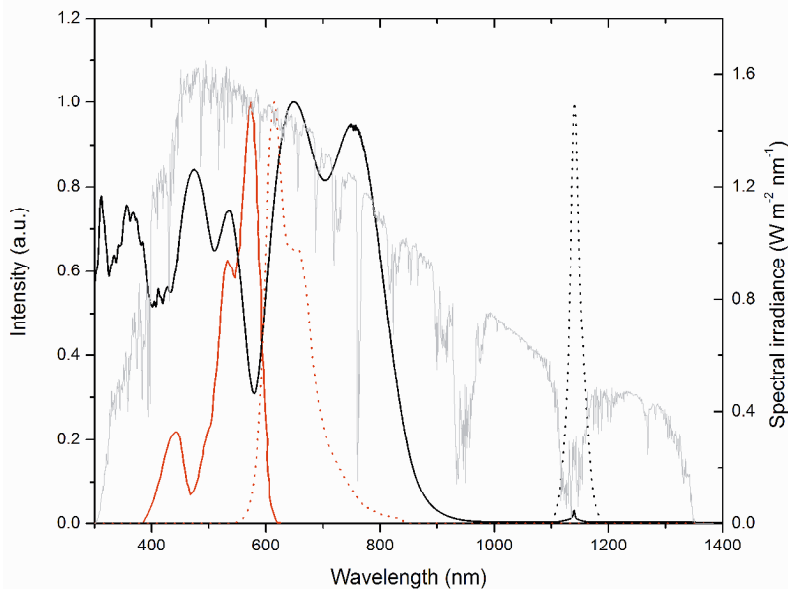


Figure 8.8: Absorption spectra of $\text{CaI}_2:\text{Tm}$ (black solid line) and the Red 305 dye [24] (red solid line), the emission spectra of $\text{CaI}_2:\text{Tm}$ (black dotted line) and the Red 305 dye (red dotted line) and the AM1.5 solar spectrum (ASTM G173-03) (grey line).

8.5. References

- [1] B. Norton, P.C. Eames, T.K. Mallick, M.J. Huang, S.J. McCormack, J.D. Mondol, Y.G. Yohanis; *Sol. Energy* 85 (2011) 1629.
- [2] W.H. Weber, J. Lambe; *Appl. Optics* 15 (1976) 2299.
- [3] A. Goetzberger, W. Greube; *Appl. Phys. A-Mater.* 14 (1977) 123.
- [4] J.S. Batchelder, A.H. Zewail, T. Cole; *Appl. Opt.* 18 (1979) 3090.
- [5] R.W. Olson, R.F. Loring, M.D. Fayer; *Appl. Opt.* 20 (1981) 2934.
- [6] T. Diemel, C. Bauer, I. Dolamic, D. Brühwiler; *Sol. Energy* 84 (2010) 1366.
- [7] O.M. ten Kate, K.M. Hooning, E. van der Kolk; *Appl. Opt.* (accepted).
- [8] J.R. Peterson, W. Xu, S. Dai; *Chem. Mater.* 7 (1995) 1686.
- [9] W.J. Schipper, A. Meijerink, G. Blasse; *J. Lumin.* 62 (1994) 55.

- [10] Q. Zeng, Z. Pei, S. Wang, Q. Su; *Spectrosc. Lett.* 32 (1999) 895.
- [11] J. Grimm, O.S. Wenger, K.W. Krämer, H.U. Güdel; *J. Lumin.* 126 (2007) 590.
- [12] E. Beurer, J. Grimm, P. Gerner, H.U. Güdel; *J. Am. Chem. Soc.* 128 (2006) 3110.
- [13] J. Grimm, E. Beurer, H.U. Güdel; *Inorg. Chem.* 45 (2006) 10905.
- [14] P. Kubelka, F. Munk, *Z. Technische Physik* 12 (1931) 593.
- [15] H. Blum; *Z. Phys. Chem., Abt. B* 22 (1933) 298.
- [16] G.H. Dieke; H.M. Crosswhite; *Appl. Opt.* 2 (1963) 675.
- [17] R. Hofstadter, E.W. O'Dell, C.T. Schmidt; *Rev. Sci. Instrum.* 35 (1964) 246.
- [18] P. Dorenbos; *J. Lumin.* 104 (2003) 239.
- [19] P. Dorenbos; *J. Phys.-Cond. Mat.* 15 (2003) 575.
- [20] J.A. Hernandez, W.K. Cory, J.O. Rubio; *Jpn. J. Appl. Phys.* 18 (1979) 533.
- [21] T. Tsuboi, H. Witzke, D.S. McClure; *J. Lumin.* 24-25 (1981) 305.
- [22] A.J. Hernandez, H.S. Murrieta, F. Jaque, O.J. Rubio; *Solid St. Commun.* 39 (1981) 1061.
- [23] P. Dorenbos; *Phys. Rev. B* 62 (2000) 15650.
- [24] O.J. Rubio; *J. Phys. Chem. Solids* 52 (1991) 101.
- [25] O.S. Wenger, C. Wickleder, K.W. Krämer, H.U. Güdel; *J. Lumin.* 94-95 (2001) 101.
- [25] L. Desmet, A.J.M. Ras, D.K.G. de Boer, M.G. Debije; *Opt. Lett.* 37 (2012) 3087.
- [26] M.G. Debije, P.C. Verbunt; *Adv. Energ. Mater.* 2 (2012) 12.
- [27] R. Kamada, W.N. Shafarman, R.W. Birkmire; *Sol. Energ. Mater. Sol. C.* 94 (2010) 451.

Chapter 9

Optical properties of $\text{Eu}^{2+}/\text{Eu}^{3+}$ mixed valence, silicon nitride based materials

The content of this chapter has been published as: O.M. ten Kate, T. Vranken, E. van der Kolk, A.P.J. Jansen, H.T. Hintzen; "Optical properties of $\text{Eu}^{2+}/\text{Eu}^{3+}$ mixed valence, silicon nitride based materials", Journal of Solid State Chemistry 213 (2014) 126-131.

Eu_2SiN_3 , a mixed valence europium nitridosilicate, has been prepared via solid-state reaction synthesis and its oxidation behavior and optical properties have been determined. Furthermore, the stability of several isostructural compounds of the type $\text{M}^{2+}\text{L}^{3+}\text{SiN}_3$ has been predicted by using density functional theory calculations, and verified by the actual synthesis of CaLaSiN_3 , CaEuSiN_3 and EuLaSiN_3 . The band gap of CaLaSiN_3 was found around 3.2 eV giving the material its yellow color. Eu_2SiN_3 on the other hand is black due to a combination of the 4f-5d absorption band of Eu^{2+} and the charge transfer band of Eu^{3+} . Thermogravimetric analysis and Raman spectroscopic study of Eu_2SiN_3 revealed that oxidation of this compound in dry air takes place via a nitrogen retention complex.

9.1 Introduction

Over the last fifteen years several europium containing silicon nitride or aluminum silicon nitride based compounds have been reported, including $\text{Eu}_2\text{Si}_5\text{N}_8$ [1], $\text{M}_2\text{Si}_5\text{N}_8:\text{Eu}$ (M=Ca,Sr,Ba) [2,3], $\text{LaSi}_3\text{N}_5:\text{Eu}$ [4], $\text{EuYbSi}_4\text{N}_7$ [1], $\text{MYSi}_4\text{N}_7:\text{Eu}$ (M=Sr,Ba) [5,6], $\text{MSiN}_2:\text{Eu}$ (M=Ca,Sr,Ba) [9,10], $\text{BaSi}_7\text{N}_{10}:\text{Eu}$ [11], $\text{SrSi}_6\text{N}_8:\text{Eu}$ [12], $\text{MAlSiN}_3:\text{Eu}$ (M=Ca,Sr) [7,8], $\text{Ba}_2\text{AlSi}_5\text{N}_9:\text{Eu}$ [13] and $\text{SrAlSi}_4\text{N}_7:\text{Eu}$ [14]. In

all these materials europium is observed in the divalent state and not in the trivalent state, as opposed to europium in EuN itself, or in many oxides, in which Eu is often present in the trivalent state. Characteristic for the presence of Eu^{2+} are $4f$ - $5d$ absorption bands of which the position of the lowest energy $4f$ - $5d$ band shifts from circa 380 nm in $\text{BaSi}_7\text{N}_{10}:\text{Eu}^{2+}$ to 590 nm in $\text{CaAlSiN}_3:\text{Eu}^{2+}$. In some of these compounds $4f$ to $5d$ excitation is followed by efficient $5d$ to $4f$ emission in the orange to red region, especially in $\text{CaAlSiN}_3:\text{Eu}^{2+}$ and $\text{Sr}_2\text{Si}_5\text{N}_8:\text{Eu}^{2+}$, which play a key role as red-emitting phosphors for LEDs. [15]

Recently, Zeuner et al. reported the synthesis and structure determination of the Eu_2SiN_3 compound, which is a non-branched chain-type nitridosilicate. [16] An interesting property of the material is that it has two crystallographic distinct Eu sites at which one site is occupied by Eu^{2+} ions, while the other site is occupied by Eu^{3+} ions, making it, by our knowledge, the only mixed-valence europium nitridosilicate reported so far, and even the only nitridosilicate in which Eu^{3+} is observed. What is also noticeable about Eu_2SiN_3 is the black color of the material, indicating that Eu_2SiN_3 has a small band gap located in the infrared. However, the exact size of this gap and the origin of the transition involved have not been reported.

In this chapter the Eu_2SiN_3 compound is prepared via a solid-state reaction synthesis and its crystal structure and oxidation behavior are studied. Furthermore, the stability of several related $\text{M}^{2+}\text{L}^{3+}\text{SiN}_3$ compounds with the same structure are discussed, in which Eu is substituted by other rare-earth or alkaline earth metals like Y, La, Ca, Sr or Ba, by making use of density functional theory (DFT) calculations. On the basis of these DFT calculations CaLaSiN_3 , CaEuSiN_3 and EuLaSiN_3 were successfully synthesized. Finally, the optical properties of these different compounds are determined, and the nature of the optical transitions involved, are discussed.

9.2 Experimental

9.2.1 Synthesis

For the synthesis of Eu_2SiN_3 , EuN was first prepared by the nitridation of europium metal (CSRE, 99.9%, lumps) in a tube furnace at 850 °C for 24 hours. The EuN was then mixed together with Si_3N_4 (Permascand, P95H, alpha content 93.2 wt.-%, oxygen content 1.5 wt.-%) and ground in an agate mortar. The mixture was then heated in a furnace at 1350 °C in a N_2/H_2 (10%) atmosphere. CaLaSiN_3 , CaEuSiN_3 and EuLaSiN_3 were made in a similar way from La powder (CSRE, 99%) and Ca_3N_2 (Alfa Aesar, 200 mesh, 98%), heated at 1400 °C. Note that all handlings were carried out in a nitrogen filled glove box in order to prevent oxidation of the starting materials and final product. The tube furnace used during synthesis was directly connected to this glove box.

9.2.2 Measurements

Crystalline phases were checked by means of X-ray powder diffraction (XRD) analysis with a Bruker D4 Endeavor with Cu K_α radiation. Diffraction data were collected by step scanning with a step size of 0.005° in 2θ and a counting time of 1 s per step. Diffuse reflectance measurements in the UV/visible range were performed with a Perkin Elmer LS50B spectrophotometer with Xe lamp and an R952 photomultiplier. White BaSO_4 and black felt were used as a reference. Diffuse reflectance spectra in the red and infrared range were recorded with a Bruker Vertex 80v FT interferometer, using W as a light source and cooled MCT, InGaAs and Si detectors. KBr was taken as a reference. To protect the samples from the atmosphere, airtight sample holders were used. Luminescence of the samples was checked with an XP2254B PMT for visible light emission and a Hamamatsu H10330A-75 NIR PMT for infrared emission with two double grating monochromators using a xenon lamp as a light source. A helium cryostat was used to perform measurements at a temperature of 10 K. Differential thermal analysis

(DTA) experiments were performed on a Mettler Toledo TGA/SDTA851e in a 70 μL alumina sample holder in flowing dry air (50 mL/min). Raman spectroscopy was carried out on a Jobin-Yvon LabRam 010 (30 mW 633 nm HeNe laser, 1800 mm^{-1} grating).

9.2.3 Calculations

Density functional theory (DFT) calculations were performed on some hypothetical $\text{M}^{2+}\text{L}^{3+}\text{SiN}_3$ compounds using the Vienna Ab-Initio Simulation Package (VASP) [17] using the Projector Augmented Wave (PAW) method to describe ionic interactions. The Generalized Gradient Approximation (GGA) was used for the exchange-correlation functionals, with the PW91 [18] exchange correlation function. The pseudopotentials used were supplied with the VASP package. The largest ENMAX value from the POTCAR-file was used automatically by VASP as the cut-off energy for the plane wave basis set. The K-points mesh was generated for each calculation using the Monkhorst-Pack grid method. [19] Calculations were repeated with increasing K-points mesh sizes until converged results were obtained.

9.3 Results and discussion

9.3.1 Characterization of Eu_2SiN_3

In Figure 9.1 the X-ray diffraction pattern of a Eu_2SiN_3 powder sample is shown and compared with the Eu_2SiN_3 pattern from Zeuner et al. obtained from single crystal data. [16] All diffraction peaks observed in the pattern of the prepared sample correspond with matching relative intensities to diffraction peaks in the reference pattern, indicating that the same phase is obtained. The reference structure is an orthorhombic crystal of space group $Cmca$ (64) with unit cell dimensions a , b and c being 5.423(11), 10.610(2) and 11.629(2) \AA respectively, with a unit cell volume of 669.1(2) \AA^3 . The lattice parameters a , b and c of the

prepared powder sample as found by Rietveld refinement are 5.430, 10.623 and 11.660 Å respectively, resulting in a unit cell volume of 672.6 Å³. The fit of the diffraction pattern with the refined lattice parameters has been included in Figure 9.1.

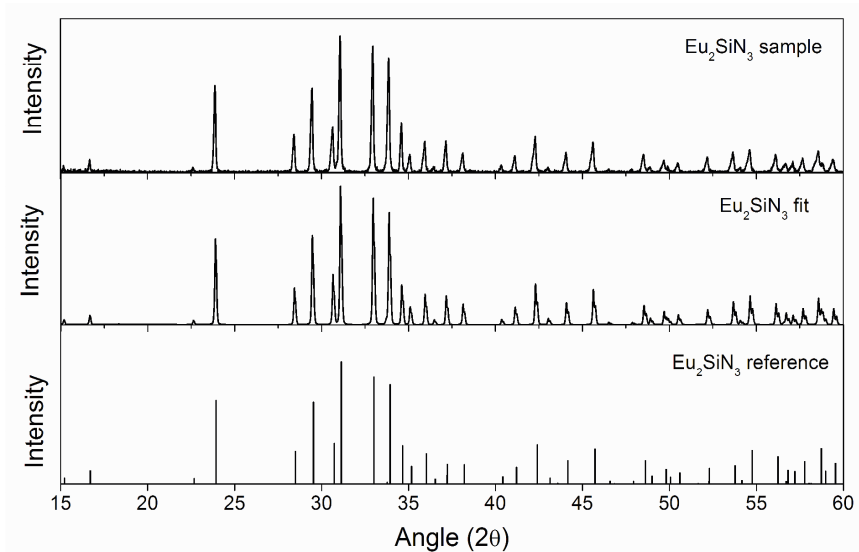


Figure 9.1: X-ray diffraction pattern of a Eu_2SiN_3 sample (above) compared with the reference Eu_2SiN_3 pattern obtained from Zeuner et al. [16] (below). The middle pattern is the fit of the measured pattern with the refined lattice parameters.

The slightly larger lattice parameters found for the powder sample prepared via solid-state synthesis could be caused by the incorporation of some oxygen atoms in the lattice as a result of the exposure to small amounts of oxygen during preparation or the presence of some oxygen in the starting compounds, in particular Si_3N_4 . The plausibility of this reasoning has been checked by preparing a sample with the composition $\text{Eu}_2\text{SiN}_2\text{O}$ as an extreme case in which a large amount of oxygen is incorporated. This results in an XRD pattern containing a Eu_2SiN_3 like phase, but with diffraction peaks well shifted to smaller angles, indicating much larger lattice parameters. Note that the larger lattice parameters by the incorporation of oxygen also make sense if one considers the radii of the different

ions involved. The combined Shannon radii of a Eu^{2+} and an O^{2-} ion is about 5% larger than the combined radii of a Eu^{3+} and a N^{3-} ion [20], supporting the idea that substitution of an $\text{Eu}^{3+}\text{N}^{3-}$ pair by an $\text{Eu}^{2+}\text{O}^{2-}$ pair will increase lattice parameters.

9.3.2 Oxidation behavior of Eu_2SiN_3

Thermogravimetric analysis (TGA) was performed on the Eu_2SiN_3 sample in order to study its oxidation behavior. Keeping a Eu_2SiN_3 sample at room temperature for 48 hours in a flow of dry air resulted in a mass increase of only 0.9%, indicating a very incomplete reaction, since complete oxidation from Eu_2SiN_3 to Eu_2SiO_5 would result in a mass increase of 10.2%.

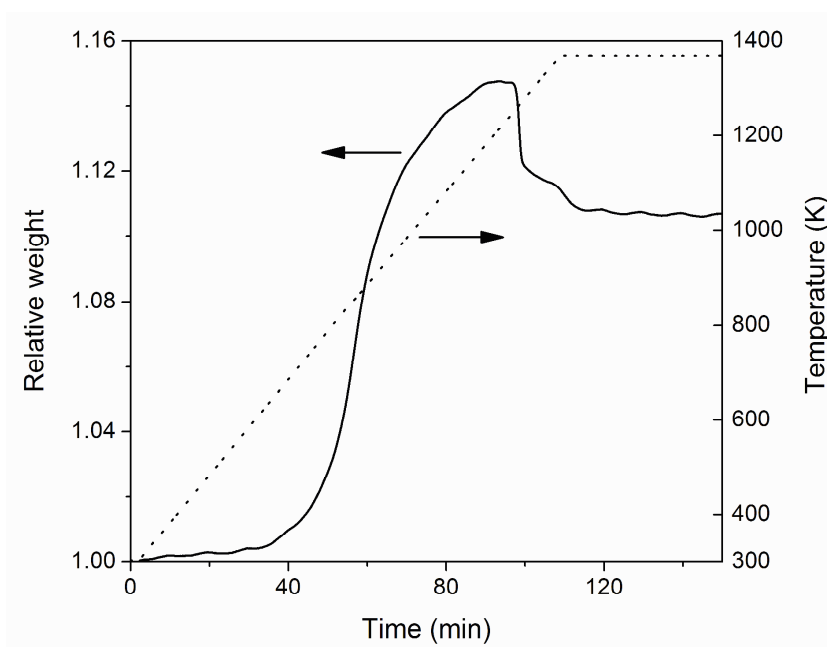


Figure 9.2: TGA curve of the oxidation of Eu_2SiN_3 in dry air.

To investigate the oxidation behavior of Eu_2SiN_3 in dry air at higher temperatures, the sample was heated with at a rate of 10 K/min up to 1373 K. The resulting TGA

curve is shown in Figure 9.2. From this curve it can be seen that the final mass increase is about 10.6%, which is very well in agreement with the theoretically predicted value of 10.2% for complete oxidation to Eu_2SiO_5 . The formation of a Eu_2SiO_5 phase has also been confirmed with XRD (JCPDS 00-040-0286).

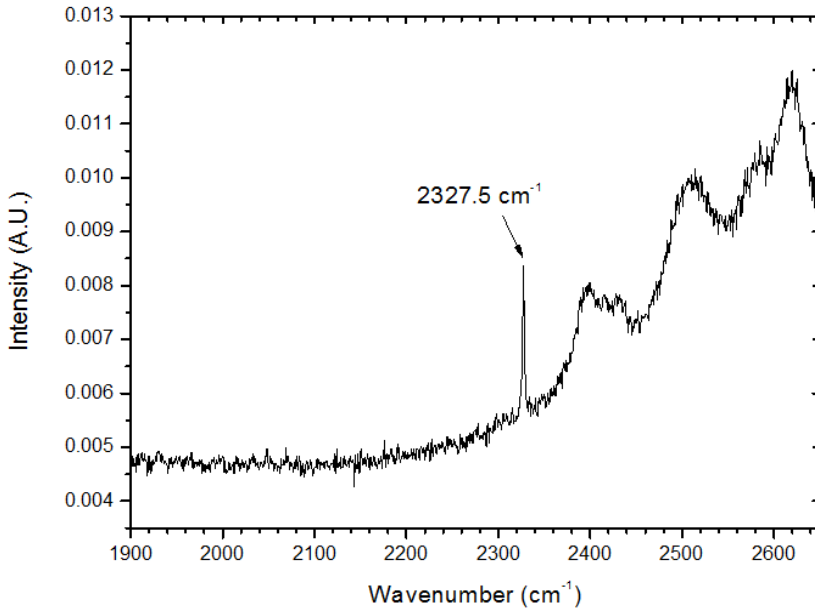


Figure 9.3: Raman spectroscopy measurement on the isolated intermediate compound from the TGA measurement on Eu_2SiN_3 .

However, before the sample reaches its final mass, it is observed that during the oxidation process a point is reached at which the mass of the sample is 14.7% larger than the starting mass and 3.7% larger than the final mass that is obtained. This indicates that during the oxidation process an intermediate compound is formed of which the mass is higher than the mass of the final compound. A similar phenomenon has been observed during the oxidation of $\text{Y}_4\text{Si}_2\text{O}_7\text{N}_2$ [21] and LaTiO_2N [22,23], where it was attributed to a nitrogen retention complex, meaning that an intermediary complex is formed in which the N_2 that is formed during oxidation is still trapped in the compound, while oxygen has already been incorporated. This presence of N_2 entities is confirmed with Raman spectroscopy,

which yields a weak signal at 2327.5 cm^{-1} (Figure 9.3). This value is close to the value of 2330.4 cm^{-1} reported for N_2 gas. [23] At higher temperatures the trapped N_2 molecule escapes from the compound resulting in a mass decrease.

9.3.3 DFT calculations

Density functional theory (DFT) calculations were performed in order to investigate the relative stabilities of several $\text{M}^{2+}\text{L}^{3+}\text{SiN}_3$ compounds, with M being Mg, Ca, Sr or Ba and L being Y or La. The energies obtained by the calculations are compared with the combined energies of the LN and MSiN_2 compounds. The reason for relating the calculations to these compounds is that these materials are observed in the XRD pattern in case the MLSiN_3 compound is not formed. The crystal structures, atomic coordinates and Wyckoff site information were obtained from Gál et al. [24] and Römer et al. [25] for MgSiN_2 , CaSiN_2 , SrSiN_2 and BaSiN_2 and from Kempter et al. [26] for YN and LaN. For all MLSiN_3 compounds information about the atomic sites of Eu_2SiN_3 from Zeuner et al. [16] was used. In the calculations all structures were relaxed by minimizing the energy. The results of the calculations performed are summarized in Table 9.1. A negative energy, meaning that the MLSiN_3 compound is energetically favorable over the LN+ MSiN_2 combination, is found for CaYSiN_3 , CaLaSiN_3 and SrLaSiN_3 , while all other combinations show a positive energy. It should however be noted that a negative number does not necessarily imply that such a compound can be obtained, since compounds with different crystal structures or other stoichiometric ratios that were not taken into account in the calculations might still be more stable. Neither does a positive number imply that synthesis of the compound will be impossible under any conditions.

Table 9.1: Energy differences in kJ/mol between LN+MSiN₂ mixture and the MLSiN₃ compound for various M²⁺ and L³⁺ cations, as obtained by DFT calculations. A negative energy difference indicates the MLSiN₃ compound is energetically favored.

	Mg	Ca	Sr	Ba
Y	88.57	-16.77	7.79	75.98
La	71.02	-50.64	-44.58	1.84

In order to do the DFT calculations for the stability of Eu₂SiN₃ itself, structural information on EuSiN₂ would be required for comparison. However, the EuSiN₂ compound has never been reported in literature. As an alternative a hypothetical EuSiN₂ has therefore been considered with the same space group as SrSiN₂ and using the same input data for the unit cell, as the Eu²⁺ ionic radius is similar to the one of Sr²⁺. [20] As a result an energy difference of -36.14 kJ/mol is obtained, which means that Eu₂SiN₃ is energetically favored over the EuN+EuSiN₂ combination. This is in agreement with the experimental fact that the compound can actually be synthesized.

Based on the DFT results, one may suggest that the ratio between the Shannon ionic radii [20] of the L³⁺ and the M²⁺ ions is a determining factor for the stability of the MLSiN₃ compound over the LN+MSiN₂ mixture. For large L³⁺/M²⁺ ratios like La³⁺/Mg²⁺ (1.43) and Y³⁺/Mg²⁺ (1.25) the compounds are calculated to be unstable, just as is the case for small L³⁺/M²⁺ ratios like Y³⁺/Sr²⁺ (0.76), La³⁺/Ba²⁺ (0.76) and Y³⁺/Ba²⁺ (0.67). The compounds with intermediary ratios on the other hand Y³⁺/Ca²⁺ (0.90), La³⁺/Ca²⁺ (1.03) and La³⁺/Sr²⁺ (0.87) are calculated to be stable. Also the Eu³⁺/Eu²⁺ ratio (0.81) falls within the intermediary range.

By relaxing the M²⁺L³⁺SiN₃ structures to minimal energy in the DFT calculations, optimized lattice constants for these compounds are obtained. These results are in agreement with what one can expect by taking into account the ionic sizes of the M²⁺ and L³⁺ ions. This is illustrated in Figure 9.4, in which the calculated unit cell volume is plotted against the size of the M²⁺ ion (based on the Shannon ionic radius), showing a linear increase in unit cell volume with

increasing M^{2+} ionic size. Furthermore, the data point for Eu_2SiN_3 obtained from literature [16] and also shown in Figure 9.4 is situated between the curves of the Y^{3+} and La^{3+} series. This is in agreement with the ionic radius of Eu^{3+} (0.947 Å) being between those of Y^{3+} (0.9 Å) and La^{3+} (1.032 Å).

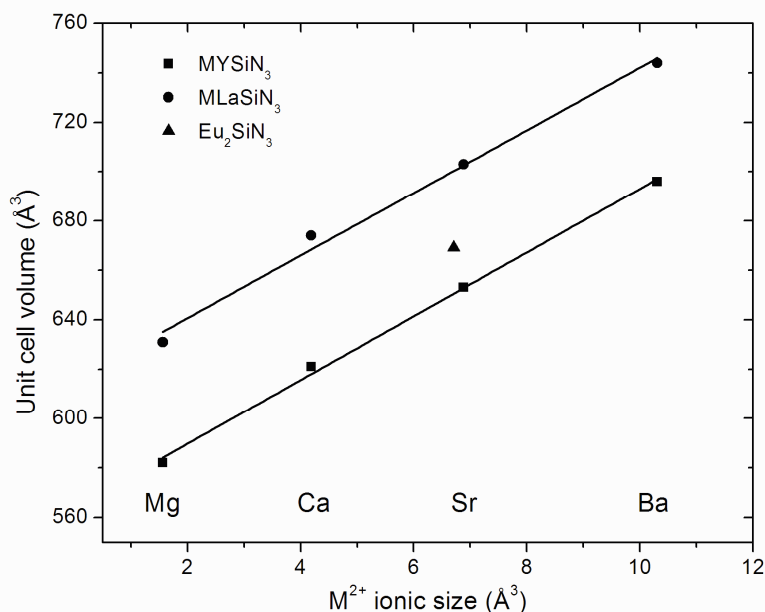


Figure 9.4: Unit cell volume of the $M^{2+}L^{3+}\text{SiN}_3$ compounds, as obtained by DFT calculations, as a function of the M^{2+} ionic size (based on the Shannon ionic radius with coordination number VI [20]). The unit cell volume of Eu_2SiN_3 is obtained from literature. [16]

9.3.4 Characterization of novel $M^{2+}L^{3+}\text{SiN}_3$ compounds

According to the DFT calculations, CaLaSiN_3 would be the energetically most favorable compound of the ones considered. It was therefore investigated whether this material could actually be prepared via a solid-state reaction synthesis. The diffraction pattern of the material is shown in Figure 9.5 and is compared with the Eu_2SiN_3 reference pattern. As can be seen, a pattern very similar to the one of

Eu_2SiN_3 is obtained, which could be fit using refined lattice parameters, as shown in Figure 9.5 as well. Only small diffraction peaks observed around 32° and 39.2° 2θ could not be indexed, indicating that a very small fraction of an unknown secondary phase might be present in the sample. The lattice parameters a , b and c of the CaLaSiN_3 sample were determined to be 5.456, 10.619 and 11.624 Å respectively, giving a unit cell volume of 673.4 Å³. Note that the unit cell volume is close to the value of CaLaSiN_3 that was calculated by DFT (Figure 9.4).

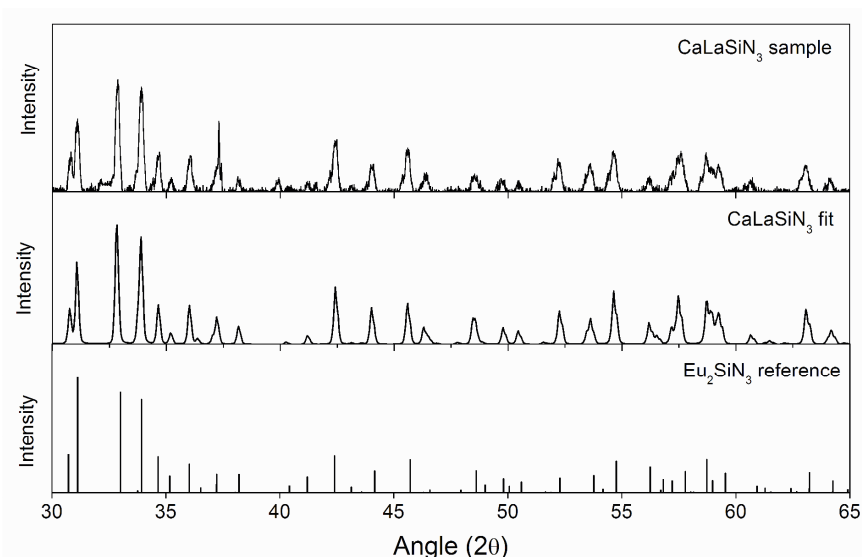


Figure 9.5: X-ray diffraction pattern of a CaLaSiN_3 sample (above), compared with the reference Eu_2SiN_3 pattern obtained from Zeuner et al. [16] (below). The middle pattern is the fit of the measured pattern with the refined lattice parameters.

Another compound that was synthesized is CaEuSiN_3 , of which the XRD pattern is shown in Figure 9.6. A pattern is obtained similar to the Eu_2SiN_3 reference pattern, but all diffraction peaks are considerably shifted to larger angles, as can be seen by the fit that is shown in Figure 9.6. A few reflections could not be attributed to CaEuSiN_3 , most notably the one at 34.6° 2θ . The lattice parameters of the CaEuSiN_3 sample were determined to be 5.403, 10.479 and 11.482 Å for a , b and c respectively, giving a unit cell volume of 650.2 Å³. Note that the lattice parameters

that were obtained for Eu_2SiN_3 prepared via the same synthesis method, i.e. 5.430, 10.623 and 11.660 Å for a , b and c respectively, are considerably larger than the ones obtained for CaEuSiN_3 . The shrinkage of the lattice parameters and unit cell volume from Eu_2SiN_3 to CaEuSiN_3 can well be explained if one considers that the Shannon ionic radius of Ca^{2+} is much smaller than that of Eu^{2+} . [20] Notice that the lattice parameters and unit cell volume of CaLaSiN_3 discussed above are very similar to the ones obtained for Eu_2SiN_3 . Apparently, the fact that Ca^{2+} ions are smaller than Eu^{2+} ions is compensated by the fact that La^{3+} ions are larger than Eu^{3+} ions.

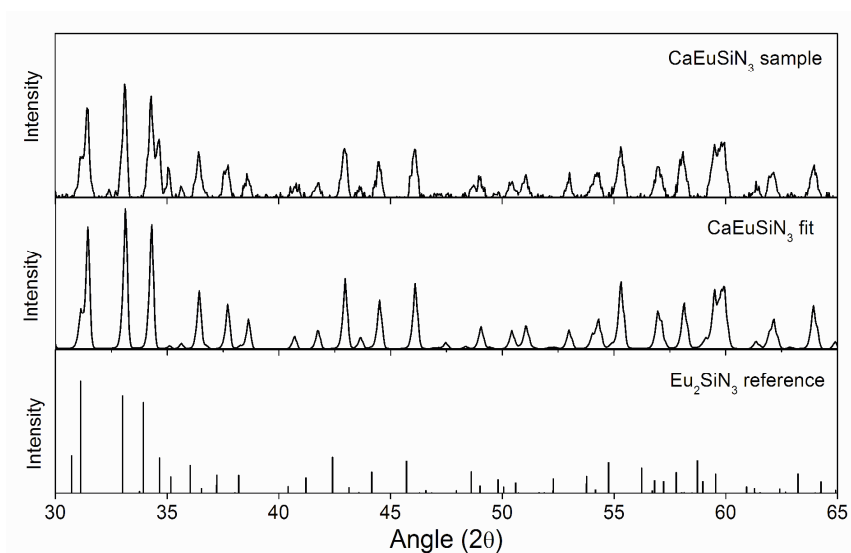


Figure 9.6: X-ray diffraction pattern of a CaEuSiN_3 sample (above) compared with the reference Eu_2SiN_3 pattern obtained from Zeuner et al. [16] (below). The middle pattern is the fit of the measured pattern with the refined lattice parameters.

Repeating the synthesis with Eu and La in order to synthesize EuLaSiN_3 results in a powder of which the XRD pattern is shown in Figure 9.7. Also for this compound a Eu_2SiN_3 like structure is obtained, with the main difference that the diffraction peaks are now shifted to smaller 2θ values, giving larger lattice parameters. The fit of the pattern with the refined lattice parameters has been included in Figure 9.7 as

well. All reflections observed in the pattern could be attributed to the EuLaSiN_3 structure. The lattice parameters were determined to be 5.487, 10.870 and 11.897 Å for a , b and c respectively, resulting in a unit cell volume of 709.6 Å³. The much larger lattice parameters for EuLaSiN_3 as compared to Eu_2SiN_3 and CaLaSiN_3 can well be explained by the larger size of the La^{3+} ion as compared to the size of the Eu^{3+} ion and by the larger size of the Eu^{2+} ion as compared to the Ca^{2+} ion. Note that the unit cell volume found for EuLaSiN_3 is close to the value predicted for SrLaSiN_3 with the DFT calculations (Figure 9.4), which is not unexpected since the Eu^{2+} ion is similar in size to the Sr^{2+} ion. The unit cell volumes and lattice parameters of CaLaSiN_3 , CaEuSiN_3 , EuLaSiN_3 and Eu_2SiN_3 are summarized in Table 9.2.

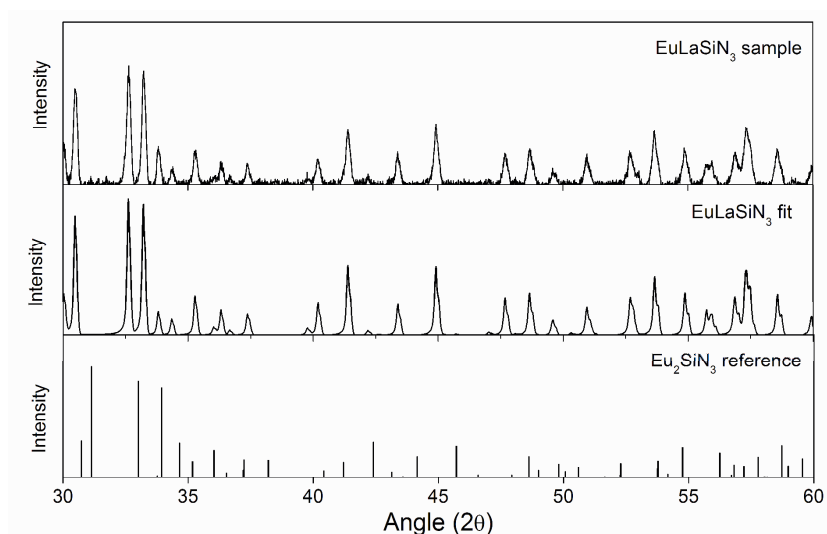


Figure 9.7: X-ray diffraction pattern of a EuLaSiN_3 sample (above) compared with the reference Eu_2SiN_3 pattern obtained from Zeuner et al. [16] (below). The middle pattern is the fit of the measured pattern with the refined lattice parameters.

Table 9.2: Lattice parameters a , b and c and unit cell volume V of the $M^{2+}L^{3+}SiN_3$ compounds prepared by solid-state reaction synthesis.

	a (Å)	b (Å)	c (Å)	V (Å ³)
CaEuSiN₃	5.403	10.479	11.482	650.2
Eu₂SiN₃	5.430	10.623	11.660	672.6
CaLaSiN₃	5.456	10.619	11.624	673.4
EuLaSiN₃	5.487	10.870	11.897	709.6

Based on the DFT calculations discussed in section 9.3.3 it was noticed that the $M^{2+}L^{3+}SiN_3$ compounds are calculated to be stable when the L^{3+}/M^{2+} ionic ratio falls roughly in the range between 0.8 and 1.2. The ratios of the ionic radii for La^{3+}/Eu^{2+} and Eu^{3+}/Ca^{2+} are 0.88 and 0.95 respectively, and thus fall within the stable range, being in agreement with the fact that $EuLaSiN_3$ and $CaEuSiN_3$ could both be synthesized.

9.3.5 Optical properties

In Figure 9.8 the diffuse reflectance spectrum of Eu_2SiN_3 is shown. As can be seen from the spectrum, the material strongly absorbs all visible light, giving the material its typical black color. Besides this strong absorption band, some absorption lines are observed between 0.2 and 0.7 eV. These are the typical $4f-4f$ absorption lines of Eu^{3+} from the 7F_0 ground state to the 7F_3 , 7F_4 , 7F_5 and 7F_6 excited states.

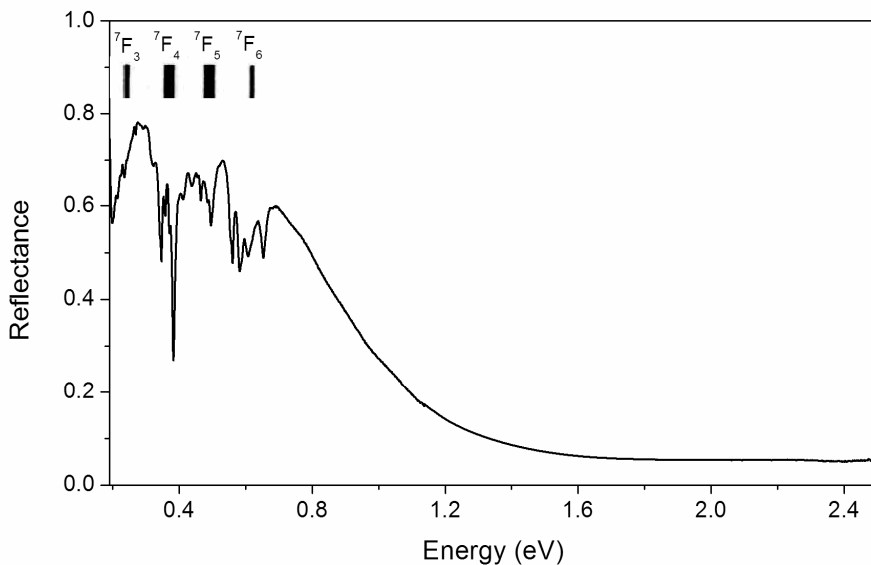


Figure 9.8: Diffuse reflectance spectrum of Eu_2SiN_3 .

In Figure 9.9 the diffuse reflectance spectra are shown of an undoped and a 2% and a 5% Eu doped CaLaSiN_3 sample. A strong absorption band in the UV/blue part of the spectrum, starting at 2.7 eV and going to higher energy, is observed in the undoped sample and is in agreement with the fact that the CaLaSiN_3 sample has a yellow color. The absorption can be attributed to the valence to conduction band transition of CaLaSiN_3 . In the europium doped samples a second strong absorption band is observed between 1 and 3 eV. The typical Eu^{3+} absorption lines in the infrared around 0.6 eV that were observed in the Eu_2SiN_3 sample are practically absent. Zooming in on that part of the spectrum only reveals some very weak features that might be attributed to a small Eu^{3+} fraction. It is therefore believed that most of the europium is present in the divalent state and that the strong absorption band between 1 and 3 eV can be related to $\text{Eu}^{2+} f-d$ absorption. It should however be noted that the samples have been prepared according to the stoichiometry $\text{Ca}_{1-x}\text{Eu}_x\text{LaSiN}_3$, thus with the intention to dope Eu on the Ca position.

No emission from the Eu doped CaLaSiN_3 sample after excitation with UV or visible light is observed and this emission does also not appear when the sample is cooled down to 10 K. This implies that Eu^{2+} d - f emission cannot take place in CaLaSiN_3 . An explanation for this might be that the lowest $5d$ state of Eu^{2+} is located inside the conduction band of CaLaSiN_3 .

In the diffuse reflectance spectrum of CaEuSiN_3 , shown in Figure 9.9, the typical $4f$ - $4f$ lines of Eu^{3+} are clearly observed around 0.6 eV, similar to Eu_2SiN_3 . Besides, a strong absorption band is present, which starts around 0.8 eV. The absorption spectrum of EuLaSiN_3 is also shown in Figure 9.9 and looks similar to the one of CaEuSiN_3 in a way that in this spectrum the Eu^{3+} f - f absorption lines are also observed, as well as a strong absorption band at higher energies. However, the f - f absorption lines are about ten times weaker, and the shape of the absorption band is different in that the absorption around 1.2 eV is much stronger.

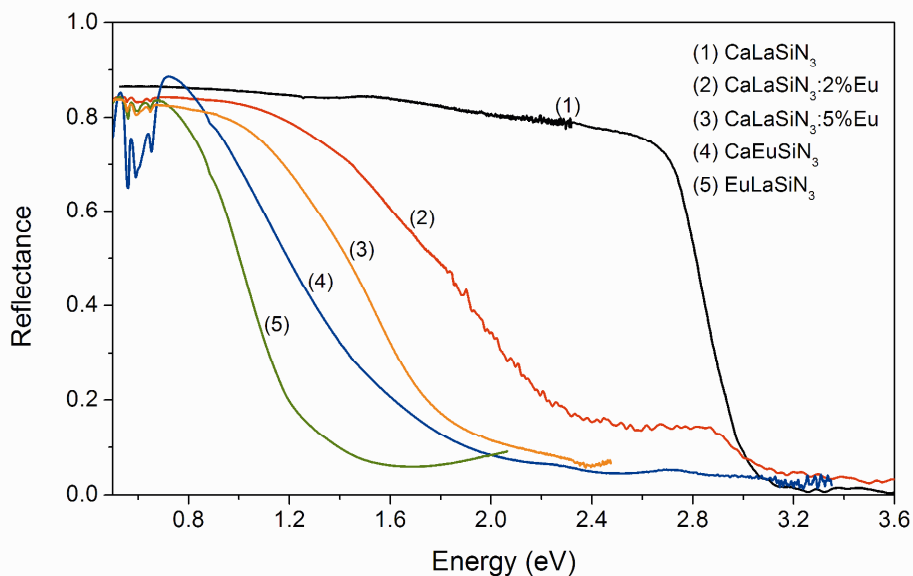


Figure 9.9: Diffuse reflectance spectra of undoped CaLaSiN_3 (1), 2% Eu doped CaLaSiN_3 (2), 5% Eu doped CaLaSiN_3 (3), CaEuSiN_3 (4) and EuLaSiN_3 (5).

The origin of the broad band visible light absorption in Eu_2SiN_3 , CaEuSiN_3 and EuLaSiN_3 can be related to either Eu^{2+} $4f-5d$ absorption or to a Eu^{3+} charge transfer (CT) band. In Eu_2SiN_3 both Eu^{2+} and Eu^{3+} are present, as is required for charge neutrality of the compound, and which has also been confirmed by Zeuner et al. [16] with Mössbauer spectroscopy. In CaEuSiN_3 on the other hand, most of the Eu atoms need to be in the trivalent state in order to achieve charge neutrality, since Ca is necessarily in the divalent state, while for similar reasons the Eu in EuLaSiN_3 needs to be in the divalent state. Note however that one can be sure that also in EuLaSiN_3 at least a part of the Eu is in the trivalent state, since the $f-f$ absorption lines of Eu^{3+} are observed in its diffuse reflectance spectrum, though weaker than in CaEuSiN_3 . The presence of Eu^{2+} in EuLaSiN_3 can not be confirmed in the same way because Eu^{2+} $f-f$ lines do not exist in the infrared or visible part of the spectrum and the Eu^{2+} $f-d$ absorption band is difficult to distinguish from either a Eu^{3+} charge transfer band or a combination of both. However, a clear difference can be seen between the diffuse reflectance spectra of CaEuSiN_3 and EuLaSiN_3 in which the latter one has a much stronger absorption around 1.2 eV, which suggests the influence of the $4f-5d$ absorption band.

It should be noted that the position of the Eu^{2+} $4f-5d$ absorption band is at very low energy compared to the $4f-5d$ band in many other compounds. Based on the above spectra the $4f^7 \rightarrow 4f^6[{}^7\text{F}_0]5d^1$ absorption band should be around 1 eV in Eu_2SiN_3 , which is significantly lower than the same band in hundreds of compounds summarized by Dorenbos et al. [27], where EuO has the lowest energy absorption band at 1.42 eV. Nevertheless, it is not expected that this low $4f-5d$ absorption band is impossible. Most compounds summarized in the reference concerns oxides or fluorides, both of which are known for their relatively high energy $4f-5d$ transitions as compared to nitrides. Additionally, the $4f-5d$ absorption of Eu^{2+} tends to drop to lower energies when increasing the metal to silicon ratio in metal (aluminum)silicon nitrides, due to an increasing centroid shift with decreasing Si content. A $4f-5d$ transition at much lower energy than in $\text{Sr}_2\text{Si}_5\text{N}_8:\text{Eu}^{2+}$ or $\text{CaAlSiN}_3:\text{Eu}^{2+}$ is therefore not unexpected. Finally it should be noted that compounds with 100% Eu^{2+} concentrations tend to have a larger redshift

of the $4f$ - $5d$ absorption as compared to compounds containing only a few percent of Eu^{2+} . [27]

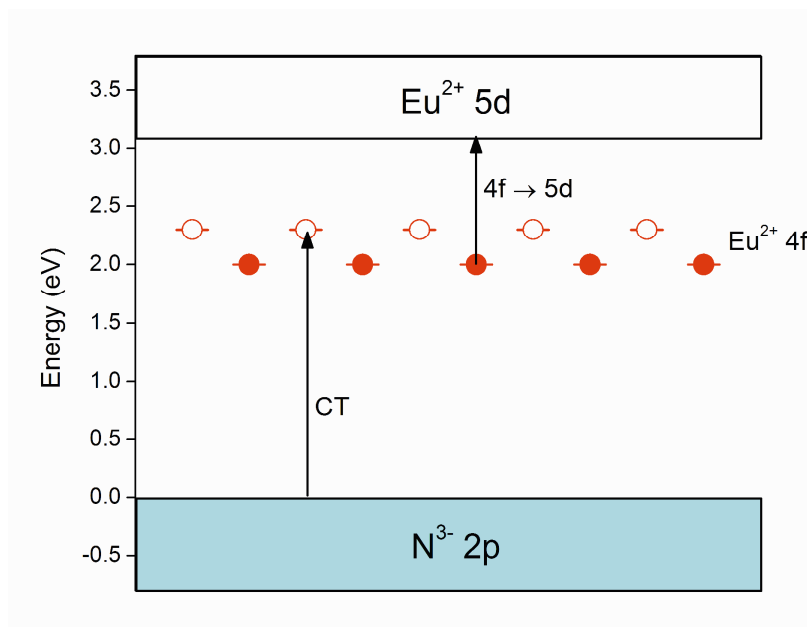


Figure 9.10: Best estimate of the energy level scheme of Eu_2SiN_3 showing the occupied $\text{N}^{3-} 2p$ band (blue rectangle), unoccupied $\text{Eu}^{2+} 5d$ band (white rectangle), occupied $\text{Eu}^{2+} 4f$ ground states (filled red circles) and unoccupied Eu^{2+} ground states (open red circles).

A schematic energy scheme of Eu_2SiN_3 is shown in Figure 9.10. In the figure the filled $\text{N}^{3-} 2p$ orbitals and the empty $5d$ band of the Eu^{2+} ions are shown. In the gap between these two bands the $\text{Eu}^{2+} 4f$ ground states are depicted. Half of these states are at somewhat higher energy than the other half as a consequence of the two different Eu sites in the lattice. The states at higher energy are empty resulting in trivalent europium, while the other half are filled resulting in divalent europium. The energy difference between the top of the $\text{N}^{3-} 2p$ band and the empty $4f$ states corresponds with the charge transfer band of Eu^{3+} , while the energy between the filled $4f$ states and the bottom of the $\text{Eu}^{2+} 5d$ band indicates the energy of the

lowest $4f$ - $5d$ absorption band. Note that the Eu^{2+} $4f$ ground states form a partially filled intermediate band in between the N^{3-} $2p$ band and the Eu^{2+} $5d$ band.

9.4 Conclusions

Eu_2SiN_3 was successfully synthesized via a solid-state synthesis and the oxidation of the compound in dry air was found to come along with a nitrogen retention complex similar to the oxidation of $\text{Y}_4\text{Si}_2\text{O}_7\text{N}_2$. With DFT calculations it was calculated that CaLaSiN_3 was likely to be a stable compound isostructural to Eu_2SiN_3 . Furthermore it was experimentally shown that CaLaSiN_3 , as well as the related CaEuSiN_3 and EuLaSiN_3 compounds, could actually be made via solid-state synthesis and have a similar crystal structure. For CaLaSiN_3 a band gap around 3.2 eV was observed giving the material its yellow color, while CaEuSiN_3 and EuLaSiN_3 have dark brown colors due to CT absorption of Eu^{3+} and a relatively low lying $4f$ - $5d$ absorption of Eu^{2+} respectively. Additionally it was found that the black color of Eu_2SiN_3 is due to a combination of the charge transfer band of Eu^{3+} and the $4f$ - $5d$ absorption band of Eu^{2+} .

It is well known that the energy of the $4f$ - $5d$ absorption band of a divalent lanthanide ion like Eu^{2+} is proportional to the $4f$ - $5d$ absorption band of a trivalent lanthanide ion like Ce^{3+} , Pr^{3+} or Tb^{3+} in the same host. [28] Low energy $4f$ - $5d$ transitions for these ions are therefore expected in CaLaSiN_3 .

The DFT calculations predict that SrLaSiN_3 and CaYSiN_3 will be stable as well. First attempts to synthesize these compounds results in samples of which the XRD patterns contain a phase with a Eu_2SiN_3 like structure with shifted lattice parameters. A study on the synthesis of SrLaSiN_3 and CaYSiN_3 may therefore be of interest, as well as doping these compounds with europium, which may also lead to low energy $4f$ - $5d$ transitions and a further understanding on the energy level positions in these types of compounds.

9.5 References

- [1] H. Huppertz, W. Schnick; *Acta Cryst. C* 53 (1997) 1751.
- [2] H.A. Höpfe, H. Lutz, P. Morys, W. Schnick, A. Seilmeier; *J. Phys. Chem. Sol.* 61 (2000) 2001.
- [3] Y.Q. Li, J.E.J. van Steen, J.W.H. van Krevel, G. Botty, A.C.A. Delsing, F.J. DiSalvo, G. de With, H.T. Hintzen; *J. Alloy. Compds.* 417 (2006) 273.
- [4] K. Uheda, H. Takizawa, T. Endo, H. Yamane, M. Shimada, C.M. Wang, M. Mitomo; *J. Lumin.* 87 (2000) 967.
- [5] Y.Q. Li, C.M. Fang, G. de With, H.T. Hintzen; *J. Solid State Chem.* 177 (2004) 4687.
- [6] Y.Q. Li, G. de With, H.T. Hintzen; *J. Alloy. Compds.* 385 (2004) 1.
- [7] K. Uheda, N. Hirosaki, Y. Yamamoto, A. Naito, T. Nakajima, H. Yamamoto; *Electrochem. Solid St.* 9 (2006) H22.
- [8] H. Watanabe, H. Yamane, N. Kijima; *J. Solid State Chem.* 181 (2008) 1848.
- [9] C.J. Duan, X.J. Wang, W.M. Otten, A.C.A. Delsing, J.T. Zhao, H.T. Hintzen; *Chem. Mater.* 20 (2008) 1597.
- [10] Y.Q. Li; *Int. J. Appl. Ceram. Technol.* (2009) 1.
- [11] Y.Q. Li, A.C.A. Delsing, R. Metselaar, G. de With, H.T. Hintzen; *J. Alloys. Compds.* 487 (2009) 28.
- [12] K. Shioi, N. Hirosaki, R.J. Xie, T. Takeda, Y.Q. Li; *J. Mater. Sci.* 43 (2008) 5659.
- [13] J.A. Kechele, C. Hecht, O. Oeckler, J. Schmedt auf der Günne, P.J. Schmidt, W. Schnick; *Chem. Mater.* 21 (2009) 1288.
- [14] C. Hecht, F. Stadler, P.J. Schmidt, J. Schmedt auf der Günne, V. Baumann, W. Schnick; *Chem. Mater.* 21 (2009) 1595.
- [15] S.E. Brinkley, N. Pfaff, K.A. Denault, Z. Zhang, H.T. Hintzen, R. Seshadri, S. Nakamura, S.P. DenBaars; *Appl. Phys. Lett.* 99 (2011) 241106.
- [16] M. Zeuner, S. Pagano, P. Matthes, D. Bichler, D. Johrendt, T. Harmening, R. Pöttgen, W. Schnick; *J. Am. Chem. Soc.* 131 (2009) 11242.

- [17] G. Kresse, J. Furthmüller; Vienna Ab-Initio Simulation Package; University of Vienna, Vienna, Austria, 2001.
- [18] J.P. Perdew, J.A. Chevary, S.H. Vosko, K.A. Jackson, M.R. Pederson, D.J. Singh, C. Fiolhais; Phys. Rev. B 46 (1992) 6671.
- [19] H.J. Monkhorst, J.D. Pack; Phys. Rev. B 13 (1976) 5188.
- [20] R. Shannon; Acta Crystallogr. A 32 (1976) 751.
- [21] J.W.H. van Krevel, H.T. Hintzen, R. Metselaar, L. Le Gendre, R. Marchand; Solid State Sci. 3 (2001) 49.
- [22] L. Le Gendre, R. Marchand, Y. Laurent; J. Eur. Ceram. Soc. 17 (1997) 1813.
- [23] L. Le Gendre, R. Marchand, B. Piriou; Eur. J. Solid State Inorg. Chem. 34 (1997) 973.
- [24] Z.A. Gál, P.M. Mallinson, H.J. Orchard, S.J. Clarke; Inorg. Chem. 43 (2004) 3998.
- [25] S.R. Römer, P. Kroll, W. Schnick; J. Phys.-Condens. Mat. 21 (2009) 275407.
- [26] C.P. Kempter, N.H. Krikorian, J.C. McGuire; J. Phys. Chem. 61 (1957) 1237.
- [27] P. Dorenbos; J. Lumin. 104 (2003) 239.
- [28] P. Dorenbos; J. Phys.-Condens. Mat. 15 (2003) 4797.

Chapter 10

Low energy $4f$ - $5d$ transitions in lanthanide doped CaLaSiN_3 with low degree of cross-linking between SiN_4 tetrahedra

The content of this chapter has been accepted for publication in Journal of Physics: Condensed Matter as: O.M. ten Kate, H.T. Hintzen, E. van der Kolk; “Low energy $4f$ - $5d$ transitions in lanthanide doped CaLaSiN_3 with low degree of cross-linking between SiN_4 tetrahedra”.

CaLaSiN_3 samples doped with Eu, Yb, Sm, Ce and Pr have been prepared via solid-state reaction synthesis and the optical properties have been studied. Both Yb and Sm were only observed in the trivalent state due to the fact that their Ln^{2+} ground states are located inside or very close to the conduction band of the CaLaSiN_3 host lattice. Doping with Ce^{3+} or Eu^{2+} resulted in a very low energy Ce^{3+} or Eu^{2+} $4f$ - $5d$ absorption band around 1.9 eV (650 nm) and 1.4 eV (885 nm) respectively. The Ce^{3+} $5d$ - $4f$ emission appeared to be quenched, just as the Eu^{2+} $5d$ - $4f$ emission, which can be explained as the result of auto-ionization.

10.1 Introduction

Ternary and quaternary silicon nitride based materials are composed of SiN_4 tetrahedrons in combination with alkali, alkaline earth and/or rare earth metal ions. The optical and luminescence properties of this class of materials are strongly affected by the metal to silicon ratio. When increasing the relative amount of metal, the degree of condensation, as determined by the silicon to nitrogen ratio, decreases

in the order of Si_3N_4 , SrSi_6N_8 [1], $\text{MSi}_7\text{N}_{10}$ ($M = \text{Sr}, \text{Ba}$) [2,3], $\text{M}_2\text{Si}_5\text{N}_8$ ($M = \text{Ca}, \text{Sr}, \text{Ba}$) [4,5], MYbSi_4N_7 ($M = \text{Sr}, \text{Ba}$) [6], MSiN_2 ($M = \text{Ca}, \text{Sr}, \text{Ba}$) [7], $\text{Ba}_5\text{Si}_2\text{N}_6$ [8] and M_4SiN_4 ($M = \text{Ca}, \text{Ba}$) [9,10]. A lower degree of condensation reduces the stability of the compound under atmospheric conditions, making for example BaSiN_2 , $\text{Ba}_5\text{Si}_2\text{N}_6$ and Ba_4SiN_4 water and air sensitive.

The degree of condensation not only influences the stability of the silicon nitride based compounds, but it also influences the energy difference between the $4f$ ground state and the $5d$ states of the lanthanides incorporated in these compounds when they are substituted on the metal sites. As an example, the wavelength of the lowest energy $4f$ - $5d$ transition of Eu^{2+} increases from about 380 nm in $\text{BaSi}_7\text{N}_{10}:\text{Eu}^{2+}$ [11] to about 520 nm in $\text{BaSiN}_2:\text{Eu}^{2+}$ [12] and increases from about 425 nm in $\text{SrSi}_6\text{N}_8:\text{Eu}^{2+}$ [13] to about 620 nm in $\text{Sr}_2\text{Si}_5\text{N}_8:\text{Eu}^{2+}$ [14,15]. In this aspect Eu^{2+} doped CaLaSiN_3 , and the related compounds EuLaSiN_3 and Eu_2SiN_3 are an extreme case, as recently reported by us [16]. The degree of condensation is relatively low and the lowest energy Eu^{2+} $4f$ - $5d$ transition is about 1240 nm in Eu_2SiN_3 and 885 nm in Eu^{2+} doped CaLaSiN_3 . The Eu^{2+} $4f$ - $5d$ energy in Eu_2SiN_3 is the lowest as compared to a whole range of other compounds. [17] Since it is known that the $4f$ - $5d$ energy of Eu^{2+} in a host lattice is related to the $4f$ - $5d$ energies of the other divalent and trivalent lanthanides in the same compound [18], the $4f$ - $5d$ energy of a trivalent lanthanide ion in this host, such as Ce^{3+} , is also expected to be at a very low energy, which might be of interest in the search for red or infrared emitting phosphors. The $4f$ - $5d$ transitions of Ce^{3+} and Pr^{3+} in CaLaSiN_3 are therefore studied in this work.

Besides the low energy $4f$ - $5d$ absorption band, another interesting property of Eu_2SiN_3 is the presence of two crystallographic different Eu sites of which one site is occupied by Eu^{2+} ions, while the other site is occupied by Eu^{3+} ions. [19] This raises the question whether other lanthanides could also be present with two different valencies in this class of materials. For this reason the optical properties of Sm and Yb as dopants in this compound are reported because these two elements are, next to Eu, often observed in the divalent and the trivalent state.

10.2 Experimental

10.2.1 Synthesis

All materials have been prepared via a high temperature solid-state reaction synthesis in a tube furnace that is connected to a nitrogen filled glove-box. For the synthesis of CaLaSiN₃, Ca₃N₂ (Alfa Aesar, 200 mesh, 98%) was mixed in a glove-box together with Si₃N₄ (Permascand, P95H, alpha content 93.2 wt.-%, oxygen content 1.5 wt.-%) and La powder (CSRE, 99%, 200 mesh) and ground in a mortar. The mixture was then heated twice, with intermediate grinding in between, in a furnace directly connected to this glove-box at 1400 °C for 12 hours in a N₂/H₂(10%) atmosphere. CaLaSiN₃ doped with the lanthanides were made in a similar way by adding Yb powder (Alfa Aesar, -325 mesh, 99.9%), Sm powder (Sigma Aldrich, -40 mesh, 99%), Ce powder (Sigma Aldrich, -40 mesh, 99.9%), Pr powder (Sigma Aldrich, -40 mesh, 99.9%) or EuN_x (prepared by the nitridation of europium metal (CSRE, 99.9%, lumps)) to the starting mixture.

10.2.2 Characterization and optical measurements

Crystalline phases were checked with X-ray powder diffraction (XRD) analysis with a Bruker D4 Endeavor with Cu K α radiation. Diffraction data were collected by step scanning from 12° to 65° in 2θ with a step size of 0.05° and a counting time of 1 s per step. Diffuse reflectance measurements in the UV/visible range were performed with a Perkin Elmer LS50B spectrophotometer with Xe lamp and an R952 photomultiplier. White BaSO₄ and black felt were used as a reference. Diffuse reflectance spectra in the red and infrared range were recorded with a Bruker Vertex 80v FT interferometer, using a tungsten lamp as a light source and TGS, InGaAs and Si detectors. KBr was taken as a reference. Excitation and emission measurements were recorded with a XP2254B PMT for visible light emission and a Hamamatsu H10330A-75 NIR PMT for infrared emission with two double grating monochromators using a xenon lamp as a light source.

10.3 Results and discussion

10.3.1 Phase formation

The X-ray diffraction pattern of CaLaSiN_3 is shown and discussed in reference [16]. All peaks could be related to the CaLaSiN_3 structure with space group $Cmca$ (64) except for some small diffraction peaks observed around 32° and 39.2° 2θ that could not be identified. The X-ray diffraction patterns of CaLaSiN_3 doped with 2% of a certain lanthanide are similar to that of the undoped one.

10.3.2 Ytterbium doped CaLaSiN_3

In Figure 10.1 the diffuse reflectance spectrum of a 2% Yb doped CaLaSiN_3 sample is shown and compared with an undoped sample. In the Yb doped sample, a relatively weak absorption feature is observed around 1.25 eV, as well as a strong absorption band above 2.5 eV. The first one, in the infrared, can be assigned to the well-known $4f-4f$ transition of Yb^{3+} from the $^2F_{7/2}$ ground state to the $^2F_{5/2}$ excited state, indicating that Yb is present in the trivalent state. The latter one, in the blue/UV part of the spectrum, is also observed in the undoped sample and is therefore attributed to host lattice absorption.

Excitation of the Yb doped sample with blue or UV light results in an emission line around 1.25 eV, as is also shown in Figure 10.1 (line 4). This emission can be assigned to the $f-f$ emission of Yb^{3+} from the $^2F_{5/2}$ excited state to the $^2F_{7/2}$ ground state. Besides this emission, no other emissions were observed. The excitation spectrum of this emission shows a broad band starting around 2.5 eV with a maximum at 3.4 eV. The origin of this band is host lattice excitation, possibly in combination with a charge transfer (CT) excitation due the transfer of an electron from nitrogen towards Yb^{3+} , which gives rise to the shoulder that is observed in the excitation spectrum around 3.0 eV. This indicates that the Yb^{3+} CT energy is about 3.1 eV, which is about the same energy as the energy of the CaLaSiN_3 host lattice absorption according to the diffuse reflectance spectrum.

This is different in other Yb³⁺ doped silicon nitride based compounds like LaSi₃N₅:Yb [20], YSi₃N₅:Yb [20] and SrAlSi₄N₇:Yb [21]. These materials have a somewhat larger band gap and in these compounds the CT band is clearly observed in the absorption and excitation spectra below the band gap energy.

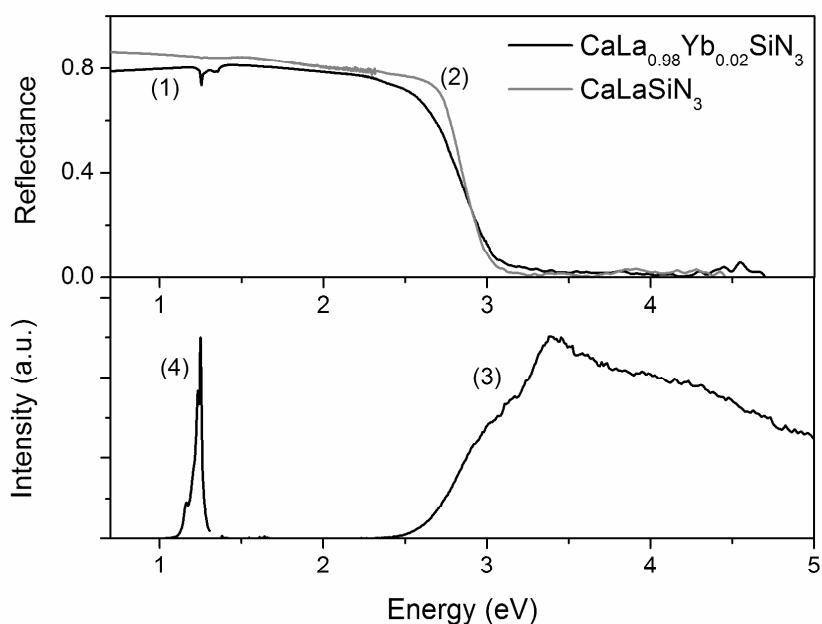


Figure 10.1: Diffuse reflectance spectrum of (1) CaLa_{0.98}Yb_{0.02}SiN₃ and (2) undoped CaLaSiN₃; and (3) excitation spectrum of the 1.25 eV emission and (4) emission spectrum of CaLa_{0.98}Yb_{0.02}SiN₃ excited at 3.1 eV.

In several Yb doped silicon nitride based compounds like SrAlSi₄N₇:Yb [21] and CaAlSiN₃:Yb [22] the Yb ion has been observed in the divalent state, as well as the trivalent state. However, no indications, for example in the form of 4*f*-5*d* absorption or 5*d*-4*f* emission, were found for the presence of Yb²⁺ in CaLaSiN₃. Synthesis of a sample with a stoichiometry Ca_{0.98}Yb_{0.02}LaSiN₃ or CaLa_{0.98}Yb_{0.02}SiN₃ both resulted in the presence of Yb³⁺ in comparable amounts. Furthermore, a fully doped Yb compound with the composition of Yb₂SiN₃ or YbLaSiN₃ (in which Yb is formally present in the divalent state) could not be

obtained. Synthesis resulted in a mixture of starting materials and unidentified phases.

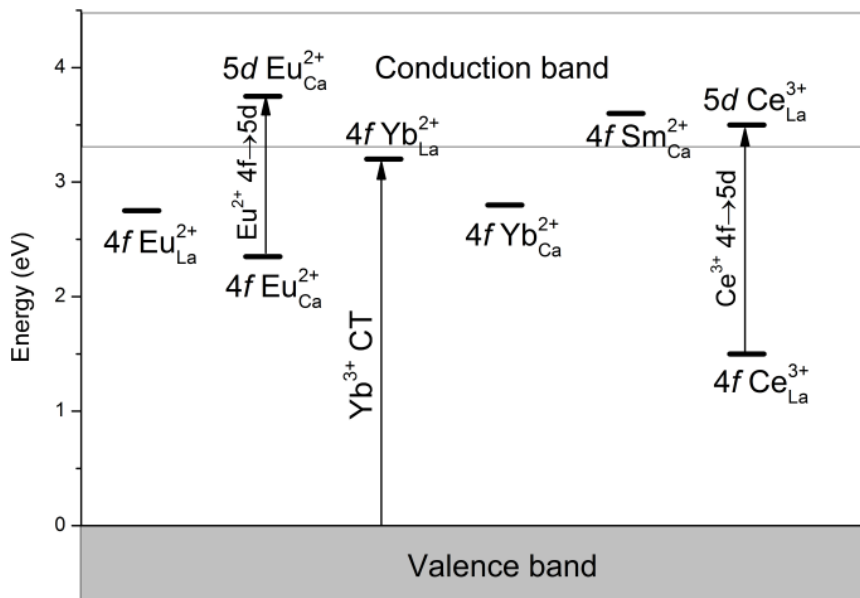


Figure 10.2: Estimation of the energy level positions of the lowest energy $4f$ and $5d$ levels of Eu^{2+} , Yb^{2+} , Sm^{2+} and Ce^{3+} on the La and Ca sites in CaLaSiN_3 relative to the top of the valence band.

Based on the diffuse reflectance spectrum, showing full host lattice absorption above 3.1 eV, the energy difference between the top of the valence band and the bottom of the conduction band is estimated at 3.3 eV. The $\text{Yb}^{2+}4f$ ground state should therefore be located just below the conduction band, as shown in Figure 10.2, since the Yb^{3+} CT energy of 3.1 eV is determined by the energy difference between the top of the valence band and the $\text{Yb}^{2+} 4f$ ground state. [23] As a result, Yb is unlikely to be formed in the divalent state, because Yb^{2+} will easily be oxidized to the trivalent state during synthesis, even under reducing atmospheric conditions, due to the small energy difference between the bottom of the conduction band and the $\text{Yb}^{2+} 4f$ ground state. [24] The $4f$ ground state of Yb^{2+} on a

Ca site is expected to be closer to the valence band than the 4f ground state of Yb²⁺ on a La site, because it will cost more energy to remove an electron from a divalent ion located on a divalent Ca site and bring it to the vacuum than when the ion would be located on a trivalent La site. If one assumes that Yb³⁺ is located on the La site, the 4f ground state of Yb²⁺ located on the Ca site could be somewhat below the bottom of the conduction band. However, it is expected that the energy difference between Yb²⁺ on the two crystallographic sites will be less than 0.5 eV since the 4f electron binding energy (with respect to the vacuum level) does not vary more than 0.5 eV. [25] This implies that also on the Ca site the 4f ground state of Yb²⁺ should still be close to the bottom of the conduction band, as represented in Figure 10.2, making Yb²⁺ unlikely to be formed. This would explain why Yb²⁺ containing Yb₂SiN₃ and YbLaSiN₃ could not be synthesized, and might not exist.

10.3.3. Europium doped CaLaSiN₃

It has been reported elsewhere [16] that no Eu²⁺ *d-f* emission was observed in 2% Eu doped CaLaSiN₃ after excitation with visible or UV light. This can now be explained using the results shown in Figure 10.2 for Yb doped CaLaSiN₃. The 4f ground state of Eu²⁺, if at the same crystallographic site, should be about 0.45 eV lower in energy than the ground state of Yb²⁺. [16] The 4f ground state of Eu²⁺ on the La site should therefore be located very close to the bottom of the conduction band, resulting in Eu³⁺. It is expected that the Eu²⁺ ground state is about 0.4 eV lower in energy on the Ca site, just as discussed above for Yb, which shifts the 4f ground state of Eu²⁺ apparently far enough below the bottom of the conduction band (i.e. below the Fermi level) to be stable as a divalent ion, as evidenced by the existence of EuLaSiN₃ and Eu₂SiN₃. [16,19] However, it is still unlikely that it is located more than 1 eV below the bottom of the conduction band. This implies, taking into account a lowest energy Eu²⁺ 4f-5d transition of 1.4 eV for Eu²⁺ doped CaLaSiN₃ [16], that the lowest energy 5d state of Eu²⁺ is located inside the conduction band (see Figure 10.2) causing the loss of an electron to the conduction band instead of 5d-4f emission. This quenching process is referred to as auto-

ionization and has been studied in detail in for example $\text{LaAlO}_3:\text{Ce}^{3+}$ [26] and $\text{CaF}_2:\text{Yb}^{2+}$ [27].

10.3.4 Samarium doped CaLaSiN_3

In the diffuse reflectance spectrum of a 2% Sm doped sample (Figure 10.3) several absorption features are observed between 0.8 and 1.3 eV as well as a very small peak around 2.6 eV. These absorptions can be attributed to $4f$ - $4f$ absorption lines of Sm^{3+} , as indicated in Figure 10.3. At higher energy above 2.8 eV host lattice absorption is observed as before. No f - f or f - d absorptions can be seen that can be related to Sm^{2+} . The ground state of Sm^{2+} is about 0.8 eV higher in energy [18] than the ground state of Yb^{2+} , making Sm^{2+} even more unstable than Yb^{2+} , since the $4f$ ground state of Sm^{2+} is even further inside the conduction band of the CaLaSiN_3 host lattice (see Figure 10.2).

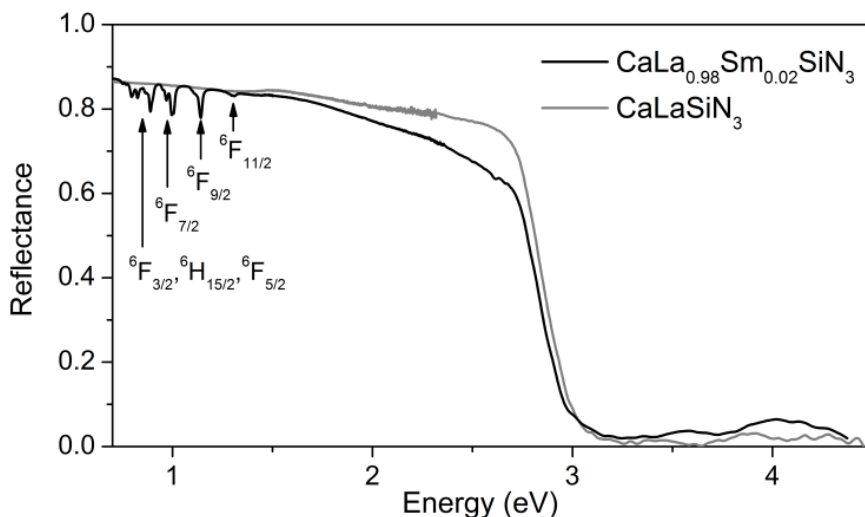


Figure 10.3: Diffuse reflectance spectrum of (1) $\text{CaLa}_{0.98}\text{Sm}_{0.02}\text{SiN}_3$ and (2) undoped CaLaSiN_3 .

The predictions for Sm are confirmed by luminescence excitation and emission spectra. Host excitation with UV light (4.28 eV) results in the emission spectrum

shown in Figure 10.4. It shows emission lines with maxima at 2.17, 2.04, 1.89 and, much weaker, 1.72 eV, due to emissions from the $^4G_{5/2}$ state to the $^6H_{5/2}$, $^6H_{7/2}$, $^6H_{9/2}$ and $^6H_{11/2}$ states of Sm^{3+} respectively. Furthermore a weak emission band is observed around 2.75 eV that cannot be assigned to any known transition of the Sm^{3+} ion and might be related to self-trapped exciton emission. The excitation spectrum of the 4f lines consists of several absorption lines between 2.2 and 3.2 eV that can be assigned to Sm^{3+} *f-f* transitions.

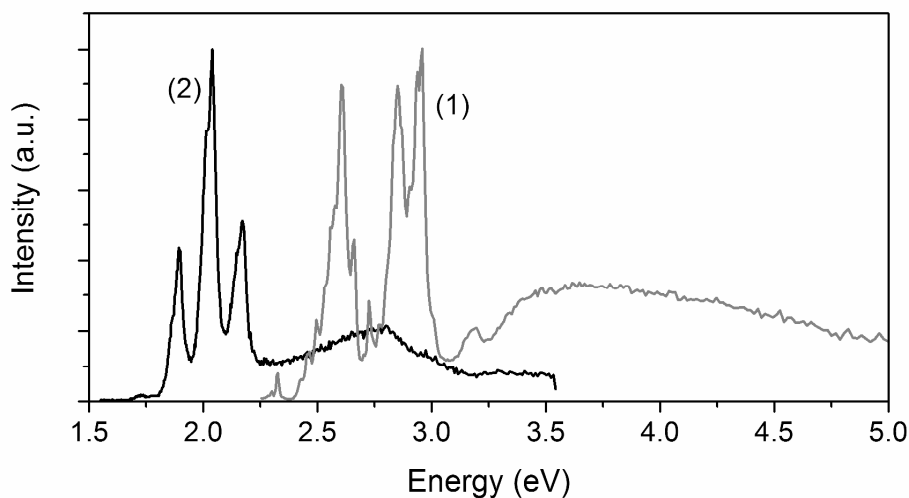


Figure 10.4: (1) Excitation spectrum of the 2.04 eV emission and (2) emission spectrum (excitation with 4.28 eV light) of $CaLa_{0.98}Sm_{0.02}SiN_3$.

10.3.5 Cerium doped $CaLaSiN_3$

The diffuse reflectance spectrum of a 2% Ce doped $CaLaSiN_3$ sample is shown in Figure 10.5. The Ce^{3+} *f-f* transition from the $^2F_{5/2}$ ground state to the $^2F_{7/2}$ excited state can be observed in the infrared between 0.2 and 0.45 eV. At higher energy a broad absorption band is observed starting at 1.4 eV with a maximum around 1.9 eV, as well as the earlier observed host lattice absorption above 2.8 eV. The band at about 1.9 eV can be assigned to Ce^{3+} *f-d* absorption. Note that, just as for Eu^{2+} ,

the energy of the Ce^{3+} f - d absorption is very low as compared to the f - d absorption band of Ce^{3+} in many other compounds. [28] Only the lowest energy Ce^{3+} $4f$ - $5d$ transition in $\text{MgSc}_2\text{S}_4:\text{Ce}^{3+}$ around 2.0 eV [29] is in the same range.

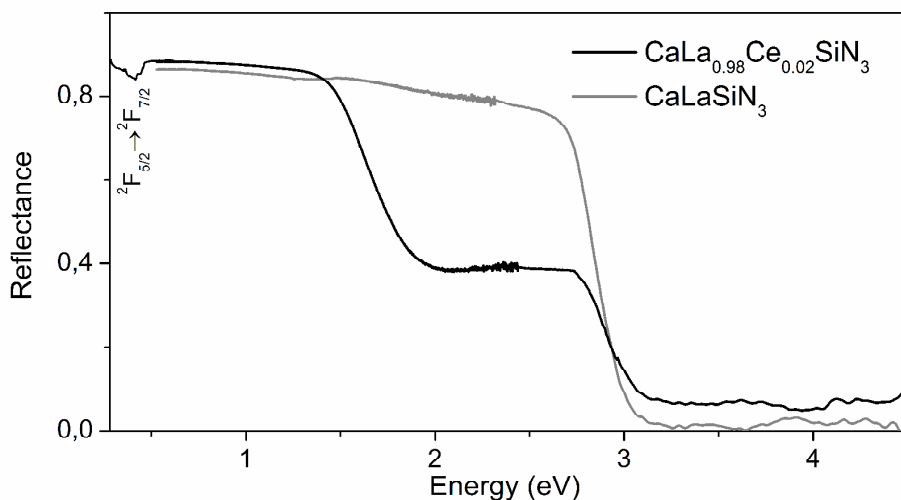


Figure 10.5: Diffuse reflectance spectrum of (1) $\text{CaLa}_{0.98}\text{Ce}_{0.02}\text{SiN}_3$ and (2) undoped CaLaSiN_3 .

No luminescence was observed after excitation with UV or visible light, indicating that all Ce^{3+} d - f emission is quenched. Cooling down the sample to a temperature of 10 K did not result in any emission either. This can be understood by considering the position of the Ce^{3+} $5d$ energy levels relative to the conduction band as depicted in Figure 10.2. Since it was concluded before that the Eu^{2+} $4f$ ground state on the lanthanum site is located about 0.5 eV below the bottom of the conduction band, we can estimate, by using the relations obtained by Dorenbos for the energy differences between divalent and trivalent lanthanide ions, that the Ce^{3+} $4f$ ground state is located about 1.7 eV below the bottom of the conduction band. The Ce^{3+} $4f$ - $5d$ transition observed around 1.9 eV thus means that the lowest energy Ce^{3+} $5d$ state is located inside the conduction band (see Figure 10.2), which explains why no Ce^{3+} d - f emission is observed as a consequence of quenching due to auto-ionization.

Ce³⁺ and Eu²⁺ 4f-5d transitions in CaLaSiN₃ have been observed around 1.9 and 1.4 eV respectively. These transitions are at the lowest energy observed so far compared to similar transitions in other compounds. [17,28] The unusual low energy of 4f-5d transitions in CaLaSiN₃ can be understood by considering that most of these other compounds are oxides and fluorides. The 4f-5d transitions in nitrides are generally of lower energy than in oxides or fluorides due to a lower electronegativity of the nitrides, resulting in a stronger nephelauxetic effect and thus a larger centroid shift. [30,31] Furthermore, CaLaSiN₃ has as a relatively high metal to silicon ratio as compared to other nitridosilicates, which lowers the degree of condensation and further reduces the energy of the 4f-5d transition.

3.6 Praseodymium doped CaLaSiN₃

The relatively low energy of the Ce³⁺ 4f-5d transition observed around 1.9 eV suggests low energy 4f-5d transitions for Pr³⁺ as well. However, the lowest energy Pr³⁺ 4f-5d transition is generally 1.5 eV higher in energy than the transition in Ce³⁺. This gives a lowest energy Pr³⁺ 4f-5d transition of around 3.5 eV, which is, though at a relatively low energy for Pr³⁺, still higher in energy than the band gap of CaLaSiN₃. As a result no 4f-5d transitions can be observed in the absorption spectrum of Pr³⁺ doped CaLaSiN₃ shown in Figure 10.6. Note that the typical Pr³⁺ 4f-4f absorptions from the ³H₄ ground state to the ¹G₄ (around 0.8 eV), ¹D₂ (around 2.0 eV) and ³P_J (around 2.5 eV) excited states can clearly be observed, as expected.

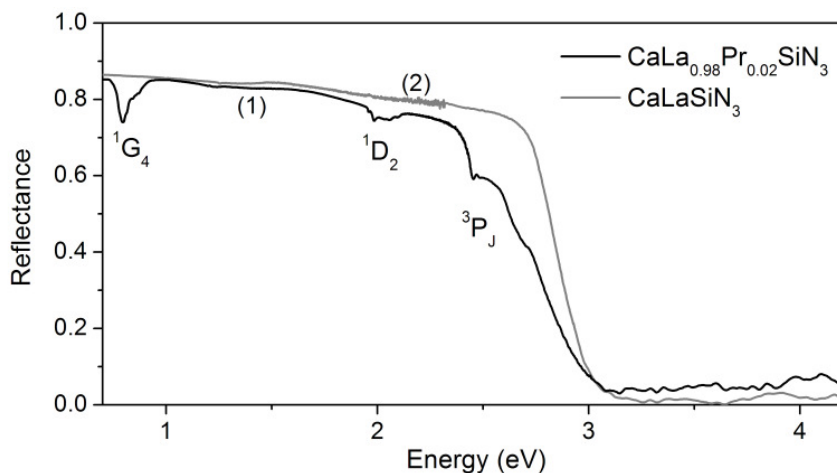


Figure 10.6: Diffuse reflectance spectrum of (1) $\text{CaLa}_{0.98}\text{Pr}_{0.02}\text{SiN}_3$ and (2) undoped CaLaSiN_3 .

10.4 Conclusions

This work shows that a very low degree of condensation of SiN_4 tetrahedra in the nitridosilicates results in a record low energy $4f$ - $5d$ transition of both Ce^{3+} and Eu^{2+} around 650 and 885 nm respectively. At the same time the low degree of condensation results in a smaller band gap and places the $4f$ ground states of Eu^{2+} and Ce^{3+} relatively close to the conduction band. As a result the $5d$ - $4f$ emission of Ce^{3+} and Eu^{2+} is quenched because the excited $5d$ states are located too close to or even inside the conduction band despite the low energy $4f$ - $5d$ transition.

Our work strongly underlines the importance of the energy of the divalent lanthanide ion ground state relative to the conduction band as reviewed earlier by Rogers et al. [32] and Dorenbos [33]. The existence of mixed valence Eu_2SiN_3 with both divalent and trivalent Eu ions appears to be caused by the small differences between the Eu^{2+} ground state energy relative to the conduction band of the two different crystallographic sites in the structure, that is only just right for Eu but not for all the other lanthanide ions. The inability to make YbLaSiN_3 or Yb^{2+} doped CaLaSiN_3 is the result of the Yb^{2+} ground state being too close to the conduction

band. The presence of the 3+ valence for Sm and Pr is caused by the fact that the 2+ ground state of these ions is inside the conduction band and therefore unstable.

10.5 References

- [1] F. Stadler, O. Oeckler, J. Senker, H. A. Höpfe, P. Kroll, W. Schnick; *Angew. Chem.* 117 (2005) 573.
- [2] C.M. Fang, H.T. Hintzen, G. de With; *J. Alloy. Compds.* 336 (2002) 1.
- [3] G. Pilet, H.A. Höpfe, W. Schnick, S. Esmailzadeh; *Solid State Sci.* 7 (2005) 391.
- [4] T. Schlieper, W. Schnick; *Z. Anorg. Allg. Chem.* 621 (1995) 1037.
- [5] T. Schlieper, W. Milius, W. Schnick; *Z. Anorg. Allg. Chem.* 621 (1995) 1380.
- [6] H. Huppertz, W. Schnick; *Z. Anorg. Allg. Chem.* 623 (1997) 212.
- [7] Z.A. Gál, P.M. Mallinson, H.J. Orchard, S.J. Clarke; *Inorg. Chem.* 43 (2004) 3998.
- [8] H. Yamane, F.J. DiSalvo; *J. Alloy. Compds.* 240 (1996) 33.
- [9] Y. Laurent; *Rev. Chim. Miner.* 5 (1968) 1019.
- [10] G. Lang; *C.R. Acad. Sci. II C* 268 (1969) 1785.
- [11] Y.Q. Li, A.C.A. Delsing, R. Metselaar, G. de With, H.T. Hintzen; *J. Alloy. Compds.* 487 (2009) 28-33.
- [12] C.J. Duan, X.J. Wang, W.M. Otten, A.C.A. Delsing, J.T. Zhao, H.T. Hintzen; *Chem. Mater.* 20 (2008) 1597.
- [13] K. Shioi, N. Hirosaki, R.J. Xie, T. Takeda, Y.Q. Li; *J. Mater. Sci.* 43 (2008) 5659.
- [14] Y.Q. Li, J.E.J. van Steen, J.W.H. van Krevel, G. Botty, A.C.A. Delsing, F.J. DiSalvo, G. de With, H.T. Hintzen; *J. Alloy. Compds.* 417 (2006) 273.
- [15] O.M. ten Kate, Z. Zhang, P. Dorenbos, H.T. Hintzen, E. van der Kolk; *J. Solid State Chem.* 197 (2013) 209.
- [16] O.M. ten Kate, T. Vranken, E. van der Kolk, A.P.J. Jansen, H.T. Hintzen; *J. Solid State Chem.* 213 (2014) 126.
- [17] P. Dorenbos; *J. Lumin.* 104 (2003) 239.

- [18] P. Dorenbos; *J. Phys.-Condens. Mat.* 15 (2003) 4797.
- [19] M. Zeuner, S. Pagano, P. Matthes, D. Bichler, D. Johrendt, T. Harmening, R. Pöttgen, W. Schnick; *J. Am. Chem. Soc.* 131 (2009) 11242.
- [20] O.M. ten Kate, H.T. Hintzen; P. Dorenbos; E. van der Kolk; *J. Mater. Chem.* 21 (2011) 18289.
- [21] Z. Zhang, O.M. ten Kate, A.C.A. Delsing, Z. Man, R. Xie, Y. Shen, M.J.H. Stevens, P.H.L. Notten, P. Dorenbos, J. Zhao, H.T. Hintzen; *J. Mater. Chem. C* 1 (2013) 7856.
- [22] Z. Zhang, O.M. ten Kate, A.C.A. Delsing, M.J.H. Stevens, J. Zhao, P.H.L. Notten, P. Dorenbos, H.T. Hintzen; *J. Mater. Chem.* 22 (2012) 23871.
- [23] P. Dorenbos; *J. Phys.-Condens. Mat.* 15 (2003) 8417.
- [24] P. Dorenbos; *J. Lumin.* 122-123 (2007) 315.
- [25] P. Dorenbos; *J. Lumin.* 135 (2013) 93.
- [26] E. van der Kolk, J.T.M. de Haas, A.J.J. Bos, C.W.E. van Eijk, P. Dorenbos; *J. Appl. Phys.* 101 (2007) 083703.
- [27] B. Moine, B. Courtois, C. Pedrini; *J. Phys. France* 50 (1989) 2105.
- [28] P. Dorenbos; *J. Lumin.* 91 (2000) 155.
- [29] M.M. Yuta, W.B. White, *J. Electrochem. Soc.* 139 (1992) 2347.
- [30] P. Dorenbos; *J. Lumin.* 136 (2013) 122.
- [31] M. Mikami, N. Kijima; *Opt. Mater.* 33 (2010) 145.
- [32] E. Rogers, P. Dorenbos, E. van der Kolk; *New Journal of Physics* 13 (2011) 093038.
- [33] P. Dorenbos; *J. Mater. Chem.* 22 (2012) 22344

Summary

Using solar cells to generate electricity would be a widely available, clean and sustainable way to supply the world with the electricity it needs everyday. Photovoltaic research over the last decades has resulted in solar panels, mostly made out of crystalline silicon (c-Si), that are nowadays available on the market. However, the relatively high price of solar electricity from these panels as compared to electricity from other energy sources such as coal, gas and nuclear power, requires new and more advanced concepts that result in cheaper and more efficient solar cells.

One of the concepts to improve solar cell efficiency is based on luminescent spectral conversion materials. Once integrated as a layer on top of a solar cell, these materials should absorb that fraction of the solar spectrum for which the cell has a poor response and convert the light into longer wavelengths for which the cell is more efficient. A concept to reduce costs of solar electricity and improve its integration into the built environment is to use relatively cheap luminescent materials in a so called luminescent solar concentrator (LSC) or power window. In an LSC window the solar light is absorbed and reemitted by a luminescent material, and because most of the emitted light is trapped inside the window like in an optical fiber cable, the light will be concentrated at the small edges of the window where PV cells are attached, reducing the amount of relatively expensive solar cells needed. Finding new types of luminescent materials for spectral conversion and luminescent solar concentration and investigating their optical properties are the main topics of this thesis.

The solar spectrum consists of a wide range of photons of different wavelengths from the UV up to the infrared. Many solar cells, particularly CdTe, but also CIGS and GaSb cells, are less efficient for blue and UV light than for red light. The efficiency of these cells might therefore be enhanced by the integration of a spectral shifting layer. In chapter 2 it has been calculated, based on the IQE curves of state-of-the-art cells, that the efficiency of existing CdTe and GaSb cells

can be enhanced with a relative percentage of 24 and 27 respectively if spectral shifting layers would be positioned on these cells.

Interesting candidate luminescent materials are lanthanide doped nitridosilicates. First of all because their luminescent properties can be tuned by varying their structure and composition, but secondly because amorphous silicon nitride is already used on top of solar cells as an anti-reflection and surface passivation layer. The optical properties of lanthanide doped silicon nitride based materials and their applicability as solar spectral conversion layers are therefore reported in chapters 3 and 4. It was found that LaSi_3N_5 can be doped with Yb^{3+} , resulting in a broad relatively low energy charge transfer (CT) absorption band around 400 nm. Due to this transition $\text{LaSi}_3\text{N}_5:\text{Yb}^{3+}$ absorbs UV and blue light and reemits the light via a narrow Yb^{3+} $4f-4f$ transition around 1000 nm. This would make it a suitable spectral conversion material in combination with c-Si cells, because the 1000 nm emission is just above the Si band gap. However, due to the low energy of the CT band, a large fraction of the emission is directly quenched to the ground state, making the spectral conversion quite inefficient. It has been shown that the CT band can be shifted upwards to 320 nm by replacing La by Y, which results in a more efficient UV to infrared conversion, but at the same time reduces the amount of solar light that can be absorbed.

In order to deeper understand the valencies and optical properties of different lanthanides when doped in silicon nitride based materials and with it their applicability as spectral conversion materials, a study of a series of lanthanide doped $\text{M}_2\text{Si}_5\text{N}_8$ ($\text{M} = \text{Ca}, \text{Sr}, \text{Ba}$) phosphors are reported in chapter 4. This study resulted in the construction of energy level diagrams with which the properties of other lanthanides in these hosts can be predicted. It was found that Tb^{3+} substitutes on both a low energy and a high energy site in $\text{Ca}_2\text{Si}_5\text{N}_8$, giving rise to a difference in the Tb^{3+} $f-f$ emissions between Tb^{3+} ions substituted at different sites. Furthermore a Sm^{3+} CT band has been observed in $\text{Ca}_2\text{Si}_5\text{N}_8$ and $\text{Sr}_2\text{Si}_5\text{N}_8$.

Instead of improving solar cell efficiency by just shifting the UV and blue photons to longer wavelengths, much higher efficiencies can be obtained with so called quantum cutting layers that cut a high energy photon into two lower energy

photons that can still be absorbed by the solar cell. Efficiency calculations in chapter 2 show that an ideal quantum cutting layer enhances solar cell efficiencies with a relative percentage of 12 for c-Si solar cells to 85 for GaSb cells. But although this principle is known to work in a Tb^{3+} - Yb^{3+} co-doped material, where a blue photon absorbed by Tb^{3+} is transferred to two neighboring Yb^{3+} ions, the actual application in any real device is still a castle in the air not only due to poor UV and blue light absorption by Tb^{3+} , but also due the need for very high Yb^{3+} concentrations that are required for an efficient energy transfer, but that at the same time quench the Yb^{3+} *f-f* emission. Other lanthanide couples have therefore been proposed, such as Pr^{3+} - Yb^{3+} and Ce^{3+} - Yb^{3+} couples. Unfortunately, it was shown in chapter 5 that for these couples additional problems arise. In case of the Pr^{3+} - Yb^{3+} ion couple back-transfer was observed from an excited Yb^{3+} ion to the $^1\text{G}_4$ level of Pr^{3+} resulting in emissions too far in the infrared that cannot be absorbed anymore by a Si solar cell. In case of the Ce^{3+} - Yb^{3+} ion couple it was shown that the energy transfer from Ce^{3+} to Yb^{3+} does not necessarily go via a quantum cutting process, but is more likely to take place via a charge transfer in which no quantum cutting is involved, but only spectral shifting.

For solar cells with small band gaps such as GaSb and Ge cells, quantum tripling layers might be useful, in which a high energy photon is not cut into two lower energy photons but into three photons that can still be absorbed by the solar cell. Tm^{3+} doped $\text{La}_2\text{BaZnO}_5$ has been studied for this purpose and is reported in chapter 6. It was concluded that due to the small distances between the Tm^{3+} ions, the cross-relaxations between neighboring Tm^{3+} ions become more efficient. This results in a decrease of emissions from the $^1\text{G}_4$ state with increasing Tm^{3+} concentrations in favor of an enhanced $^3\text{F}_4 \rightarrow ^3\text{H}_6$ emission around 1700 nm. For relatively high Tm concentrations, however, concentration quenching starts to limit the efficiency.

Luminescent materials might be used in an LSC to trap solar light in a waveguide and concentrate the emitted light on small solar cells at the edges. Though this concept exists already for more than 40 years, any commercial application has not yet been realized, because a luminescent material that fulfills all

necessary requirements has never been found. The material should be able to absorb a broad part of the solar spectrum and reemit the light with a near unity quantum efficiency without self-absorbing the emitted light. Especially the self-absorption before the light reaches the LSC-PV edge severely limits the efficiency of a power window of any practical dimensions. With the self-absorption model presented in chapter 7 it has been calculated that the efficiency of an LSC with a radius of 50 cm containing a Red 305 dye decreases with a factor of four due to self-absorption. A strongly absorbing, efficiently emitting material with no self-absorption is therefore required and seems to be found in a class of Tm^{2+} doped halides that are discussed in chapter 8. Doping Tm^{2+} in simple halide structures as NaCl, NaI or CaI_2 resulted in strong $4f-5d$ absorption by Tm^{2+} . Because of splitting of the $Tm^{2+} 4f^{12}5d^1$ configuration in many different levels, the $4f-5d$ absorption has a wide range from the UV up to as far as 900 nm. After absorption the light is efficiently emitted around 1140 nm due to a $Tm^{2+} 4f-4f$ transition with limited self-absorption. The materials might therefore lead to colorless tinted power windows that can be integrated into buildings, with power efficiencies that could be more than four times higher than those obtained with LSCs based on existing organic dyes.

As mentioned before, the optical properties of lanthanide doped silicon nitride based materials can be tuned by changing their structures and compositions. Tuning is achieved for example by reducing the Si to N ratio, which makes these materials more sensitive to oxidation, but at the same time results in lower energy $4f-5d$ transitions. An extreme example of this are the $MLSiN_3$ compounds discussed in chapter 9 and 10 in which M is a divalent and L is a trivalent ion. Interestingly, both the divalent and the trivalent site can be occupied by europium, resulting in mixed valence Eu_2SiN_3 , which is the only nitridosilicate reported so far in which europium is present in the trivalent state. It was found that the black color of Eu_2SiN_3 is due to a very low energy $4f-5d$ transition of Eu^{2+} and a low energy CT band of Eu^{3+} . The existence of materials with a similar structure has been predicted with density functional theory calculations and three new compounds were actually synthesized and optically characterized: $EuLaSiN_3$, $CaEuSiN_3$ and

CaLaSiN₃. When the latter one was doped with Eu²⁺ or Ce³⁺, very low energy 4*f*-5*d* transitions were observed for these ions, as compared to the same transitions observed in other compounds.

The different topics discussed in this thesis have in common that they are related to the question whether the luminescent properties of lanthanide ions can be used to improve PV devices. Some approaches, such as the Yb³⁺ CT band for spectral conversion, turned out to be inefficient and any application of this concept seems far away. Nevertheless, more knowledge about the energy levels of the lanthanides in silicon nitride based materials was obtained, which might be useful for other research. Some other concepts on the other hand seem to have more potential towards future PV application. Nice examples hereof are the Tm²⁺ doped halides, of which the application in a power window has been patented recently (EP19564-Vi/t; *Tm²⁺ materials for solar radiation conversion devices*). These strongly absorbing luminescent materials without self-absorption might find their way towards building integrated power windows.

Samenvatting

Het opwekken van elektriciteit met behulp van zonnecellen zou een schone, duurzame en breed toepasbare manier zijn om de wereld in haar dagelijkse elektriciteitsbehoefte te voorzien. Het zonnecelonderzoek van de afgelopen decennia heeft geleid tot zonnepanelen, voornamelijk gemaakt van kristallijn silicium, die vandaag de dag commercieel verkrijgbaar zijn. Maar de elektriciteit die met zonnecellen opgewekt wordt, is nog altijd relatief duur ten opzichte van de traditionelere energiebronnen als kolen, gas en uranium. Nieuwe, geavanceerde concepten die leiden tot efficiëntere en goedkopere zonnecellen zijn daarom gewenst.

Een van de manieren om de efficiëntie van zonnecellen te verbeteren is gebaseerd op luminescerende spectrale conversiematerialen. Eenmaal gepositioneerd als een laag bovenop een zonnecel moeten deze materialen de fractie van het zonlicht waarvoor de cel een slechte respons heeft, omzetten naar licht van langere golflengtes waarvoor de cel efficiënter is. Een manier om de kosten van elektriciteit uit zonne-energie te reduceren, is een zogenaamde luminescerende zonneconcentrator of stroomraam. Hierin wordt het zonlicht geabsorbeerd en opnieuw geëmitteerd door een luminescerend materiaal. Doordat het meeste geëmitteerde licht opgesloten zit in het raam, net als in een glasvezelkabel, zal het licht geconcentreerd worden op de smalle randen van het raam waar zonnecellen zijn bevestigd. Hierdoor kan de benodigde hoeveelheid dure zonnecellen worden verminderd. Het vinden van nieuwe luminescerende materialen voor zonnecellen en het bestuderen van de optische eigenschappen van deze materialen zijn de belangrijkste onderwerpen van dit proefschrift.

Het zonlicht bestaat uit een breed spectrum aan fotonen met verschillende golflengten van het UV tot in het infrarood. Veel zonnecellen, in het bijzonder CdTe, maar ook GaSb en CIGS, zijn minder efficiënt voor blauw en UV licht dan voor rood licht. De efficiëntie van deze cellen kan daarom verbeterd worden door de integratie van een spectrale conversielaag. In hoofdstuk 2 is berekend op basis

van interne kwantumefficiëntiecurves dat de efficiëntie van bestaande CdTe en GaSb cellen met respectievelijk 24% en 27% verbeterd kunnen worden als er spectrale conversielagen op deze cellen geplaatst worden.

De met lanthaniden gedoteerde nitridosilicaten zijn interessante kandidaten voor toepassing als spectrale conversiematerialen voor zonnecellen. Ten eerste omdat de luminescentie-eigenschappen geoptimaliseerd kunnen worden door de structuur en compositie van deze materialen te variëren, maar ook omdat amorf siliciumnitride al toegepast wordt op zonnecellen als anti-reflectie- en oppervlaktepassivatielaag. De optische eigenschappen van de met lanthaniden gedoteerde op siliciumnitride gebaseerde materialen en hun toepasbaarheid als spectrale conversielagen op zonnecellen zijn daarom gerapporteerd in hoofdstukken 3 en 4. Er werd aangetoond dat LaSi_3N_5 gedoteerd kan worden met Yb^{3+} , wat resulteert in een brede ladingsoverdrachtsabsorptieband bij een relatief lage energie rond 400 nm. Ten gevolge van deze overgang absorbeert $\text{LaSi}_3\text{N}_5:\text{Yb}^{3+}$ UV en blauw licht en emitteert het dit licht weer via een smalle Yb^{3+} $4f-4f$ overgang rond 1000 nm. Dit zou het tot een geschikt spectrale conversiemateriaal maken in combinatie met kristallijn silicium zonnecellen, omdat de emissie van 1000 nm net iets hoger dan de bandkloof van silicium ligt. De lage energie van de ladingsoverdrachtsband heeft echter tot gevolg dat er een grote kans is tot directe relaxatie naar de grondtoestand zonder dat er emissie plaatsvindt, waardoor de efficiëntie van de spectrale conversie vrij laag is. De ladingsoverdrachtsband kan naar 320 nm verschoven worden door lanthaan te vervangen door yttrium, wat zorgt voor een efficiëntere UV naar infrarood conversie. Tegelijkertijd zorgt de substitutie er echter voor dat het materiaal veel minder zonlicht kan absorberen.

Met als doel de valenties en optische eigenschappen van de lanthaniden in nitridosilicaten beter te begrijpen en de toepasbaarheid als spectrale conversiematerialen te bepalen, zijn de met lanthaniden gedoteerde $\text{M}_2\text{Si}_5\text{N}_8$ -verbindingen ($\text{M} = \text{Ca}, \text{Sr}, \text{Ba}$) in hoofdstuk 4 gerapporteerd. Deze studie heeft geleid tot de constructie van energieschema's waarmee de eigenschappen van de lanthaniden in deze gastroosters voorspeld kunnen worden. Er werd onder andere

gevonden dat Tb^{3+} zowel op een lage als een hoge energiepositie in $Ca_2Si_5N_8$ gesubstitueerd kan worden, wat zorgt voor een verschil in Tb^{3+} $f-f$ emissies tussen Tb^{3+} ionen die op de verschillende posities zitten. Daarnaast werd er een Sm^{3+} ladingsoverdrachtsband waargenomen in $Ca_2Si_5N_8$ en $Sr_2Si_5N_8$.

In plaats van de efficiëntie van zonnecellen te verbeteren door de UV en blauwe fotonen slechts te converteren naar langere golflengten, zouden veel hogere efficiënties verkregen kunnen worden met zogenaamde kwantumknippende lagen. Deze kunnen een hoog energetisch foton splitsen in twee fotonen met een lagere energie die beide nog steeds in de zonnecel geabsorbeerd kunnen worden. Efficiëntieberekeningen in hoofdstuk 2 laten zien dat een ideale kwantumknippende laag de zonnecel efficiënties met relatief 12% zou kunnen verbeteren in het geval van kristallijn silicium zonnecellen en met 85% in het geval van GaSb cellen. Maar ondanks dat het principe werkt in een Tb^{3+} - Yb^{3+} gecodoteerd materiaal, waarin een door Tb^{3+} geabsorbeerd blauw foton overgedragen wordt aan twee naburige Yb^{3+} ionen, is de daadwerkelijke toepassing op een echte zonnecel nog steeds een luchtkasteel. Niet alleen vanwege de zwakke absorptie van blauw en UV licht door Tb^{3+} , maar ook vanwege de erg hoge Yb^{3+} -concentratie die nodig is voor een efficiënte energieoverdracht maar die tegelijkertijd de Yb^{3+} $f-f$ emissie stilt. Daarom zijn er alternatieve lanthanidekoppels voorgesteld, zoals Pr^{3+} - Yb^{3+} en Ce^{3+} - Yb^{3+} . Helaas werd er in hoofdstuk 5 laten zien dat deze koppels tot andere problemen leiden. In het geval van het Pr^{3+} - Yb^{3+} koppel werd waargenomen dat de energie teruggaat van een aangeslagen Yb^{3+} ion naar het 1G_4 niveau van Pr^{3+} , wat zorgt voor emissies te ver in het infrarood die niet meer door een silicium zonnecel geabsorbeerd kunnen worden. En in het geval van het Ce^{3+} - Yb^{3+} koppel werd aangetoond dat de energieoverdracht van Ce^{3+} naar Yb^{3+} niet noodzakelijkerwijs plaatsvindt via een kwantumknipproces, maar dat het veel waarschijnlijker is dat er een ladingsoverdrachtsproces plaatsvindt, hetgeen niet resulteert in een verdubbeling van het aantal fotonen, maar slechts in spectrale verschuiving.

Voor zonnecellen met een kleine bandkloof zoals GaSb en Ge cellen, zouden kwantumverdrievoudigende lagen, waarin een hoog energetisch foton gesplitst

wordt in drie in plaats van twee fotonen, rendabel kunnen zijn. Tm^{3+} gedoteerd $\text{La}_2\text{BaZnO}_5$ werd daarom bestudeerd en is in hoofdstuk 6 gerapporteerd. Er werd geconcludeerd dat door de kleine afstanden tussen de Tm^{3+} ionen in dit materiaal de kruisrelaxaties tussen naburige Tm^{3+} ionen efficiënter worden. Dit resulteert in een afname van de emissie vanuit de $^1\text{G}_4$ toestand bij toenemende Tm^{3+} concentraties ten gunste van een verhoogde $^3\text{F}_4 \rightarrow ^3\text{H}_6$ emissie rond 1700 nm. Bij relatief hoge Tm^{3+} concentraties wordt de efficiëntie echter gelimiteerd door concentratiestilling.

Luminescerende zonneconcentrators kunnen gebruikt worden om zonlicht in te vangen in een golfgeleider en het geëmitteerde licht te concentreren op kleine zonnecellen aan de randen. Alhoewel dit concept al meer dan veertig jaar bestaat, is een commerciële toepassing nog niet gerealiseerd, omdat een geschikt luminescerend materiaal dat aan alle eisen voldoet nog niet gevonden is. Het materiaal zou in staat moeten zijn een groot deel van het zonnenspectrum te absorberen en licht te emitteren met een hoge kwantumefficiëntie zonder zelfabsorptie van het geëmitteerde licht. Met name de zelfabsorptie voordat het licht de randen van het raam bereikt limiteert de efficiëntie fors. Met het zelfabsorptiemodel dat gepresenteerd is in hoofdstuk 7 is berekend dat de efficiëntie van een stroomraam met een straal van 50 cm waarin de Red 305 kleurstof zit, afneemt met een factor vier ten gevolge van zelfabsorptie. Een sterk absorberend, efficiënt emitterend materiaal zonder zelfabsorptie is daarom gewenst. Een groep van Tm^{2+} gedoteerde haliden die besproken wordt in hoofdstuk 8 lijkt deze gewenste eigenschappen te bezitten. Het doteren van Tm^{2+} in eenvoudige haliden zoals NaCl, NaI of CaI_2 resulteert in een sterke $4f-5d$ overgang van Tm^{2+} . Vanwege de opsplitsing van de $\text{Tm}^{2+} 4f^{12}5d^1$ configuratie in veel verschillende niveaus heeft de $4f-5d$ absorptie een groot bereik van het UV tot aan 900 nm. Na absorptie wordt het licht efficiënt geëmitteerd rond 1140 nm vanwege een $\text{Tm}^{2+} 4f-4f$ overgang die weinig zelfabsorptie heeft. De materialen hebben dus de potentie te leiden tot kleurloze getinte stroomramen die in gebouwen kunnen worden geïntegreerd met efficiënties die meer dan vier keer hoger kunnen zijn dan de

efficiënties die behaald worden met stroomramen die gebaseerd zijn op bestaande organische kleurstoffen.

Zoals eerder genoemd kunnen de optische eigenschappen van de met lanthaniden gedoteerde nitridosilicaten afgesteld worden door de structuur en compositie aan te passen. Het afstellen wordt bewerkstelligd door bijvoorbeeld de Si-over-N-verhouding te verkleinen. Hierdoor worden deze materialen gevoeliger voor oxidatie, maar komen tegelijkertijd de $4f-5d$ overgangen bij lagere energie te liggen. Een extreem voorbeeld hiervan zijn de $MLSiN_3$ verbindingen die besproken zijn in hoofdstukken 9 en 10, alwaar M een tweewaardig en L een driewaardig kation is. Interessant is dat zowel de tweewaardige als de driewaardige positie door europiumionen bezet kunnen worden, wat resulteert in Eu_2SiN_3 met een gemengde valentie. Dit is de enige bekende nitridosilicaat waarin europium aanwezig is in de driewaardige toestand. De zwarte kleur van dit materiaal werd verklaard door een combinatie van een laag-energetische $4f-5d$ overgang van Eu^{2+} en een laag-energetische ladingsoverdrachtsband van Eu^{3+} . Het bestaan van materialen met een vergelijkbare structuur kon worden voorspeld met dichtheidsfunctionaaltheorieberekeningen en drie nieuwe verbindingen werden ook daadwerkelijk gemaakt en optisch gekarakteriseerd: $EuLaSiN_3$, $CaEuSiN_3$ en $CaLaSiN_3$. Het doteren van Eu^{2+} of Ce^{3+} in $CaLaSiN_3$ resulteerde in $4f-5d$ overgangen met een zeer lage energie in vergelijking met dezelfde overgangen die waargenomen zijn in andere verbindingen.

De verschillende onderwerpen die in die proefschrift behandeld zijn, hebben gemeen dat ze gerelateerd zijn aan de vraag of de luminescentie-eigenschappen van de lanthanide-ionen gebruikt kunnen worden om zonnecellen te verbeteren. Sommige concepten, zoals spectrale conversie via de Yb^{3+} ladingsoverdrachtsband, bleken niet efficiënt te zijn. Desalniettemin, werd er wel meer kennis verkregen over de energieniveaus van de lanthaniden in nitridosilicaten, hetgeen mogelijk van nut kan zijn bij toekomstig onderzoek. Andere concepten daarentegen hebben meer potentie om in de toekomst toegepast te kunnen worden, met name de Tm^{2+} gedoteerde haliden voor stroomramen die onlangs gepatenteerd zijn (EP19564-Vi/td; *Tm²⁺ materials for solar radiation conversion devices*). Deze sterk

absorberende luminescerende materialen zonder zelfabsorptie kunnen mogelijk leiden tot stroomramen die in gebouwen kunnen worden geïntegreerd.

Acknowledgements

All other chapters of this thesis have been written, so it is time to write the final, and probably by far most read chapter of this whole thesis: the acknowledgements. In this way I would like to thank everyone who has contributed in either a direct or indirect way to this thesis and without whom this thesis would not have become to what it is now. Of all people that fall in that category there are a few that I would like to mention explicitly.

First of all I would like to thank my supervisor and copromotor Erik van der Kolk. Of course for giving me the opportunity to carry out this PhD project, but especially for his enthusiasm and ideas and the fruitful discussions we had. I am also very thankful to my promotor Pieter Dorenbos for keeping a watch on the progress of the PhD project and for his knowledge on the energy levels of the lanthanides, which appeared to be of great help for explaining the experimental results. Special thanks are there also for Bert Hintzen who initially introduced me in Eindhoven to the field of luminescent materials research. I very much appreciate his useful comments and suggestions on my papers during the whole PhD project, especially concerning the silicon nitride based materials.

My thanks also go to Anneke Delsing for her great help in the lab in Eindhoven. Thanks to her reparations I could continue using the furnace each time after it broke. I also very much appreciate the help of Zhijun Zhang for bringing my samples in and out of the furnace, which saved me a lot of extra travelling between Delft and Eindhoven. I appreciate the discussions we had on the nitride based materials.

I would like to thank Karl Krämer for giving me the opportunity to visit his group in Bern in order to synthesize the Tm^{2+} doped halides and I thank Daniel Biner for his help with the experimental work over there. Speaking about Tm^{2+} doped materials, I should of course not forget to mention Bert Swart. Thanks to his preparedness to use the quartz burner for melting the powders, we were able to create the black powders in Delft as well.

There are two chapters in this thesis that would for sure not have existed in the present form without the help of two Master students. The experimental work and DFT calculations on Eu_2SiN_3 related materials by Thomas Vranken were of great importance for chapter 9 and the Matlab work done by Koen Hooning on the self-absorption in luminescent solar concentrators gave rise to chapter 7 of this thesis. I thank both of you for your contributions to this work.

Furthermore I would like to thank Michiel de Jong for our discussions on silicon nitrides and Tm^{2+} doped halides and on the efficiency calculations of spectral conversion materials. I also thank Johan de Haas and John Vlieland for their technical assistance in the lab, Edith Rogers for her help with the Bruker and Oleksandra Ivashchenko for designing the cover of this thesis.

Doing four years of PhD research would have been much less fun without any colleagues around whether it was at the coffee table, during lunch, at the bar, at conferences, in Val Thorens or somewhere else. I thank you all for having a great time.

Finally, I want to thank Anne ten Kate and William van der Graaff for their willingness to support me as paranymphs during my thesis defense. And I am grateful to all my friends and family for their company and support during the last four years.

Melvin
Delft, July 2014

Curriculum vitae

Otmar Melvin ten Kate was born on 13 June 1986 in Delft. He obtained his gymnasium diploma at the Stedelijk Gymnasium Breda in 2004. During the period from 2004 to 2010, Melvin did his bachelor and master studies in Chemical Engineering and Chemistry at Eindhoven University of Technology. The master was concluded with a project on ‘p-type and n-type materials for tandem polymer solar cells’ in the group of prof. dr. ir. R.A.J. Janssen.

In February 2010 Melvin started a PhD project entitled ‘Spectral conversion materials for solar cells’, which was part of the Joint Solar Programme (JSP) of the Stichting voor Fundamenteel Onderzoek der Materie (FOM). The project was supervised by prof. dr. P. Dorenbos, dr. E. van der Kolk and dr. H.T. Hintzen and was carried out at Delft University of Technology and Eindhoven University of Technology. The results of this PhD project are presented in this thesis.



List of publications

E. van der Kolk, **O.M. ten Kate**, J.W. Wiegman, D. Biner, K.W. Krämer
Enhanced 1G_4 emission in $\text{NaLaF}_4:\text{Pr}^{3+}, \text{Yb}^{3+}$ and charge transfer in $\text{NaLaF}_4:\text{Ce}^{3+}, \text{Yb}^{3+}$ studied by Fourier transform luminescence spectroscopy
Optical Materials 33 (2011) 1024-1027.

O.M. ten Kate, H.T. Hintzen, P. Dorenbos, E. van der Kolk
 Yb^{3+} doped LaSi_3N_5 and YSi_3N_5 with low energy charge transfer for near infrared light-emitting diode and solar cell application
Journal of Materials Chemistry 21 (2011) 18289-18294.

Z. Zhang, **O.M. ten Kate**, A. Delsing, E. van der Kolk, P.H.L. Notten, P. Dorenbos, J. Zhao, H.T. Hintzen
Photoluminescence properties and energy level locations of RE^{3+} ($\text{RE} = \text{Pr}, \text{Sm}, \text{Tb}, \text{Tb/Ce}$) in CaAlSiN_3 phosphors
Journal of Materials Chemistry 22 (2012) 9813-9820.

Z. Zhang, **O.M. ten Kate**, A.C.A. Delsing, M.J.H. Stevens, J. Zhao, P.H.L. Notten, P. Dorenbos, H.T. Hintzen
Photoluminescence properties of Yb^{2+} in CaAlSiN_3 as a novel red-emitting phosphor for white LEDs
Journal of Materials Chemistry 22 (2012) 23871-23876.

O.M. ten Kate, Z. Zhang, P. Dorenbos, H.T. Hintzen, E. van der Kolk
4f and 5d energy levels of the divalent and trivalent lanthanide ions in $\text{M}_2\text{Si}_5\text{N}_8$ ($\text{M} = \text{Ca}, \text{Sr}, \text{Ba}$)
Journal of Solid State Chemistry 197 (2013) 209-217.

O.M. ten Kate, M. de Jong, H.T. Hintzen, E. van der Kolk

Efficiency enhancement calculations of state-of-the-art solar cells by luminescent layers with spectral shifting, quantum cutting, and quantum tripling function

Journal of Applied Physics 114 (2013) 084502.

Z. Zhang, **O.M. ten Kate**, A.C.A. Delsing, Z. Man, R. Xie, Y. Shen, M.J.H. Stevens, P.H.L. Notten, P. Dorenbos, J. Zhao, H.T. Hintzen

Preparation, electronic structure and photoluminescence properties of RE (RE = Ce, Yb)-activated SrAlSi₄N₇ phosphors

Journal of Materials Chemistry C 1 (2013) 7856-7865.

O.M. ten Kate, T. Vranken, E. van der Kolk, A.P.J. Jansen, H.T. Hintzen

Optical properties of Eu²⁺/Eu³⁺ mixed valence, silicon nitride based materials

Journal of Solid State Chemistry 213 (2014) 126-131.

O.M. ten Kate, K.M. Hooning, E. van der Kolk

Quantifying self-absorption losses in luminescent solar concentrators

Applied Optics (accepted for publication)

O.M. ten Kate, H.T. Hintzen, E. van der Kolk

Low energy 4f-5d transitions in lanthanide doped CaLaSiN₃ with low degree of cross-linking between SiN₄ tetrahedra

Journal of Physics: Condensed Matter (accepted for publication)

O.M. ten Kate, E. van der Kolk

Quantum tripling in Tm³⁺ doped La₂BaZnO₅ phosphors for efficiency enhancement of small band gap solar cells

Journal of Luminescence (submitted)

Z. Zhang, **O.M. ten Kate**, A. Delsing, P. Dorenbos, J. Zhao, H.T. Hintzen
Photoluminescence properties of Pr^{3+} , Sm^{3+} and Tb^{3+} doped $SrAlSi_4N_7$ and energy level locations of rare earth ions in $SrAlSi_4N_7$
Journal of Materials Chemistry C (submitted)

O.M. ten Kate, K.W. Krämer, E. van der Kolk
Self-absorption free ultra broad-band absorbing, colorless, Tm^{2+} doped halides for highly efficient luminescent solar concentrators
Advanced Energy Materials (submitted)

